POLITECNICO DI MILANO

Facoltà di Ingegneria Industriale

Corso di Laurea in
Ingegneria Energetica

Modeling On/Off – Design performance of solar tower plants

Relatore: Prof. Stefano CAMPANARI

Co-relatore: Prof. David SÁNCHEZ
(*Universidad de Sevilla*)

Co-relatore: Prof. Paolo SILVA

Co-relatore: Ing. Giampaolo MANZOLINI

Co-relatore: Prof. Giovanni FRACASTORO
(*Politecnico di Torino*)

Tesi di Laurea di:

Filippo COLZI Matr. 721437

Stefano PETRUCCI Matr. 719471

Anno Accademico 2008 - 2009

Ringraziamenti

Sinceri ringraziamenti a tutti quelli che hanno contribuito allo sviluppo di questo lavoro, dal punto di vista didattico e da quello personale. Grazie ai Prof. Campanari e Silva e all'Ing. Manzolini per la supervisione, il supporto didattico e per averci sostenuto fin dall'inizio in questa collaborazione Italo-Spagnola. Grazie per il tempo dedicato e l'attento lavoro di comunicazione sia nell'ambito della Tesi stessa che della pubblicazione correlata. Grazie anche al Prof. Fracastoro, del Politecnico di Torino, per la sua collaborazione. Grazie ai Dott. Giostri e Saccilotto per averci permesso di utilizzare il loro lavoro nella fase iniziale del progetto.

Gracias al Prof. Sanchez, para todo el tiempo y la pasion que ha dedicado a este trabajo, para el continuo y costante soporte en todos los sentidos, para su competencia y profesionalidad y para hacernos siempre sentir a gusto! Gracias tambien a Jose, y a todos los miembros del Departemento de Maquinas y Motores Termicos de la Universidad de Sevilla que nos han aconsejado y ayudado de una o otra manera durante los ultimos meses.

Grazie ai nostri genitori, per averci permesso di arrivare a questo punto e per averci assecondato e sostenuto in questo progetto. Grazie a tutti gli altri membri delle famiglie: fratelli, sorelle, cugini, nonni e zii!

Grazie a Tecla (soprattutto da parte di Filippo!), per tante cose, ma sopratutto per la pazienza avuta in questi mesi. E grazie a tutti i nostri amici, sempre fondamentali! A quelli comuni del Politecnico di Milano, in particolare a quelli che ci hanno ospitato nel vagabondaggio di questi mesi, e a quelli di sempre delle rispettive città natali!

Y como olvidarse de los compañeros de nuestra permanencia Sevillana! Gracias a Dario y Rafa, los compañeros de piso mas cabrones que hubieramos podido encontrar! Gracias a Maria, Santi, Lollo el loco (que nos ha enseñado como son todas..), el volador Simonetti y Lollo, Anna Paola, Carola, Papalaus, 'mbare Rodrigo y su padre (de Alfalfa), Gloria, Alessia, Marta, Susy, Luigi, Negrita, Laura, Ester, Cate, Cosimo, Fabian, Camilla, Massi, Francisco y su mitico almuerzo, Flaminia y Ares, Anto y Lucia, Brucio y el Manzo, Ismael, Campo, Cruz, Marco (o Pasquale?), Wudy, la Alameda, la Hamburgeseria de Menendez Pelayo, el Cune, Dress, el equipo de Dos Hermanas y todos los otros que nos han permitido relajarnos despues de las horas de trabajo. Os echaremos de menos!!!

Index

Figures index

Tables index

Sommario

Al giorno d'oggi le centrali solari a concentrazione con tecnologia a torre e a cilindro parabolico rappresentano una delle opportunità più interessanti nel campo della produzione di energia elettrica da fonte rinnovabile. Attualmente la potenza totale installata nel mondo è nell'ordine dei 550 MW, con meno del 10% basato sullo schema a torre, ma altri 10000 MW sono in costruzione o annunciati. Nonostante queste forti prospettive di sviluppo, prevedere le prestazioni di questo tipo di impianti è ancora difficile, soprattutto a causa delle incertezze legate al campo solare, la cui descrizione è spesso solamente sperimentale. La maggior parte dei modelli attualmente disponibili utilizza un approccio molto generale, mirando ad analizzare la fattibilità economica dell'impianto e, in genere, trascurando una dettagliata modellazione termodinamica dei componenti.

È importante ricordare che, a causa della intrinseca irregolarità e in un certo senso imprevedibilità della fonte primaria sfruttata da questo tipo di centrale, gli impianti sono soggetti a condizioni di lavoro estremamente variabili. Per questa ragione è stato sviluppato un modello per la previsione dei bilanci energetici e delle prestazioni di centrali solari in diverse condizioni ambientali e di radiazione solare, con l'obiettivo di comprendere meglio il comportamento degli impianti, di migliorare le loro prestazioni e di ottimizzare le loro condizioni operative. Un'analisi delle condizioni nominali (on-design) è necessaria per definire la miglior configurazione dell'impianto, mentre una simulazione di condizioni a carico parziale (off-design), che illustri la risposta del sistema di fronte a valori di radiazione solare diversi da quelli di progetto, può aiutare nella gestione del sistema, eventualmente anticipando le variazioni delle condizioni esterne.

Il modello sviluppato dimostra la sua funzionalità in fase di progetto in tre modi differenti. Da una parte permette di calcolare e ottimizzare le prestazioni dell'impianto in condizioni nominali, sviluppando un'analisi di sensitività dei parametri coinvolti. Dall'altra parte, varie condizioni di fuori progetto possono essere studiate e, pertanto, è possibile portare avanti un'analisi di lungo termine, ad esempio annuale, di tipo termodinamico e, in futuro, di tipo economico. Infine, permette l'identificazione di condizioni operative indesiderate di uno o più componenti che possano pregiudicare il corretto funzionamento dell'impianto, quali ad esempio una frazione troppo alta di vapore nel

generatore di vapore, una pressione troppo bassa nel degasatore, la cavitazione delle pompe o altre situazioni inappropriate per la turbina a vapore.

Il codice è implementato in Matlab e incorpora due sotto-modelli che descrivono il blocco di potenza ed il ricevitore solare; un modello del campo solare non è stato sviluppato in quanto una rappresentazione veritiera della distribuzione della radiazione sul ricevitore/generatore di vapore è ottenuta attraverso l'utilizzo di dati reali corrispondenti al funzionamento della centrale PS10.

Il modello esegue inizialmente un'analisi di on-design, basata sull'utilizzo di alcuni parametri di input definiti dall'utente, quali la potenza in uscita o la pressione del vapor vivo e di condensazione, e di altri parametri più specifici riguardanti sia il blocco di potenza che il ricevitore, quali l'efficienza della turbina o le dimensioni delle tubature, che possono essere impostati con dei valori di default o modificati in base alle necessità Il risultato è riassumibile in un bilancio termico e di massa sia del blocco di potenza che del generatore di vapore in condizioni nominali, cui si aggiunge un dimensionamento preliminare del ricevitore.

In seguito, l'analisi di off-design è portata avanti concentrandosi sulle variazioni di input termico sulla torre, che sono sostanzialmente rappresentate grazie all'introduzione di mappe di radiazione modificate sui pannelli del generatore di vapore. Le nuove condizioni di funzionamento sono calcolate in funzione dell'input termico e delle condizioni di lavoro a carico parziale, in modalità sliding-pressure, della turbina.

Per permettere un'opportuna descrizione del lavoro svolto e dei risultati ottenuti, il presente documento è stato suddiviso in nove capitoli. Il primo capitolo presenta una descrizione generale dello stato dell'arte nel campo dello sfruttamento a scopi energetici della radiazione solare, concentrandosi in particolare sulla tecnologia a concentrazione e sulle sue prospettive di sviluppo. Successivamente, nel secondo capitolo si riportano i principi guida e gli strumenti principali utilizzati nella generazione del codice di calcolo, mentre i capitoli 3 e 4 affrontano la descrizione dettagliata dei due componenti più caratteristici della tipologia di impianto studiato: il campo solare a specchi ed il ricevitore centrale. La spiegazione dettagliata del codice di calcolo appositamente sviluppato per la descrizione del suddetto ricevitore è quindi riportata nel capitolo 5. Il capitolo successivo analizza invece le caratteristiche principali del blocco di potenza e l'approccio utilizzato per la descrizione del

suo comportamento in condizioni di progetto. I risultati della modellazione dell'intero impianto in condizioni di on-design e dell'analisi parametrica su diverse variabili sono riportati nel capitolo 7. I capitoli 8 e 9, infine, riportano la descrizione del modello sviluppato per simulare le condizioni di off-design e i risultati delle simulazioni stesse. Un'analisi su diverse strategie di regolazione delle stazioni di pompaggio e del condensatore è inclusa nella stessa sezione.

Parole chiave: Solare a torre, Impianto solare a concentrazione, Ricevitore solare, Energia rinnovabile, Modello termodinamico

Abstract

Nowadays, solar tower and parabolic trough power plants represent one of the most interesting opportunities in the field of energy production through renewable sources. At present, the total power installed in the world is in the order of 550 MW with less than 10% based on the tower scheme and other 10000 MW are already under construction or announced. However, despite these announces, performance prediction of this kind of plants is still difficult, mainly due to the uncertainties on solar field whose description is often only experimental. Most of the models available nowadays employ a very general description, aimed at analyzing the plant economic feasibility but, in the main, neglecting a detailed thermodynamic modeling of plant components.

It is worth noting that, due to the random and somewhat unpredictable nature of the primary energy source exploited by the power plant, these facilities are subjected to extremely variable working conditions. For these reasons, a model for the prediction of solar plant energy balances and performances for different ambient conditions and solar radiations is developed with the aim to better understand the plant behavior, improve performances and optimize the plant working conditions. An on-design analysis is necessary to define the best plant configuration, while off-design simulation, that illustrates the system response to radiation conditions other than nominal, can help system management maybe anticipating external condition variation.

The developed model demonstrates its functionality during the design process in three ways. On one hand it allows to calculate and optimize the performance of the plant at rated conditions, developing a sensitivity analysis of the parameters involved. On the other hand, various off-design conditions can be studied and, consequently, it would be possible to carry out a long term –for instance yearly- thermodynamic and, in the future, economical analysis. Finally, it allows detecting undesirable operating conditions of one or more components that could eventually lead to a not admissible operation of the plant: for example a too high vapor fraction in the steam generator, a too low deaerator pressure, cavitation of pumps or other situations that are not appropriate for the steam turbine.

The code is implemented in Matlab and incorporates two sub-models that describe the power block and the solar receiver, while the solar field has not

been developed because a reliable representation of the radiation distribution on the receiver/steam generator is taken from available data corresponding to the PS10 plant.

The model performs initially an on-design analysis, based on input specifications defined by the user like rated output or live steam and condensing pressures, and more specific parameters regarding either power block or boiler as turbine efficiency or piping size, which can be set according to default values or modified voluntarily. The result is summarized by the heat and mass balance of both power block and steam generator at rated operation, together with a preliminary sizing of the boiler.

Then, the off-design analysis is carried out focusing on thermal input variations at the tower, which is in practice introduced by a modified radiation map on the panels of the steam generator. New, stable working conditions are calculated depending on the heat input and on the sliding pressure operation of the turbine at off-design.

Key words: Solar tower power; Concentrating solar power plant; Solar receiver; Renewable energy; Thermodynamic model.

Introduction

Since the first industrial revolution, in the second half of the eighteenth century, humanity has been looking for new energy sources necessary to improve its life conditions. During those years, a change in the behavior of primary energy exploitation took place, switching from wood to coal. This event was driven by the birth of the first steam machines and their application to transportation, where fuels with higher specific energy were needed.
During the second industrial revolution in the nineteenth century. oil and electricity began to gain importance in the world energy scenario as it can be seen nowadays. In the last 150 years the energy consumption has increased at an annual rate of about 2.3% [1] and today the major contribution is due to the fossil fuels.

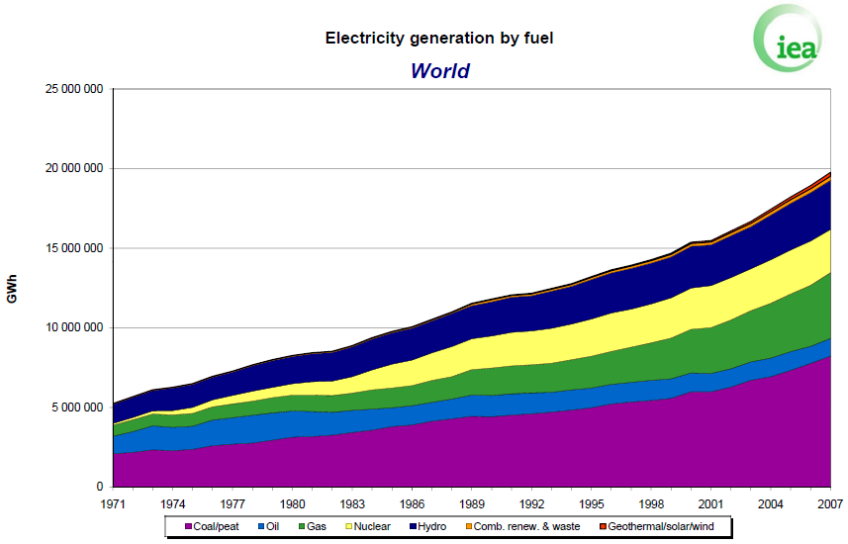

Figure 0.1: World electricity generation by fuel [2]

In the first years of the XX century, new sources began to be exploited as hydroelectric, geothermal (the first geothermal plant was built in Larderello, Italy, in 1905), natural gas, nuclear, biomass and even solar and wind energy, but fossil sources remained the main reference.
Presently, more than 80% of primary energy consumption and 57% of energy production is based on fossil fuels. In particular, in Spain, the energy system relies on an 82.6% on fossil fuels. According to “Ministerio de Industria, Turismo y Comercio” the primary energy consumption in 2007 was 20236 ktep

of coal, 70848 ktep of oil, 31602 ktep of natural gas, 14360 ktep from nuclear power, 3161 ktep from hydroelectric conversion, 3119 ktep from wind, 1238 ktep from biomass, 319 ktep from biogas, 67 ktep from photovoltaic system and 2 ktep from thermo-solar conversion [2].The continuous increase in energy demand, combined with the unbalanced system that is primarily based on fossil fuels, brings two relevant problems:

1) Greenhouse effect.
2) Starvation of fossil fuel reserves, with a subsequent increase in their price.

The first is claimed to be causing heating of the surface of our planet due to the presence, in the atmosphere, of gases that absorb and emit infrared radiation. Even though the correlation between planet temperature and CO_2 concentration in atmosphere has not been demonstrated scientifically, there are too many evidences that point on this direction. During the last *United Nations Climate Change Conference 2009* held in Copenhagen, a political consciousness of the problem came out. To prove it, it is sufficient to look at the second point of the agreement that reads: "*We agree that deep cuts in global emissions are required according to science, and as documented by the IPCC Fourth Assessment Report with a view to reduce global emissions so as to hold the increase in global temperature below 2 degrees Celsius* […]"[3]. It is surely undeniable that during the last 150 years the concentration of greenhouse gases has increased critically as shown by the *IPCC* (Intergovernmental panel on climate change):

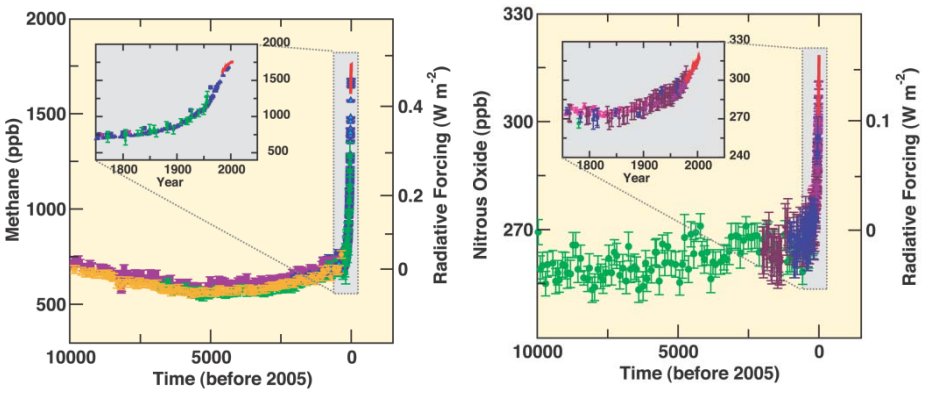

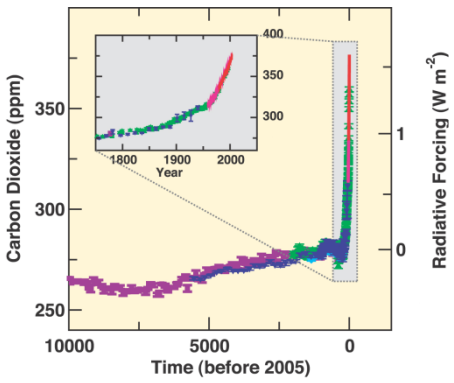

Figure 0.2: Greenhouse gases concentration [4]

The second aspect (fossil fuel reserve reduction) has caused different periods of price fluctuation of every kind of good, giving way to market collapse risks and increasing the international relevance of those few countries that export oil.

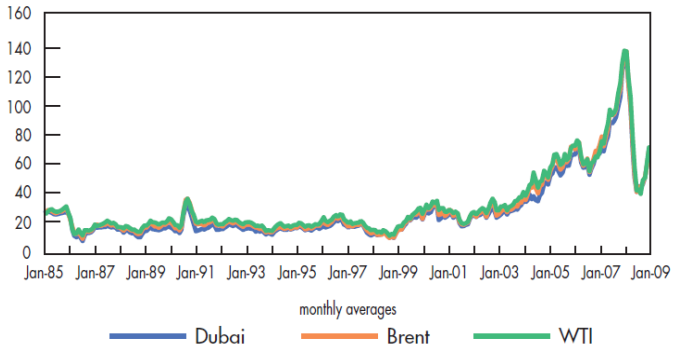

Figure 0.3: Crude oil price US $/barrel [2]

With the aim of mitigating these problems, actions must be taken in two parallel ways:

1) Increasing the energy production using renewable sources.

2) Using fossil sources with CCS (Carbon Capture and Storage) systems.

Regarding this second option, there are many different studies that are trying to make capturing the CO_2 fraction of the exhaust flow economically sustainable. These techniques are classified according to the point of the process where separation is performed:

a) CO_2 removal from the fuel (*pre-combustion method*)

b) CO_2 removal from the exhaust gases (*post-combustion method)*

c) O_2 combustion (*oxy-fuel combustion)*

Using these systems, a reduction of 80-90% in CO_2 emissions could be obtained, though there are several difficulties regarding the high price of the technology.

Surely, the first option (increase of energy production from renewable sources) has begun to be really exploited considering the hydroelectric and geothermal plants all over the world and even wind conversion has become competitive. In this context, the potential of solar energy exploitation could be a key point to reach the objectives outlined by the Copenhagen meeting and in the *IEA's World Energy Outlook (WEO)* that proposes a great effort in the renewable field and energy efficiency field to reach a concentration of 450 ppm CO_2-eq in 2030 (*450 scenario)*:

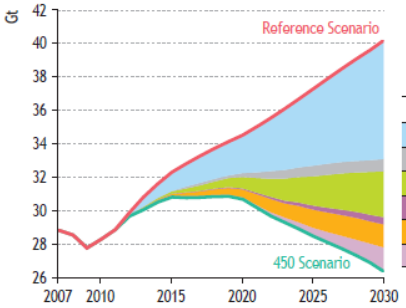

	Abatement (Mt CO_2)		Investment ($2008 billion)	
	2020	2030	2010-2020	2021-2030
Efficiency	2 517	7 880	1 999	5 586
End-use	2 284	7 145	1 933	5 551
Power plants	233	735	66	35
Renewables	680	2 741	527	2 260
Biofuels	57	429	27	378
Nuclear	493	1 380	125	491
CCS	102	1 410	56	646

Figure 0.4: CO_2 abatement according to IEA strategy [5]

As shown in figure 0.4, renewable sources will play a crucial role to reach IEA targets and, hence, huge investments are foreseen in these technologies. Among all the renewable sources, concentrating solar power seems to have the greatest potential due to the fact that this technology is at the beginning of its evolution and there is still room for cost-reduction and performance improvement, considering the number of companies involved in its expansion:

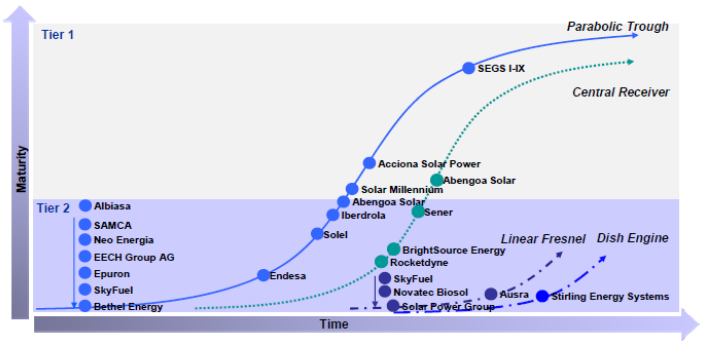

Figure 0.5:CSP development curve [6]

Using solar energy for electricity generation has several advantages that favor its great development:

1) It can produce electricity and/or heat in hours (around midday and in the summer season) when the consumption is higher.

2) It can be matched with other energetic sources, renewable or fossil.
3) It is available everywhere in the planet even if the main potential is in the so-called “sun belt”, in particular in the area of North Africa and Middle East.
4) It can help to reach the target of greenhouse gas reduction fixed by the international community.
5) It can exploit not used land and create work in relatively poor countries as those in North Africa.

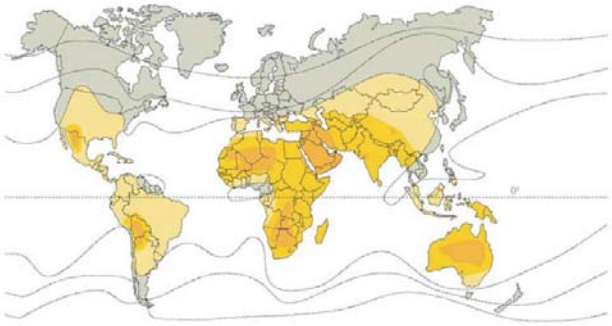

Figure 0.6: World radiation map within "sunbelt"

Looking at the last point it is important to underline that the major radiative contribution is present in the “Sun Belt”. This area extends from latitudes 35° N to 35° S and receives thousands of times the global energy requested, as it can be seen in the figure 0.6. For this reason the Mediterranean area can be an “energy link” between Europe and North Africa. On 13th July 2008 the Heads of States and governments of the Euro-Mediterranean countries, meeting in Paris, proposed the Mediterranean Solar Plan (MSP) in order to improve the security of the energy supply in EU countries as well as to meet the increasing domestic demand trough renewable energy sources and to boost economic development in the “Union for the Mediterranean” non-EU countries. In this project, the construction of several solar plants in North Africa, where there is a huge availability of sun power, is involved. Moreover, different studies have demonstrated that the electricity consumption of Europe would be satisfied if the solar energy irradiating an area equal to just 0.4% of the Sahara desert were used, or 2% for the world energy demand
[7].

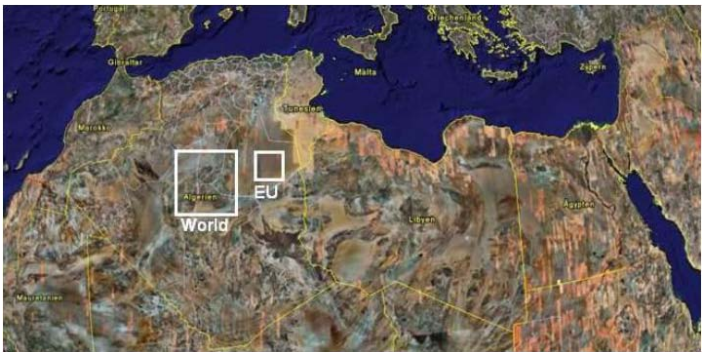

Figure 0.7: Sahara use for EU and World electricity demand

This suggestive data shows the enormous potential of solar energy, especially in CSP (Concentrating solar power) technologies, in the next years.

1. Solar energy

1.1 Solar radiation

The sun is a star that behaves as a black body at the temperature of 5777 K. Inside its core several fusion reactions supply the energy that the sun emits, the most important of which is the process where hydrogen combines to form helium. This energy is then transferred from the interior to the external surface by a succession of radiative and convective processes.

The sun irradiates to the Universe $\mathbf{3.8 \times 10^{14} TW}$ but, due to the high distance $\mathbf{1.495 \times 10^{11} m}$ and the dimensions of the two bodies, only 172500 TW are intercepted by the Earth. This amount of energy is defined by the *solar constant*, G_{sc} =1367 W/m^2, which represent the mean value of thermal power received, outside the atmosphere, per unit area normal to the propagation direction. Nevertheless, the effective radiation received from the sun can vary from this value due to the following aspects:

1) Periodic variations of intrinsic solar radiation related to sunspot activities (less than ± 1.5%)
2) Variation of earth-sun distance in the range of ± 3%

Regarding the spectral distribution, most of the solar radiation is concentrated on wavelengths ranging from 0.15 to 4 μm, where three spectrums are found; visible-between 0.4 and 0.74 μm-, ultraviolet -less than 0.4 μm- and infrared – above 0.74 μm-. In practice, this spectal distribution is modified due to:

1) Atmospheric scattering by air molecules, water and dust
2) Atmospheric absorption by O_3, H_2O and CO_2

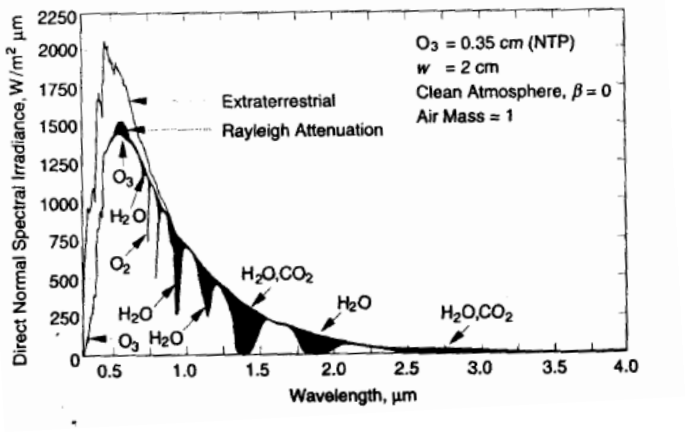

Figure 1.1: Real solar radiation spectrum

1.1.1 Scattering

Scattering of radiation is caused by interactions with air molecules, water, and dust. The degree to which scattering occurs is a function of the number of particles through which the radiation must pass and the size of the particles relative to the wavelength λ. Three different kinds of scattering are identified with respect to this latter aspect:

1) *Rayleigh scattering*: it involves very small molecules (~ 10% of λ: N_2 and O_2) that deflect radiation in every direction. The effect is directly proportional to the atmosphere thickness and inversely proportion to the 4^{th} power of λ, what means that it is significant only for $\lambda < 0.6$ μm.
2) *Mie scattering*: it involves larger particles (~ 10% - 1000% of λ) like water vapour molecules and airborne particles (dust, salt crystals, smoke). As the previous case, it is in inverse proportion to λ and directly proportional to the atmosphere thickness.
3) *Non selective scattering*: it involves larger airborne particles, like water drops and ice crystals, that re-emit a widespread white light. It depends on the concentration and the extension of the aerosol and it does not depend on λ. For this reason, it is very variable with the atmospheric condition and cannot be easily forecasted.

1.1.2 Absorption

Absorption of radiation is due to the presence of certain molecules found in the atmosphere, mainly O_3, CO_2, H_2O, N_2O and CH_4, that re-emit radiation in the infrared band. Every molecule has its own characteristic absorption band like, for instance, O_3, which absorbs radiation with $\lambda < 0.29$ μm, thus protecting the Earth from the UV radiation. The water molecules have different absorptivities at 1, 1.4 and 1.8 μm, while over 2.5 μm the combined effect with CO_2 makes the atmosphere opaque to infrared radiation (Fig. 1.1).

The effects described bring about a substantial modification of the solar spectrum that will be as relevant as thick is the atmosphere crossed. For this reason it is useful to have a reference unit, called *Air Mass*, that is equal to 1 when the sky trasmittance is equal to that at the equator with the sun in zenithal position and at sea level.

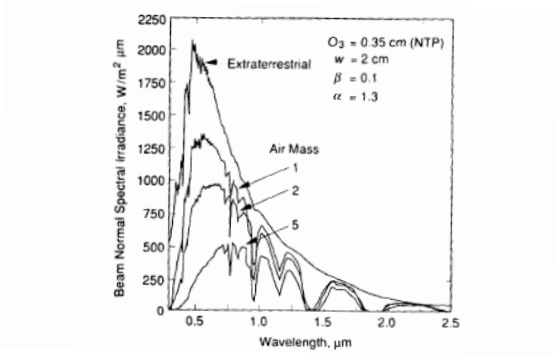

Figure1.2: Air mass effect [8]

In reality the spectral distribution of total radiation depends also on the spectral distribution of the diffuse radiation. Some studies have led to the conclusion that, in the wavelength range from 0.35 to 0.80 μm, the distribution of diffuse radiation is similar to that of the total beam radiation. The diffuse radiation is a very important component because it is the principal contribution when there are clouds in the sky. Some technologies, like photovoltaic conversion, can use this part of the radiation to generate electricity bit others like concentrating solar power systems cannot exploit it. The diffuse component has a distribution similar to the total component but shifted to the short-wave end of the spectrum:

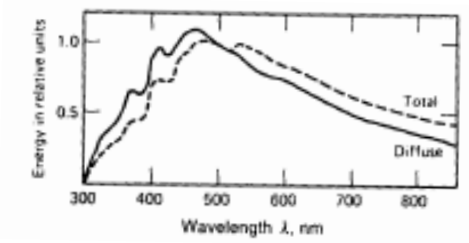

Figure 1.3: Energy distribution of total and diffuse radiation

1.2 Solar energy power technologies

During the last years very different ways to exploit the solar radiation have been studied with different results. The two main technologies are photovoltaic conversion and thermal conversion.

1.2.1 Photovoltaic technology

A photovoltaic (PV) system can produce electricity using solar radiation directly and converts both the beam and diffuse component. These systems work thanks to the *photovoltaic effect*: photons of light knocking electrons into a higher state of energy can create electricity. To obtain this effect some particular materials have to be used. These materials, known as semiconductors (monocrystalline silicon, polycrystalline, cadmium telluride, gallium arsenide), can transfer electrons generated from material's exposure to radiation of sufficient energy from one material to another, resulting in the buildup of a voltage between two electrodes.
To obtain this effect photons must have a sufficient energy to overcome the "Energy gap" between a valence band and a conduction band; this energy is equal to 1.12 eV in the silicon case.
In order to have a continuous flux of electrons there will be, at the same time, a surplus of electrons and holes. To obtain this configuration the semiconductor is usually doped with boron atoms (that have an electron less than Si) creating a p-junction and with phosphorus atoms (that have an electron more than Si) creating an n-junction. This way, a p-n junction can be made where there is a flux of electrons from "p" to "n" sides while holes diffuse from "n" to "p" sides. The different concentration of positive and negative charge build the potential difference and so the electric current.

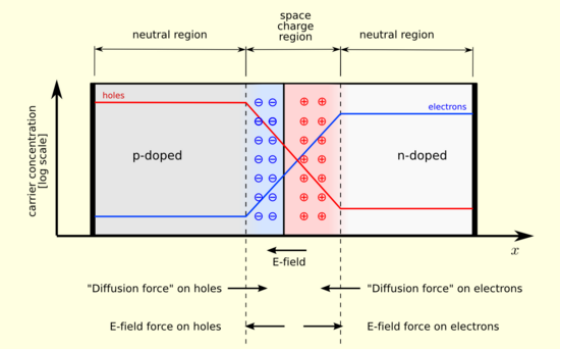

Figure 1.4: p-n junction

The base of this technology is the *solar cell* that produces up to 1.5 W-peak in on-design condition (T=25°, I=1000 W/m^2). Solar cells are assembled to create a module (50 W) and then a number of modules are linked together in series or in parallel to achieve the desired current and potential.
Photovoltaic applications can be divided into two main blocks:

Stand-alone applications: are used to cover the electric demand in rural zones especially, where the conventional electric grid does not supply energy. This kind of applications need storage systems, inverters and regulators.
Grid connected applications: all the energy produced is injected to the grid and. many times. there are incentives that support this kind of applications.
The processes to obtain silicon of the right pureness are very energy intensive, this bringing a very high manufacturing cost (now 4000-7000 €/kW). For this reason, this technology is only competitive if significant financial incentives are given as in Japan, Germany, Italy and France where governments aid has yielded a demand and production growth.
World solar PV commercial installations reached a record with 5.95 GW in 2008 (110% annual growth) where Spain's 285% growth pushed Germany into second place in the market ranking while US is ranked third.

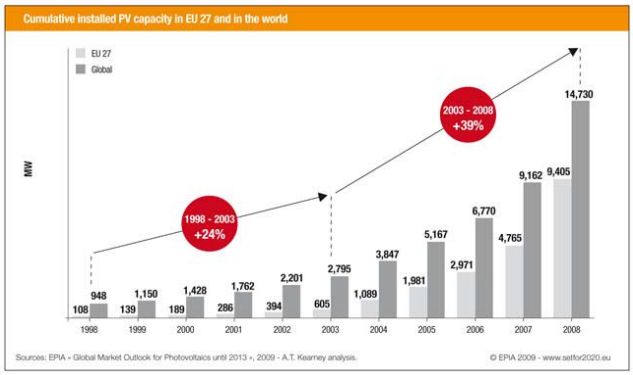

Figure 1.5: Installed PV capacity [9]

In this perspective, different studies are under development in order to reduce the PV material costs especially in the "thin film" field as CdTe, CIGS and amorphous Si.
Due to high cost of materials, experts underline that it can be smart to use PV technology only for little application where all the advantages can be exploited, leaving the great electrical production to other kind of technologies. Even if this idea is shared by most experts, a few plants of 40 and 60 MW have been set up in Spain and Germany, the largest of them being the *Olmedilla photovoltaic park*, in Olmedilla de Alarcon (Castilla-La Mancha), Spain, that with its 60 MW emphasizes the great attention of the Spanish government towards the solar energy conversion.

Figure 1.6: Olmedilla photovoltaic park

1.2.2 Thermoelectric conversion

Instead of the PV systems, that convert solar radiation into electricity directly, thermoelectric systems need to produce a vector fluid (steam) that can be used in a traditional power cycle.
These technologies are under development and new plants are expected to be set up in the next years.
There are two main groups that differ by the presence or not of a concentrating system:
No concentrating radiation plants: solar chimney power plants, solar ponds.
Concentrating solar power (CSP): parabolic trough power plants, solar thermal tower power plants, solar dishes and Fresnel collector power plants.
It is clear that the more persuasive option is the second one, because solar concentration is necessary to obtain higher working temperature and therefore higher efficiency.
The problem of CSP plants is that they can only make use of direct solar radiation and for this reason they must be built in areas that are very sunny and have a small presence of clouds along year (e.g. 2600-2700 kWh/m^2 in desert areas of USA, 2000 kWh/m^2 in Andalucia, Spain). This feature limits the competitiveness of CSP plants to the sun belt area. A common thought among the experts is to promote small photovoltaic plants for those areas (like north Europe) where direct radiation is low and medium-big (more than 1 MW) CSP plants in southern areas.

1.3 Non concentrating solar power plants

1.3.1 Solar ponds

A solar pond is a sort of big solar thermal collector (like those used for house heating purpose) that incorporates heat storage. This technology can have different applications like heating, desalination, refrigeration and power generation.
It is a pool of saltwater that collects and stores solar energy. Naturally saltwater forms a vertical salinity gradient in which water with low-salinity stays on top of water with higher salinity. When solar radiation is absorbed by water, its temperature increases. If the water did not have a high salt concentration the effect of the temperature would be a density gradient that decreased with depth. On the contrary, for water with high salinity, a salinity gradient is formed that increases with depth, preventing heat in the lower layers from moving upwards by convection. In this way the temperature at the bottom of the pond reaches over 90°C while the temperature at the top remains at 30°C.
This temperature difference can be used for many purposes like driving an organic Rankine cycle or a low temperature gradient Stirling engine for generating electricity.
The efficiency of this kind of systems is very low due to the low-grade heat available. For a higher temperature of 80°C and an ambient temperature of 20°C the maximum theoretical efficiency of a power plant's is 17%. (theoretical Carnot efficiency).This low efficiency is justified thinking that the cost of this plant can be quite modes since it only includes ORC components and salts (typically $NaHCO_3$).

Figure 1.7:Solar pond El Paso, Texas, USA

1.3.2 Solar chimney power plant

This technology combines three well known aspects: the chimney effect, the greenhouse effect and the wind turbine conversion. Its working principle is very simple to understand: by a very large greenhouse-like structure around the base of a tall chimney, air is heated by solar radiation, resulting in a convection movement: air rises up the tower driving turbines that produce electricity.
There are two significant factors affecting the power/efficiency of these applications:

1) *Size of the collector area*: a larger collector produces a greater volume of warmed air.
2) *Chimney height*: a larger chimney increases the stack effect.

In order to increase the thermal capacity, heat can be stored inside the collector area. An idea could be using water tubes under the collector reaching, according to the water level, more hours of energy-production.
Turbines can be installed in different configurations:

- In a ring around the base of the tower, with horizontal axis.
- A single vertical axis turbine inside the chimney.

Solar updraft towers have low efficiency but, at the same time, the cost per square meter of solar collection is low too.
Several difficulties stand out against this technology. Constructing these plants is quite difficult: for an electric output of 200 MW a 7 kilometers in diameter collector and a 1000 meters high chimney [10] are necessary. To make it more cost effective, it is possible to combine the land used for the updraft tower with other uses, as positioning solar collector or photovoltaics underneath the tower collector.
Despite the evident feasibility problems, different projects have been proposed during the last years: in Ciudad Real, Spain (40 MW), Buronga, Australia and Namibia (400 MW).
In reality, the only tower ever built and put in operation was that one at Manzanares (150 km south of Madrid, Spain). This plant consisted of a 195 meters chimney and a 10 meters in diameter collection area, for a nominal power output of 50 kW. This pilot plant operated for eight years, from 1982 to 1989 when, the cheap low quality materials used for the construction caused the fall of the tower in the course of a storm.

Figure 1.8: Manzanares solar chimney power plant

1.4 Concentrating solar power plants

Concentrating solar power plants use a technology based on the conversion of the direct component of solar radiation into high temperature thermal energy and then into electricity, heat or mechanical work. To obtain a higher level of energy per unit area, concentrators (mirrors or lens) are used.
Solar radiation received by a *collection surface* A_c, is redirected onto an *absorption surface* A_{abs}. The ratio between these two surfaces is one of the most representative indicators of the system and is called *concentration ratio* C_r. The collection system receives and concentrates the solar radiation on an absorber where solar radiation is converted into thermal energy (normally increasing the enthalpy of a fluid that later is used in a conventional power plant).
Concentrating solar power plants allow to exploit more efficiently the solar radiation, with respect to non concentrating systems, because of the higher temperatures reached by the working fluid. In fact, according to Stefan-Boltzmann law (infrared radiation emitted by the pipes is proportional to the 4^{th} power of absolute temperature), the efficiency of the receiver decreases with increasing operating temperature but, for a specific operative temperature, this efficiency is higher for higher concentration ratios (Fig. 1.9) as long as receiver emissivity is reduced for the wavelength corresponding to its operating temperature. Therefore, the total efficiency always shows an optimum that depends on temperature and C_r.

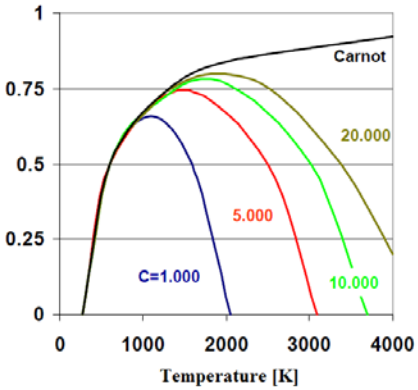

Figure 1.9: Cr influence on cycle efficiency [11]

In practice, the concentration ratio has limiting values for a geometrical reason. From the Earth, the Sun subtends an angle of 32' that corresponds to a semi-angle θ_s of $\mathbf{4.653 \times 10^{-3}}$rad. Therefore, the direct component of the solar radiation does not consist of perfectly parallel beams but it is distributed in a cone that will not reach a receiver of small dimensions completely.
For a 3D concentrator (solar tower) the limit is:

$$C_{r,3D} = \frac{1}{\sin^2 \theta_s} = 46189 \tag{1.1}$$

For a 2D concentrator (parabolic trough):

$$C_{r,2D} = \frac{1}{\sin \theta_s} = 215 \tag{1.2}$$

The actual values of concentration ratio are distant from the values above, showing good development perspectives.

A thermal solar power plant consists of a number of subsystems: collector/concentrator, receiver/absorber, power converter, heat storage and, probably, conventional burner/boiler.
The collection system concentrates and re-directs the solar radiation towards the absorber where radiation is transformed into thermal energy used to power the cycle.
A heat storage system or a conventional fossil fuel boiler is needed to provide energy to the power cycle when solar radiation is not available, permitting the plant to produce electricity according to the demand. This is a great benefit for the electric system in terms of stability but reduces the overall efficiency of the system for each kWh produced from fossil fuels (this comment does not apply to the operation with heat storage systems).

Presently, there are four principal technologies of CSP plants:

1) *Parabolic trough*: these plants concentrate solar radiation on a focus line, where the absorber is located, by mean of parabolic mirrors (i.e. linear collectors/concentrators are used). Nowadays, it is the most developed and widespread technology.
2) *Parabolic dish*: these plants focus all the solar radiation collected by a dish onto a single point where a receiver captures the concentrated energy and transforms it into heat (i.e. bi-dimensional collectors are used). Most of the times, the receiver is incorporated into a Stirling engine.
3) *Fresnel reflector*: these plants are similar to the parabolic trough systems but instead of parabolic mirrors, a series of long, narrow, flat mirrors are used.
4) *Solar tower*: these plants, by means of a heliostat field, concentrate solar radiation on a point where an absorber is located. This point is actually an "area" that is located at the top of a high tower.

1.4.1 Parabolic trough

The parabolic trough technology is, among all the solar thermal power systems, the one that has reached the highest level of commercial maturity. The presence of 9 SEGS plants in the Mojave Desert (USA) for a total power of 354 MWe has helped a strong development of the technology producing, until now, more than 13 TWh. In Europe, this technology has been carried out recently thanks to Andasol I and II plants (100 MW), in the province of Granada, which went online in March 2009.

Figure 1.10: Andasol I and II parabolic trough power plants

These plants use linear parabolic concentrators that track the Sun, rotating on a single axis, and focus the radiation on a receiver tube that runs along the focal line, hence transferring heat to a thermal fluid that flows inside the trough. This fluid is then used as thermal input in a steam generator as in traditional plants

The concentrator consists of:

- A *steel structure* that keeps the correct position of the mirrors even under wind or other atmospheric loads.
- A *reflecting surface* that is a common glass mirror with proper curvature and low iron content to improve its transmittance.

Parabolic collectors usually have an aperture of about 6 m, a concentrating ratio of 61-80 (e.g. SEGS) and a length of 100-150 m, with the aim of reducing the cost of the tracking mechanism and the losses at the end of the collector.

The absorbing pipe is a key element in parabolic trough plants. For temperatures less than 300°C, the absorber could be made of stainless steel coated with cobalt or chromium; instead, for the temperature level reached actually, vacuum tubes are preferred. These absorbers are made by an internal stainless steel pipe with a proper selective coating and an external glass pipe, separated by a vacuum annulus (approximately 0.013 Pa). The selective coating has a high absorptivity (> 90%) for the short wavelength typical of solar radiation and a low emissivity (< 30%) in the infrared spectrum that is the typical band in which the absorber re-emits to atmosphere.

Regarding what flows inside the pipe, several working fluids can be used in parabolic trough plants:

- Synthetic oils
- Mineral oils
- Molten salts
- Water
- Ionic liquids
- Air or other gases

If the temperatures desired are moderate (< 200°C), demineralized water might be the best choice but, nowadays, the main working fluid is synthetic oil (e.g. Therminol® VP-1) thanks to its low vapor pressure, that allows working at modest pressure and with economic materials reaching 390°C. Currently under development is the usage of molten salts mixtures ($NaNO_3$ – KNO_3) that can reach temperature of about 550°C, improving cycle efficiency but showing some technological problems:

1) High solidification temperature (142°C – 238°C, depending on salt composition). For this reason, the mixture must be kept fluid during start-ups by pre-heating the pipes and during the night by a system that makes the fluid flows continuously.
2) High corrosiveness that makes it necessary to use more expensive pipes and components.

Direct seam generation is likely to be the next step in parabolic trough evolution. The problems with it are linked to the fact that a phase change must take place inside the pipes that the very high pressure requested. This kind of technology has been studied in the DISS project at the "Plataforma Solar de Almeria" producing superheated steam at 400°C/100 bar.

Regarding the performance of this technology, different types of losses are identified in these plants:

- *Shadow losses*: between a parabolic mirror and another.
- *Losses for no interception*: due to single axis rotation
- *Optical losses*: reflectivity of parabolic concentrator, interception factor (not all the radiation reflected by the mirror reach the absorber), transmittance of the glass, absorbance of selective coating.
- *Thermal losses*: conductive, convective and radiative losses of the absorber.

Because of the losses indicated, the thermal efficiency of this kind of plants is in the range 60-80% and the overall efficiency from collector to grid is around 15%.
To increase the working hours and then the dispatchable current, commercial plants utilizing parabolic trough are of the hybrid type, using fossil fuels for night hours operation.

Another important aspect of these plants is the storage system that consists of two tanks: a hot tank that receives the hot fluid from the solar field and a cold tank. The first one is filled during hours of peak insolation and then emptied when solar radiation is not sufficient to produce steam. The hot fluid, flowing through a heat exchanger produces steam and is then stored in the cold tank.
For the storage system molten salts are normally used, taking advantage of the fact that they do not have environmental impact, are safe and cost less then synthetic oil.

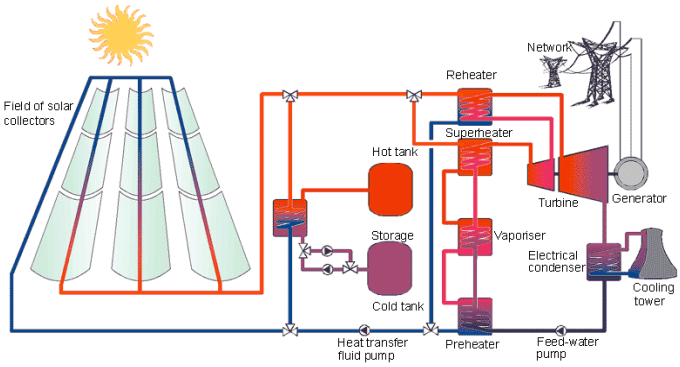

Figure 1.11: Parabolic trough plant and storage

1.4.2 Parabolic dish

A solar parabolic dish system is composed by:

- A large *parabolic dish* that tracks the Sun by a rotational movement along two orthogonal axes and concentrates the solar radiation on a receiver set at the focal point.
- A *thermal engine* placed at the top of the receiver that uses a working fluid heated by the concentrated radiation.

Parabolic dishes are characterized by a high efficiency, modularity and autonomy but until now reliability problems, related to the receiver/engine block working at very high temperature, and high costs have obstructed their entry in power generation market.

The parabolic dish can be made by discrete elements (facets) that approximate the geometry of a paraboloid or by a continuous metallic membrane that approximates the ideal geometry.
With this particular geometry, it is possible to reach a concentration ratio C_r of almost 3000, what means very high temperature on the absorber and, therefore, increased solar to electric energy conversion efficiency of circa 31.25%. Thus, a 10 m in diameter dish is able to supply 30 kWe in presence of a solar flux of 1000 W/m^2 [12].

Regarding the receiver, this component has two functions: absorbing the solar radiation reflected by the concentrator and transferring this energy to the working fluid of a thermal engine associated. Usually, the receivers used in parabolic dishes are of the cavity type in order to reduce radiative and convective losses.
Until now, two kinds of receiver have been used:

1) *Pipes receiver*: the absorber consists of several pipes in which the working fluid of the engine flows. The high temperatures of these

absorbers (800°C) make it difficult to use selective coatings due to the great overlap between absorbed and emitted radiation.

2) *Reflux receiver (heat pipe)*: these receivers use a liquid metal (usually Sodium) that evaporates at the absorbing surface and condenses on the pipes inside which the working fluid flows. With this solution really high heat transfer coefficient can be obtained (800 W/cm^2) and the metal condensation allows a more uniform heating of the working fluid.

The power system is a thermal engine, most of the times a Stirling reciprocating engine or a Brayton cycle gas turbine.

In Stirling engines, the working fluid is usually Hydrogen or Helium that is alternately cooled, compressed until 20 MPa pressure, heated until 700°C and then expanded to start the cycle again. Normally, sodium is adopted as intermediate fluid for these engines.
Brayton engines, instead, use air as working fluid with a maximum pressure of 0.25 MPa and a turbine inlet temperature of 850°C. This kind of applications, thanks to the high working fluid temperature, can reach an efficiency of 25-27%. In these systems, the receiver is a volumetric absorber where solar concentrated radiation passes through a quartz window and is absorbed by a honeycomb-like system that provides a high exchange surface.

Figure 1.12: Parabolic dishes with Stirling engine

1.4.3 Concentrating linear Fresnel reflector

A linear Fresnel collector is a type of concentrating solar power system that, instead of using parabolic reflectors (as the parabolic trough), employs flat mirrors simulating a continuous surface to collect and concentrate solar energy, therefore reducing construction problems and costs.

The system consists of :

- *Long parallel rows of mirrors* that can rotate around their longitudinal axis and concentrate solar radiation on a linear receiver that is suspended at a certain height above the mirror plane. A geometry of this type allows to dispose two or more receivers in parallel in order to have a single receiver shared by a number of mirrors, optimizing the land use and minimizing mirror blocks.
- *The absorbing pipe* that is, essentially, the same used in parabolic trough systems, even if it works at lower temperature because of the lower achievable concentration ratio (in the order of 20).

Good exploitation of land, lightness, simplicity of construction and low cost are promoting a fast development of this technology, even if low capacity of concentration and therefore low working temperatures limit its efficiency.
One of the plants currently in operation (since March 2009) is the Fresnel plant 1.4 MW PE1 of Novatec Biosol, located in Murcia (South of Spain). This plant is characterized by an absorber tube positioned in the focal line at 7.4 m above the ground where water evaporates directly into saturated steam at 270°C and at a pressure of 55 bar.

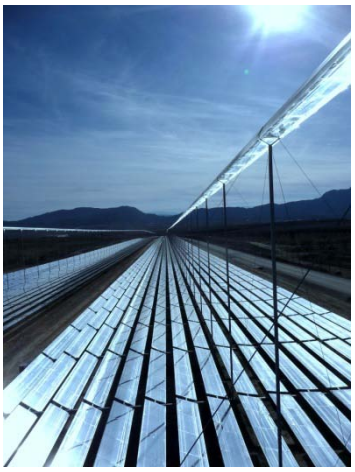

Figure 1.13: PE1 Concentrating linear Fresnel plant in South of Spain

1.4.4 Solar power tower

The last technology described is the *solar power tower* that will be largely explained in the following parts of this work.
These plants use mirrors called *heliostats* that track the sun by a two axes rotational movement, concentrating the sunlight onto a receiver that is normally placed at the top of a tower. In the receiver, the concentrated solar radiation is converted into thermal energy by means of a transport fluid.

Solar towers concentrate solar radiation in three dimensions (in a point, theoretically) and for this reason they can reach high concentrating ratios and therefore working temperatures (1000°C in the future).
The main components of a tower plant are:

1) The heliostats field
2) The tower
3) The receiver
4) The power block

The *heliostat field* is the most characteristic component of this kind of plants and constitutes about 50% of the total cost [14]. Each heliostat is formed by:

- Reflective surface, for example glass mirrors with optical characteristics similar to parabolic trough or reflective surface containing polymeric film with high reflectivity that has the inconvenient of a reduced useful life.
- Supporting structure.
- Tracking system.
- Control system.

The heliostat distribution on the ground meets technical-economical criteria that take into account:

- Shadows created amongst neighbor heliostats.
- Radiation block by the heliostat that is placed ahead.
- Tower height.
- Land costs.

This optimization process brings to an "heliostat field" that can be:

- *North field* (South for the southern hemisphere): used for high latitude (as Europe); for example, in Spain, both power towers at Sanlucar la Mayor, PS10 and PS20, have heliostat fields of this type.
- *Circular field*: used in low latitude where the sun stays high most of the day; for example the heliostat field that operated at the Solar Two plant in Barstow, USA.

Figure 1.14: Circular heliostat field of "Solar Two" plant

Figure 1.15: North heliostat field of "PS10" plant

The *tower*, whether made of metal or concrete, has the function of supporting the receiver that must be placed at a certain height above the heliostat field, in order to reduce shadows and blocks losses.

Figure 1.16: Concrete tower of the PS10

The *receiver*, instead, is the device where the concentrated solar radiation is converted into thermal energy. During the short story of central receiver technology very different types have been proposed, designed, tested and built [23]:

- From a geometrical point of view there are two configurations: *cavity receivers* (as CESA 1, SOLGAS, PS10) and *external receivers*. The external ones can be again classified in: *flat* (SSPS-ASR, Phoebus TSA), *cylindrical* (Solar One, Solar Two) and *semi-cylindrical* (first PS10 version).
- For the heat transfer mechanism: *direct* and *indirect absorption receivers.* Another differentiation is among: *tubular* (Solar One, Solar Two, CESA-1, ASR, GAST), *plate* and *volumetric* (atmospheric or pressurized).
- For the working fluid: *steam-water* with either superheating and boiling (Solar One, CESA-1) or only with boiling (PS10, SOLGAS, Colon Solar, STEOR); *air* (Phoebus-TSA, GAST); *molten salts* (Solar Two); *molten sodium* (SSPS ASR).

The use of air is quite interesting because the high concentrating ratio (~ 2000) allows this technology to reach higher working temperatures when the working fluid is a gas. In this case, a volumetric receiver pressurized at 1.5 MPa can increase the gas temperature up to 800°C (with metallic absorber) or 1200°C (with ceramic absorber). Therefore, this technology is suitable to be incorporated into a combined gas and steam cycle where the air leaving the compressor is sent to the receiver, heated there and then expanded in the turbine. Another option of the receiver layout is positioning it at the base of the tower, obtaining a better optical efficiency, a more stable distribution of heat flux and a simpler plant (all the devices are placed at ground level). Obviously, an hyperbolic reflector is necessary to conduct the radiation down to the receiver.

The principal energy processes (losses) that occur in a solar tower power plant are:

1. Collection losses.
   1.1. Geometrical losses: they are a function of the solar field geometry (relative position of plant elements and the Sun): *cosine factor* (reduction of visible area due to the inclination of the heliostat with respect to the sunbeam direction), shadow *losses*, *blockage losses.*
   1.2. Optical losses: *reflectivity losses.*
2. *Solar radiation transmission through the atmosphere* due absorption and dispersion processes.
3. *Losses in the* t*ransportation of concentrated energy from collectors to receiver.*
4. *Losses in the photothermic conversion*:
   4.1. *Radiative losses.*
   4.2. *Convective losses.*
   4.3. *Conduction losses.*

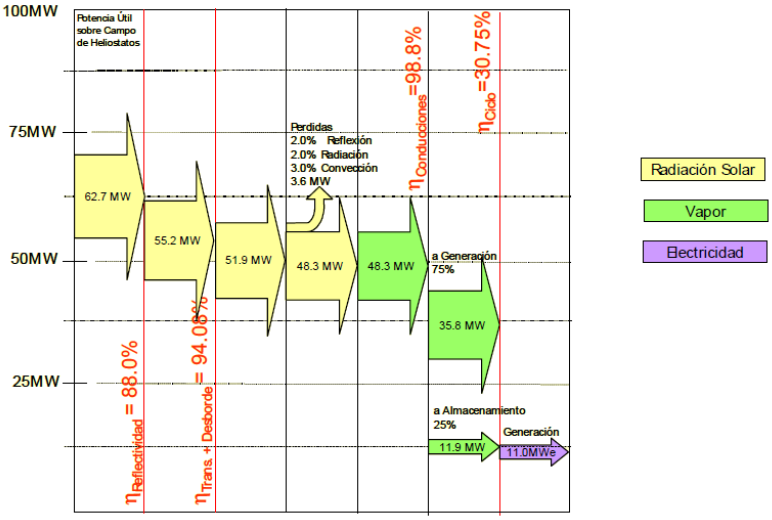

Figure 1.17:PS10 energy balance

1.4.5 Main technological parameters of CSP technologies

To have an immediate idea of the principal parameters of each CSP technology, table 1.1 is shown [12] where:

- *Peak solar efficiency*: is the net electric production divided by the normal beam solar radiation.
- *Load factor*: plant's working hours divided by 8760 hours per year.

Table 1.1: Principal CSP parameters

	Power [MWe]	Concentrating ratio	Peak solar efficiency [%]	Yearly average solar efficiency [%]	Thermodynamic cycle efficiency [%]	Load factor [%]	Covered surface [m^2/(MWh/a)]
Parabolic trough	10-200	70-80	21	10-15 17-18*	30-40 ST	24 25-70*	6-8
Fresnel collector	10-200	25-100	20	9-11	30-40 ST	25-70*	4-6
Solar power tower	10-150	300-1000	20 35*	8-10 15-25*	30-40 ST 45-55 CC	25-70*	8-12
Parabolic dish	0.01-0.04	1000-3000	29	16-18 18-23*	30-40 SE 20-30 GT	25*	8-12

These values have either been confirmed for existing plants in operation or projected from pilot plant performance (*).

In the column of thermodynamic cycle efficiency: ST stands for steam turbine, CC for combined cycle, GT for gas turbine and SE for Stirling engine.
What can be noticed is that the first two technologies can reach very high power output and have a low footprint. Instead, the solar tower power plant demands a higher area (8-12 m^2/(MWh/a)) but, due to the high concentrating ratio, higher temperature can be reached and therefore higher cycle efficiency are possible.

1.5 Actual and future scenery of CSP plants

As it has been shown in the previous sections, the CSP conversion is a reality even if the "great step" didn't occur yet.
The main obstacle that, until now, has prevented CPS plants from taking off is the high investment cost: from 2.5 to 4 times higher than fossil fuel plants [12], with a higher incidence of O&M costs and a lower load factor, that have made the kWh cost twice that one of fossil fuel plants. From this point of view, evaluation of "external costs" due to CO_2 emissions by traditional plants could represent a decisive element for the CSP spread.
Additionally, if thermosolar power plants are to reach real competitiveness on the market, they should be able to provide energy when it is requested by users, independently from solar radiation variability. This would only be possible if concentrating solar power plants have an adequate storage system.
Another characteristic that could help to spread the technology is the possibility to integrate CSP plants into traditional plants in order to increase their total power output and efficiency. In this way, reducing investment costs and controlling power would be possible.
A further aspect that could push the CSP market is linked to the possibility of locating solar plants in areas of high radiation and then transferring the energy that exceeds the local demand to countries with a higher electric demand. Long distance transportation of electricity is possible by high voltage direct current submarine cables (HVDC, High Voltage Direct Current). This aspect has been already mentioned in the introduction, considering the possibility of using part of the Sahara desert to satisfy the European demand by concentrating solar power plants (as proposed by the DESERTEC project).

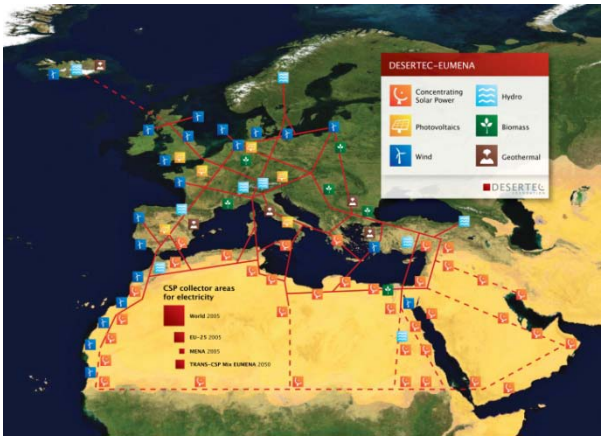

Figure 1.18: DESERTEC map

1.5.1 Operative plants

Presently, the total installed capacity that makes use of CSP technology is 667 MWe worldwide, the big part of which is located in USA and Spain. Little plants have also been built in Germany, Israel and Australia.

Table 1.2: List of operative CSP plants

Power [MW]	Type	Name	Country	Location
354	Parabolic trough	SEGS	USA	Mojave desert, California
64	Parabolic trough	Nevada solar One	USA	Boulder City, Nevada
100	Parabolic trough	Andasol	Spain	Granada
50	Parabolic trough	Energia solar de Puertollano	Spain	Puertollano, Ciudad Real
50	Parabolic trough	Alvarado 1	Spain	Badajoz
20	Solar tower	PS20	Spain	Seville
11	Solar tower	PS10	Spain	Seville
5	Fresnel	Kimberlina solar thermal energy plant	USA	Bakersfield, California
5	Solar tower	Sierra sun tower	USA	Lancaster, California
2	Fresnel	Liddell Power Station Solar Steam Generator	Australia	New South Wales
1.5	Parabolic dish	Maricopa solar	USA	Peoria,

				Arizona
1.5	Solar tower	Jülich solar tower	Germany	Jülich
1.4	Solar tower	THEMIS Solar power tower	France	Pyrenees-Orientales
1.4	Fresnel	Puerto Errado 1	Spain	Murcia
1	Parabolic trough	Saguaro solar power station	Usa	Red rock Arizona
1	Parabolic trough	Keahole solar power	USA	Hawaii
0.1	Solar tower	Kibbutz Samar Power Flower	Israel	Kibbutz Samar

In particular, the first 7 plants are the most important because of their large size and because they are the living examples that CSP technology is feasible and reliable. Looking more in detail:

SEGS: The Solar Energy Generating Systems consist of 9 parabolic trough plants started-up between 1985 and 1991 and being, unquestionably, the reference point of parabolic trough technology. The first one is the 13.8 MWe SEGS I with a concentrating ratio of 61 and mineral oil storage with 3 hours of capacity. It produces saturated steam at 36 bar which is later superheated until 416° in a gas boiler. SEGS II is a 30 MWe plant without any storage. SEGS III, IV, V are 30 MW plants with a concentration ratio of 71 that use mineral oil heated until 349°C as working fluid. The critical change happened with SEGS VIII and IX that have a nominal power of 80 MW, an availability of 95% and a land occupation of 2.86 ha/MW.
Nevada Solar One: This 64 MWe parabolic trough plant does not have storage system but it has an auxiliary traditional boiler. The oil enters the solar field at 350°C and leaves at 395°C producing 134 GWh yearly.
PS10 and PS20: The PS10 was started up on the 30th March 2007.It consists of a steam turbine of 11 MWe, 624 heliostats of 120 m^2 that cover 55 ha and a receiver made by 4 panels at the top of a tower of 125 m that produces saturated steam at 250°C and 40 bar. This plant needs 6.8 m^2/kW of heliostats, which is 54.5 m^2/kW in footprint (ground) and therefore 5.5 ha/MW (double with respect to SEGS plants). The PS20 is like the PS10 but the net power is 20 MWe. It consists of 1255 heliostats of 120 m^2 and a receiver placed at the top of a 165 m tower.
Andasol I and II: Andasol I and II were completed in 2008 and 2009 respectively. The main difference with respect to the SEGS plants is the molten salts storage system that allows the plant to work for 7.5 hours at nominal power. It is composed by two tanks: a cold tank at 291°C and a hot tank at 384°C. Each plant covers 195 ha, what is almost twice the necessary solar field because of the huge storage system.

Planta solar Puertollano: It was started up in May 2009. The land occupation is about 200 ha and according to estimations it will produce about 114 GWh per year.

Figure 1.19: Planta solar Puertollano, Spain

1.5.2 Immediate future

A large numbers of solar plants are under construction or in the process of obtaining the necessary licenses. The majority of these plants, especially parabolic trough with thermal storage, will be set up in Spain. A total of 2133 MW are expected to be put in operation in the next years.

Table 1.3: CSP plants under construction

Power [MW]	Type	Name	Country	Location
150	Parabolic trough	Solnova 1,3,4	Spain	Seville
150	Parabolic trough	Extresol 1-3	Spain	Badajoz
100	Parabolic trough	Andasol 3-4	Spain	Granada
100	Parabolic trough	Palma del Rio 1,2	Spain	Cordoba
100	Parabolic trough	Helioenergy 1,2	Spain	Ecija
100	Parabolic trough	Solaben 1,2	Spain	Lagrosan
100	Parabolic trough	Valle solar power station	Spain	Cadiz
100	Parabolic trough	Aste 1A, 1B	Spain	Ciudad Real
100	Parabolic trough	Thermosol 1+2	Spain	Badajoz
100	Parabolic trough	Helios 1+2	Spain	Ciudad Real
50	Parabolic trough	Majadas de Tietar	Spain	Cacares
50	Parabolic trough	Lebrija-1	Spain	Lebrija
50	Parabolic trough	Manchasol -1	Spain	Ciudad Real
50	Parabolic trough	La Florida	Spain	Badajoz
50	Parabolic trough	La Dehesa	Spain	Badajoz
50	Parabolic trough	Axtesol 2	Spain	Badajoz
50	Parabolic trough	Arenales PS	Spain	Seville
50	Parabolic trough	Serrezuella	Spain	Badajoz

		Solar 2		
50	Parabolic trough	El Reboso 2	Spain	Seville
50	Parabolic trough	Moron	Spain	Seville
50	Parabolic trough	Olivenza 1	Spain	Badajoz
50	Parabolic trough	Medellin	Spain	Badajoz
50	Parabolic trough	Valdetorres	Spain	Badajoz
50	Parabolic trough	Badajoz 2	Spain	Badajoz
50	Parabolic trough	Santa Amalia	Spain	Badajoz
50	Parabolic trough	Torrefresnada	Spain	Badajoz
50	Parabolic trough	La puebla 2	Spain	Seville
25	Parabolic trough	Termosolar Borges	Spain	Lerida
17	Solar tower	Gemasolar	Spain	Seville
1	Parabolic dish	Renovalia	Spain	Albacete
75	ISCC	Martin next generation solar energy center	USA	Florida
20	ISCC	Kuraymat plant	Egypt	Kuraymat
25	ISCC	Hassi R'mel integrated solar combined cycle power station	Algeria	Hassi R'mel
20	ISCC	Beni Mathar plant	Marocco	Beni Mathar

Figure 1.20: Map of operative and under construction CSP plants in Spain

Particularly interesting is the GEMASOLAR tower power plant because it incorporates technologically advanced concepts. The plant will use molten salts both as working fluid and as storage fluid, and it is composed by 2500 heliostats in a circular field covering 142 ha. The receiver is circular with a diameter of 8-

10 m and a height of 9-11 m placed at the top of a 130 m tower. The molten salts mixture will work at on operative temperature between 290 and 565°C.
The main characteristic is the heat storage that has been designed to let the turbine work for 15 hours at nominal power. According to the promoter reports, the plant will produce 110000 MWh per year and will work for 6500 hours per year [13].

Figure 1.21: Gemasolar plant under construction

Besides this innovative plant, table 1.3 shows that there are other attractive technologies like the Integrated Solar Combined Cycle (ISCC) in North Africa (Egypt, Algeria, Marocco). For example the Hassi R'Mel integrated solar combined cycle power station, which will be built near Hassi R'Mel in Algeria, will combine a 25 MW parabolic trough concentrating solar power array in conjunction with a 130 MW combined cycle gas turbine plant. This solution brings some thermodynamic benefits linked to the fact that the solar energy is used to heat the working fluid at a low temperature, leaving the precious fossil fuel energy for the higher temperature.

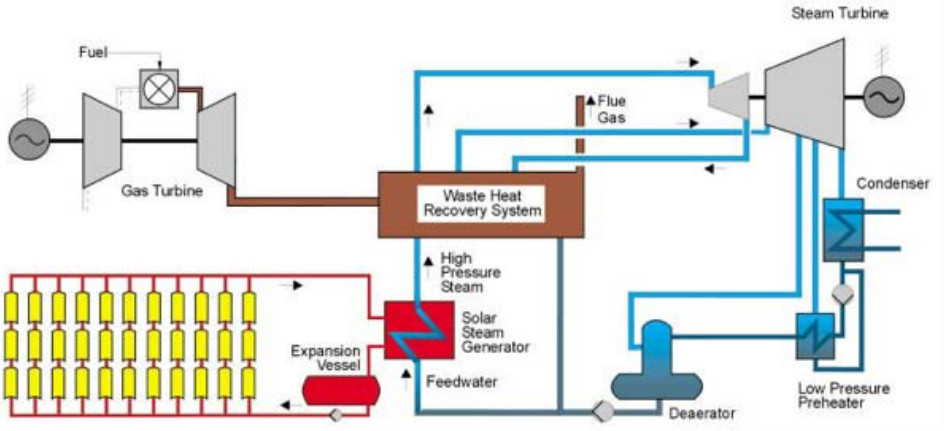

Figure 1.22: An ISCC scheme

1.5.3 Announced projects

The rapid growth of CSP is clearly shown by the many projects presented, especially in USA and Spain, that will be built in the next years.
For example, CSP projects accounting 7600 MW are under review just in USA. Of them, 1500 MW correspond to solar power towers, 4100 MW to parabolic trough plants, 1600 MW to parabolic dishes and 300 MW to Fresnel reflectors.
The State of California is surely the most active in this scenario. In fact the federal Bureau of Land Management (BLM) land has received requests encompassing more than 300,000 acres for the development of approximately 34 large solar thermal power plants totaling approximately 24000 MW.

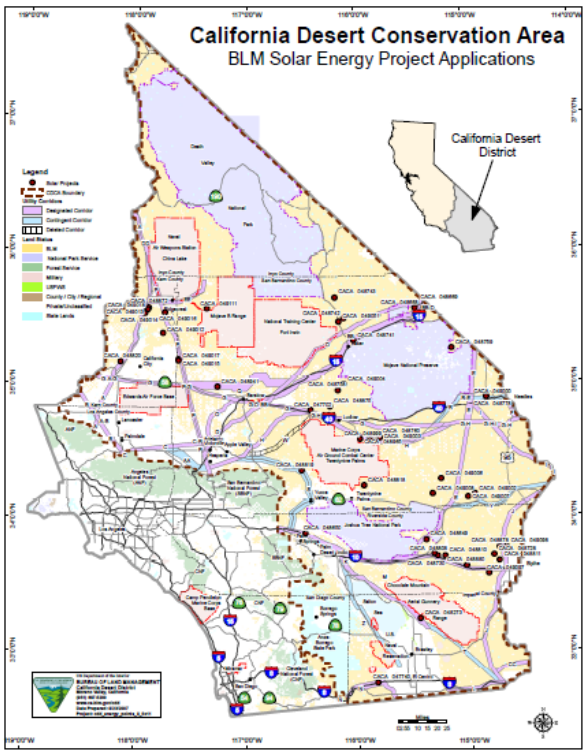

Figure 1.23: California CSP projects

In Spain, other 1100 MW of CSP plants are projected; 120 MW of which correspond to solar tower power technology, 1000 MW to parabolic trough and 10 MW to Fresnel reflector.

In the rest of the world more than 4000 MW should be installed, mainly in China, Morocco, Australia and Israel but, in most cases the technology has not been selected yet.

2. THE MODEL

2.1 Main Objectives

In spite of the remarkable announced development just described, the behavior of Solar Tower power plants is still quite unpredictable, due to the somewhat random evolution of heat input, and its description is often left to measurements.

The models available nowadays often focus on the design and performances of the solar field or, on the other hand, employ a very general description, aimed at analyzing the plant economic feasibility; in both cases a detailed thermodynamic modeling of plant components is neglected. This is mostly caused by the prevailing cost of the solar field, which usually accounts for more than half of the total cost of the plant, while the power block costs typically represent only 15-20% [15].

Nevertheless, having a model to analyze, in a short time, the expected behavior of the plant with different "input" conditions has been conceived as an interesting step in the way to enhance plant performances.

An on design analysis could indeed help at optimizing the components in terms of several characteristics, therefore defining the best plant configuration.

On the other side, due to the random and somewhat unpredictable nature of the primary energy source exploited by the power plant, these facilities are subjected to extremely variable working conditions. An off design analysis could then give an interesting basis for the management phase of the system, trying to react in the best possible way to changes of the external conditions.

The aim of the model is then to describe the plant behavior both in nominal and in part-load conditions, focusing in particular on the receiver and on the power-block and leaving the solar field for future works.

2.2 Required features of the model

To make it suitable for a lot of different situations and users, the characteristics that have been chosen for the model are:

- Simplicity
- Low computational time

- Possibility to introduce new aspects
- User friendly interface

The first two aspects are actually interconnected and they are obtained thanks to the use of appropriate simplifications and assumptions. Without compromising the reliability of the model, indeed, in some cases the choices have been taken considering these two features as fundamental. As example, the thermal efficiency of the receiver is assumed fixed to the 92% and the behavior of the condensate pump is studied with simplified relations due to its marginal power consumption. These two choices let the program work in an extremely faster way, but do not affect its accuracy or reliability; the first assumption is indeed based on real experimental values that have been moreover confirmed by another thermal model specifically designed to validate the former, while the influence of the condensate pump on global plant performances is known to be practically negligible.

To allow for possible developments of the model, this has been designed to permit a very easy implementation of new aspects and components. With regard to the power-block, the structure of the code has been kept quite linear and it is expected that a future developer of the model could in a few time understand how and where to intervene.

Aiming to allow the interaction of not extremely expert users also, a user's friendly graphical interface has been developed, which will be described in detail later.

2.3 Software choice

Several software are nowadays available to write simulating codes, and the choice has been taken in a progressive way.

The first, simplest approach to the model has been indeed done through the software Microsoft Office Excel; this permits an intuitive and clear vision of all the considered variables and of the relations that exist among them. To approach the more complicated receiver model, instructions in Visual Basic language can be defined in the Excel environment.

With the need of a more detailed description of the system and the increase of the number of iterative cycles required, the software Excel has been abandoned and the optimal choice has appeared to be the software MATLAB.

MATLAB® is a high-level technical computing language and interactive environment for algorithm development, data visualization, data analysis, and numeric computation. As claimed by the producer firm, *The MathWorks*, using the MATLAB product allows solving technical computing problems faster than with traditional programming languages, such as C, C++, and Fortran.

The essential characteristics that make this software suitable for the modeling of a solar tower power plant are its capability in managing non-linear equations systems and its stability in working with multi-variables iterative processes. Moreover, the huge diffusion of this tool both in the Academic and in the Industrial Research Centers will allow a large number of hypothetical users of the model to run it and to eventually manage and modify it.

The possibility to develop a quite "flexible" graphical interface has represented another winning point for the choice of MATLAB.

To develop the analysis of the power-block, also the software EES (Engineering Equations Solver) has been tested; interesting tools in terms of fluid properties analysis are present in this software but the solving procedure has demonstrated to be less stable than the MATLAB one and quite difficult to understand (absence of a real debug mode).

In the end, the software MATLAB 7.5.0 (R2007b) has so been chosen for the development of the model.

2.4 Model structure and functioning

The global model is basically composed by two different main sub-models, one related to the power block and one related to the solar central receiver (simply called "boiler"), the most significant component of a solar tower power plant.

Both sub-models include features to perform calculations either at on or off design conditions. In particular the on-design situation has been identified as the insolation conditions of March 21st at 12.00, in Southern Spain, with 1000 W/m^2 irradiance at ground level.

The on-design model is based on the plant layout and a set of assumptions taken directly from the PS10 power plant. Most of these assumptions are aimed at setting the "default" values of the model, though they can be easily modified by the users. The objective of the on-design analysis is to determine the characteristics of a solar tower power plant with the required electrical power output.

The working principle of the model is so the following (for a more detailed description see Chapters 5, 6, and 8):

Once started the program, the user introduces some characteristics of the desired plant:

- net power output desired [MW]
- drum pressure [bar]

Additionally, many other parameters such as the pumps characteristics in the boiler or the turbine isentropic efficiency can be changed, substituting the default values.

Thanks to the models of boiler and power block, joined together, the program, after a few minutes, yields the following output:

- thermodynamic properties at each relevant point of the plant (heat balance)
- dimensions of the central receiver
- detailed characteristics of the flow inside the pipes of the boiler

More in particular, the power-block model is used to identify the total water/steam mass flow needed to produce the required power, which will later be used as input to the "boiler submodel" in order to calculate the dimensions of the solar receiver. A simple scheme of this procedure is reported in Figure 2.1.

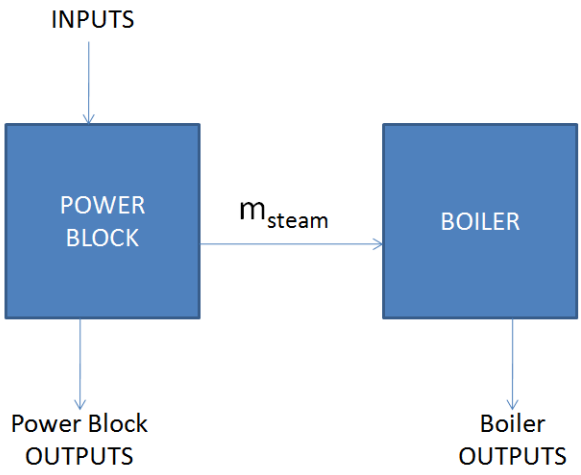

Figure 2.1: Schematic on-design model procedure

In this way, the user knows practically everything about the functioning of the plant in on design conditions and, in particular, he can estimate accurately the dimensions of the receiver needed to generate the steam mass flow able to produce the electrical power demanded. Approximate dimensions of the solar field and the tower are also provided.

Once defined the plant characteristics in nominal conditions, the user can choose to study the same plant with a lower incoming radiation. In this case, indeed, the reduced heat input cuts down steam production what, in turn, makes live steam pressure, and therefore drum pressure at the boiler, decrease due to the sliding pressure part load operation of the steam turbine. It becomes therefore necessary to define the new operating point of the plant.

The evaluation of the new equilibrium is executed thanks to the coordination of the off design models of boiler and power block. Once chosen by the user the new radiation map, the program proceeds with the calculations providing the following output data:

- electrical net power produced by the turbine/generator
- thermodynamic properties at each point of the plant
- detailed description of the boiler.

The choice of different pumping stations and condenser control modes is also possible, in order to define the best strategies to manage the plant during part-loads.

As said, the code works finding the new drum pressure by an iterative interaction between boiler and power block models. More precisely, the boiler model calculates the new steam production from the new radiation map, still using the on-design drum pressure; this value is then given as input to the power-block submodel, which corrects the drum pressure value according to the steam turbine functioning and sends it back to the boiler model. This model is thus able to calculate a new steam production, according to the new radiation map and also to the new pressure (Figures 2.2 and 2.3). After a few iterations of the type described, the values of steam mass flow and drum pressure converge to a solution.

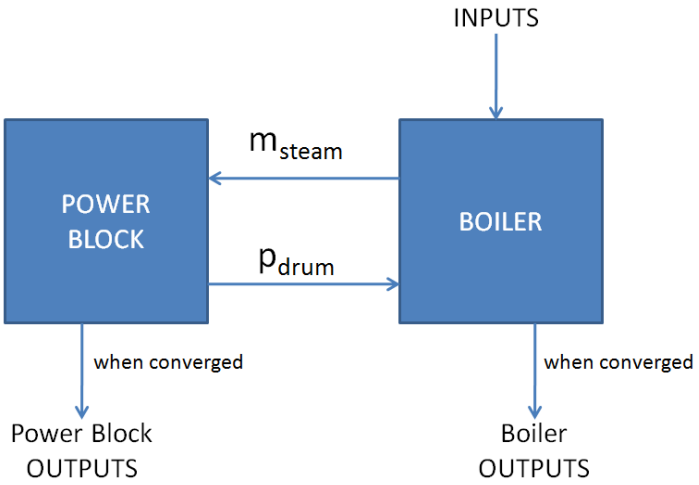

Figure 2.2: Schematic off-design model procedure

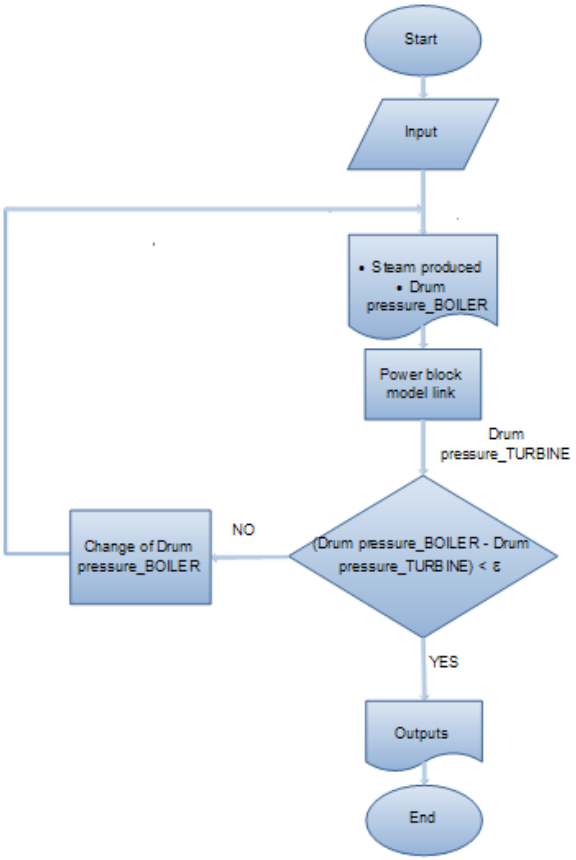

Figure 2.3: Off-design model flow chart

2.5 Main sub-routines adopted

Among the advantages in the use of the software MATLAB, there is the presence of several built-in or easy-to-add subroutines. Two of them have most of all demonstrated to be extremely useful for the development of the model, the sub-routine XSteam and the sub-routine fsolve.

XSteam

XSteam is a MATLAB implementation of the IAPWS IF97 standard formulation, created by Magnus Holmgren in 2006. More precisely, it is a database of steam and water properties based on the "International Association for Properties of Water and Steam" Industrial Formulation 1997 (IAPWS IF-97). XSteam provides very accurate steam and water properties in ranges from 0-1000 bar and 0-2000°C and it is often used in process Engineering Industry. Provided thermodynamic properties are:

- Temperature
- Pressure
- Enthalpy
- Specific volume
- Density
- Specific entropy
- Specific internal energy
- Specific isobaric heat capacity
- Specific isochoric heat capacity
- Speed of sound
- Viscosity
- Vapour fraction

In case of superheated steam or subcooled water, all properties can be calculated having two known inputs, which can be for instance pressure and temperature or pressure and enthalpy. In case of wet steam a more careful choice has to be made considering that pressure and temperature are not sufficient to calculate the other characteristics. Knowing one of them and enthalpy or steam quality, all the properties can be anyway defined. [16].

XSteam has been fundamental to completely determine the thermodynamic properties of the sections of the plant and has allowed the construction of a rapid and dynamic model, eliminating the need to interpolate water properties from tables.

fsolve

The sub-routine fsolve is the MATLAB tool to solve systems of nonlinear equations. To use fsolve, the problem has to be specified in the form $F(x) = 0$,

where x is a vector and F(x) is a function that returns a vector value. The normal procedure consists in creating a function *fun* where a vector of the unknown variables (x) and a vector with the relative equations (F) are defined.

Then, giving the instruction

[x,fval,exitflag] =fsolve(*fun*,x0)

the program starts from the initial guesses defined in the vector x0 and tries to iteratively solve the equations described in *fun*. Once terminated, it returns the value of the objective function *fun* at the solution x and a value exitflag that describes the reason why the algorithm terminated, according to the conventions reported in Table 2.1

Table 2.1: Exitflag value

Exitflag value	Reason for algorithm termination
1	Function converged to a solution x.
2	Change in x was smaller than the specified tolerance.
3	Change in the residual was smaller than the specified tolerance.
4	Magnitude of search direction was smaller than the specified tolerance.
0	Number of iterations exceeded options.MaxIter or number of function evaluations exceeded options.FunEvals.
-1	Algorithm was terminated by the output function.
-2	Algorithm appears to be converging to a point that is not a root.
-3	Trust radius became too small.
-4	Line search cannot sufficiently decrease the residual along the current search direction.

The control on the exitflag value is a fundamental step during the simulation process, considering that a value different from 1 enlightens a possible incorrect solution.

The tool fsolve is able to solve the system adopting different algorithms. A first relevant choice is to use the so-called Large Scale Algorithms or the Medium

Scale Algorithms; not pretending to enter into the details, we can say that the common (and default) choice is to use Medium Scale Algorithms. Within these, three possibilities are available: the first and default one is the trust-region dogleg method, but also the Gauss-Newton and the Levenberg-Marquardt method can be used [17]. Proper descriptions of these methods can be found in [18-20].

It has to be noticed that the default trust-region dogleg method can only be used when the system of equations is square, i.e., the number of equations equals the number of unknowns. For the Levenberg-Marquardt and Gauss-Newton methods, instead, the system of equations does not need to be square. In any case, it can be said that the number of equations must be at least as many as the length of x.

For the plant simulating model, the sub-routine fsolve has the task to solve the system of equations that describe the power-block side, both in on and off-design conditions (a deeper description is provided in the following sections). The use of this tool permits writing the code with a simple and intuitive structure, avoiding the problems of developing complex and multi-variables loops.

2.6 Graphical User Interface

The main objective of developing the model is to provide a useful tool for many different potential users both in the Academic and in the Energy Industry sector.

The creation of a user friendly and at the same time effective graphical interface has therefore represented an important part of the work.

The program is basically composed by four phases, each one of which has a dedicated screen in the graphical interface.

- On-design inputs definition

- On-design model results

- Off-design inputs definition

- Off-design model results

On design inputs definition

The screen has been designed to let the user define the desired plant characteristics in terms of power production and drum pressure. Moreover, all the assumptions made for the on-design model are displayed and can be modified according to the user's needs. To allow an easier data introduction, the screen has been divided in different panels and sub-panels.

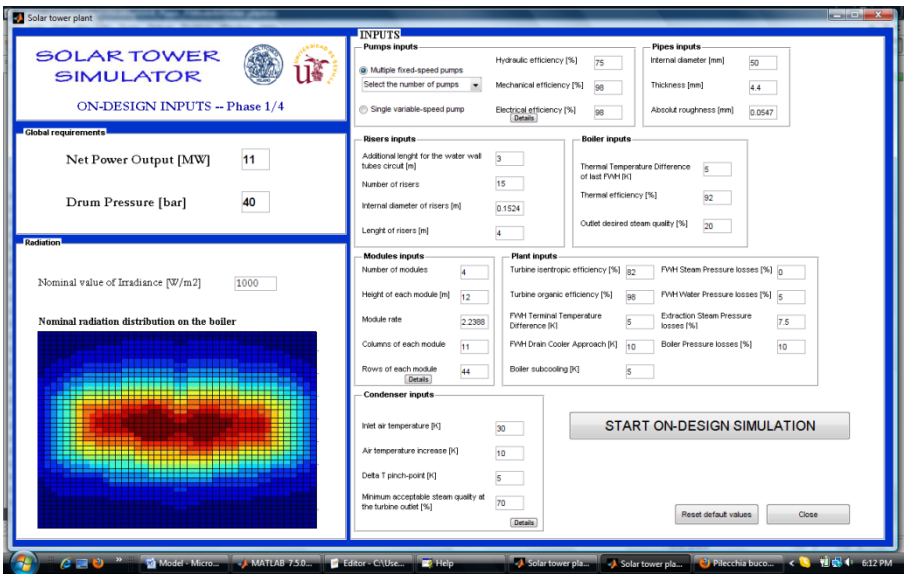

Figure 2.4: On-design inputs screen

On-design model results

The screen displays the outputs of the on-design model. These have been classified in "boiler outputs" and "power-block outputs", each of which is again sub-divided in "Numerical" and "Graphical" results. Both the numerical and graphical outputs have indeed been considered to be useful for a total comprehension of the plant behaviour and characteristics. Several tables and graphs are available in this section, and the results can be saved as jpeg images and Excel tables. Proper buttons are included to let the user skip to off-design analysis or go back and start another on-design simulation.

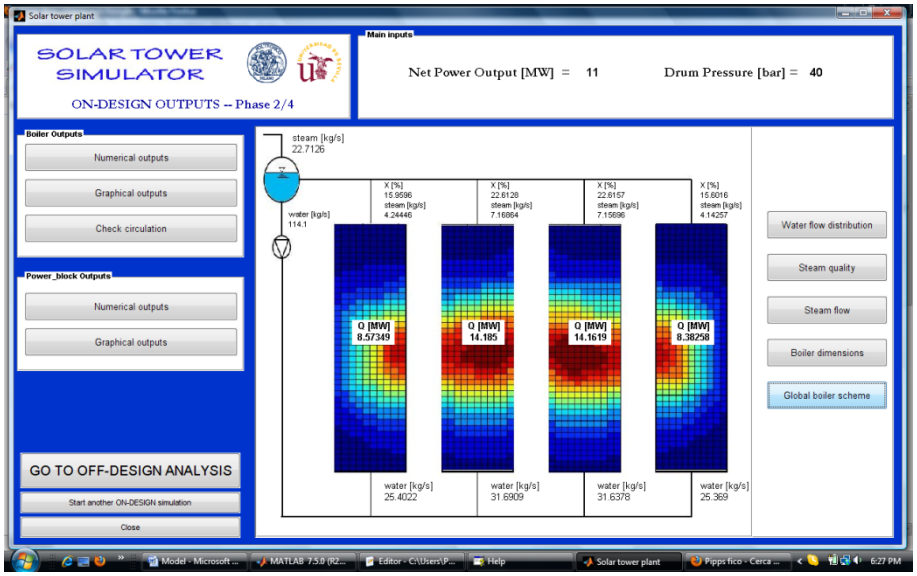

Figure 2.5: On-design outputs sample screen

Off-design inputs definition

In the off-design inputs phase, the user can choose among different radiation maps and can define the condenser part-load regulation strategy. The values of the main on-design inputs are recalled in order to let a better confrontation.

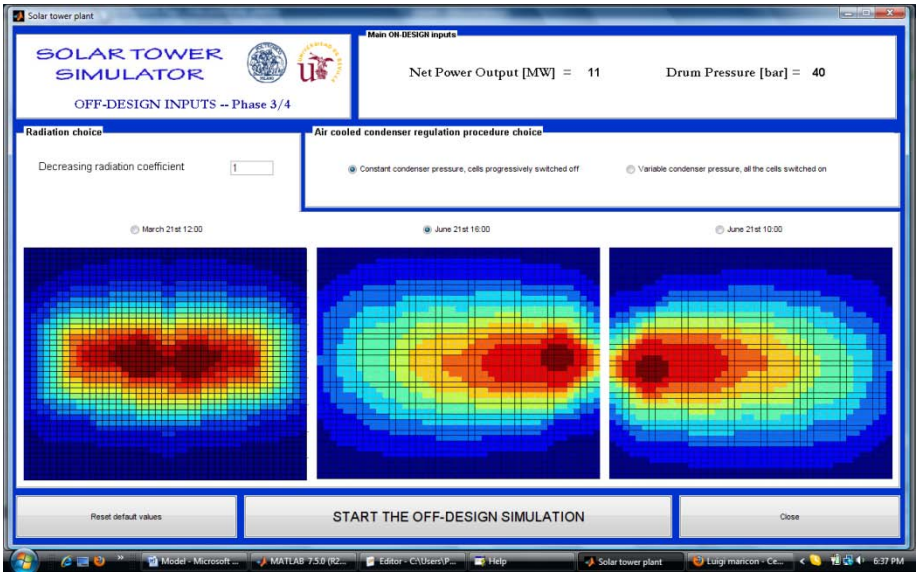

Figure 2.6: Off-design inputs screen

Off-design model results

The off design model results page traces out the on design results one, displaying numerical and graphical results both for boiler and power-block. Where possible, the graphical representations include also the on-design results, to let an immediate understanding of the plant behaviour.

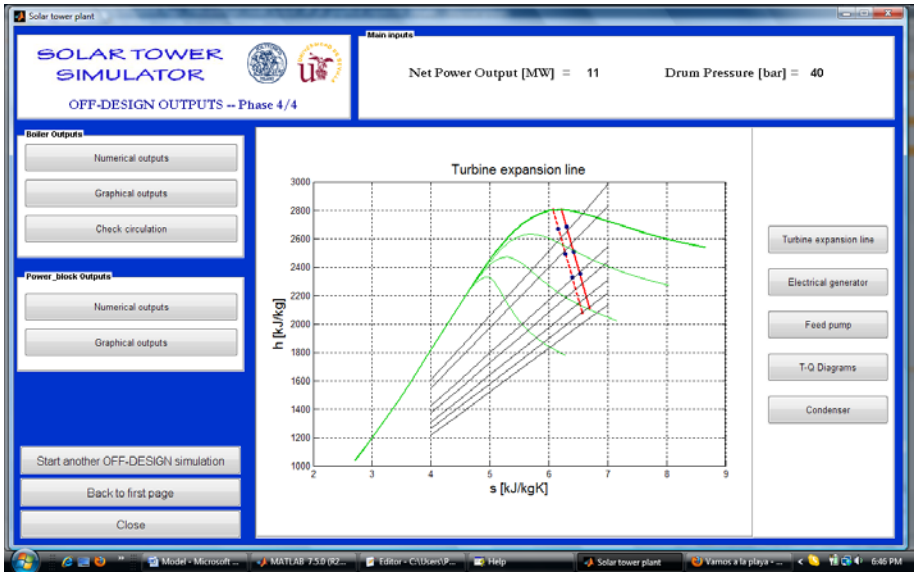

Figure 2.7: Off-design outputs sample screen

Keeping in mind that a part of potential users could be non-technician, the interface has been thought to have several explications and to guide the user continously. For example, by clicking a “Details” button in the on-design inputs screen additional information on the components is displayed. Error messages have been incorporated too.

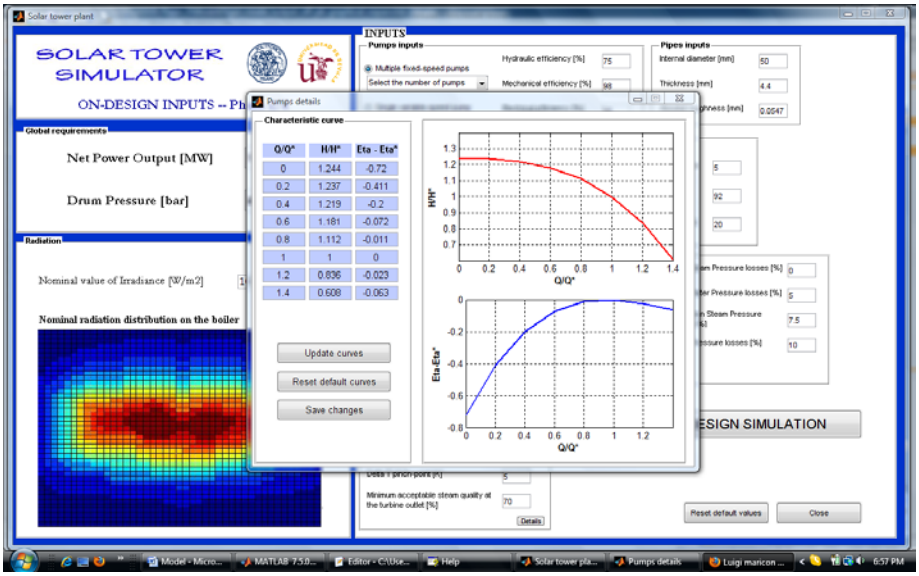

Figure 2.8: Pumps details sub-screen

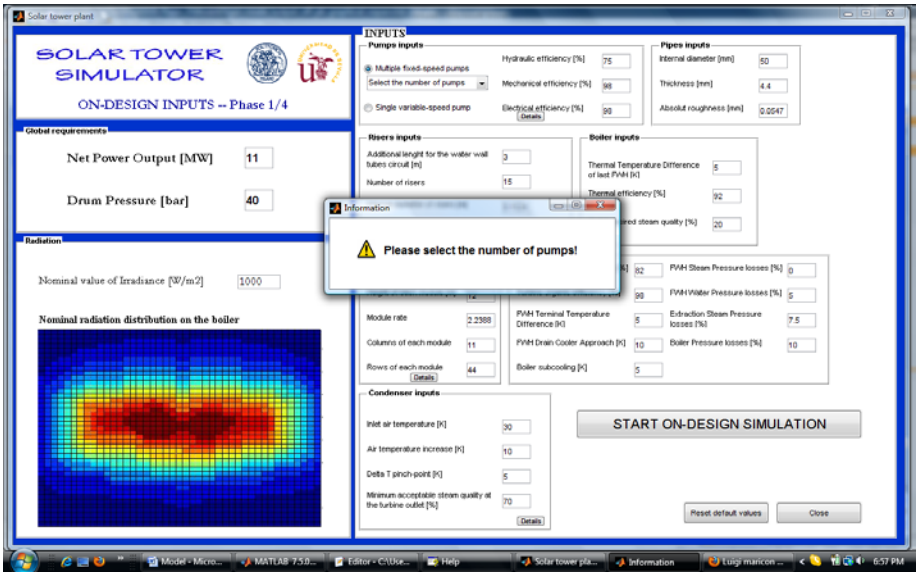

Figure 2.9: Information message

3. Collector Subsystem

The collector subsystem for a solar central receiver is responsible for the interception, redirection, and concentration of direct solar radiation to the receiver, located in the top of the tower. The collector subsystem consists of a field of tracking mirrors, called heliostats, and a tracking control system to maintain the direct solar radiation continuously focused on the receiver while energy is being collected. During cloud passages and transients, the controls must defocus the field and react to prevent the reflected energy from damaging the receiver, the tower, or other structures, or from creating unsafe conditions in the airspace around the plant [21,22].

3.1 Basic Optics and performances

Solar concentrators follow the basic principles of Snell's law of reflection: in a specular surface the reflection angle equals the angle of incidence. Nevertheless, in real mirrors with intrinsic and constructional errors, the reflected ray distribution is better described with "cone optics" and the error associated to the reflected ray direction takes the shape of a normal distribution function (Figure 3.1).

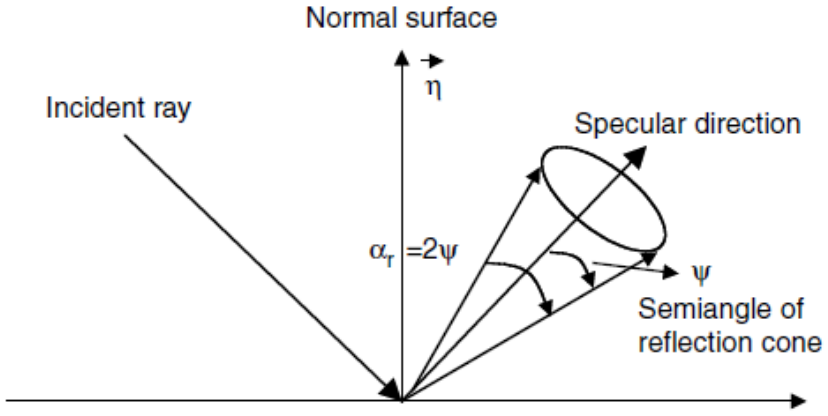

Figure 3.1: Geometry of reflection according to the principles of Snell

The errors of a typical reflecting solar concentrator may be either microscopic (specularity) or macroscopic (waviness of the mirror and error of curvature).
All the errors together end up modifying the direction of the normal compared to the reference reflecting element, but it is useful to discriminate between

microscopic and macroscopic errors. Microscopic errors are indeed intrinsic to the material; they depend on the fabrication process, and can be measured at the lab with mirror samples. Macroscopic errors are instead characteristic of the concentrator and of the erection process. They should therefore be measured and quantified with the final system in operation.

The parameter best defining the "macroscopic" quality of a reflective concentrator is the slope error (β), the angle between the normal to the reference surface N_0 and the normal to the real reflecting surface N (Figure 3.2).

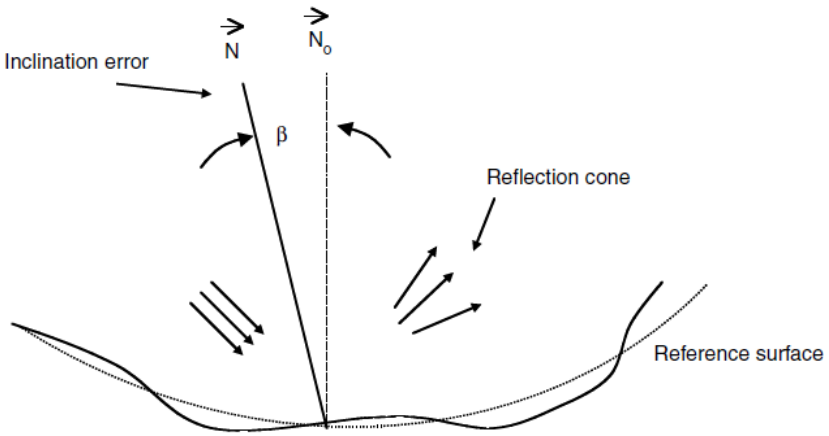

Figure 3.2:Normal error produced by grainy texture of the material and deficient curvature of the concentrator

Together with an error contribution given from a not-perfect aiming of the tracking system, the inclination error determines the so-called beam quality of the concentrator reflector. In order to approximate these nonsystematic errors, a statistical approach is commonly used; hence, the beam quality is often referred as the total standard deviation of a solar concentrator:

$$\sigma_c^2 = \sigma_{sp+wav}^2 + \sigma_{curvature}^2 + \sigma_{tracking}^2 \quad (3.1)$$

where σ_{sp+wav} is the beam standard deviation due to specularity and waviness (measured with reflected rays from material samples using a reflectometer), $\sigma_{curvature}$ is the beam standard deviation due to curving (and should be measured on the concentrator itself), and $\sigma_{tracking}$ is the beam standard deviation due to aiming point and other drive mechanism-related sources of error.
A more precise description of the heliostat characteristics is anyway given from the so-called *total error of the image*, which includes also the effect known as "sunshape effect".

It should indeed also be taken into account that solar rays coming directly from the solar disc are not completely collimated, but have a certain solid angle. The subtended solid angle is 32'; this means an angular radius of 4.653 mrad or 16' of arc. Therefore, even an ideal parabolic concentrator would reflect the image of the sun on a spot having the same target-to-mirror solid angle. This means that for an ideal heliostat located 500 m from the optical target or focal point, the theoretical diameter of the spot would be 4.7 m.

Moreover, dispersion and absorption effects on the solar photosphere modify the uniform distribution of the expected irradiance from an ideal blackbody. Because of this modification, the sunshape is more realistically represented by a "limb-darkened" distribution than by the ideal uniform distribution; the sun is indeed darker near the rim than at the center.

The total error of the image, also known as degraded sun, would so be the convolution of the beam quality of the concentrator with the sun shape.

$$\sigma_D^2 = \sigma_{suns\,hape}^2 + \sigma_c^2 \tag{3.2}$$

The consequence of the convolution of all the above mentioned errors from the sun, tracking system and reflecting surface, leads to the fact that the spot and energy profile obtained on a flat absorber can be approximated to a Gaussian shape, as shown in Figure 3.3 [22].

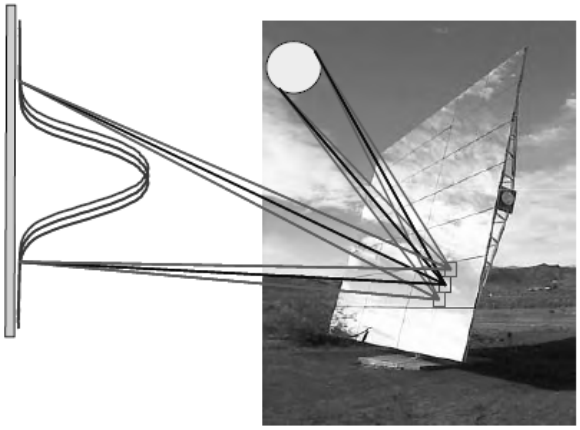

Figure 3.3: Effect of the size of the sun and other errors on the reflected image with a real heliostat

In addition to these effects, characteristics of the specific sun-heliostat-receiver interaction, other losses must be considered to properly describe the performance of a heliostat field.

The performance of the heliostat field is indeed defined in terms of the optical efficiency, which is equal to the ratio of the net power intercepted by the receiver to the product of the direct insolation and the total mirror area.
As just said, several losses components are considered, known as cosine effect, blocking, shadowing, mirror reflectivity, atmospheric transmission, and receiver spillage [21]. In Figure 3.4 a schematic representation of some of these losses is reported.

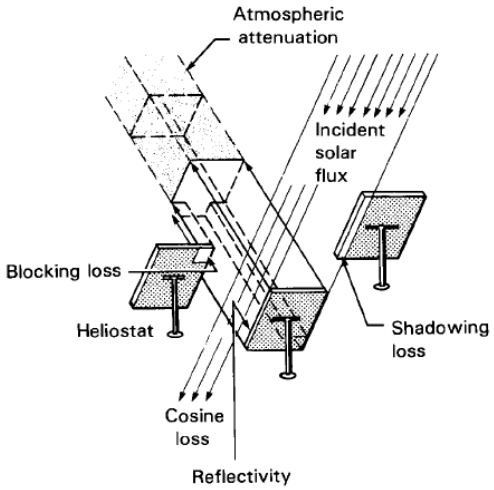

Figure 3.4: Collector field optical losses

3.1.1 The cosine effect

The amount of insolation reflected by the heliostat is proportional to the amount of sunlight intercepted. The reflected power is proportional to the cosine of the angle (cosine effect) between the heliostat mirror normal and the incident sun rays; the ratio of the projected mirror area that is perpendicular to the solar beams over the total area of the heliostat determines the magnitude of the cosine effect.
The heliostat is oriented so that the incident sunlight is reflected onto the receiver. If the sun is due south and low in the sky, as it is in winter, then the heliostats due north of the tower will be almost perpendicular to the sun's rays and, therefore, have almost the maximum cosine efficiency of 1.0. At the same time, heliostats due south of the tower will have a low cosine efficiency. Since the greatest fraction of the annual insolation occurs when the sun is in the southern sky, the annual average cosine will be greatest in the northern part of the heliostat field. Thus, in the northern hemisphere, heliostat fields are usually biased toward the north of the tower. [21]

3.1.2 Blocking

Blocking of reflected rays is also an important limitation on spacing heliostats. Blocking is produced by neighboring heliostats. To avoid blocking losses, the distance Δx between the heliostat rows must be calculated according to the following equation: [22]

$$\Delta x = x \cdot \frac{z_s}{z_T} \tag{3.3}$$

where:
$x =$ distance between the heliostat and the tower
$z_s =$ heliostat vertical dimension
$z_T =$ geometrical tower height above ground

3.1.3 Shadowing

Shading produced by neighboring heliostats also has to be taken into account. This occurs mostly at low sun angles and in the middle of the field where blocking conditions would allow close spacing. The shadows move during the day and year, as does the heliostat orientation, so there is no simple rule. In addition, the tower or other objects may also cast a shadow over part of the heliostat field. Usually shadowing in the field is calculated by projecting the outlines of the heliostats aligned, the tower and anything else that casts a shadow onto a plane perpendicular to the center sunray. Classical computer codes like HELIOS provide this calculation [22].

3.1.4 Mirror reflectivity

The heliostats do not reflect the whole solar radiation that impinges their surface because part of this radiation is absorbed by the glass. The ratio between the incoming and the reflected radiation is called reflectivity and depends on the radiation wave length. To quantify this factor, a mean value for the whole solar spectrum is normally used. It has to be noticed that the mirror cleanliness influences the reflectivity value remarkably [23].

3.1.5 Atmospheric transmission

Not all the sunlight that leaves the heliostats reaches the vicinity of the receiver. Some of the energy is scattered and absorbed by the atmosphere; this effect is referred to as the attenuation loss. In a day with good visibility, this effect will

have a small percentage of energy loss per kilometer. The losses increase when water vapor or aerosol content in the atmosphere is high. [21]

3.1.6 Receiver spillage

The size of the image formed by a heliostat depends on mirror focusing and canting, on the size of the heliostat and, as already mentioned above, on the size of the sun and on irregularities in the heliostat surface. A focused heliostat cannot produce a point image because of the finite size of the sun. However, a focused heliostat can produce an overall smaller image than an unfocused heliostat because the effect of heliostat size on image size is reduced (Figure 3.5).

If the receiver is not big enough to intercept the entire image of the heliostat, some of the energy will be "spilled" around the receiver. Although spillage can be eliminated by increasing the size of the receiver, at some point increased size becomes counterproductive due to increased receiver losses and receiver costs exceed the value of the additional energy intercepted by the receiver. [21,24]

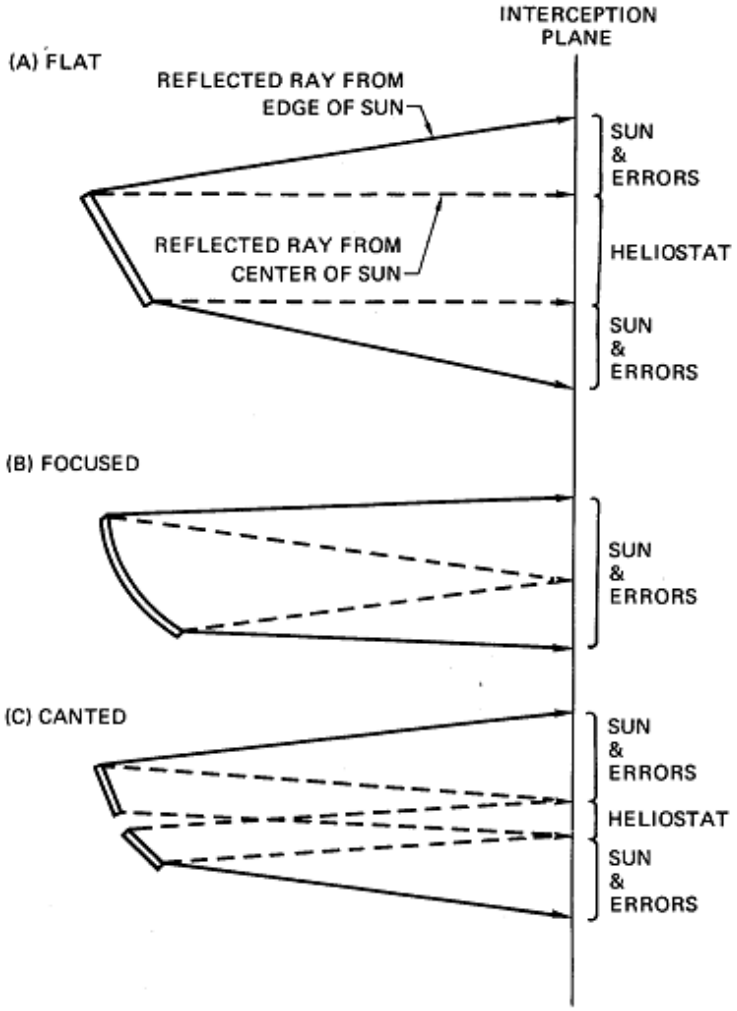

Figure 3.5: Schematic of Images Formed by Flat (A), Focused (B), and Canted (C) Heliostats

3.2 Field layout

The heliostat field is a very important subsystem of a solar tower power plant and it contributes about 50% to the total cost [14]. From this, the attention paid on the disposition of the different heliostats has been remarkable in the last 30 years, with the development of several different approaches and methods.

Moreover, two recent studies about solar power towers (SPT) conclude that improved solar fields and scaled-up power blocks provide the largest cost reduction opportunities. But as the size of the SPT system increases, the optical efficiency declines. Thus, in the last few years, efforts are being done to look for an efficient re-optimization of the system [25].

The first big differentiation of a solar field is between a north and a surround configuration.

In a surround field configuration, heliostats are arranged around a centrally located tower. In the north field configuration (or for plants located in the southern hemisphere, a south field configuration), instead, all heliostats are arranged on the north side of the tower.

Representative collector fields are shown in Figures 3.6 and 3.7 for surround and north-side fields, respectively [22].

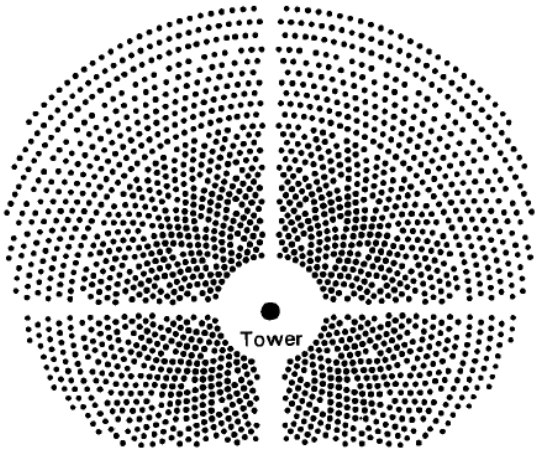

Figure 3.6: Typical Surround Field configuration

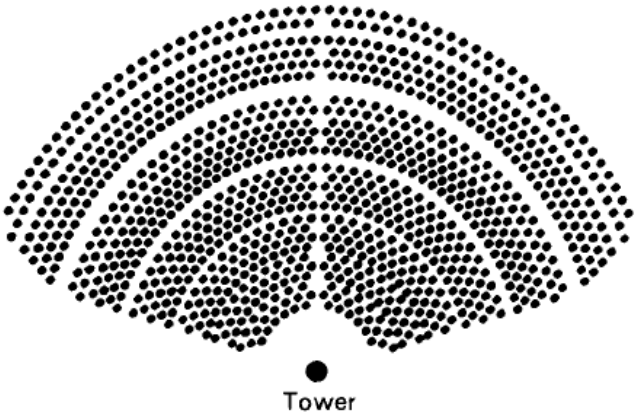

Figure 3.7: Typical North Field configuration

These two classical configurations are complemented by a new one proposed by eSolar in the Sierra Suntower demonstration plant in California. The particular features of this plant will be briefly reported in Section 3.4.3.

As for all the other parameters regarding the disposition of the heliostat field, the choices are made to obtain the best optical efficiency possible.
Talking about the north-field or surround configuration, the main factor that affects whether choose one or the other is the cosine effect. As already said, indeed, because the reflective surface of the heliostat is not normal to the incident rays, its effective area is reduced by the cosine of the angle of incidence. Optical studies and experimental data show that the annual average cosine varies from about 0.9 at two tower heights north of the tower to about 0.7 at two tower heights south of the tower [22]. As an example, we report in Figure 3.8 the cosine efficiency "distribution" calculated for the just mentioned Sierra Suntower demonstration plant [26].

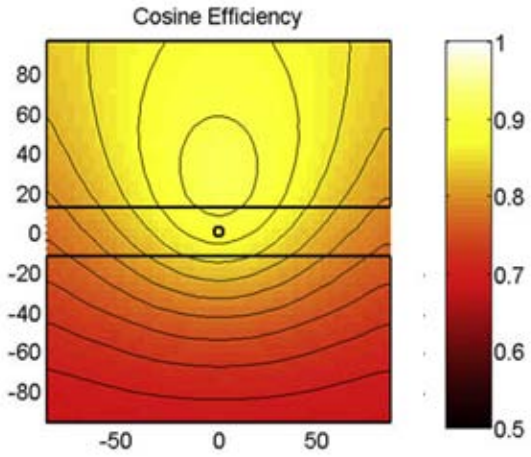

Figure 3.8: Cosine efficiency distribution in the Sierra Suntower solar field

Of course, annual average cosine is highly dependent on site latitude. Consequently, in places close to the equator, where the sun position remains high in the sky for long periods of time, a surround field would be the best option to make the best use of land and reduce tower height. North (or south in the southern hemisphere) fields, instead, improve performance as latitude increases; at Italian/Spanish latitudes, it is generally more convenient to arrange all the heliostats on the north side of the tower [23].

The position of each heliostat, and therefore the integral optimization of the heliostat field, is then decided by a trade-off between cost and performance parameters. This trade-off considers the cost of heliostats, land, and interconnecting wiring. It is worth noting that cost and performance often have reverse trends, so that when heliostats are packed closer to one another, blocking and shadowing penalties increase, but related costs for land and wiring decrease [22].

While both shadowing and blocking increase when heliostats are close together, blocking has a more pronounced effect on the layout of heliostat fields. As heliostats are placed at greater radial distances from the tower, the receiver appears to be closer to the horizon. Therefore, heliostats must be placed at greater radial separations to be able to see the receiver [21]. In Figure 3.9 the Blocking and Shading Efficiency for the Sierra Suntower plant is reported.

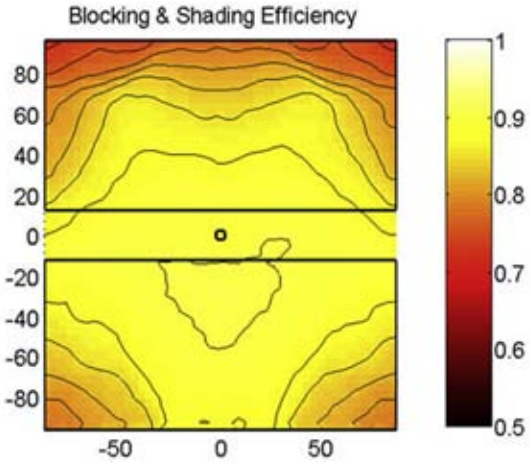

Figure 3.9: Blocking & Shading Efficiency distribution in the Sierra Suntower solar field

As a design option within the collector field, alternate heliostat arrangements are possible. In this sense, the two arrangements concentrating most efforts to date are the "cornfield" and the radial stagger arrangements. In the cornfield arrangement, heliostats are laid out along straight lines with uniform rectangular spacing being maintained throughout the section.

In the radial stagger arrangement, originated by the University of Houston in the 1970s, heliostats are laid out along radial spokes emanating from the concentric circles centered at the tower. The staggered characteristic of the layout means that no heliostat is placed directly in front of another heliostat in adjacent rings along a spoke to the tower. In this way, a reflected beam from one heliostat passes between its adjacent neighbors on the way to the receiver. The radial stagger layout pattern is illustrated in Figure 3.10 [22].

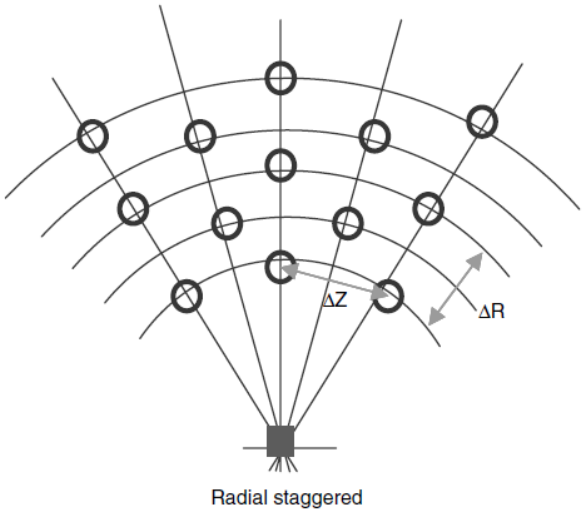

Figure 3.10: Radial staggered field layout, where ΔZ is representing the azimuthal spacing and ΔR represents the radial spacing

The typical radial stagger and north-south cornfield configurations can also be "mixed", to generate a north-south stagger or a radial cornfield layout. This has been studied for the development of the heliostat field of a pioneer 1 MW solar thermal central receiver system in China [27].

Figure 3.11 show the optimization study of the different arrangements.

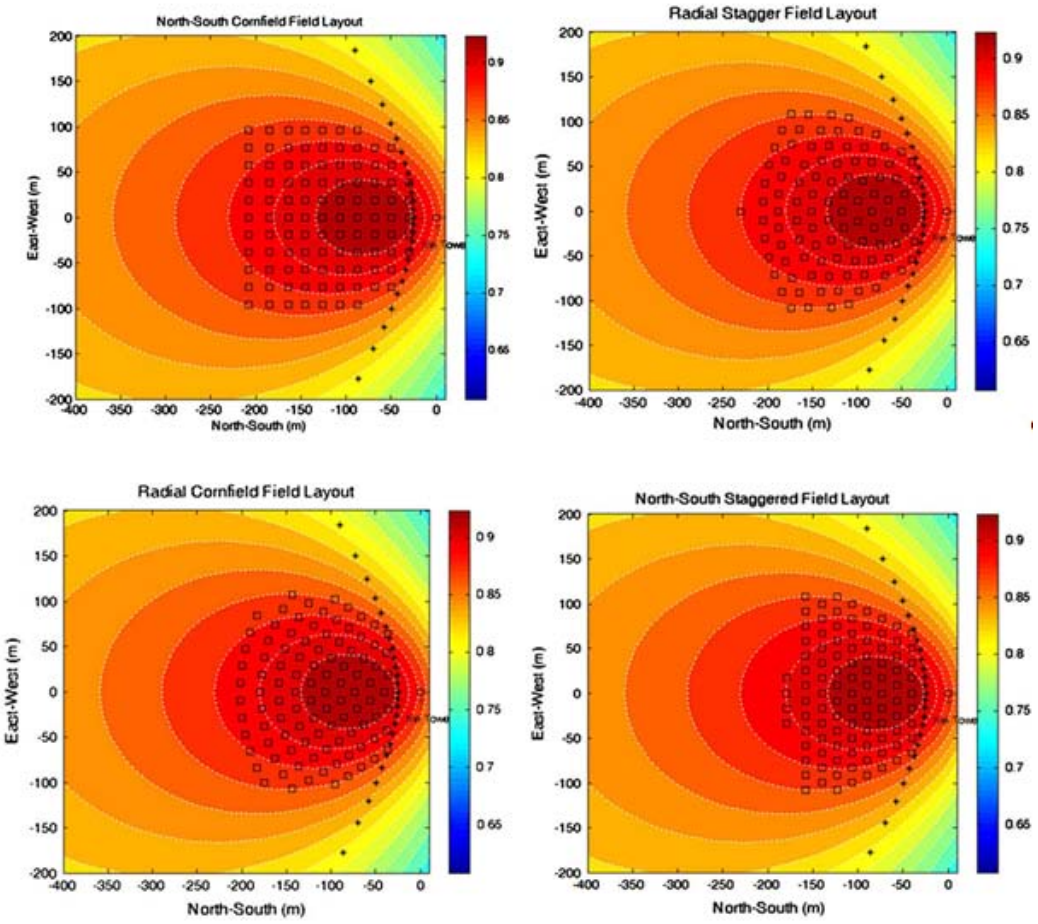

Figure 3.11: Efficiency distribution and representation of North-South cornfield, Radial staggered, Radial cornfield and North-South staggered layouts

Different studies, including this last one, have shown that the radial stagger arrangement is the most efficient for a given land area. As a result, collector field designs for major central receiver systems are based on the radial stagger pattern.

3.2.1 Existing Optimization Software

Because of the large area of land required, complex optimization algorithms are used to maximize the annual energy produced by unit of land surface; in these analyses, the heliostats are subjected to complex performance factors, which must be optimized over the hours of daylight in the year [22].

Yet in the eighties, several Fortran codes used for the design and simulation of solar thermal central receiver plants were written; among others, the following codes are representative: HELIOS, ASPOC, HFLCAL, RCELL, MIRVAL and SOLERGY.

One of the most popular codes in use since the 1980s for optimization of central receiver subsystems is DELSOL, developed by SANDIA laboratories and progressively updated till DELSOL3 [24] and its last version WinDelsol 1.0 for the use in Windows environment.

In DELSOL3, the radially staggered distribution is adopted, and pre-arranged grids based on the tower height versus row-to-radius ratio are created. This geometrical procedure provides a smart solution to the problem with good optimization of computing resources. In the code, radial staggered geometries reveal as extremely efficient to optimize tower height vs. receiver dimensions vs. field layout to achieve the lowest Levelized Electricity Cost [28].

Figure 3.12 shows a breakdown of efficiency maps for the different performance factors in a typical one-sided north heliostat field. It may be deduced that the heliostat density is greatest at the inner boundary and decreases with increasing radial distance from the tower. The average land coverage ratio is typically 0.20–0.25 [22].

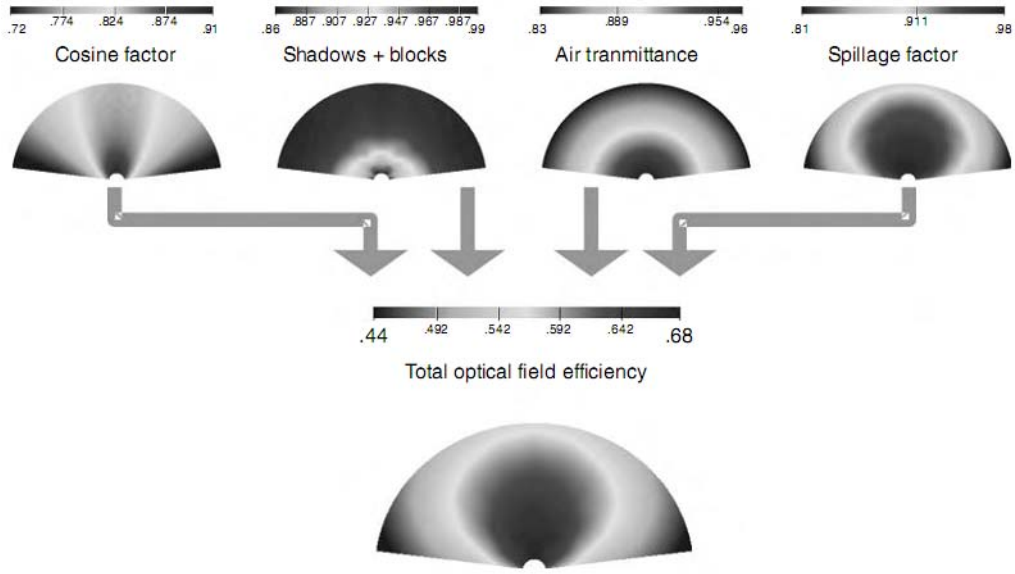

Figure 3.12: Mapping of total optical efficiency of a north field area of heliostats and its breakdown into the losses components.

To try to overcome the philosophy and the structure of the classical codes, Sanchez and Romero proposed in 2004 a completely new approach with a flexible modular structure in MATLAB environment.

The basic idea of the code is that with today's computers, it is possible to calculate the yearly energy available at any point in a site for a given tower height, "the yearly normalized energy surface" YNES. Yearly efficiency maps can be generated based on the cosine factor, the spillage factor, and the site atmospheric attenuation coefficient using real direct normal irradiance data (DNI) within a reasonable computational time. The first heliostat can then be placed on the position with the maximum energy available at the minimum distance from the tower as defined by the user (inner boundary). Once the heliostat is set, yearly normalized shadowing and blocking are added, appropriately modifying the YNES. The next step is to look for the best place on the YNES to locate the following heliostat. Once the new heliostat is located, the YNES is modified again and so forth. The heliostat field thus grows heliostat by heliostat and for this reason this methodology is known as HGM, that is to say Heliostats Growth Method [28].

Figures 3.13 and 3.14 respectively show the YNES without heliostats and the YNES considering shadowing and blocking of the first 10 heliostats.

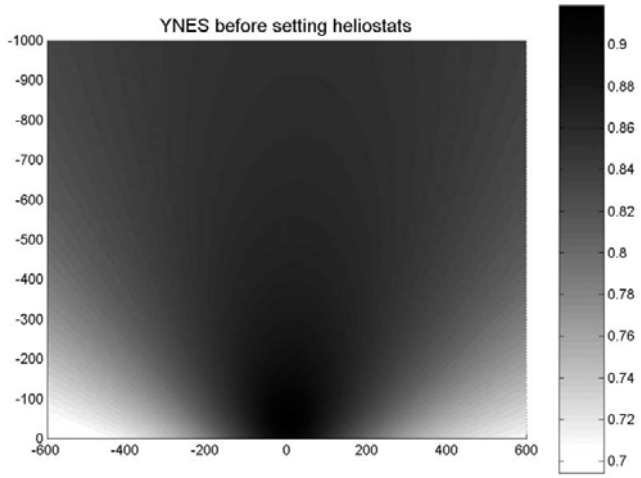

Figure 3.13: Example of Yearly Normalized Energy Surface distribution before the heliostats setting.

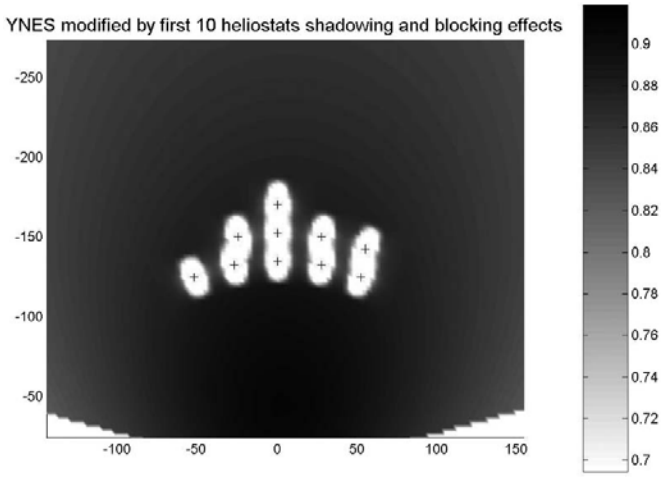

Figure 3.14: Example of YNES distribution after the positioning of the first 10 heliostats

Just in the last months, another code for the design and analysis of the heliostat fields has been proposed by Wei et al. and it has been put in practice for the design of the DANAH power demonstration plant, in China [14].

According to Wei, the iterative calculation of the annual efficiency of heliostat in the code developed by Sanchez and Romero results in a very low response speed. In addition, the layout pattern is not regular and it is difficult to optimize the receiver tilt angle and size as well as the tower height.

To face these problems, in the new method the field layout is made automatically according to the no-blocking loss condition and the heliostats are located at the positions where the annual incident cosine value is higher. In this way, the blocking and cosine losses are lowered. Because the optimization of the distance between fore-and-aft two rows of heliostat is avoided, the computer time is reduced effectively. Different field arrangements have been studied with this method and the results have already been shown in Figure 3.11 .

In the last years, eSolar produced a MATLAB-based ray-tracing tool to be used in designing its heliostat fields. This optical modeling software allows for a rapid evaluation of alternative field layouts and aiming strategies, and predicts the resultant flux distribution at the receiver [26]. The detailed explanation of the code is not currently public, although images of the Sierra Suntower field simulation are already available (Figure 3.15).

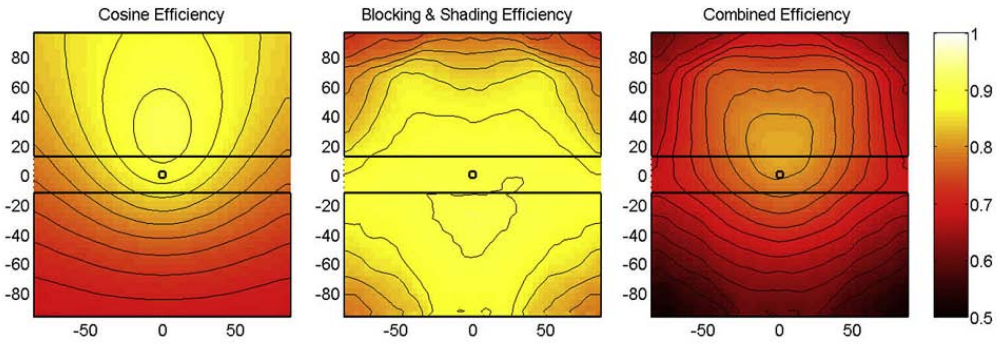

Fig. 2. Heliostat field cosine, blocking and shading, and combined optical efficiency plots.

Figure 3.15: Sierra Suntower Heliostat field cosine, blocking and shading, and combined optical efficiency plots.

3.3 Heliostats

The heliostat is the main element of the collector subsystem. Mature low-cost heliostats consist of a reflecting surface, a support structure (frame), a two-axes tracking mechanism, pedestal, foundation, and control system (Figure 3.16).

Figure 3.16: The 120 m^2 SENER heliostat under testing at the PSA

Since the first-generation units, heliostats have demonstrated beam qualities below 2.5 mrad that are good enough for practical applications in solar towers, so the main focus of development is aimed at cost reduction.[22]
Besides, the heliostat itself is the least dependent central receiver system component on overall system considerations; that is, specific heliostat designs

are not required for each type of receiver heat transport fluid, receiver configuration, or end use application of thermal energy. This independence permits design emphasis to be placed on mass production as a means of reducing the unit cost of the heliostat, recognizing that the collector system represents a major portion of the overall system cost [21]

From the first modern heliostats, developed in the early 1970's, the heliostat size has steadily increased. This growth was brought about by a continual effort to reduce the specific costs of heliostats (in $/m2) since the costs of the drive assemblies and pedestal were found to be, within reasonable limits, relatively insensitive to glass (mirror) area. The increase in reflective surface area for each pedestal drive assembly was shown to be beneficial in reducing the specific costs by spreading these relatively fixed costs over more reflective area. This reduction in the number of heliostats for a fixed system-required-mirror area also reduces the cost of installation and the number of field control components.[21] The upper limit to this advantage is that the larger the area, the higher the optical errors and wind and washing problems are.[22]

A second line of development is devoted to the use of new light reflective materials like polymer reflectors and of composites materials in the supporting structure; an important example is the stretched-membrane heliostats. The stretched membrane drum consists of a metal ring to which prestressed 0.4-mm stainless steel membranes are welded. One of the membranes is glued to a polymer reflector or thin mirrors and a vacuum is created inside the plenum with a controlled blower to ensure curvature. Figure 3.17 illustrates the two development lines of heliostats over time [21].

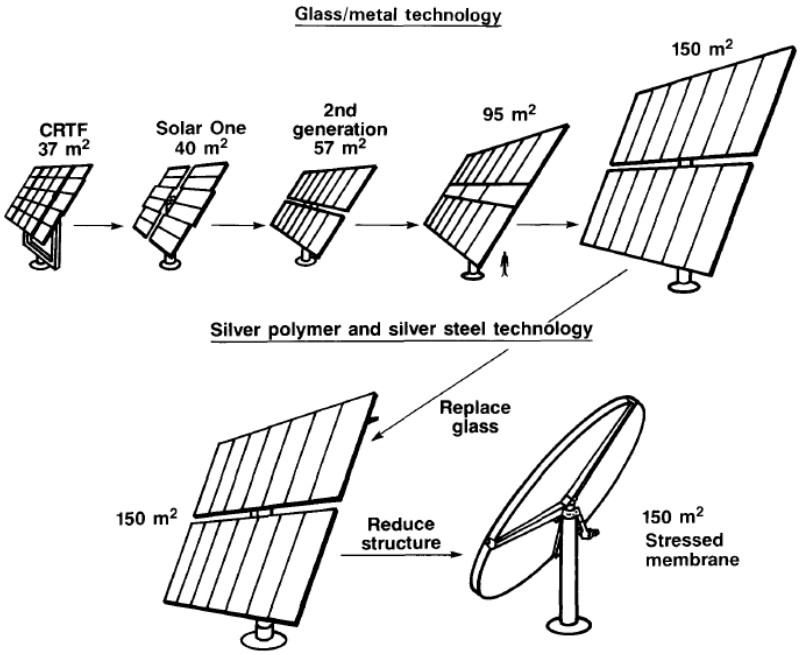

Figure 3.17: Pictorial representation of Heliostat Development

In the U.S.A., the latest development in glass/metal technology is the 150 m^2 ATS heliostat (Alpert and Houser 1990), which presents an Estimated production costs for sustainable market scenarios around \$130/m^2–\$200/m^2 (Figure 3.18).

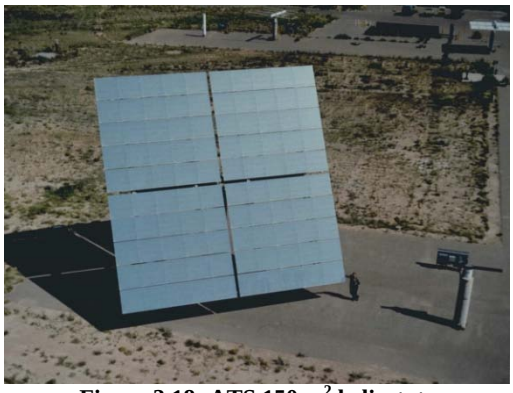

Figure 3.18: ATS 150 m^2 heliostat.

Figure 3.19: ASM-150 stretched membrane heliostat

The stretched-membrane milestone is instead the 150 m2 Steinmuller heliostat ASM-150 with an excellent beam quality of 2 mrad (Figure 3.19). In spite of the good quality achieved by stretched membranes, projected costs are higher than the more mature glass/metal units [22].

The heliostat itself is made up of several major components which are briefly described below.

3.3.1 Reflector

The reflector or mirror module consists of a silvered glass mirror and some support structure in glass/metal heliostats or a reflective polymer-coated metal membrane in stressed membrane heliostats.
Each glass/metal heliostat is made up of multiple mirror modules, called facets, which are usually rectangular and present a slight concave curvature and a canting with respect to the plane of the support structure to better focus the reflected sunlight on the receiver [21].

3.3.2 Reflector Support Structure

The reflector support structure supports the ensemble of mirror modules. Usually this structure consists of a main beam or torque tube with several cross beams. The main beam is attached to the drive system while the mirror modules are attached to the cross beams (Figure 3.20). Truss type beams are the preferred option especially for larger heliostats because their depth can be varied to provide the required stiffness, with little weight penalty. A roll-formed section, while good for small depths, has a solid web which makes deep roll-formed sections weigh more and has less stability than truss type beams [21].

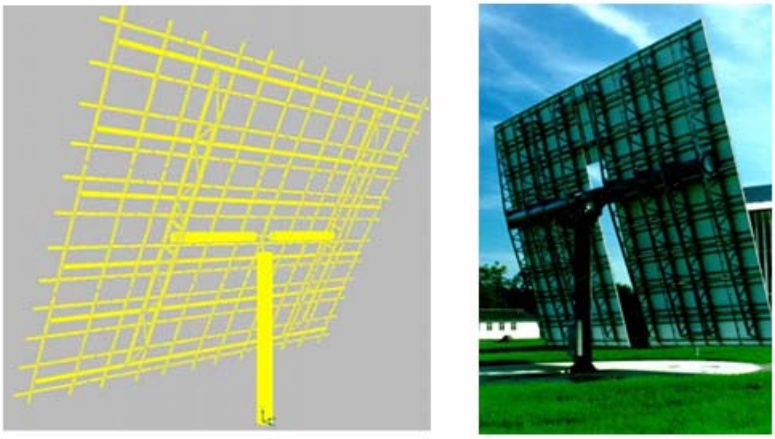

Figure 3.20: CAD and real examples of support structures.

3.3.3 Pedestal and Foundation

Past work has identified the single pedestal mounted heliostat as the preferred configuration. A pedestal mount costs less and both drives may be located at the top of the pedestal. Heliostat foundations have been studied for different heliostat sizes and soil types. When soil conditions permit it, a drilled pier type foundation is the most cost effective [21].

Figure 3.21: Example of heliostat pedestal.

3.3.4 Drive Systems

Since the solar receiver is located in a fixed position, the entire collector field must track the sun in such a way that each and every heliostat individually places its surface normal to the bisection of the angle subtended by sun and the solar receiver. Figure 3.22 shows the variability of elevation angles in a heliostat field and identifies the elevation angle.

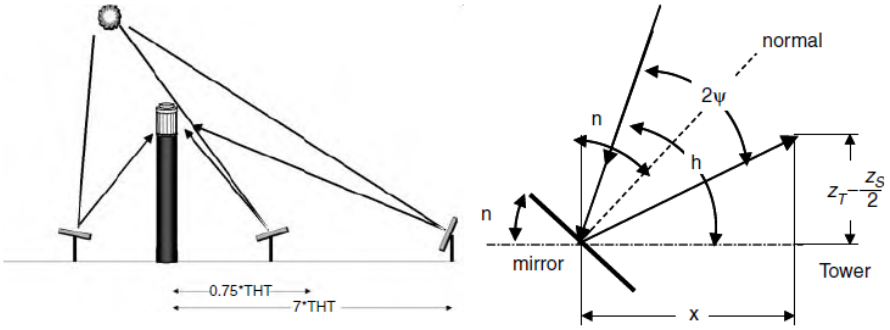

Figure 3.22 Visualization of the off-axis optics of heliostats representing different inclination angles of mirrors located in a heliostat field (Left). Geometrical definition of elevation angle n (Right).

The geometrical definition of the inclination angle (n in Figure 3.22) of a single heliostat is a function of the tower height, of its distance from the tower and of the incidence angle of the sun. Assuming Z_S is the heliostat vertical dimension and Z_T is the geometrical tower height above ground-level, the so-called optical tower height may be defined as the elevation of the center of the receiver aperture area above the pivot point of the heliostat (Z_T-Z_S/2). [22]

$$\psi = h + n - 90° \tag{3.4}$$

$$90° - n = arctan\left[\frac{z_T - z_S/2}{x}\right] + \psi \tag{3.5}$$

$$n = \frac{180° - h - arctan\left[\frac{z_T - z_S/2}{x}\right]}{2} \tag{3.6}$$

Clearly, heliostats require two axes drive systems. Many different system axes have been considered but all the systems currently in use or proposed are based on the use of azimuth and elevation axes because of their lower cost.

Heliostat drives should have the following characteristics:

- Sufficiently robust to support their own weight, the movable structure and wind loads, and rigid enough to avoid low frequency vibrations
- Able to generate extremely slow movement, with high reduction ratios (up to 40,000:1)
- Highly accurate positioning (use of encoders) and no free movement
- Able to ensure relatively fast return to stow position in case of high winds or other dangerous weather conditions
- Resistance to outdoor exposure
- Easy maintenance
- Low-cost manufacture and operation

The most common drive mechanism configuration makes use of worm-gear systems for both elevation and azimuth axes [22].

3.3.5 Heliostat Control

Control of CRS is more complicated than other types of solar thermal power plants since optics are off-axis and each and every heliostat individually tracks the sun. The control system in a central receiver system is naturally separated into the heliostat field control system (HFCS) and the receiver and power system control system (RPSCS) [22]. Without pretending to enter in the details, the main purpose of the HFCS is to keep each heliostat positioned at the desired coordinates at all times, depending on power system demand. The control system must update the sun position and calculate new heliostat positions every few seconds since the angular relationship between the sun, the heliostat, and the receiver changes continuously as the sun moves at about 0.07 milliradians per second [21].

Two types of control systems have been considered for heliostat use: open loop and closed loop. In an open loop system, the heliostat is programmed to point using temporal and geometric algorithms in the control computer software. In a closed loop system, a sun sensor provides feedback to the control computer about whether the heliostat is pointing in the right direction to illuminate the receiver. Because of lower costs, an open loop system is the preferred approach.

The general purpose of the HFCS is so to generate a uniform time-spatial distribution of the temperature on the volumetric receiver by controlling the timed insertion of an associated group of heliostats at predefined aiming points on the receiver by modifying the aiming point coordinates and changing from one heliostat group to another during operation. This is accomplished by a proper HFCS aiming point strategy [22].

The heliostat local control is also responsible for all the emergency and security maneuvers and suntracking calculations, as well as communication with the control room. The current trend is to increase the heliostat intelligence and autonomy. In addition, some drive mechanism options consider the use of wireless communications and PV power supply, eliminating the need for cabling and trenching. This is the case of the stand-alone heliostat developed at the PSA in Spain, where a field of 92 such heliostats is in operation [22].

3.3.6 Heliostats maintenance

It cannot be forgotten that the heliostats performance depends heavily on the maintenance activity. Optimum plant performance requires maintenance of high mirror reflectivity, which is remarkably reduced by soiling. A periodic heliostat cleaning is so required to remove dust/dirt. To do that, special machines have been developed, which allows a semi-automatic mirror cleaning procedure.

3.4 Examples of existing collector fields

3.4.1 Solar One and Solar Two

The 10-MWe Solar One Pilot Plant, was the largest demonstration of first-generation power-tower technology and operated from 1982 to 1988 in the Mojave Desert about 12 miles east of Barstow, California.

The plant was designed to produce at least 10 MWg net for a period of 7.8 hours on the plant's best design day (summer solstice) and for a period of 4 hours on the plant's worst design day (winter solstice).

The Collector System was composed by 1818 Martin Marietta heliostats, each of them with a reflective surface area of 39.1 m^2.

The heliostat field had so a total reflective area of 71130 m- and surrounded the central receiver tower, with 1240 of the heliostats in the north portion of the field and 578 in the south portion (Figure 3.23).

The mirrors had an average clean reflectivity of 0.903; this average is area weighted for the mixture of low- and high-iron glass used in the field. Each

mirror assembly was attached to a geared drive unit for azimuth and elevation control. The drive unit was mounted on a fixed pedestal. The entire heliostat unit was designed to track the sun in winds up to 45 miles/hr.

The locations of the heliostats in the field were determined by computer codes developed by the University of Houston. These locations produce optimum field performance on an annual basis. The field redirects approximately 70% of the annual incident solar energy to the receiver [29].

Figure 3.23: Solar One power plant

Solar One became Solar Two in 1994, when the DSG receiver was replaced by a new molten-salt system and a second ring of heliostats was added, making a total of 1926 heliostats with a total area of 82,750m²

In this procedure, the Solar One heliostat field, the tower, and the turbine/generator required only minimal modifications. The original 1818 heliostats from Solar One were reused, with the inner 17 rows of heliostats refocused for the smaller Solar Two receiver. Damaged or missing facets on these heliostats were replaced with mirrors from a defunct photovoltaic power plant. Also, 108 large-area (95 m^2) Lugo heliostats (so named because many of their parts were salvaged from the defunct Lugo photovoltaic plant) were added to the south part of the field to improve the flux profile of the receiver (Figure 3.24) [30].

Figure 3.24: Solar Two power plant (from Google Earth)

3.4.2 PS10 and PS20

Planta Solar 10 (or PS10) has been the first solar power tower in the world to commercially generate electricity and deliver it reliably to the grid. It has a nominal power of 11 MWe and its construction finished in 2006, in Sanlucar la Mayor, a few kilometers west of Sevilla [31].

PS10 heliostat field is composed by 624 heliostats for a total reflective surface of 75.216m2. It is arranged in a north field, with 35 circular rows around the 100 m-high tower and occupies 55 ha of ground surface.

Each heliostat, Sanlúcar 120 type, is a mobile 121 m^2 curved reflective surface mirror that concentrates solar radiation on a receiver placed on top of the 100 m tower. For this purpose, every heliostat is spherically curved so its focal point is at a distance equal to the slant range to the receiver.

The Sanlúcar 120 heliostat (Figure 3.25) is composed by 28 (7rows and 4 columns) curved facets manufactured with high reflectance mirror in order to provide the required optical properties to the heliostat field. Heliostat field has been designed using the latest calculation procedures and simulation tools with the objective of minimizing losses by cosine, shadowing, blocking, air transmittance and spillage effects. In this sense annual mean cosine effect in PS10 plant is over 81% and losses because shadows and blocks are not higher than 4.5% on an annual basis.

The high accuracy 2 axes sun tracking that is required for projecting the sun disk image onto the receiver is provided by a mechanical drive guided by a local control system. This local control system takes the responsibility of receiving sun position information from a higher control level that calculates sun azimuth and elevation values employing high accuracy correlations. It is also in charge of detecting heliostat current position and comparing it to the required to attack the receiver at a pre-selected aiming point [32].

Figure 3.25: Sanlucar 120 Heliostat

Figure 3.26: PS10 solar field

PS20 finished in 2009, is the world's second power tower plant in commercial use. PS20 features a number of significant technological improvements with respect to PS10. These enhancements, developed by Abengoa Solar, include a higher-efficiency receiver, various improvements in the control and operational systems, and a better thermal energy storage system

PS20 solar field follows the same guidelines than the ones of PS10. Due to the higher power output, the number of heliostats is 1255, each of them of the Sanlúcar 120 type. The receiver is located on the top of a 165 m-high tower [33].

Figure 3.27: PS10 and PS20

3.4.3 Sierra SunTower Solar Generating Station

Sierra SunTower Solar Generating Station is a 5 MW plant developed by eSolar and located in Southern California. This plant design is characterized by the peculiar approach followed by the realizing company. eSolar has indeed approached the problem of heliostat field cost by emphasizing small size, low cost, easy installation, and high-volume manufacturing of heliostat field components.

The north and south rectangular heliostat fields are so composed of a large numbers of small heliostats, creating an arrangement unlike other central receiver plants.

The heliostat fields have been designed through a MATLAB-based ray-tracing tool and the rectangular field boundary has been chosen to simplify construction and to allow many fields to be tiled efficiently on the available land (Figure 3.28).

Figure 3.28: Sierra Suntower power plant

eSolar heliostats represent a significant departure from the "bigger is better" progression in heliostat design over the past 30 years [62]. Instead, eSolar has designed small (1.14 m2) heliostats, allowing the vast majority of construction and assembly to take place at factories, which minimizes on-site labor costs

The heliostat support structure comprises a truss to link many heliostats together into a rigid framework and ballast weight to stabilize the assembly under wind load (Figure 3.29). This design contributes to the minimal on-site labor, because the hardware is manufactured in an off-site factory and requires no ground penetration.

Figure 3.29: eSolar heliostat

The heliostat design compares favorably to other demonstrated systems. For example, the steel requirement per square meter of reflector is approximately 15 kg in eSolar's second-generation heliostat, compared to over 30 kg for the 150 m2 ATS (Advanced Thermal Systems Inc.) heliostat. This reduction in weight is in large part possible due to the small size of the heliostats, which keeps them close to the ground where wind loads are significantly reduced. The high field density also contributes to decreased wind loads on the heliostats through increased attenuation within the field [26].

3.4.4 Solar Tres/Gemasolar

After the decommissioning of the Solar Two plat in California, in 1999, started the project to realize the Solar Tres plant in Fuentes de Andalucia (Sevilla).

The plant is nowadays under construction and will incorporate significant technological innovations, among which is the solar collection system and also a molten-salt heat storage system that is capable of attaining temperatures exceeding 500ºC.

The solar field will have a surround configuration and will be composed by 2,500 heliostats occupying 185 hectares (Figure 3.30). The heliostats are the SENER heliostats, developed by the homonymous firm and with a reflective surface of approximately 120 m^2 [13].

Figure 3.30: Gemasolar project representation

3.5 Model approach to the collector subsystem

Due to the high number of heliostats and to the different position and movements of each of them, an accurate modeling of a collector subsystem requires a quite complicated code and a significant computational time. Preferring to design an easier and more rapid model, it has so been decided to use a simplified approach to keep in consideration the solar field design and behavior.

Firstly, the thermal power entering in the central receiver is defined not through the direct tracing of each heliostat reflected radiation, but through pre-designed radiation maps. During the functioning of the PS10 plant, indeed, proper measurement instruments are able to detect the radiation that hits the receiver, and to draw a "map" of its distribution on the panels' surface. A deeper description of the radiation map is carried on in chapter 4.5.

What is important to notice is that the use of real radiation maps, theoretically available for a big number of weather conditions, lets the model be faster and not suffer from the errors related to the sub-model of the collector field.

During the on design analysis, however, giving the user approximate information on the extension of the solar field required for the desired plant has been considered useful and an extrapolation from data regarding the real PS10 field are used and managed.

It has to be made clear that the following equations and results presented here are used only to give a general idea on the heliostat field and on the tower height, but that in order to have reliable values it is essential to use a proper simulation model.

To start, we have considered a "global" field efficiency of the PS10, calculated from the available data of the plant at rated conditions [31]:

nominal radiation: 981 W/m^2

number of heliostats: 624

heliostat reflective surface: 121 m^2

Thermal power reaching the receiver: 51.9 MW$_t$

Simply multiplying the first three values we can define the ideal power collected by the field:

$$Power\ collected = 981 * 624 * 121 = 74.069\ MW \qquad (3.8)$$

The ratio from this value to the thermal power really reaching the tower receiver gives then the value of a "global" field efficiency, which includes cosine effect, shadowing, blocking, mirror reflectivity, atmospheric absorption and receiver spillages.

$$Global\ field\ efficiency = \frac{51.9}{74.069} = 0.70069 = 70\% \quad (3.9)$$

Once calculated this efficiency, we can hypothesize that it remains constant for each size of the plant; the simple expressions above, can so be managed and reused to calculate an approximate needed mirror surface.

For example, an approximate indication for the mirror surface needed for a 30 MWe solar plant would be calculated in the following way:

$Receiver\ Thermal\ Power = 123.17\ MWt$ (calculated with the model)

$$Total\ reflective\ surface = \frac{Receiver\ Thermal\ Power}{Irradiance * Field\ efficiency} = \frac{123.17 * 10^6}{981 * 0.7} = 179\ 370\ m^2 \quad (3.10)$$

Considering that the same heliostats adopted in the PS10 (Sanlucar 120) are used, the number of heliostats and, always in an approximate way, the ground occupation (footprint) can be defined.

$$Number\ of\ heliostats = \frac{Total\ reflective\ surface}{Heliostat\ reflective\ surface} = \frac{179\ 370}{121} = 1\ 482 \quad (3.11)$$

For the calculus of the ground surface occupation we can refer to the global surface occupied by the PS10 field, equal to 55 ha (550 000 m2). Knowing that this surface is made to host 624 heliostats, a mean value of ground-surface for heliostat can be defined:

$$Heliostat\ ground\ occupation = \frac{550\ 000}{624} = 881.4\ m^2 \quad (3.12)$$

For the 30 MWe plant, the ground required will so be approximately:

$$Footprint = Heliostat\ ground\ occupation * Number\ of\ heliostats = 1\ 482 * 881.4 = 1\ 306\ 234\ m^2 = 130.62\ ha \quad (3.13)$$

With regard to tower height, the availability of the data for both the PS10 and PS20 plants, allows us to define the equation of a line that links the number of heliostats with the tower height.

Table 3.1: PS10 and PS20 heliostats and tower data

	Heliostats number	Tower height [m]
PS10	624	120
PS20	1255	165

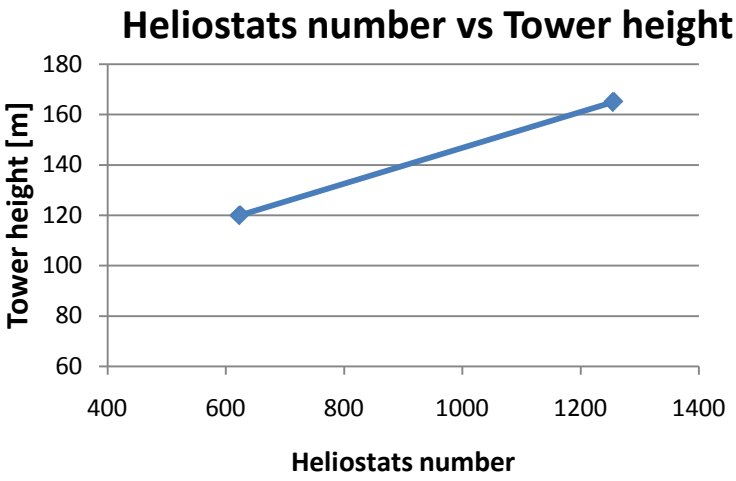

Figure 3.31: Heliostat number vs tower height

$$H_{tower} = 0.0713 * N_{heliostats} + 75.499 \quad (3.14)$$

In this way, the 30 MWe plant should employ a 181 m high tower.

It has to be noticed that the comparison between the PS10 and PS20 plant cannot be done in terms of power production since the thermal storage capacity of the two plants are indeed not proportionally scaled (PS20 presents a "longer" heat storage).

The considerations made above consider, instead, plants that are perfectly scaled-up from the PS10.

4. The tower receiver

Even though the solar receiver does not have a huge impact on capital investment (about 14% [22]), it can definitely be considered the most critical subsystem in terms of performance.
In many designs the solar receiver is a single unit that centralizes all the energy collected by the large heliostat field and that requires two main characteristics: availability and durability.
Typical operating temperatures at receiver/absorber are in the range from 500°C to 1200°C, and incident fluxes cover a wide range between 300 and over 1000 kW/m^2 [22].
Different receivers characterized by different constructive solutions, absorber materials, working fluids and heat transfer mechanisms, have been designed and tested. Therefore, to comprehend better the technology, in the first part of this section the principal differences regarding different fluids adopted and different geometry designed will be shown, while the second part will cover more in detail the boiler modeled in this work.

4.1 Receiver fluids

A first classification of receivers can be done looking at the different candidate working fluids that have been studied in the last years.
The most promising power tower receiver technologies are:

1. Molten salts technology
2. Open or closed loop volumetric air technologies
3. Water/steam technology

Roughly speaking, it can be said that researchers at the United States have bet on molten salts as the most interesting technology, as showed by the Solar Two plant that was decommissioned in 1999; on the contrary, the use of volumetric receivers either with closed air loops, for efficient integration into gas turbine cycles, or open air, for intermediate storage and/or hybridization solutions, have been promoted in Europe and Israel with projects like SOLGATE, PS10 (first version) and Colonsolar. More conservative approaches (SOLGAS initiative) pushed on saturated steam receivers.

4.1.1 Molten salts technology

Molten nitrate salts are, typically, a mixture of $NaNO_3$ and KNO_3 of variable composition even if the most commonly used is a mixture of, respectively, 60% and 40% that presents the following advantages:

- Low cost.

- Excellent heat transfer properties: 0.52 W/m K thermal conductivity and 1.6 kJ/kg K heat capacity.
- Chemical stability at maximum operating temperatures.
- Excellent high temperature energy storage fluid.
- Environmentally friendly fluid.

Depending on its particular composition the mixture liquefies at a temperature between 120°C and 240°C and can be used in conjunction with metal tubes for temperatures up to 600°C without bringing about severe corrosion problems.
Regarding mechanical integrity issues, studies [34][35] have shown that affordable values of heat flux on the receiver can be up to 800 kW/m^2, giving place to mixture temperatures around 600°C and maximum surface temperatures in the range from 650°C to 700°C.
Molten salts technology has been developed in the U.S thanks to the operation of the 10 MW_e "Solar Two" plant in Barstow, California. Among other interesting features, this technology allows making solar collection and electricity generation more independent than water/steam systems and allows, even, the incorporation of a cost-effective energy storage system [36].

Solar Two

The *Solar Two* receiver, which was the first molten-salt receiver, was tested between 1996 and 1999 and is still the technical reference for molten salt tubular technology.
It was rated to absorb 42 MW of thermal energy at an average solar energy flux of 430 kW/m^2 and 800 kW/m^2 of peak, generating steam at 535°C and 100 bar by a 35 MW_t steam generator system. The receiver consisted of 24 panels that formed a cylindrical shell around internal piping, instrumentation and salt vessels. The external surfaces of the tubes were coated with a black Pyromark paint that was robust, resistant to high temperatures and absorbed 95% of the incident sunlight. All pipes, valves, and vessels for hot salt were constructed from stainless steel because of its corrosion resistance against molten-salt at 565°C, while lower cost carbon steel was used for cold-salt pipe work because of the lower corrosiveness of the salt at 290°C. The *Solar Two* receiver showed that, at full power (34 MW absorbed), the receiver efficiency was 88% although different problems were detected [38]:

- First, a heat-trace inadequacy in a receiver drain line resulted in salt solidification between two interconnected panels. If the center of the panels were heated while the ends remained cool could oblige constrained melting that could severely damage the receiver tubes.
- Second, a tube ruptured occurred when the receiver was on sun. Salts flow to the tube was obstructed causing a lack of cooling which

resulted in a pressure failure as the extreme temperature weakened the stainless steel. The flow block was caused by debris that were accumulated in the receiver. The debris was originated in the cold salt carbon-steel piping in areas where localized overheating, due to inadequacies in the heat-tracing system, accelerated the corrosion process.

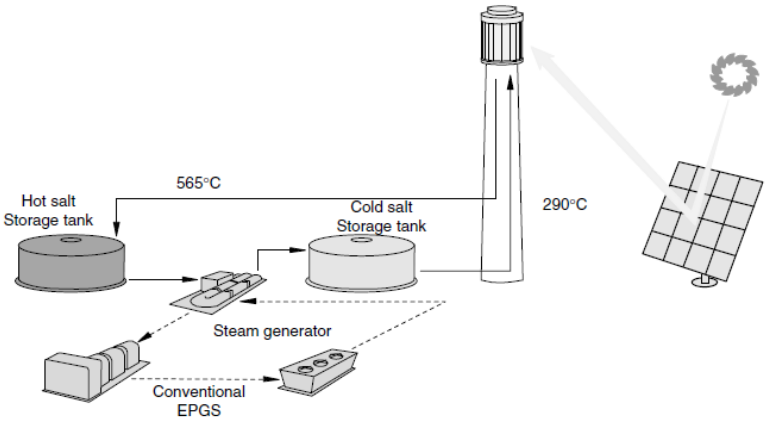

Figure 4.1:Molten salt central receiver scheme

Another characteristic problem of molten-salts technology is the high solidification temperature (120°C-240°C, depending on salt composition). When the mixture goes from solid to liquid state its specific volume increases (approximately 4.6%) and mechanical failures can take place.

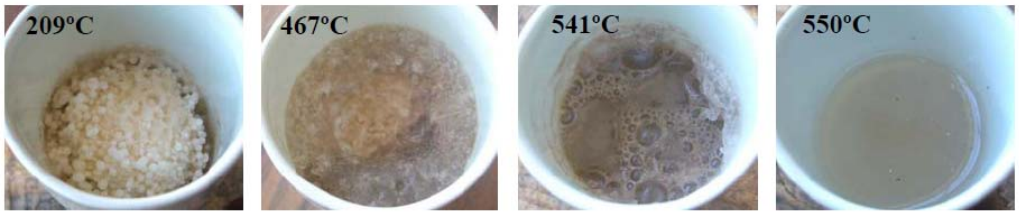

Figure 4.2:$NaNO_3$/KNO_3 mixture melting behavior [37]

Consequently it is necessary to maintain the mixture in liquid state with fusion or pre-heating systems during start-ups, or systems that guarantee a continuous circulation during the night. For example, at the Solar Two plant, before filling the boiler with salt each morning, the receiver was heated to approximately 290°C to reduce thermal stresses and to insure that solidification of salts did not take place inside the tubes. This pre-heating was achieved by focusing a selected subset of the heliostat field onto the receiver to achieve a uniform temperature

distribution both vertically and circumferentially. The problem was that the algorithm selecting and focusing heliostats on the receiver was unable to achieve the desired temperature distribution on the windward side of the receiver due to convective losses. For this reason a feedback control system was incorporated.
Differently from the receiver, both pumps and thermal storage tanks functioned as expected with heat losses rates very close to prediction.
The Solar Two work brought a few recommendations for future molten-salt receivers:

- All the pipe work of the salt loop must be made of stainless steel, while the use of mid steel for cold salt conductions must be avoided. Stainless steel pipes are much more resistant to corrosion and thus, it is safer in terms of control and installation problems related to the heat trace.
- The use of thin-walled piping must be avoided even if it more economical and allows a faster heating, since it often arrives bent or dented and has a lower corrosion tolerance.

4.1.2 Volumetric air technology

Using air as working fluid offers different benefits:

- It is free and fully available at the site.
- No risk of freezing.
- Higher temperatures can be reached and therefore the integration of solar thermal energy into more efficient thermodynamic cycles looks achievable.
- No phase change.
- Fast response to transients or changes in incident flux.
- No special safety requirements.
- No environmental impact.

The main problem of this technology is that air is a poor heat transfer medium, due to its low density and low heat conductivity, creating difficulties in the operation of tubular receivers, as already found in the GST project where two tubular receivers, one metal and one ceramic, were tested at PSA (Plataforma Solar de Almeria) in Spain.
For this reason air receivers use a different approach to gas heating based on wire, foam or appropriately shaped materials within a volume: "*volumetric receivers*".
In these receivers, highly porous structures, operating as convective heat exchangers, absorb the concentrated solar radiation inside a "volume". Therefore gas is driven through the porous material where it is heated convectively.

Volumetric absorbers are usually made of thin heat-resistant wires (in knitted or layered grids) or either metal or ceramic open-cell matrix structures. Good volumetric absorbers are very porous, allowing the radiation to penetrate deeply into the structure.
A very high specific surface combined with very small structures lead to a very efficient heat transfer with the gas, allowing to achieve very high heat fluxes (0.5 MW/m^2 to 2.5 MW/m^2) [39] .

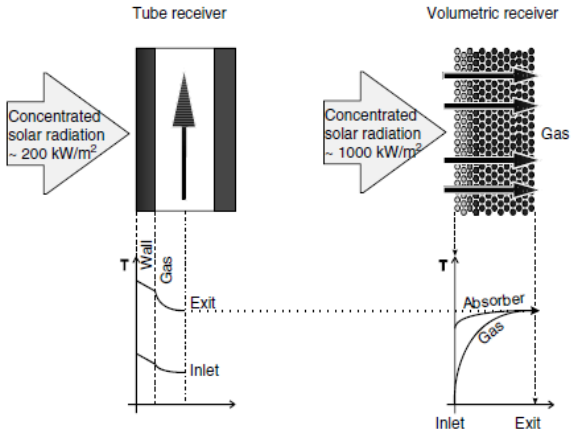

Figure 4.3:Heat transfer principles in tubular and volumetric receivers

In a pressurized version, the porous structure is placed into a pressure cavity vessel closed with a quartz glass window. Using this technology at pressures of up to 15 bar and temperatures up to 1100°C, the receiver could be employed to drive a gas-turbine or combined cycle system.
Different studies conducted about the problems of these receivers have concluded that, in highly porous absorber materials, the airflow through the absorber structure is unstable under high solar flux, leading to the mechanical failure (cracks or melting) of the absorber due to local overheating.

TSA (Technology Program Solar Air Receiver) – PHOEBUS scheme – first PS10 design

This experimental open volumetric receiver was a 2.5 MWt air-cooled receiver tested on the PSA CESA-1 tower in late 1991.
Atmospheric air was heated up through a wire mesh receiver to temperatures of about 700°C to produce steam at 480-540°C and 35-140 bar, with an average flux 300 kW/m^2 and a peak flux of 800 kW/m^2 [37]. The air went through a heat recovery steam generator with separate super-heater, re-heater, evaporator, and economizer feeding a steam turbine-generator.

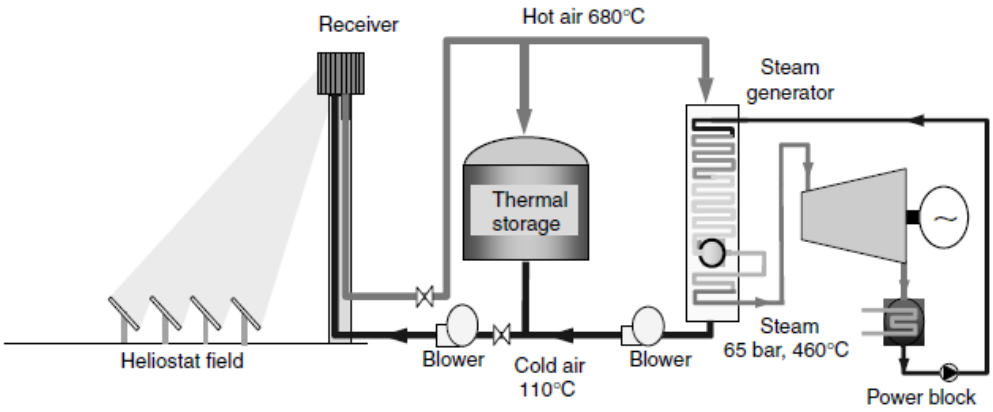

Figure 4.4: Example of solar tower power plant with air receiver

The TSA-PHOEBUS receiver was successfully operated for almost 400 h between April and December 1993, demonstrating that a receiver outlet temperature of 700°C could easily be achieved within 20 minutes of plant start-up and achieving receiver thermal efficiencies of up to 75%.

This concept, after test evaluations, was taken into consideration for the PS10 project in Spain. The plant design considered a receiver inlet temperature of 110°C and an outlet of 680°C that should have been used to produce steam at 460°C and 65 bar for an electric output of 11 MWe. Eventually, in the real plant, it was substituted with a more reliable water/steam receiver.

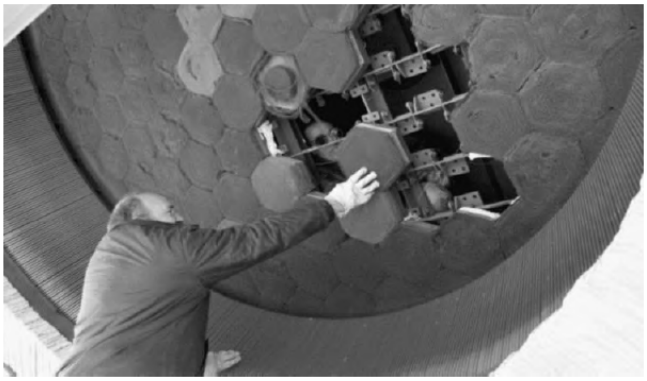

Figure 4.5: Front view of the TSA volumetric receiver

HiTRec-Solair receiver and Solar Power Tower Jülich

This technology is composed by a stainless steel support structure on the back of a set of ceramic absorber modules that form the base of the receiver. Clearly, the absorber modules are separated from the back in order to allow for axial and radial thermal expansion during start-up or shutdown.

The core element of this technology is the SiSiC absorber module which consists of an extruded parallel channel structure inserted into a cup. The inner surface of this structure is about 50 times larger than the aperture providing the maximum heat exchange surface to the air flow.

Figure 4.6: The ceramic absorber module

The support structure is a double sheet membrane that may be cooled by either ambient or recirculated air. Cooling air flows between the two sheets and, as it leaves through the sides of the segments, also cools the supporting structure. Air reaches the absorber aperture through the free spaces between segments and is mixed with ambient air. The mixture then penetrates the absorber structure and is heated up by convection. On the back of the structure, an orifice previously sized according to solar flux simulations adjusts the air mass flow rate to provide homogeneous air temperature at the outlet from the module.

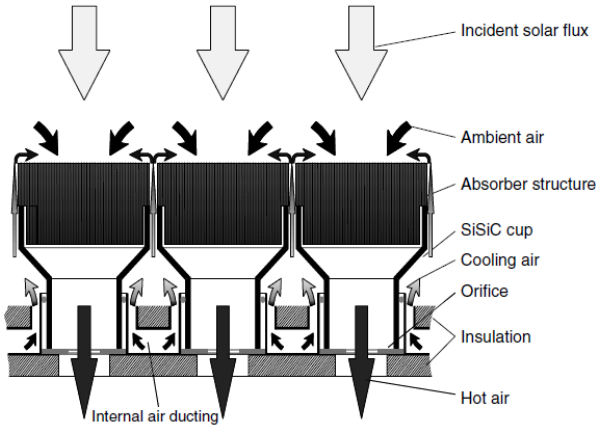

Figure 4.7: Principle in HiTRec and Solair receivers

During the tests conducted in 2003 and 2004, the Solair-3000 receiver produced air at 700-750°C with an average flux of 0.5 MW/m^2 and an efficiency of 72±9%.

These two projects (HiTRec and Solair) developed the same receiver concept and, after some prototype testing, gave way to a real plant that is the Solar Power Tower Jülich in Germany.

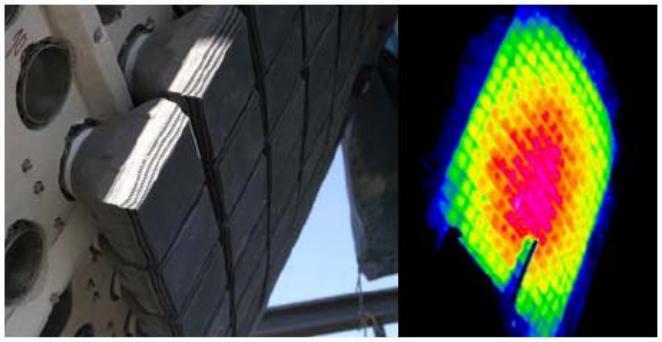

Figure 4.8: Prototype working

The Solar Tower Jülich (1.5 MW), developed with a major contribution from the German Aerospace Centre (DLR), is located in the city of Jülich in the north west of Germany and was completed at the end of 2008. The receiver of this plant is mounted on a 60 m height tower and consists of more than 1000 ceramic absorber modules incorporated in the receiver structure.
Air is heated up to 700°C and then used to generate steam in a heating tube boiler that delivers live steam at 485°C and 27 bar [40].

Figure 4.9: The Jülich plant tower

Air receiver for solar gas turbine – REFOS project

Another option for using air as working fluid are the windowed volumetric receivers that could be employed as a preheating chamber of a gas turbine combustor.

The combination of heat addition with high solar shares and high conversion efficiencies is one of the major advantages of solar gas turbine systems compared to other solar-fossil hybrid power plants. Solar gas turbine systems use concentrated solar power to heat pressurized air in a gas turbine before entering the combustion chamber. Therefore the combustion chamber only works to overcome the temperature gap between receiver outlet (800-1000°C) and turbine inlet (950-1300°C), thus providing constant turbine inlet conditions despite fluctuating solar input. Using this concept, concentrated solar energy feeding the Brayton cycle of a combined cycle plant can be converted into electricity with a solar to electric efficiency of up to 30%.

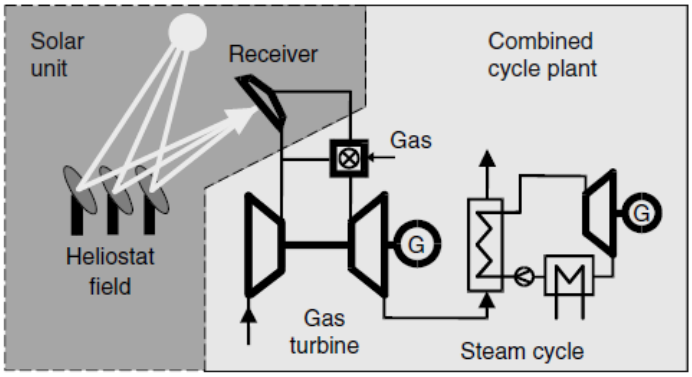

Figure 4.10: Solar air preheating system for gas turbine

For this reason, the German Aerospace Center (DLR) initiated a specific development program called REFOS, aimed at designing a windowed module able to work up to 1000°C and with pressures up to 15 bar.
The REFOS receiver consists of a cylindrical vessel containing a curved knitted absorber, a quartz dome to pressurize the air cycle and a hexagonal secondary concentrator with a 1.2 m inner diameter to increment the flux density and protect the window flange.

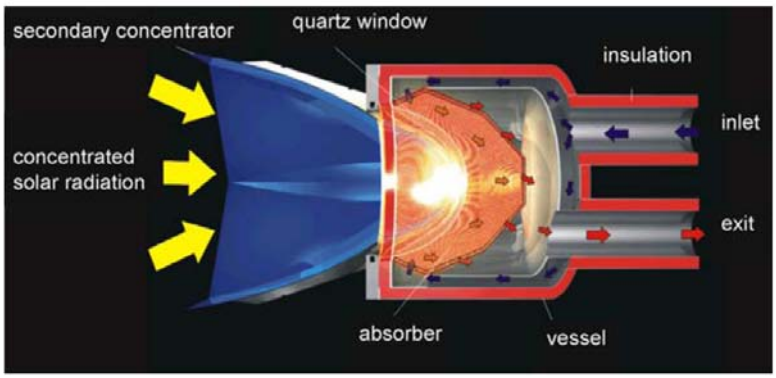

Figure 4.11: A REFOS receiver module

The development of this technology was followed by the SOLGATE project where a receiver formed by 3 modules was designed and erected in the CESA-1 solar tower test facility at the Plataforma Solar de Almeria (PSA) in Spain. The three receivers, connected in series, heated up air from 290°C to 1000°C to feed a modified helicopter gas turbine of 230 kWe.

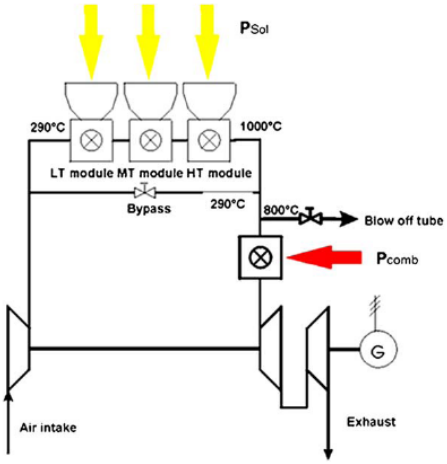

Figure 4.12: Scheme of SOLGATE concept

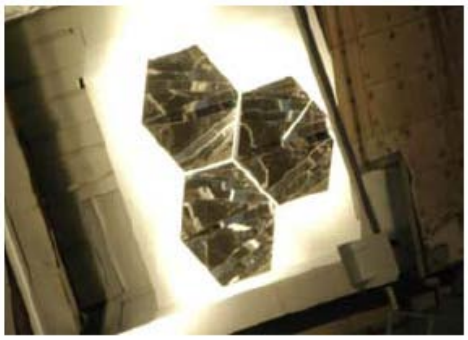

Figure 4.13: SOLGATE receiver during operation

4.1.3 Water/Steam technology

A water/steam receiver offers some thermal, logistic and economic benefits:

- The receiver fluid can be directly used in a steam-turbine cycle without further heat exchange.
- From a thermal point of view the evaporation of water offers excellent heat transfer characteristics so that this receiver can be made of less costly materials or it can be applied under high solar concentration.

At the same time, a few challenges have to be dealt with:

- Non-homogeneity of heat input onto a highly pressurized absorber tube when it is irradiated only from one side and their influences on material stability.
- Difficulty to handle the start-up and transient operation of the system.
- There is no simple solution to store large amounts of high temperature/high pressure steam, in order to operate the plant during night hours.

The water/steam receiver could be classified in two classes, according to the thermodynamic state of the steam used in the power block:

1) Saturated steam: the receiver is composed only by an evaporator.
2) Superheated steam: the receiver is composed by evaporator, super-heater and, eventually, a re-heater.

Solar One

The first solar power tower put into operation was the "Solar One" plant (10 MW_e) in the Mojave desert in California, USA. The Solar One receiver was a once-through superheated water-steam boiler with cylindrical shape that operated from 1984 to 1988.

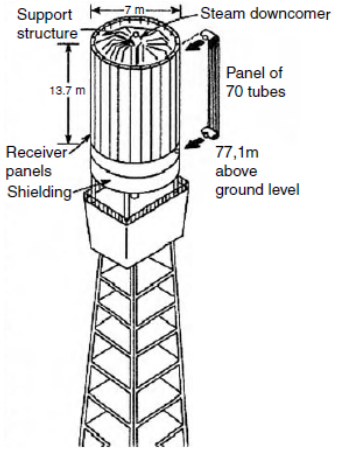

Figure 4.14: Scheme of Solar One receiver

The receiver was made by 24 rectangular panels. The six panels on the south side (lower radiation) were used to preheat feed-water after which the water was transferred to once-through boilers and superheaters on the north side. The design specifications of live steam were 516°C and 100 bar for a thermal capacity of 42 MW_t.

One of the main problems found during testing, which is typical of superheaters, was overheating and deformation in the superheating section because of solar transients and poor heat transfer. After 18 months in operation, cracking and

leaking problems were encountered at the top of the boiler, due to the fact that, during start-ups and shutdowns, the temperature gradient between the edges and the center of the tubes could be as high as 111°C.

2 MW_{th} water/steam receiver at the Weizmann Institute solar tower

This receiver was designed, fabricated, assembled and tested at the solar central receiver facility of the Weizmann Institute, Israel.
With a 2 MW_{th} heat input capacity and a maximum flux on the evaporating panels of 300 kW/m^2 , the receiver was designed to generate steam at 15 atm.
This solar steam receiver is a hexagonal shaped cavity with a 2.5x2.5m opening. Opposite the opening there are three active absorbing panels made by vertical tubes where water is forcedly circulated at a ratio of 1:25 by a pair of high capacity low-differential pressure centrifugal pumps [42].
There are not welded connections among the tubes to create a so-called “water wall” panel, in order to reduce problems originated from temperature gradients and thermal stresses.
This receiver, in nominal condition, produced 2500 kg/h of saturated steam at 15 atm and 200°C.

Figure 4.15:Weizmann Institute solar tower

CESA-1

Cesa-1 was a north-facing water-steam cavity receiver that operated 1631 h between 1983 and 1986 in the Plataforma Solar de Almeria, Spain.
The boiler consisted of three panels of A-106 Gr B carbon steel tubes and a super-heater made by more expensive X-20 Cr Mo V 121 steel.
This tower, with a nominal input irradiance of 6.7 MW_{th}, produced superheated steam at 110 bar and 525°C.

As in the Solar One receiver, important deformations were found in the superheating zone, requiring it to be operated with a lower flux. For this reason, operation had to proceed slowly during start-up and transients, penalizing efficiency (more than 45 min were required to reach nominal conditions).

The PS10 project

Production of superheated steam has brought different problems in solar receivers, as demonstrated by several plants such as Solar One and CESA-1. On the contrary, better results regarding absorber panel lifetime and controllability have been reported for saturated steam receivers, as in the Weizmann receiver.
With this kind of receiver, thanks to its better thermal behavior, a very high efficiency of the boiler can be reached, about 20% more than an air-volumetric receiver as shown by table 4.1 [22].

Table 4.1:Comparison of thermal losses and efficiency in Air Volumetric and Saturated Steam Receivers

Losses	Air [%]	Steam [%]
Reflection	7.9	2.0
Radiation	8.6	0.8
Convection	0.0	2.6
Spillage	5.0	2.1
Air return	3.7	0.0
Total efficiency	74.8	92.4

The PS10 is a tower plant of 11 MW_e located in the town of Sanlucar la Mayor, 15 km far from Seville. Thanks to 624 heliostats, the cavity receiver, composed by four tubular panels (5.36 x 12 m), produces saturated steam at 40 bar and 250°C.
It is, with its sister plant PS20 (20 MW_e), the first commercial solar power tower in the world and, for this reason, one of the reference points for this technology. Hence, this plant has been taken as reference system in this work and will be described more in detail in the following sections.

4.1.4 Water/Steam receiver problems

Different problems must be faced when adopting a water/steam central receiver. These problems are linked to two aspects:

1) Mechanical problems
2) Dynamic operative requirements

Mechanical problems: thermal stresses

One of the main problems is the temperature distribution of metallic pipes receiving radiation on a single side. This phenomenon originates, during the thermal expansion, stresses in the pipes: compression near the inner wall and extension near the outer wall. With the aim of reducing these stresses (called *bowing*), it is useful to pre-stress the pipes in the opposite way and use highly reflective surfaces in the internal side in order to make the temperature profile as homogenous as possible.

Another important aspect to deal with is allowing for pipe expansion under thermal load. For this reason the pipes are suspended in the tower structure permitting their vertical elongation in the downward direction.

Regarding dynamic aspects, it is clear that the receiver will be subjected to daily start/stop. This leads to cycle fatigue that can cause creeping of the hotter part of the boiler (SH and RH). In order to reduce this effect several measures should be taken:

- The drum diameter should be reduced, limiting its function to accumulate water instead of phase separation and using four external separators one for each side of the tower.
- The pipe-collector connections of SH/RH should be provided with forged pieces that connect more gradually different thickness, therefore reducing thermal stresses.
- The drum should be kept warm during the night by an electric heater.
- The panels should be pre-heated with auxiliary steam before letting the generated steam to flow through.

Dynamic operative requirements

Starting

This phase occurs every day and usually concludes 30 min after sunrise.
At night, the evaporators are kept hot by an electric heater with the aim of reducing thermal stresses and reducing start time.
Starts are divided in three phases:

1) Solar radiation is applied to the evaporator pipes producing steam that is used to preheat the SH/RH section. SH and RH panels are not radiated already.
2) SH and RH panels are radiated and start producing superheated steam. Until that moment, steam is re-circulated by-passing the turbine.
3) The turbine by-pass is closed gradually and the turbine is started.

Low radiation

In these conditions, the heat input is lower than the minimum requested by the turbine to work regularly (e.g. clouds passage) and, since it is absolutely necessary to keep the boiler and the rest of the plant in a state from which it can be rapidly re-started, the boiler is kept working using the remaining radiation but the turbine is by-passed. If the radiation were too low the drum would be kept at high pressure/temperature by an external electrical heater while an auxiliary gas boiler would provide steam to the.

Night stop

As the sun is setting, the solar steam generator continues to feed the turbine, which is working in “sliding pressure” mode, with decreasing pressure until a minimum drum pressure is achieved. When this condition is hit, the system is stopped and the interception valves are closed in order to maintain the drum at high pressure/temperature.

Emergency shut down

Should an alarm go off (high metal temperature, high wind speed, low level of drum water…), the mirrors would be brought to their stow position.
At this time the procedure is the same as for night shut down and so the interception valves are closed to maintain the drum pressure.

4.2 Receiver type

From a geometrical point of view, there are two general receiver configurations:

- *Cavity receiver*
- *External receiver*

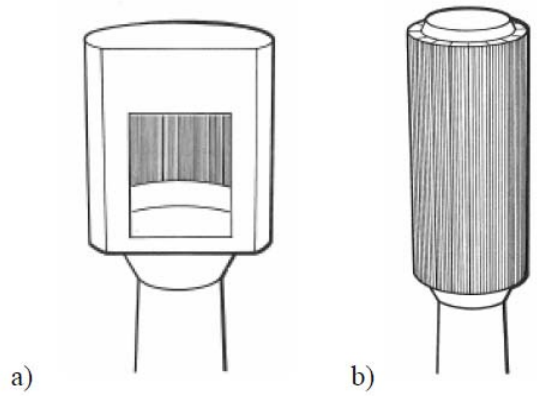

Figure 4.16:Two different types of superficial receivers: a) cavity internal receiver and b) external superficial receiver

External receivers have heat absorbing surfaces that are either flat or convex toward the heliostat field. For a large plant, an external receiver could be a multipanel polyhedron that approximates a cylinder, with a surrounding heliostat field. Instead, smaller plants typically use a north field configuration with a partial cylinder receiver, omitting most of the south-facing panels.

In a cavity receiver, the radiation reflected from the heliostats passes through an aperture into a box-like structure before impinging on the heat transfer surfaces, this box and aperture define the cavity. Even if a receiver may be composed of more than one cavity (each facing a different sector of the heliostat field), studies have demonstrated that the preferred configuration is a single cavity facing a north, in the northern hemisphere, heliostat field.
Other internal areas of the cavity such as the roof and the floor, do not normally serve as active heat absorbing surfaces. These areas must be effectively closed and insulated to minimize heat loss and to protect structure, headers, and interconnecting piping from incident flux. Although they are not exposed to high levels of direct flux, the inactive internal areas are exposed to radiation from the hot absorber panels therefore must be un-cooled preventing the achievement of high temperatures.

Several factors distinguish external and cavity receivers [21]:

- *Radiative losses*: are generally larger for external receivers since the hot receiver panels are more exposed and have larger view factors to colder ambient environment. Instead cavity receiver panels are more protected and have low view factor due to the small aperture.
- *Spillage losses*: are generally larger for cavity receiver because the heliostat radiation must fit through the relative small aperture, and

thermal and convection losses may be larger because of the large heated surface are of the cavity.

- The receiver mass and number of components are larger and generally more costly for a cavity than for an external receiver. The mass provides some thermal inertia which enables buffering of transient weather conditions and the presence of a door, in a cavity receiver, that may be closed during times of low insulation, helps to reduce thermal losses and to simplify start up procedures.
- Receiver tubes in a cavity are more protected from the effects of weather than the external receiver ones. This means less degradation of high absorptivity coatings during service.

4.3 Tower

The tower provides support for the solar receiver at the required height above the heliostat field and also provides support for the beam characterization system target, piping, and associated mechanical and electrical equipment that are located outside the tower, just below the receiver.
Primary access within the tower is by means of an elevator for transporting plant personnel and portable maintenance equipment.

Towers are constructed of steel or reinforced concrete. Steel towers are similar to guy-wire supported television transmission towers. Instead concrete towers are similar to tall chimneys of conventional fossil power plants.

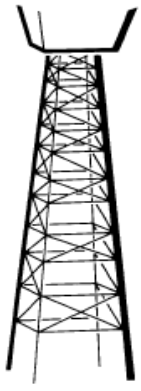

Figure 4.17: Steel tower

Figure 4.18: Reinforced concrete tower

The choice of tower construction depends primarily on the required height of the tower. Steel towers are most likely to be cost effective when the height is less than 120 m while reinforced concrete towers have been shown to be more cost effective for towers taller than 120 m [21].

4.4 Thermal behavior of a central receiver

The radiation coming from the heliostat field is reduced due to several dispersion effects as *loss caused by lack of focalization* and *loss due to the diffusion*, that cut the flux reaching the tower.
When a certain amount of flux has reached the tower it is important to understand the component that is effectively absorbed by the water inside the pipes.
In the usual design process the best performance is looked for by a variety of design tradeoffs among several loss mechanisms.

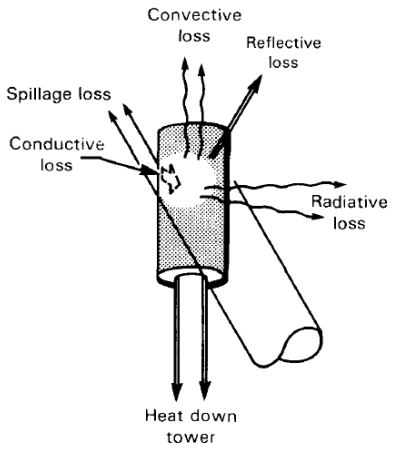

Figure 4.19:Receiver loss processes

These losses, shown in figure 4.19, include:

- *Spillage losses*: is a loss due to the fact that part of the energy reflected by the heliostat field, after accounting for atmospheric absorption between heliostat and receiver, is not intercepted by an absorber surface containing the receiver internal fluid, or re-reflected or radiated from an intermediate surface to that absorber surface.
  This component is very high for SH/RH pipes that have no membrane. Due to the cyclic work the pipes tend to be bended and to create empty spaces between two next tubes.
  A reasonable estimation of this loss is about 0.3-0.5% of the total incident radiation [41].

- *Reflection losses*: is a loss due to the light energy from the heliostat field that is scattered from the receiver surface and then escapes from it. For this reason high absorptivity paint is used on the absorber surfaces to minimize this loss. Reflection loss is generally 2-3% or less with a freshly-painted absorber surface, but may increases during service as a result of degradation of the coating.
- *Convection losses*: is the thermal energy lost in heating the air adjacent to the receiver. It is, obviously, a combination of free (thermally driven) and forced (wind driven) convection, with the free convection component usually larger.
- *Radiation losses*: is the thermal energy lost by infrared and visible light emission due to the high temperature of the receiver. Both the radiative and convective losses are a function of the temperature of the receiver and its configuration (cavity or external).
  Typical combined radiation and convection losses are in the range of 5 to 15% [21] of the peak incident energy on the receiver.
- *Conduction losses*: is the thermal energy lost through the insulating surfaces and structural members. This loss is less than 1% for a well insulated receiver and for this reason they have not be taken into consideration in the thermal model but they are present in the overall efficiency used in the plant model.
- *Radiation losses toward the tower interior*: the non radiated part of the pipes panels is covered by further panels of nonconductive material and they are coated (in the pipes side) by a continuous steel sheet with a high reflective coefficient. In this way two important effects can be obtained:
  1) Thermal effect: the heat radiated from pipes from the cold side would be dissipated and it would not contribute to the heat transfer. Instead, in this way, a large part of the radiation is re-directed towards the pipes and the working fluid.
  2) Mechanical effect: a pipe exposed to radiation on a single side tend to buckle. By a good reflection of the back non-conductive panel this effect is minimized reducing the mechanical stress on the pipes.

  The insulating panel is designed in order to assure a temperature of the cold side of the panel of 70-80°C. An average value of this loss is about 0.5-1% [41].

Cavity receivers have, in general, better thermal efficiency than external receivers. This is largely due to the reduction in radiative losses when a cavity enclosure is employed.

4.5 Modeled boiler description

The boiler considered for the creation of the model is practically inspired by the PS10 receiver.
This receiver was designed and built by *Technical-Tecnicas Reunidas*, a Spanish Engineering Company for the ABENGOA 11 MW_e plant:PS10. It is a cavity receiver with only one aperture toward North because it has been thought for a North heliostat field (in the North hemisphere).

Figure 4.20: The cavity receiver of PS10 plant under construction

The boiler studied in this model, as the PS10 and PS20 ones, is a DSG (Direct Stem Generator) receiver that uses as working fluid the same water used in the power block.
The receiver consists only in a evaporator section without the presence of economizer, or super-heater, or re-heater, because is the most economic solution thanks to the use of relatively cheap material. It is important to point out that having only boiling water in the pipes increases enormously the internal heat transfer coefficient, letting the water to cool in a very efficient way the pipes. Another important aspect of this kind of solution is that it is possible to reduce the presence of too many collectors or junctions among different pipes, that are the most critical components because of the great thermal stress suffered.

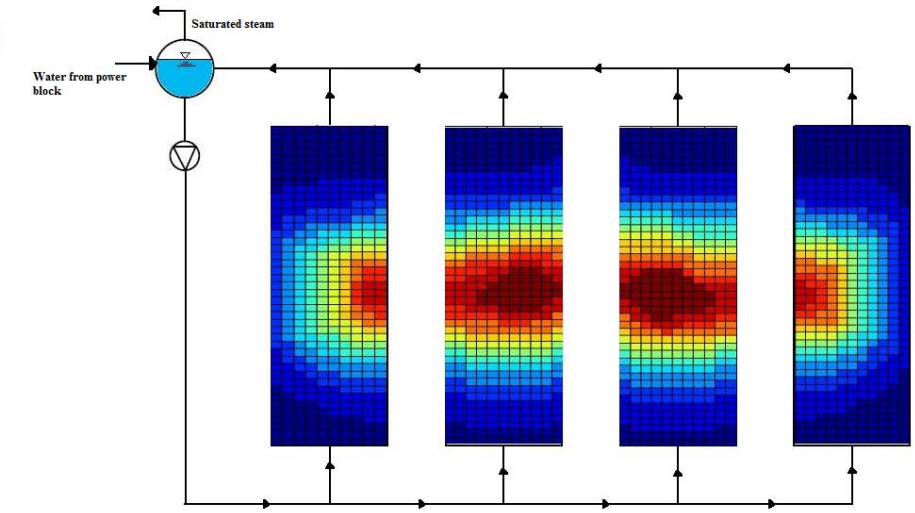

Figure 4.21: An output of the receiver model

The model of the receiver has been written in order to let the user choose among a great variety of parameters, although some aspects regarding the geometry of the boiler have been fixed.

Radiation map

The radiation map is the key input of the model. These maps have been taken as real data from the PS10 operation and consist of matrixes with a fixed number of cells containing an average flux value (radiation map resolution), expressed in kW/m^2.

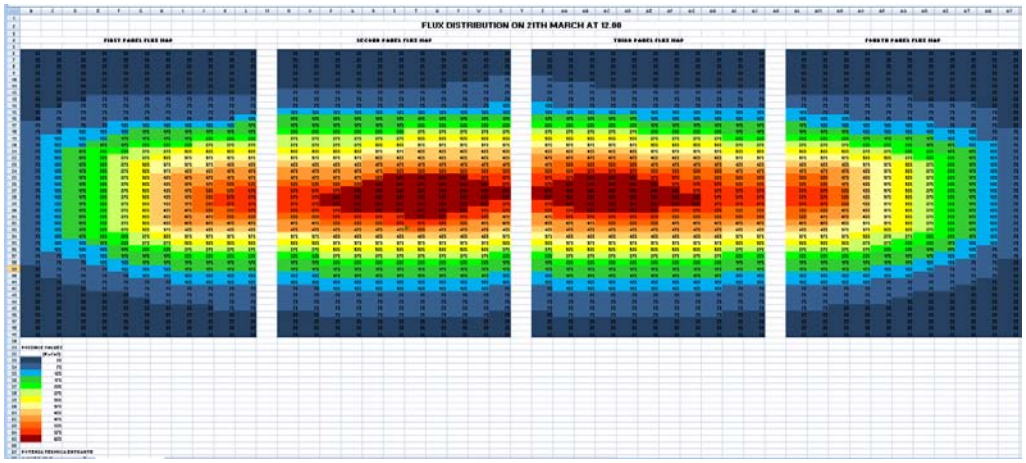

Figure 4.22:Graphical construction of radiation map in EXCEL®

As it can be seen on the figure 4.22 the radiation map consists of four tables, each one of them composed by 44x11 cells containing the average value of the solar flux in that area.
Due to the fact that these data were directly available from ABENGOA SOLAR and are, obviously, very representative of the real operation, it has been decided to maintain this layout (number of panels and cells for each panel) even for other radiation maps, for example in off-design conditions.

Number and layout of absorbing panels

As for the *radiation maps* the main geometry of the panels and their layout is fixed following the internal configuration of the PS10 plant. In this plant, as in the model, there are four panels that are placed inside the cavity of the receiver.

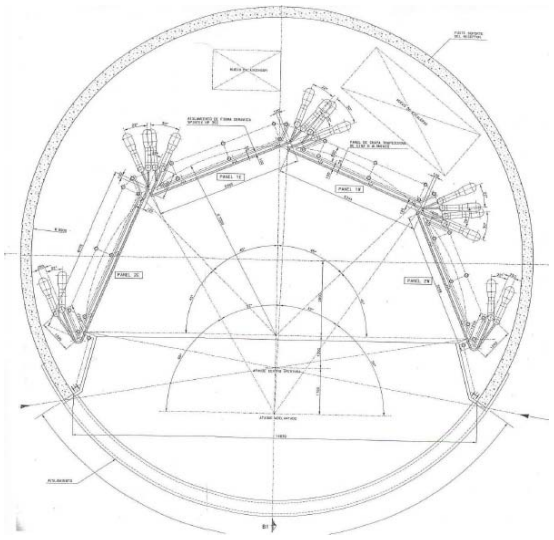

Figure 4.23:Technical design of the PS10 4 panels [31]

In the PS10 this configuration has been chosen to perform below flux limits (650 kW/m^2) minimizing spillage losses that are about 1% of the incident radiation.
Geometrical parameters regarding the panels disposition have not been considered because these information is already present in the radiation map.
Another important aspect that is fixed is the rate between height and width of each panel that is equal to 2.2388 according to the PS10 design [31].

Pipes layout

In the PS10 the boiler piping follows a particular geometry with several direction changes in order to collect in the best way the incident radiation.

In the model considered, instead, for simplicity, a simple layout has been chosen. In particular, all the pipes are vertical and do not have any bend. The subcooled water enters from the bottom and the saturated water/ steam exits from the top going to the drum.
In this way, the computational time needed to solve the model is reduced because it is possible to associate each pipe of the panels to a single column of the radiation map and, for this reason, it is possible to reduce the number of pipes studied significantly.
The real size of each column in the radiation map depends on boiler size but normally it includes more than a single pipe.
For example, for the generation of steam at 40 bar for a 15 MW_e plant, according to the model, a boiler surface of about 295 m^2 is necessary, this meaning a panel surface of 73.75 m^2 and therefore a width of each cell of the module of 0.5251 m. Considering that a single pipe has an external diameter of about 60 mm, about 8 pipes per column must be considered. In this way instead of studying the behavior of 352 pipes it is possible to study only 44 pipes.
In summary, it can be said that the resolution of the computational domain (i.e. number of pipes) is determined by the resolution of the available radiation map. With this simplification, the computational time is therefore uncoupled from the boiler size.

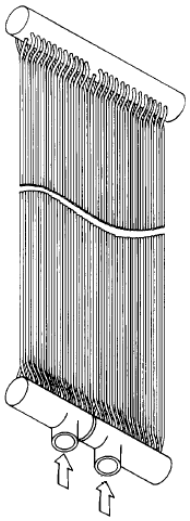

Figure 4.24: Vertical pipes layout in a solar boiler

Another important aspect to underline is that no membranes have been modeled because, as it will be explained better in paragraph 5.2.2, all thermal losses have been accounted for in an overall boiler efficiency of 92%. Therefore the amount of heat that enters the pipe, for each cell, is the total heat of each cell divided by the corresponding number of pipes in that column.

Other pipes and boiler circulation
The boiler geometry is illustrated in figure 4.25

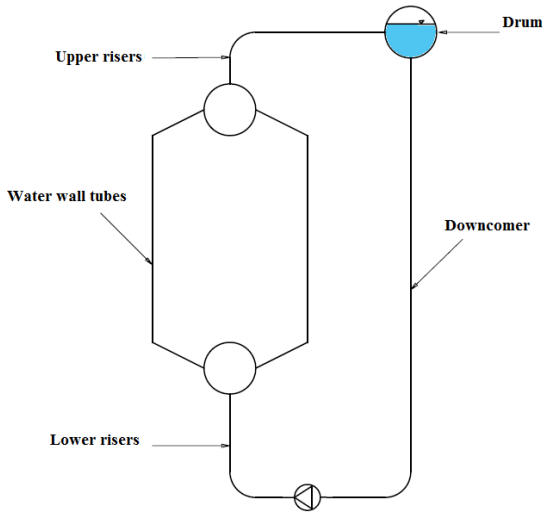

Figure 4.25:Boiler geometry

From the drum, the water flows down through the downcomers circuit, is pumped towards the water wall tubes, passes through the lower risers, then circulates inside the boiler pipes (water wall tubes) reaching the upper collector from which, by upper risers circuit, the mixture reaches the drum.
Normally this kind of steam generator, that contemplates the presence of the drum, can work either with natural circulation or forced circulation. Due to the critical condition of the pipes, which are subjected to a very high thermal flux from the heliostat field, forced circulation is preferred.
In the model developed in this work, forced circulation is assumed by default. However, the user can select the number and type of pumps: single speed pumps or variable speed pump (more explanations in paragraph 5.2.4). Eventually, once the calculations are completed, it is possible to check whether or not natural circulation is possible.

5. On-design boiler model

5.1 Inputs and assumptions

The boiler model, as the power block one, has been written in MATLAB®.
This code allows calculating some important parameters like steam flow, average steam quality, pump power, water distribution and all the thermodynamic properties of the flow cell by cell within the receiver mesh. These data, in particular the steam mass flow, are supplied to the power block module to complete all the solar plant information.

Obviously before starting the program several input parameters must be chosen by the user, bearing in mind that for a few of them, like the radiation map, there are some constrains to respect.

5.1.1 Radiation map

As it was said in paragraph 4.5 the radiation map is one of the key components of the model inasmuch as it contains all the information about the heliostat field that has not been developed in this work. Therefore an appropriate radiation map is necessary to obtain realistic results of the plant.
The map is a simple matrix of 44x44 cells (11 columns x 4 panels) that contains the average value of heat flux on the absorbing surface.
In order to have realistic results, real radiation maps have been used thanks to ABENGOA SOLAR [31]. These maps have been created in EXCEL® first, having a graphical vision of the surface, and then exported to MATLAB®.
The on-design map used was obtained on the 21st March 2007 at 12.00 when the nominal conditions of the PS10 boiler were reached:

- Irradiance: 981 W/m^2.
- Atmospheric transmittance: 95%.
- Solar azimuth position: 00.0°.
- Sun elevation: 52.2°.
- Net power onto absorber panels: 51953.86 kW.
- Peak irradiance on receiver surface: 644 kW/m^2.

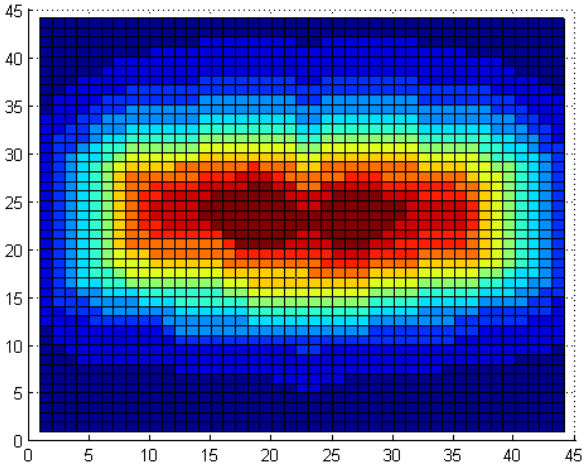

Figure 5.1:MATLAB elaboration of on-design map

The model has been written to leave the possibility to create other maps and to use them for on or off-design simulations. What is important to keep in mind, when generating radiation maps, is that the matrix must be characterized by 44x44 cells and solar flux values must be expressed in kW/m^2.
Another option that is left to the user is the possibility to scale the values of the radiation map according to the irradiance of the site. The on-design map used, in fact, shows solar flux values linked to the irradiance condition of 21st March at a site near Seville (Southern Spain) with a typical insolation of around 1000 W/m^2.
It is thought that with the same heliostat field but with different value of radiation, the flux distribution will remain the same but absolute values of each cell will change proportionally with the solar irradiance chosen.

$$flux_{new} = flux_{old} * \frac{irradianc\ e_{new}\left[\frac{W}{m^2}\right]}{1000} \tag{5.1}$$

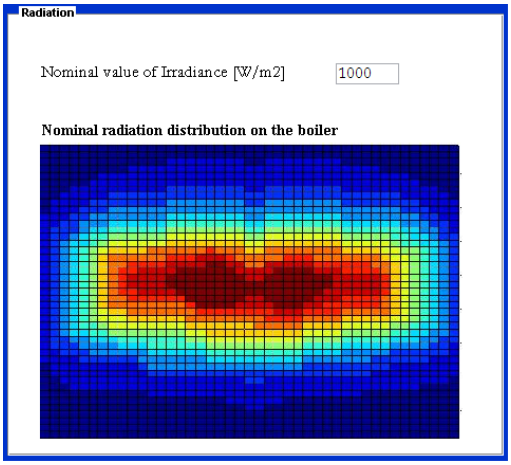

Figure 5.2: Possibility to change nominal irradiance in the model

5.1.2 Pipes

It has already been said that the arrangement of pipes is set by default (fixed) although the user is free to choose several characteristics of the pipes:

- Internal diameter
- Wall thickness
- Absolute roughness (inner wall)

Default values have been fixed even if they can be changed according to user requirements:

Table 5.1:Pipes default values

Internal diameter	[mm]	50
Thickness	[mm]	4.4
Absolute roughness	[mm]	0.0547

5.1.3 Modules

The geometry of the modules, as already said, follows the PS10 boiler design not being possible to change it.
One of the main targets of the model is sizing the solar steam generator according to the electric power requested by the user.
To obtain these values the code operates by iterative calculations. In order to reduce the computational time, a first estimation is done with the PS10 dimensions and, then, by a simple proportion, a first guess is obtained.

The default values used for the module geometry are, therefore, those of the PS10 steam generator, showed in table 5.2.

Table 5.2: Module default values (single module)

Number of modules		4
Height	[m]	12
Shape ratio	[-]	2.23880597
Columns		11
Rows		44

Differently to the other default values, these ones cannot be changed by the user.

For boiler sizing, only the height of the module is changed while the shape ratio (height to width) is kept constant at the value corresponding to the PS10 plant:

$$Shape\ ratio = \frac{Module\ \ height}{Module\ \ width} = 2.23880597 \tag{5.2}$$

5.1.4 Thermal inputs

The thermal inputs influence the thermal behavior of the boiler and of the entire plant.
These inputs are

- Overall thermal efficiency of the boiler.
- Desired average steam quality at receiver discharge.

Default values are again taken from PS10 data [32]:

Table 5.3:Thermal default values

Overall thermal efficiency	[%]	92
Outlet desired steam quality	[%]	20

The overall thermal efficiency of the boiler contains all the information about the heat transfer between the incident radiation and the working fluid that flows through the pipes. The value of 92% corresponds to the PS10 , however, a verification of this value is presented later in paragraph 5.2.2 by means of a thermal model created specifically for this purpose.

The desired average steam quality at the upper collector will influence the water distribution among all the pipes. It has already been said that the boiler considered is a saturated steam generator and, in order to exploit the great

advantages of this kind of generator (principally using low cost material due to the high thermal exchange coefficient of boiling water), it is important to set that the outlet flow does not reaches high value of steam quality. This way, the overall heat transfer coefficient will remain quite high and the pipes will be subjected to lower stresses.

5.1.5 Risers and downcomers / Natural circulation check

The length of the pipes that form the boiler circuits are defined maintaining the proportion of the PS10 tower which, considering the distance from the ground, is characterized by:

- Drum height: 120 m.
- Lower end of absorbing surface: 112 m.
- Absorbing surface height: 12 m.
- Pump level: 80 m.

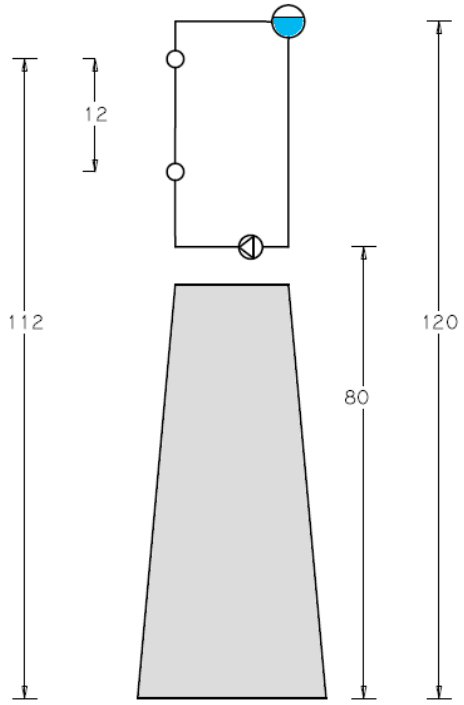

Figure 5.3:Schematic view of PS10 tower dimensions [m]

When a power is chosen by the user, an approximate height of the tower is estimated first of all (see Par. 3.5); then, the *lower end of the receiver* and the

pump level are calculated following the aforementioned approach and referring it to the tower height:

Table 5.4:Absorbing surface and pump height

Lower end of receiver	[m]	0.933*Tower_height
Pump level	[m]	0.667*Tower_height

From these three values (*tower height*, *absorbing surface end* and *pump position*) the following parameters can be estimated:

- *Upper risers length.*
- *Lower risers length.*
- *Downcomers length.*

While these values are fixed, other parameters can be chosen freely by the user:

- Additional length of water wall tubes (Boiling tubes).
- Risers:
  - Number
  - Internal diameter
- Downcomers:
  - Number
  - Internal diameter

Default values have been taken from industrial examples [43] and [65]:

Table 5.5: Risers and downcomers default values

Add. length of water wall tubes	[m]	3
RISERs		
Number		15
Intern. Diameter	[m]	0.1524
DOWNCOMERS		
Number		4
Intern. Diameter	[m]	0.3048

Knowing the complete geometry of the boiler the model proposed is able to calculate if natural circulation is possible.

5.1.6 Pumps

For the boiler, like the power block, the user can choose between single speed pump(s) or a variable speed pump.

The pump model is based on a set of standard non dimensional curves of head and efficiency against volumetric flow that are typical of multistage centrifugal pumps.
For the two categories (single and variable speed) the same characteristic curves have been chosen, with the values shown in table 5.6, where subscript *d* stands for the rated value.

Table 5.6: Pump characteristic curves values

Q/Q_d	H/H_d	η
0	1.244	0
0.2	1.237	0.309
0.4	1.219	0.52
0.6	1.181	0.648
0.8	1.112	0.709
1	1	0.72
1.2	0.836	0.697
1.4	0.608	0.657

From this table, it is possible to plot the characteristic curves: head and efficiency.

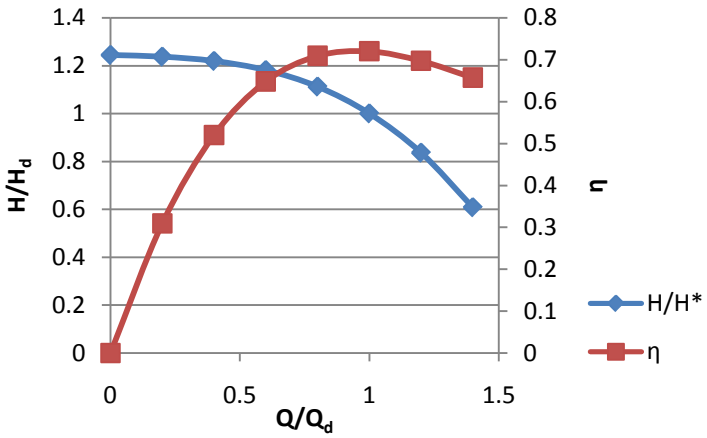

Figure 5.4: Head and efficiency curve of considered pumps

Values of table 5.6 can be changed by the user according to the kind of pump used and will later be used in the off-design mode to calculate the pump/s performances.

Three other important input parameters that can be changed are necessary to set the on-design behavior of the pump. These default values have been taken from very common experience [43] and [65].

Table 5.7: Pumps default values

Isoentropic efficiency on-design	[%]	75
Mechanical efficiency (constant)	[%]	98
Electrical efficiency on-design	[%]	98

Regarding the last point (the electrical efficiency at on-design), it is "on-design" because, really, the electrical efficiency changes according to the power absorbed. For this reason other default values have been inserted to account for performance decay at off-design operation:

Table 5.8: Default values pumps electrical efficienty

W/W_d	η_{el}/η_{el_d}
1	1
0.8	0.82
0.6	0.68
0.4	0.58
0.2	0.52
0	0.5

5.2 Boiler model

Two important aspects will be discussed in this paragraph:

1) Core calculations: pressure losses and thermal balances.
2) Model logic.

Regarding the logic of the model, it will be described how to reach two main targets:

1) Water distribution in the receiver pipes.
2) Boiler sizing: choice of the dimensions of the boiler to produce the steam requested by the power block according to user requirements.

The core idea of the model is finding the water flow distribution within the pipes of the boiler in order to have a specific average steam quality at the upper collector, as chosen by the user (e.g. 20% by default). Water distribution is set by pressure drop calculations and enthalpy balances so that in each pipe there would be the same pressure drop.

All the correlations used for the thermodynamic simulation are shown in sub paragraphs 5.2.1, 5.2.2, 5.2.3, while sub-paragraphs 5.2.5 and 5.2.6 point out the logic employed to search the solution.

5.2.1 Pressure losses

Pressure drops are very important to reduce pumping losses and to obtain a water distribution that would avoid backflow problems. Their calculation has been done by a detailed model that considers different correlations for single-phase and two-phase flow.
Generally, pressure drops are defined by three contributions: acceleration ΔP_a, gravity ΔP_g and friction ΔP_f that change according to geometrical and thermodynamic conditions.

The choice of correlations have been carried out confronting computational time and code stability among different model like Friedel [48] or Awad and Muzychka [49]. Eventually, Thom's formulation [44] resulted the best choice as proposed by Ganapathy [43].

Single phase flow

Since water is not compressible, acceleration losses are neglected.

For the gravity component:

$$\Delta P_g = 9.81496E-05 \times \frac{L}{v_f} \tag{5.3}$$

Where:
- L : Equivalent length of the cell [m]
- v_f : Average specific volume of the fluid in the cell [kg/m^3]

For the friction component:

$$\Delta P_f = 4.99853E-06 \times \frac{fV^2L}{Dv} \tag{5.4}$$

Where:
- V : fluid speed [m/s]
- D : internal diameter [m]
- v : specific volume [kg/m^3]
- f : friction factor calculated by Colebrook correlation

$$\frac{1}{\sqrt{f}} = -2 \cdot Log_{10}\left(\frac{\frac{\varepsilon}{D_{int}}}{3.7} + \frac{2.51}{Re_{D_{int}} \cdot \sqrt{f}}\right) \; with \; Re_{D_{int}} > 2300 \qquad (5.5)$$

$$f = \frac{64}{Re_{D_{int}}} \quad with \; Re_{D_{int}} < 2300 \qquad (5.6)$$

Where:

- ε: absolut roughness of pipe

Two-phase flow

For the gravity component:

$$\Delta P_g = 9.81496E-05 \times L \frac{r_4}{v} \qquad (5.7)$$

Where r4 is the *Thom's two-phase multiplication factor for gravity loss*, obtained from figure 5.5

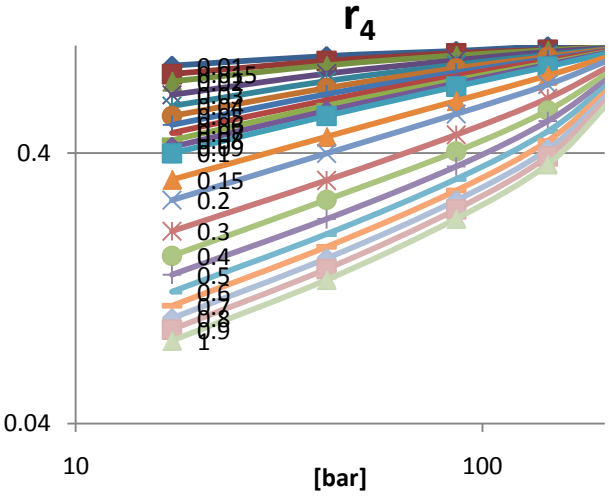

Figure 5.5: Thom's two-phase multiplication factor for gravity loss r_4

For the friction component:

$$\Delta P_f = 5.0037E-06 \times v_f \frac{fL}{D} G_i{}^2 r_3 \qquad (5.8)$$

Where:

- f : is the Fanning friction factor which is 0.25 times the Moody friction factor (calculated by Colebrook)

- G_i : is the tube-side mass velocity [kg/m2s]
- *r3* : is the Thom's two-phase multiplication factor for friction loss
- v_f : is the specific volume of saturated water [kg/m^3]

r_3 can be obtained from figure 5.6

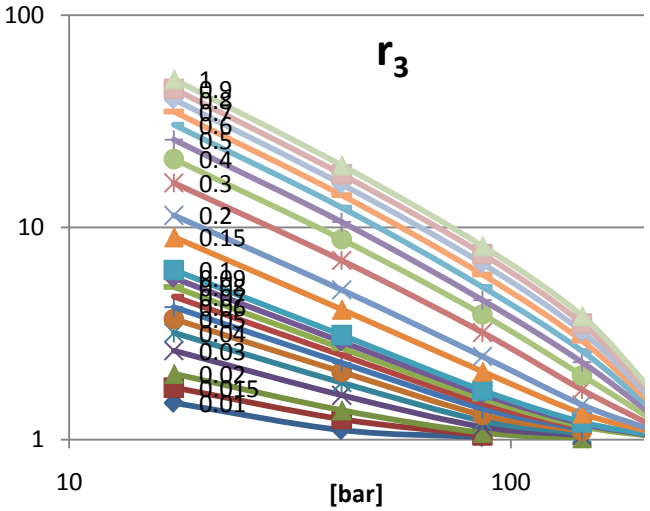

Figure 5.6: Thom's two phase multiplication factor for friction loss r_3

For the acceleration component:

$$\Delta P_a = 9.99138E - 06 \times v_f r_2 G_i \quad (5.9)$$

Where:

- r_2 is the Thom's two-phase multiplication factor for acceleration loss that can be obtained from graph 5.7

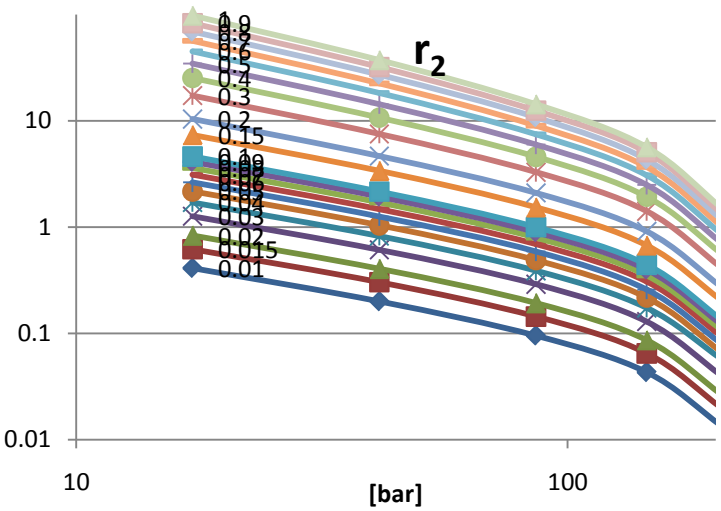

Figure 5.7: Thom's two-phase multiplication factor for acceleration loss r_2

Upper risers

For the upper risers, that do not receive heat, Thom's method can be used again [43].

For the gravity component:

$$\Delta P_{g\_up\_ris} = 0.000098 \times \left[\rho_f (1 - \alpha') + \rho_g \alpha'\right] \times L \qquad (5.10)$$

Where:

- L : is the upper risers length
- ρ_f : density of saturated water
- ρ_g : density of saturated steam
- α' : is the void fraction

The void fraction is calculated as:

$$\alpha' = \frac{\gamma x_m}{1 + x_m (\gamma - 1)} \qquad (5.11)$$

Where:

- x_m: the average steam quality
- γ : is a coefficient that changes according to the pressure

Table 5.9:γ coefficient

[bar]	γ
17.237	40
41.368	20
86.184	9.80
144.79	4.95
206.84	2.15
221.04	1

For the friction component:

$$\Delta P_{f\_up\_ris} = 4.99853E-06 \times v_f \frac{fL}{D} {G_i}^2 r_f \quad (5.12)$$

Where:

- r_f : is the two-phase friction factor for unheated tubes and it can be obtained by the graph:

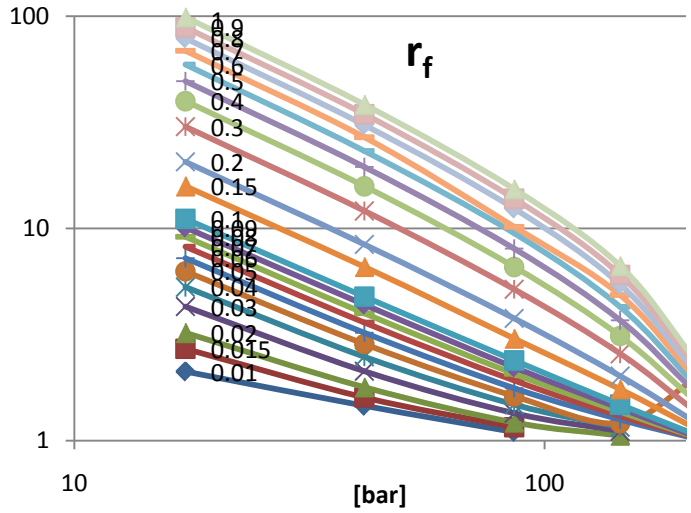

Figure 5.8: Two-phase friction factor for unheated tubes r_f

5.2.2 Thermal model

In each cell, in addition to pressure drops calculation, a thermal balance between incident radiation and water flow in the pipe is done. This balance, which yields the steam quality of the flow that enters into the following cell, is based on an overall efficiency of the boiler.

For this overall efficiency, a value of 92% is chosen according to the experimental data of the PS10 [31], although this value has also been validated creating a specific thermal model.
Figure 5.9 shows the heat transfer contributions for the panels and Figure 5.10 those for a single pipe.

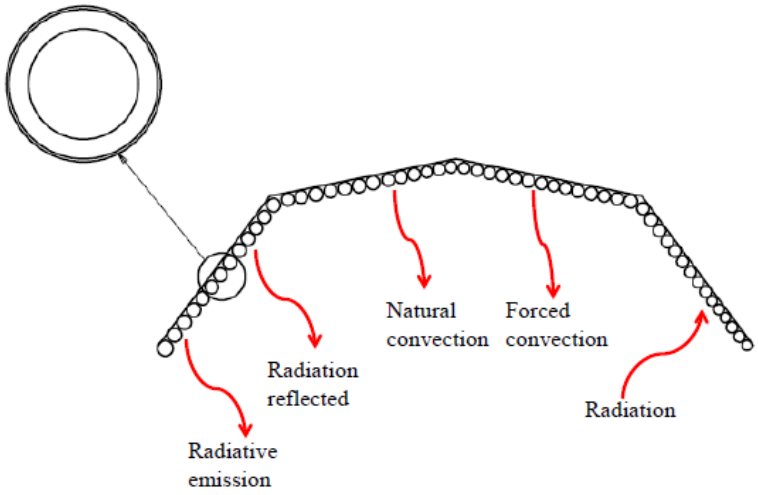

Figure 5.9: Heat transfer components in a cavity receiver

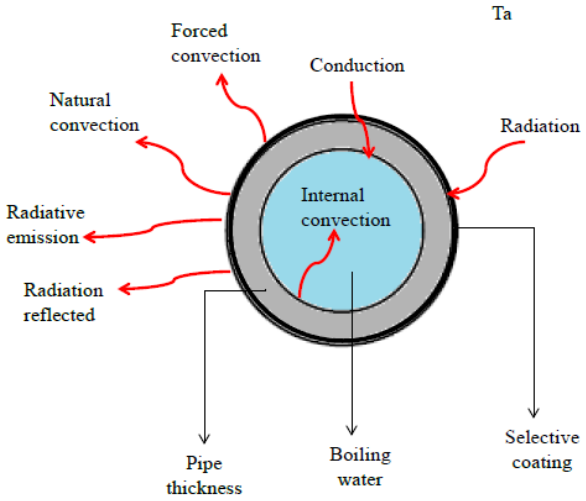

Figure 5.10:Heat transfer components for a single pipe

The *solar radiation (q_sol)* is concentrated by the heliostat field on the cavity receiver and then absorbed by the selective coating that, for a new and clean pipe, has an *absorptivity* of about 98% [31] or rather a reflectivity value of the selective coating at the solar radiation wavelengths of 2% *(q_sol_refl)*.

Part of the radiation absorbed by the coating is transferred by *conduction (q_cond)* across the metallic wall of the pipe and then transferred to the internal fluid by *internal convection (q_conv_int).*
The higher temperature of the external wall of the pipes with respect to the environment is responsible for three types of thermal losses:

- *Natural convection (q_air_ext_nat)*
- *Forced convection (q_air_ext_forc)*
- *Radiative emission (q_rad_abs_sky)*

Table 5.10: Summary of contributions to the thermal model

		Thermal transfer path	
Heat flux [W/m^2]	**Thermal transfer mechanism**	**From:**	**To:**
q_conv_int	Internal convection	Pipe internal wall	Water
q_cond	Conduction	Pipe external wall	Pipe internal wall
q_sol_refl	Reflection of solar radiation	Pipe external wall	Enviroment
q_air_ext_nat	External natural convection	Pipe external wall	Enviroment
q_air_ext_forc	External forced convection	Pipe external wall	Enviroment
q_rad_abs_sky	Radiation	Pipe external wall	Sky
q_sol	Radiation	Heliostat field	Pipe external wall

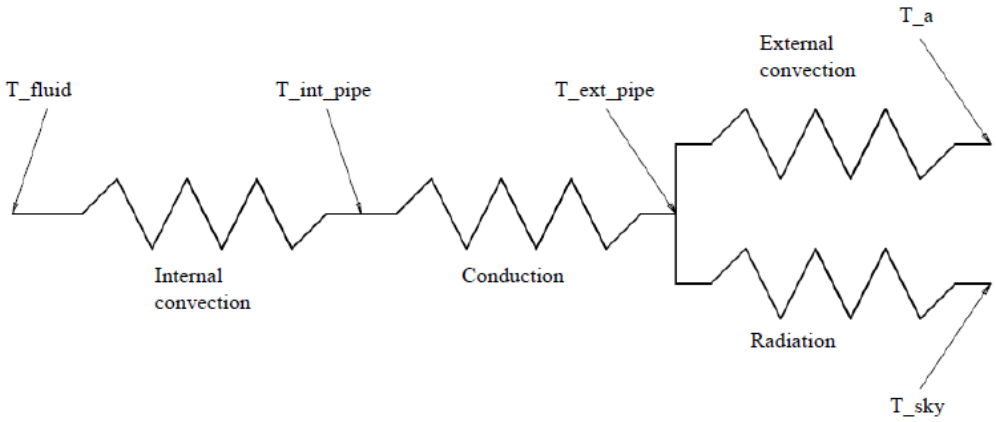

Figure 5.11:Equivalent electric circuit for a section of a pipe

From the different energy terms described in table 5.10, it is possible to develop the energy balance:

$$q_{conv_{int}} = q_{cond} \tag{5.13}$$

$$q_{cond} = q_{sol} - q_{sol_{refl}} - q_{air_{extnat}} - q_{air_{extforc}} - q_{rad_{abssky}} \tag{5.14}$$

Internal convection between fluid and pipe internal wall

According to Newton's law, convection between working fluid and inner walls of the pipe obeys the following relation:

$$q_{conv_{int}} = h_{HTF} \cdot \pi \cdot D_{int} \cdot \left(T_{fluid} - T_{int\_pipe}\right) \tag{5.15}$$

With:

$$h_{HTF} = Nu_{D\_int} \cdot \frac{k_{fluid}}{D_{int}} \tag{5.16}$$

Where:

- h_{HTF} : convection heat transfer coefficient $\left[\frac{W}{m^2 K}\right]$
- D_{int} : Pipe internal diameter $[m]$
- T_{fluid} : Temperature of working fluid $[°C]$

- T_{int_pipe} : Temperature of internal wall of the pipe [°C]
- Nu_{D_int} : Nusselt number for the internal diameter
- k_{fluid} : Thermal conductivity of the fluid $\left[\frac{W}{m\ K}\right]$

The correlations used to calculate the heat exchange coefficients both in the case of single-phase flux or two-phase flow are shown below.

a. Single-phase flow

The single-phase flux correlations are used for the liquid only or steam only flux.

a.1 Turbulent and transition flows: Gnielisky correlation

In the cases of single-phase turbulent or transition flows, Gnielisky's correlation [45] can be used:

$$Nu_{D\_int} = \frac{f_{int}/8 \cdot (Re_{D\_int} - 1000) \cdot Pr_{Tfluid}}{1 + 12.7 \cdot \sqrt{f_{int}/8} \left(Pr_{Tint}^{\ 2/3} - 1\right)} \tag{5.17}$$

where f_{int} is the friction factor obtained from the Moody diagram or, for smooth tubes, from Petukhov correlation:

$$f = \left(0.79 \cdot Re_{D\_int} - 1.64\right)^{-2} \tag{5.18}$$

this correlation is valid for:

$$\begin{Bmatrix} 3000 \leq Re_{D_{in}} \leq 5 \times 10^6 \\ 0.5 \leq Pr \leq 2000 \end{Bmatrix} \tag{5.19}$$

where:

- f_{int} : friction factor for pipes
- Pr_{Tfluid} : Prandtl number at bulk temperature
- Pr_{Tint} : Prandtl number at pipe internal wall temperature
- Re_{D_int} : Reynolds number calculated on the internal diameter

a.2 Laminar flow

If the flow is laminar, characterized by a Reynolds number lower than 2300, in the case of constant solar flux, there will be a constant Nusselt number:

$$Nu_{D\_int} = 4.36 \tag{5.20}$$

which is valid for:

$$\{Re_{D\_int} < 2300\} \tag{5.21}$$

b. Two-phase flow

Internal forced convection of boiling flows is associated with bubble formation at the inner surface of a heated tube through which a liquid is flowing.
Let us consider the flow development in a vertical tube that is subjected to a constant surface heat flux: heat transfer to the subcooled liquid that enters the tube is initially approached by *single-phase forced convection* which might be predicted using the Gnielisky correlation. Further down the tube, the wall temperature exceeds the saturation temperature of the liquid, and vaporization is initiated in the *subcooled flow boiling region*. In this region bubbles form adjacent to the heated wall and subcooled liquid flowing near the center of the tube. The thickness of the bubble region increases farther downstream, and eventually, the core of the liquid reaches the saturation temperature of the fluid. Bubbles can then exist at any radial location, and the time-averaged mass fraction of vapor in the fluid exceeds zero at any radial location. This marks the beginning of the *saturated flow boiling region*.
In this region several flow regimes are possible, as shown in figure 5.12.

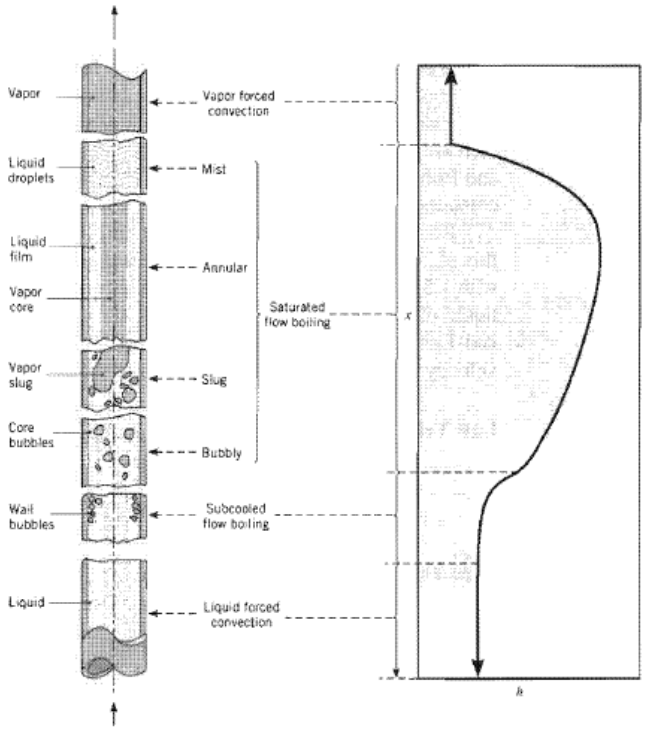

Figure 5.12:Flow regimes for forced convection boiling in a tube

In general, the heat transfer coefficient can increase by approximately one order of magnitude through the subcooled flow boiling region. Heat transfer coefficients are further increased in the early stages of the saturated flow boiling region. Instead the smallest convection coefficients exist in the forced convection with only vapor owing to the low thermal conductivity of the vapor relative to that of the liquid. For this reason, in the solar plant, with the aim of saving costs, a low steam quality at the outlet of the boiling tubes is desired (typically 20%).
In the saturated flow boiling region in circular tubes, the correlation in [45] used is:

$$\frac{h}{h_{sp}} = 0.6683\left(\frac{\rho_l}{\rho_v}\right)^{0.1} X^{0.16}(1-X)^{0.64} f(Fr) + 1058\left(\frac{q_s''}{\dot{m}'' h_{fg}}\right)^{0.7} (1-X)^{0.8} G_{s,f} \tag{5.22}$$

that is valid for:

$$\{0 < X \leq 0.8\} \tag{5.23}$$

where:

- $\dot{m}'' = \dot{m}/A_c$: is the mass flow rate per unit cross-sectional area
- $f(Fr)$: is the *stratification parameter*, and it is unity for vertical tubes (as our case)
- h_{sp} : is the single-phase convection coefficient
- $G_{s,f}$: for water is unity

Conduction through the pipe wall

The heat conduction through the steel pipe walls is given by the Fourier law that in the case of cylindrical geometry is:

$$q_{cond} = \frac{2\pi k_{T_{av\_steel}} (T_{int} - T_{ext})}{\ln(D_{ext}/D_{int})} \tag{5.24}$$

where $k_{T_{av\_steel}}$ is the thermal conductivity of steel at the average temperature between the internal and external wall temperatures.

Forced convection between pipe external surface and environment

In cavity receiver natural and forced convection are present at the same time, both of which must be considered within the thermal losses of the boiler.
For the calculation of heat losses due to forced convection, a flat plate at the average temperature of the receiver surface has been considered [46]:

$$Q_{loss,conv,fc} = h_{air,fc,ext} \cdot (T_{ext} - T_a) \cdot S \tag{5.25}$$

$$Nu_{air,fc,ext} = 0.0287 \cdot Re_{air,av}{}^{0.8} \cdot Pr_{air,av}{}^{1/3} \tag{5.26}$$

where all the thermodynamic parameters have been calculated at the average temperature between environment temperature and boiler surface temperature:

$$T_{air,av} = \frac{T_{ext} + T_a}{2} \tag{5.27}$$

Natural convection between pipe external surface and environment

Siebers and Kraabel showed that the natural convection inside the cavity was quite similar to the flat plate [46]. The natural convective heat transfer coefficient and natural convective heat loss are then given by the following equations:

$$Q_{loss,conv,nc} = h_{air,nc,ext} \cdot (T_{ext} - T_a) \cdot S \tag{5.28}$$

$$h_{air,nc,ext} = 0.81 \cdot (T_{ext} - T_a)^{0.426} \quad (5.29)$$

where all the thermodynamic parameters have been calculated as for the forced convection.

Radiation reflected from the pipes

Not all the radiation impinging the pipes is absorbed by them. In fact, a fraction is reflected due to the lower than unity absorptivity coefficient of the selective coating that covers the pipes.
This loss has been calculated considering a value of reflectivity ρ of about 2%.
Considering q_{sol} as the thermal flux value from the radiation map:

$$Q_{loss,conv,nc} = q_{sol} \cdot \rho \cdot S \quad (5.30)$$

Thermal model simulation

The thermal model explained in the preceding sections has been developed to validate the overall thermal efficiency of 92% taken from the PS10 data.
Considering a simulation for a plant of 15 MW working with live steam at 40 bar, and assuming the default values in Table 10, the losses in Table 11 are obtained.

Table 5.11: Default values used for thermal model simulation

Environmental pressure	[bar]	1
Environmental temperature	[K]	300
Sky temperature	[K]	285
Absorber emissivity (ε)	[%]	15
Absorber absorptivity (α)	[%]	98
Wind velocity	[m/s]	2

Table 5.12:Thermal losses for a 15 MW plant boiler

Total power on the boiler surface	[kW]	57124
Forced and convective losses	[kW]	2315
Radiative losses	[kW]	569
Reflection losses	[kW]	1142

Considering the values of table 5.12 the percentage of each loss referred to the total power that reaches the boiler is:

- Forced and natural convective losses: 4.05%
- Radiative losses: 1%
- Reflection losses: 2%

This means an overall efficiency of the boiler of 92.95% that is perfectly in accordance with the PS10 data.
For this reason, instead of overloading the computation duty of the model, an overall efficiency of the boiler has been used to obtain the enthalpy of the flow that leaves each cell by a simple energy balance:

$$h_{out} = \frac{\dot{Q}\eta_{boiler} + \dot{m}h_{inlet}}{\dot{m}} \tag{5.31}$$

where $\dot{Q}$ is the power that reaches the boiler surface and is taken directly from the radiation map chosen as input.

Principal thermal model outputs

The thermal model created, which is not integrated in the global model for computational time reasons, could be used, once estimated the water flow distribution, to evaluate thermal parameters for each cell of each pipe like:

- *Solar radiation (q_sol)*
- *Net heat flux to the flow (q_net)*
- *Forced convective heat loss (q_forc_air)*
- *Natural convective heat loss (q_nat_air)*
- *Radiative heat loss (q_radiative)*
- *Reflection heat loss (q_reflective)*
- *External wall pipe temperature (T_ext)*
- *Internal fluid temperature (T_fluid)*

For example, considering the same boundary conditions, as in *thermal model simulation*, the following figures show the different performance of pipes located on the side (1) and center (18) of the receiver:

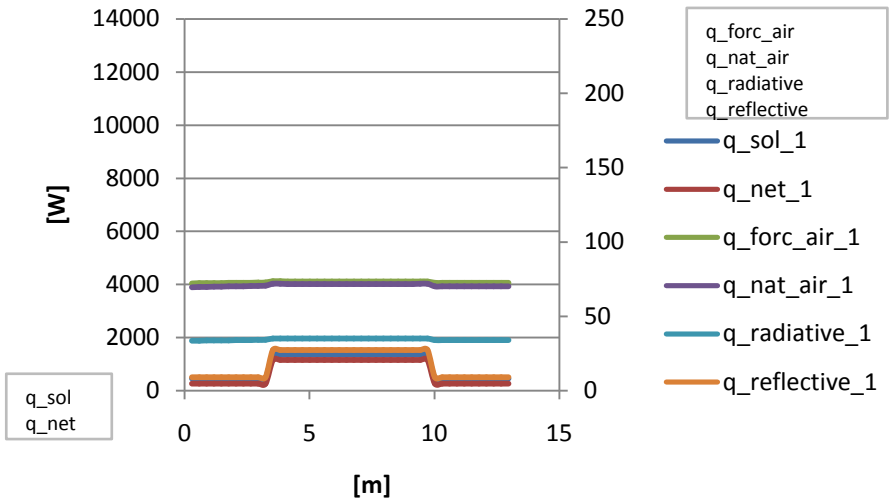

Figure 5.13: Heat fluxes for a side pipe

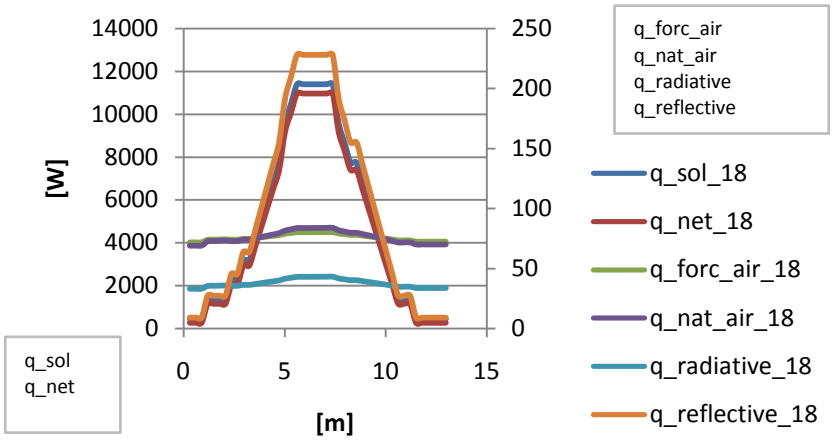

Figure 5.14: Heat fluxes for an internal pipe

For the external pipe the solar and fluid flux show a step evolution due to the discrete nature of the radiation map where there are only two values of radiation (25 kW/m^2 and 75 kW/m^2), while for the central pipe the distribution along the boiler height is more uniform.

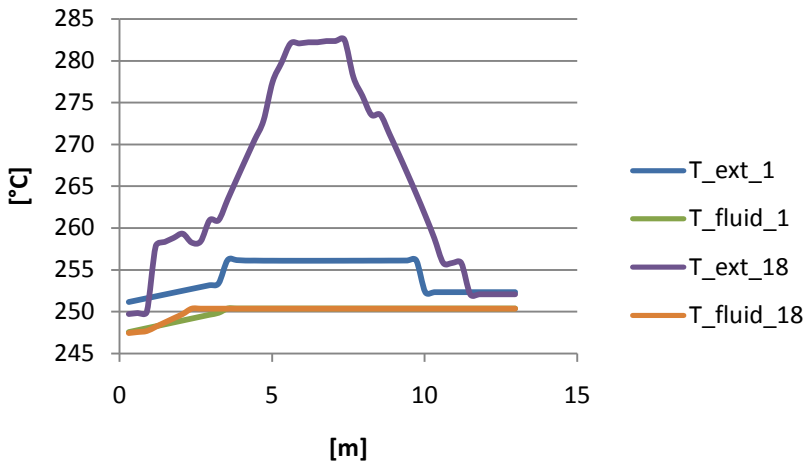

Figure 5.15:External and fluid temperature distributions for a side pipe and an internal pipe

In the external wall temperature of the external pipe (18) there are some discontinuities: the first one at 1 m is linked to the change of radiation from the radiation map while the sudden increase at about 3 m is due to vapor formation that increase too much the heat transfer coefficient. This temperature distribution is obviously approximate because in the thermal model the conduction along the height of the pipe has not been considered. Taking it into account should smooth the temperature profile along the axis.

Efficiency evaluation

As already highlighted several times, the boiler efficiency in the global model remain constant though can be set by the user. To make this choice, it is possible to use this auxiliary thermal model that evaluates the boiler efficiency at some particular conditions and, hence, estimate a new value closer to the boundary conditions of the real plant. For example, *wind velocity* and *pipe emissivity* can be changed in the model resulting in different boiler efficiencies. For a plant of 15 MW:

Table 5.13: Boiler efficiency changing wind velocity and emissivity

Wind velocity [m/s]	Pipe emissivity [%]	Efficiency [%]
1	15	93.8
5	15	90.7
10	15	87.6
1	20	93.5
1	30	92.8

From the table 5.13 , it appears that the value of 92% chosen as default is a good compromise among very different cases.

5.2.3 Thermal losses in downcomers and risers

An important parameter that affects boiler performances and dimensions is the temperature of water at the bottom collector, just before entering the pipes, which can be determined knowing the boiler geometry.
This temperature is affected by three parameters:

- Drum pressure, in particular the saturation temperature of water at this pressure.
- Downcomers length, number and diameter.
- Lower risers length, number and diameter.

The water at saturation temperature *T_sat(P_drum)* leaves the drum and flows along the downcomers reducing its enthalpy because of thermal losses (*Q_loss_down*). It is then pumped along the lower riser until the boiler inlet where it further reduces its temperature (*Q_loss_risers*).

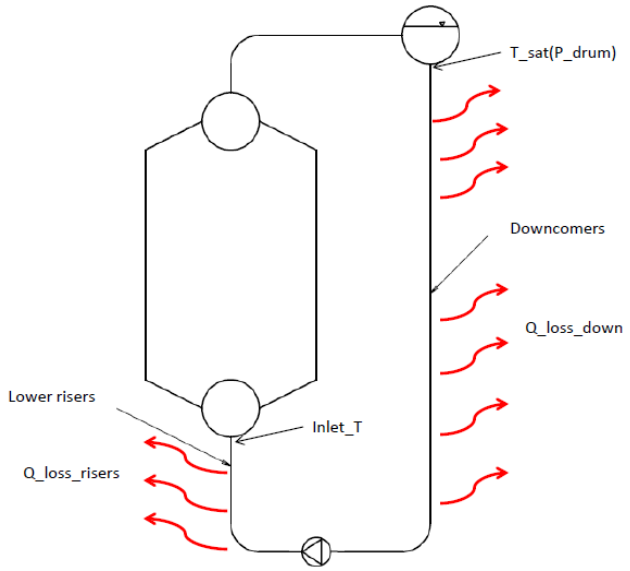

Figure 5.16:Downcomers and lower risers losses

The heat emission from steel pipes freely exposed in air has been obtained from literature values [46].

Table 5.14: Heat emission from steel pipes freely exposed in air at 20°C. [W/m]

	Pipe size [mm]												
ΔT	**15**	**20**	**25**	**32**	**40**	**50**	**65**	**80**	**100**	**150**	**200**	**250**	**300**
50	56	68	82	100	113	136	168	191	241	332	439	541	643
60	69	85	102	125	140	170	208	238	298	412	544	671	797
70	84	102	124	152	170	206	252	289	360	500	660	813	967
80	100	122	148	180	202	245	299	343	428	594	784	966	1148
100	135	164	199	243	272	330	403	464	577	804	1060	1307	1553
120	173	210	256	313	351	426	522	600	746	1042	1374	1694	2014
140	216	262	319	391	439	533	653	751	936	1308	1726	2128	2530
160	263	319	389	476	535	651	799	918	1145	1603	2115	2608	3102
180	313	381	464	569	640	780	958	1100	1374	1925	2539	3133	3726
200	368	448	546	670	754	919	1131	1297	1623	2276	3002	3705	4407
220	427	520	634	778	877	1069	1318	1510	1892	2655	3503	4323	5144
240	488	581	692	867	955	1203	1510	1728	2129	3050	4008	4947	5887
260	554	660	786	985	1086	1370	1723	1969	2429	3483	4577	5651	6725
280	625	744	885	1111	1225	1548	1949	2226	2748	3944	5182	6400	7618
300	699	833	990	1244	1372	1736	2189	2498	3086	4433	5825	7195	8564

The enthalpy of the water mass flow that reaches the boiler entrance (*inlet_h*) is obtained as:

$$inlet\_h = \frac{(mass\_flow\_total * h\_out\_drum - (Q\_loss\_down + Q\_loss\_risers))}{mass\_flow\_total} \quad (5.32)$$

where:

- *mass_flow_total* : water mass flow circulating in the boiler.
- *h_out_drum* : enthalpy of saturated liquid water at drum pressure.

5.2.4 Pumps

In the on-design code the pump study concerns basically two aspects:

- Pump/s power.
- Cavitation avoidance.

Regarding the first aspect, the pump/s must overcome all the pressure drops in the loop since water leaves the drum until it flows back again into it:

$$\Delta P_{tot} = \Delta P_{drum} + \Delta P_{upp\_ris} + \Delta P_{water\_wall} + \Delta P_{low\_ris} \quad (5.33)$$

where:

- ΔP_{drum} : is the pressure drop due to the drum, from literature [43] a fixed value of 0.013 bar has been chosen.
- ΔP_{upp_ris}: is the pressure drop in the upper risers (from the upper collector to the drum).
- ΔP_{water_wall} : is the pressure drop in the absorbing pipes.
- ΔP_{low_ris}: is the pressure drop of the lower risers (from the pump to the lower collector).

The pump/s power is calculated as:

$$W_{pump} = \frac{Q \cdot \Delta P_{tot}}{\eta_{is} \cdot \eta_m \cdot \eta_{el}} \quad (5.34)$$

where:

- W_{pump} : is the pump power [W].
- Q: is the volumetric mass flow impelled by the pump [m^3/s].
- ΔP_{tot} : is the total pressure drop [Pa].
- η_{is}: is the isentropic efficiency [%].
- η_m: is the mechanical efficiency [%].
- η_{el}: is the electrical efficiency [%].

The NPSH calculation helps to check if cavitation is likely to take place at pump suction, what might occur when the liquid vaporizes or flashes due to low local pressure and collapses at the pump as soon as the pressure increases.
The $NPSH_a$ (available) normally varies depending on pump system layout which, in our case, is determined once chosen the plant power:

$$NPSH_a = \frac{P_{drum}}{\gamma} + H_{downcomers} - \frac{P_{vap}}{\gamma} - H_{friction} \qquad (5.35)$$

where:

- γ: is $\rho \cdot g$ with ρ the water density [kg/m^3] and g the gravity acceleration [m/s^2].
- P_{drum} : is the drum pressure [Pa].
- $H_{downcomers}$: is the downcomers length [m].
- P_{vap} : is the vapor pressure of liquid at operating temperature [Pa].
- $H_{friction}$:is the friction pressure drop in the downcomers expressed in meters of H_2O [m].

In order to prevent cavitation, the pump needs that the flow has some energy at the inlet of the pump, to pass from the entry to the minimum pressure point without vapor formation. The $NPSH_r$ (requested) is calculated [66,67,68] as:

$$NPSH_r = \left(\frac{n \cdot Q^{1/2}}{157}\right)^{4/3} \qquad (5.36)$$

To avoid cavitation $NPSH_a$ must be always larger than $NPSH_r$.

5.2.5 Water flow distribution

The water flow distribution within the pipes is obtained imposing the same pressure drop along all the pipes of the boiler, as otherwise back-flow problems would arise.
Since MATLAB operates sequentially, this process is composed by two steps:

1) Average pressure drop calculation under certain conditions: a particular radiation map and a desired average steam quality at the outlet.
2) Calculation of mass flow distribution to comply with the average pressure drop estimated previously.

Average pressure drop

As aforementioned, in order to comply with the equal pressure drop and average steam quality conditions simultaneously, it is necessary to start by calculating an average pressure drop considering the following parameters:

- *h_out_wanted* : is the enthalpy at drum pressure and steam quality as requested by the user.
- *mass_flow_total* : is the total flow that should circulate inside the boiler to obtain the steam quality requested and with the radiation map chosen by the user.

$$mass\_flow\_total = \frac{radiation\_total\_incident * receiver\_eta}{(h\_out\_wanted - h\_inlet)} = \frac{Q_{in}}{(\Delta h)} \tag{5.37}$$

  where Q_{in} is the heat that reaches the flow and Δh is the enthalpy change requested.
- *mass_flow_pipe* : initially, the mass flow in each pipe is assumed the same and is obtained simply dividing the *mass_flow_total* by the number of pipes of the boiler.

Therefore, with a uniform water flow distribution, pressure drop in each pipe are calculated. Obviously these values will be different in each pipe because of the different radiative flux and, consequently, different steam production.
When all the ΔP have been estimated, an average value is calculated and imposed again as the target value for the real water mass flow estimation.

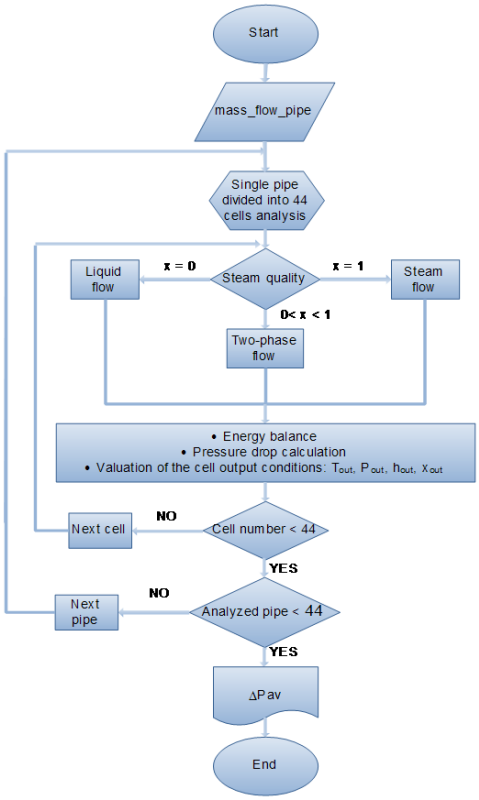

Figure 5.17: Flow diagram for the average delta P calculation

Real water flow distribution

After having calculated the average ΔP, it is possible to define the water flow distribution (fraction of water flowing through each pipe) and, then, evaluate the corresponding steam productions. The mass flow distribution is managed by a *while* cycle: the pressure drop is calculated for each pipe starting with a mass flow value equal to *mass_flow_pipe* and changing it until the difference between the pipe pressure drop ΔP_{pipe} and the ΔP_{av} is less than an arbitrary convergence criterion ε.

$$mass\_flow\_pipe(i+1) = mass\_flow\_pipe(i) \cdot \left(1 - \frac{k \cdot (\Delta P - \Delta P_{av})}{\Delta P_{av}}\right) \tag{5.38}$$

until

$$|\Delta P - \Delta P_{av}| > \varepsilon \tag{5.39}$$

Where *k* (relaxation factor) is a coefficient that can take different values depending on the proximity of the solution and helps to speed up the process.

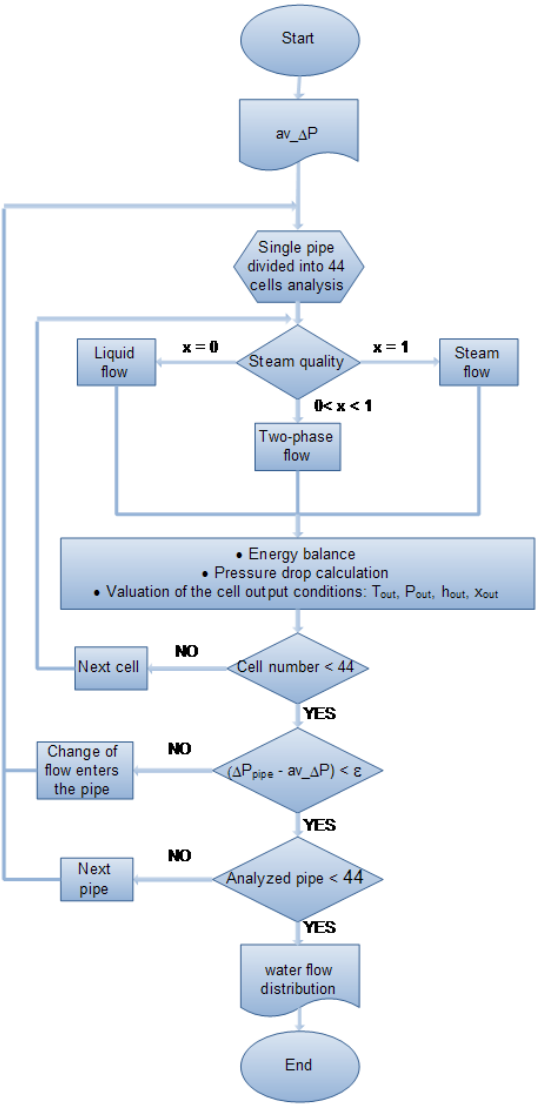

Figure 5.18:Water flow distribution calculation

5.2.6 Boiler sizing

The second target of the on-design model is estimating the dimensions of the boiler that satisfies the power block requirements. To reach this value, two steps are followed:

1) Calculation of the steam flow produced by a boiler with the dimensions of the PS10 (5.36 m wide x 12 m high).

2) The geometry of the receiver is then modified, using a *while* cycle, until the difference between the steam flow produced by the boiler *"boiler_flow"* and the steam flow requested by the turbine *"nominal_flow"* is less than an arbitrary threshold ε.

In reality, not the entire surface value is changed at each iteration but only the module width because the ratio between module height and module width is fixed (see Par. 4.5).

$$real\_width(i+1) = real\_width \cdot \left(1 - k\_1 \cdot \left(\frac{boiler\_flow - nominal\_flow}{nominal\_flow}\right)\right) \tag{5.40}$$

until

$$|boiler\_flow - nominal\_flow| > \varepsilon \tag{5.41}$$

where the relaxation factor *k_1* as in the water flow distribution case is a coefficient used to speed the process up.

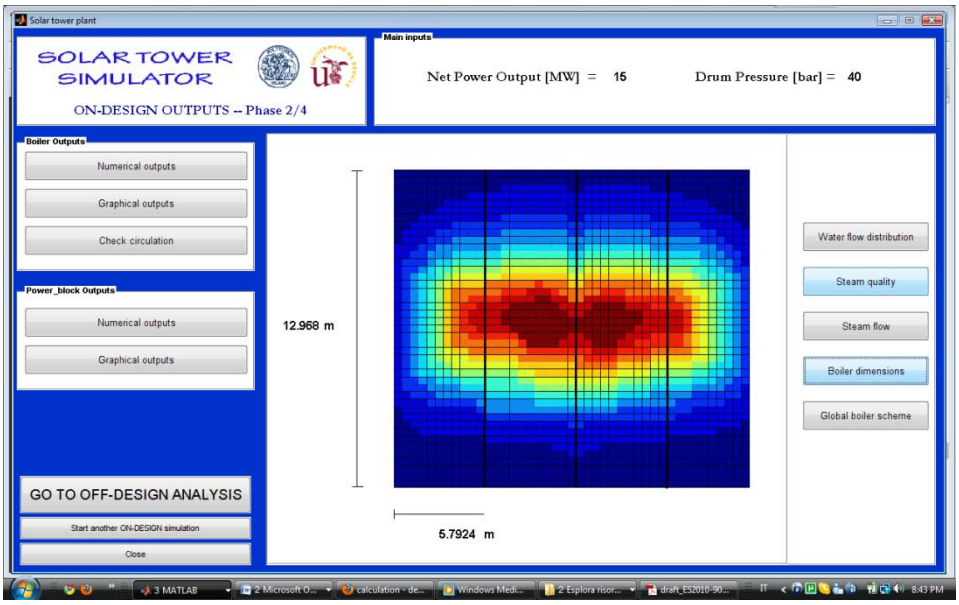

Figure 5.19:Boiler dimensions output

The entire process of the on-design model is shown in the blocks diagram in figure 5.20.

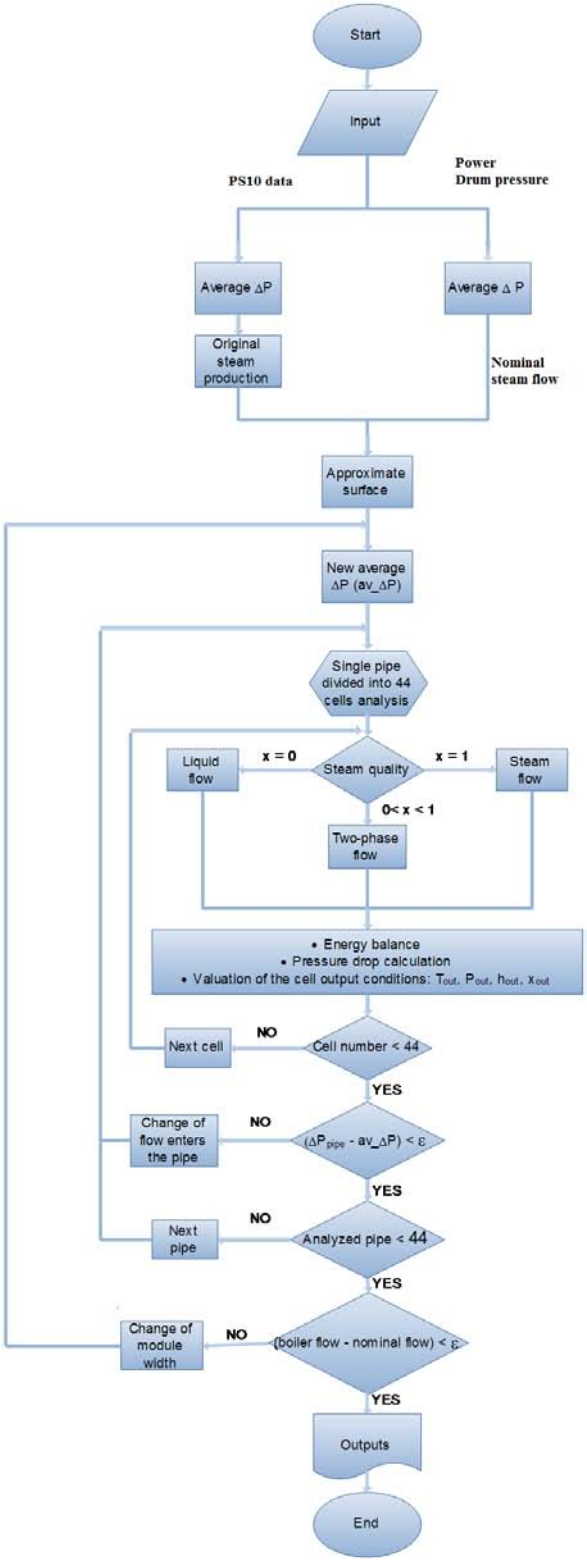

Figure 5.20: Logic of boiler on-design model

5.3 Outputs

The on-design boiler model performs useful calculation for the determination of the main thermodynamic parameters of the receiver.
The performances of the boiler can be classified according to three categories of outputs:

- Numerical outputs
- Graphical outputs
- Natural circulation check

5.3.1 Numerical outputs

Numerical outputs allow a more detailed study of the boiler performance and could be useful to deduce possible problems or critical operation.
The main numerical outputs that are shown to the user are:

- *Enthalpy*: a matrix of 44x44 that contains the enthalpy value of each cell of each pipe and could be useful to understand how the fluid is heated and evaporated along the boiler height.

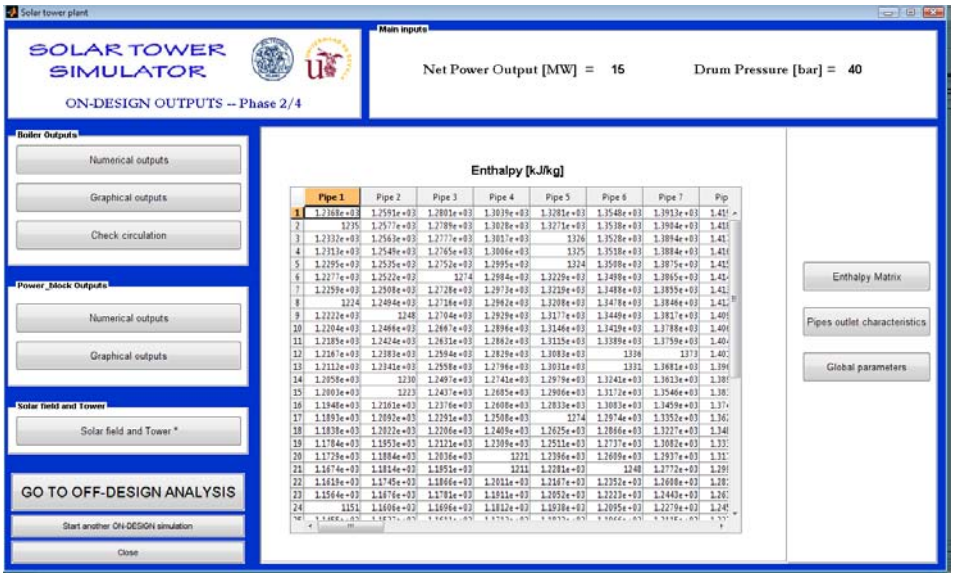

Figure 5.21:Enthalpy table

- *Total delta P of each pipe*: shows the pressure drop for each water wall pipes and could be useful to understand if a change in pipes dimensions or roughness is necessary.
- *Mass flow of each pipe*: shows the water mass flow that enters in each pipe.

- *Steam quality of each pipe*: shows the steam quality at the end of each pipe helping the user to understand if problems of pipe overheating, due to low liquid flow in the tube, can occur.
- *Steam flow of each pipe*: shows the values of steam mass flow produced by each pipe.

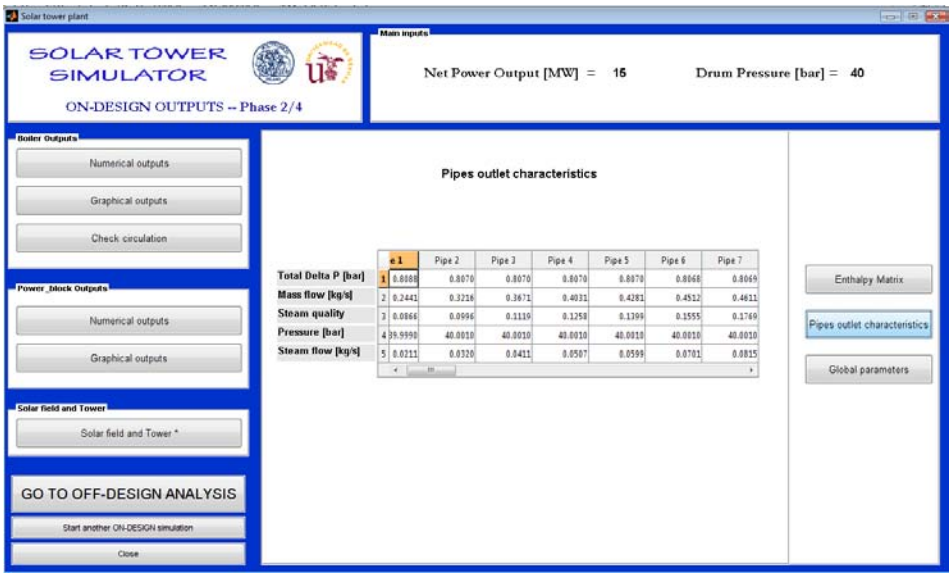

Figure 5.22:Pipes outlet characteristics

- *Total incoming thermal power*: is the total thermal power, got from the radiation map, that reaches the absorbing surface.
- *Total flow*: is the total water flow that circulates inside the boiler.
- *Steam flow*: is the total live steam flow that, from the drum, goes to the turbine.
- *Receiver surface*: is the absorbing area needed to obtain the steam flow requested by the power block.
- *Module width*: is the width of each one of the four modules.
- *Module height*: is the height of each one of the four modules.
- *Pump power*: is the power absorbed by the circulation pump/s of the boiler.
- *Steam quality*: is the average steam quality at boiler outlet.

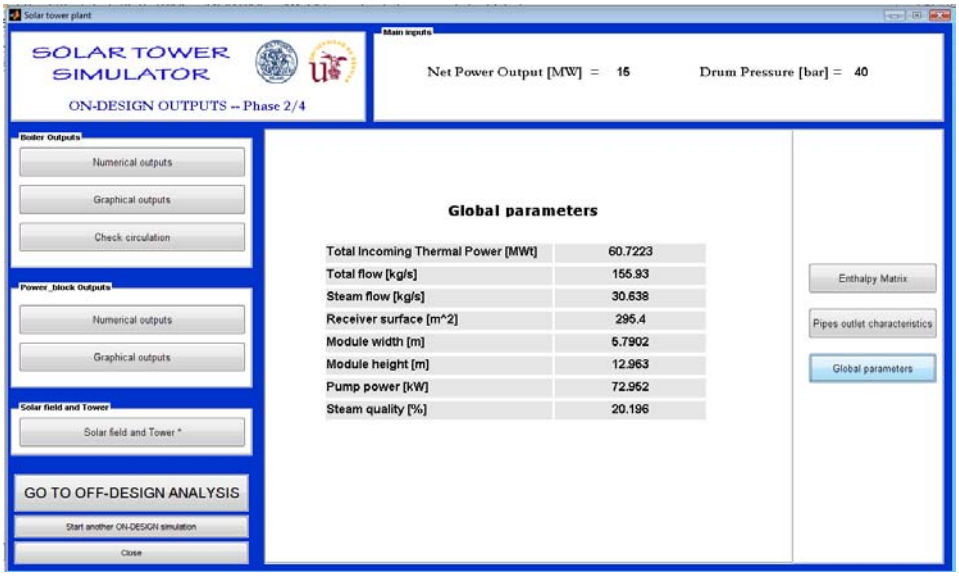

Figure 5.23:Global parameters

5.3.2 Graphical outputs

Graphical outputs, unlike numerical outputs, help the user to understand the global behavior of the boiler at a glance. All the following images are referred to a plant of 15 MW_e and 40 bar drum pressure.
The main schemes shown to the user are:

– *Water flow distribution*: by means of a bar diagram, the water flow distribution inside each pipe is shown.

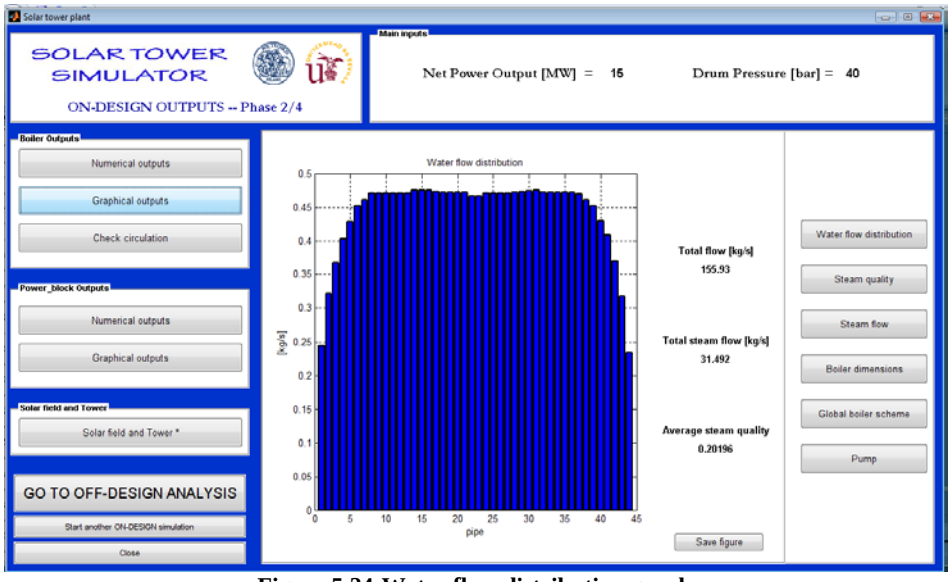

Figure 5.24:Water flow distribution graph

As seen in the Fig. 5.24, water flow in each pipe is lower for the side parts of the absorbing surface where the incident radiation is lower. This happens because the main component of the pressure drop is the gravitational one that depends on the amount of liquid flow, therefore where there is lower steam production (side parts) water flow will be lower because of the higher fraction of liquid phase. By this logic there will be more flow in the most critical parts of the boiler (where the radiation is higher) preventing the pipes from reaching dangerous temperature.

– *Steam quality*: represents the outlet steam quality for each pipe by a linear plot.

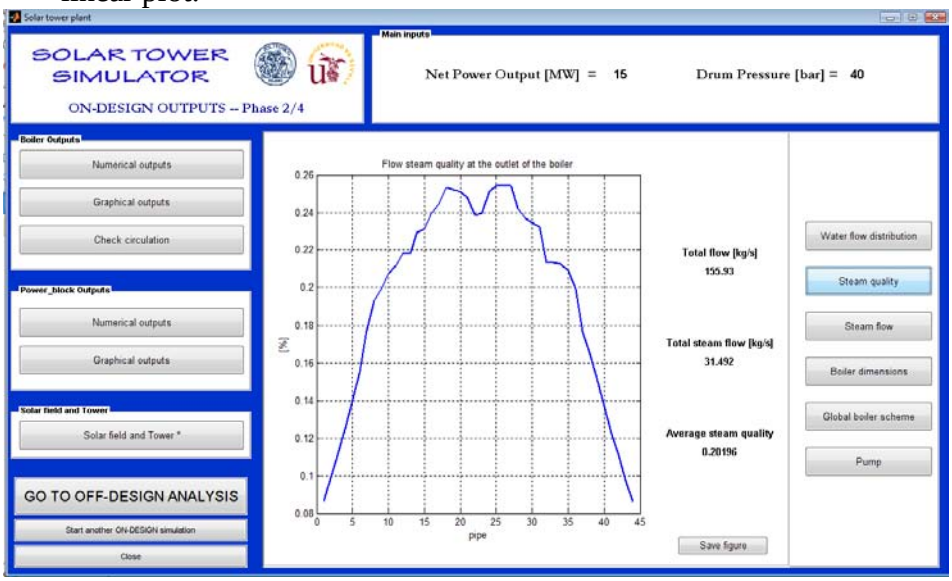

Figure 5.25:Steam quality diagram

Obviously, steam quality is higher for the central pipes where the incident radiation is bigger. The average value of the outlet steam quality is near the value imposed by the user (in this case 0.2). Looking at the vertical axis, it is immediately showed if any pipe reaches a too high steam quality that could be critical for the pipe mechanical integrity.

– *Steam flow*: shows the steam production in each pipe, highlighting the steam generation along the length of the pipe.

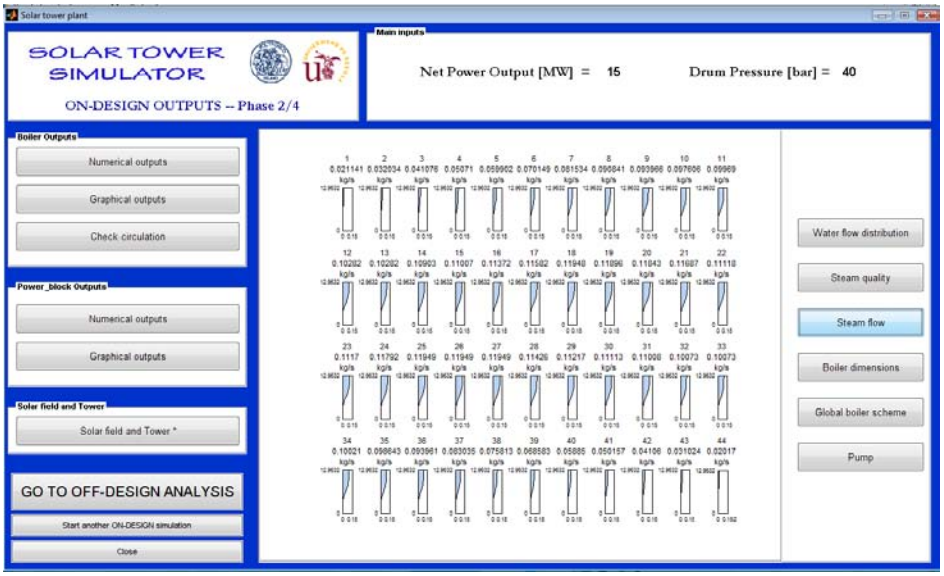

Figure 5.26: Steam flow graph

For the central pipes, where the radiation is higher, steam production is also higher and begins earlier in the pipe.

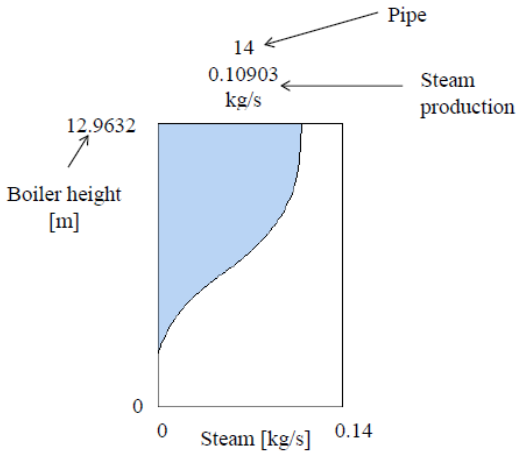

Figure 5.27: Detailed view of steam flow scheme for a pipe

– *Boiler dimensions*: shows the dimensions of a module graphically, according to the sizing calculations performed.

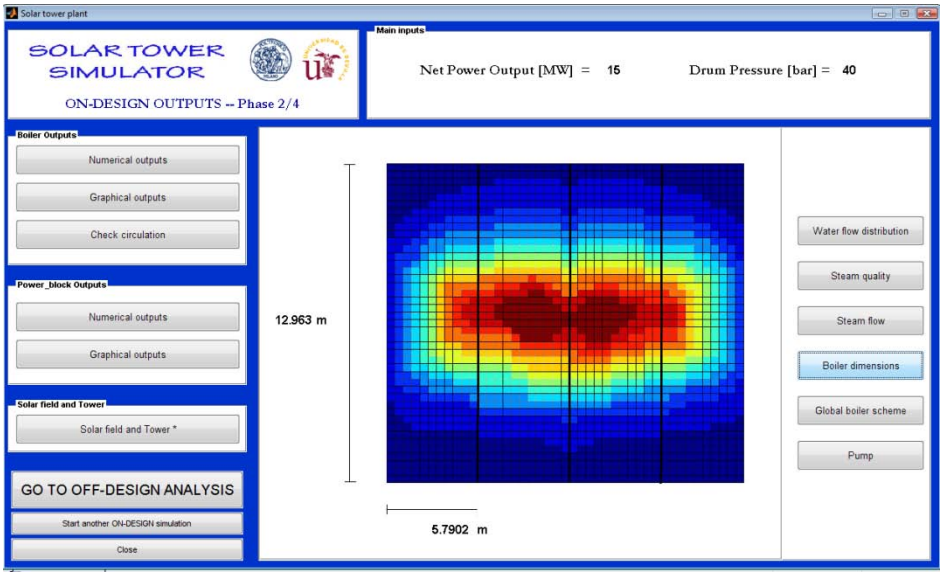

Figure 5.28:Boiler dimensions plot

– *Boiler scheme*: shows several global parameters of the boiler as:
  – Steam to power block.
  – Total water flow circulating in the boiler.
  – Water flow entering in each module.
  – Steam flow at the outlet of each module.
  – Average steam quality at the outlet of each module.
  – Incident thermal power for each module.

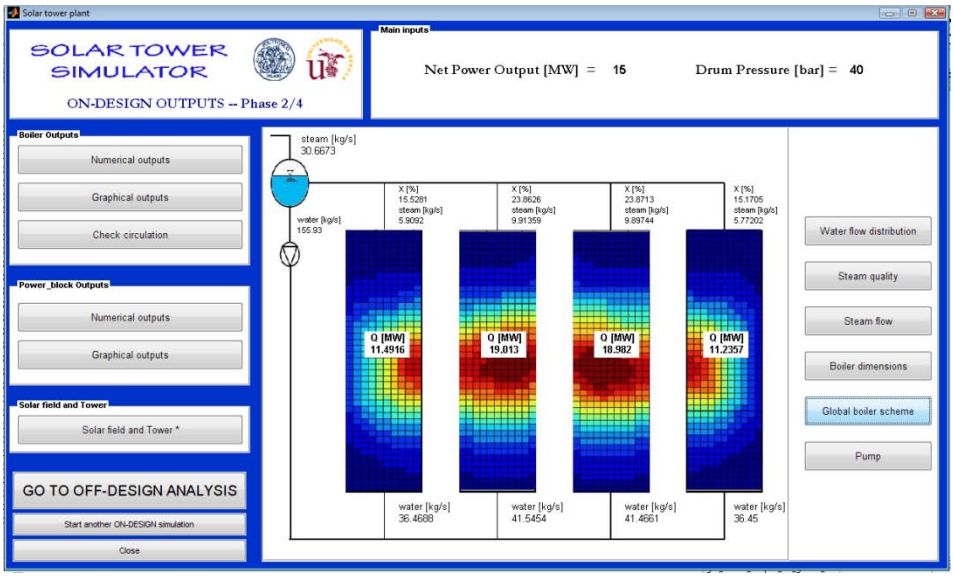

Figure 5.29:Boiler scheme

– *Pump*: shows the boiler pump characteristic curve marking the working point which is the following in on-design due to the adimensional nature of the curve:

$$\frac{H}{H_d} = 1 \tag{5.42}$$

and

$$\frac{Q}{Q_d} = 1 \tag{5.43}$$

Where $_d$ values are the on-design values.

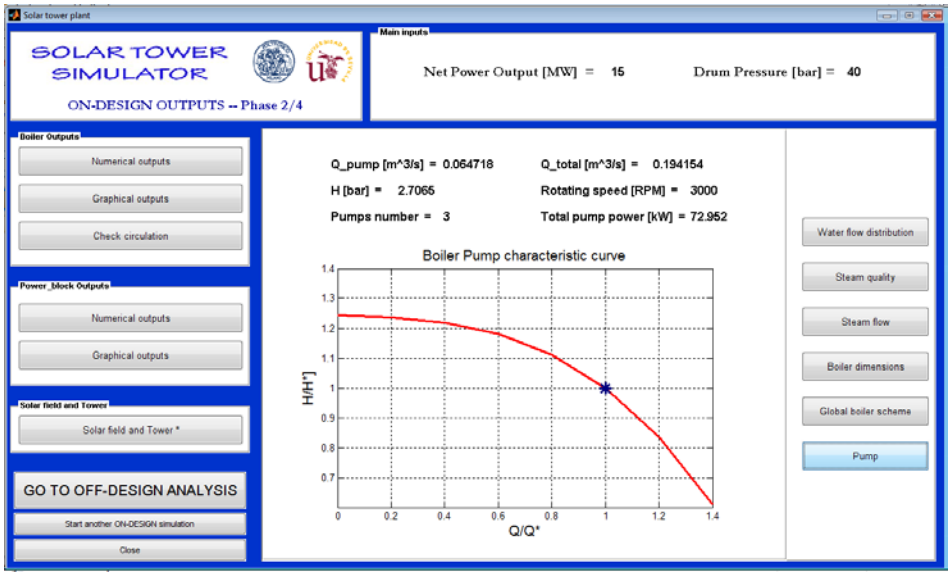

Figure 5.30:Pump graphical output

Other characteristic values of the pump/s are reported:

- *Q_pump*: volumetric flow for each pump.
- *Q_total*: total volumetric flow circulating in the boiler.
- *H*: pressure increase to the flow.
- *Rotating speed*.
- *Pumps number*.
- *Total pump power*.

5.3.3 Natural circulation check

The last aspect analyzed by the model is a simple check if natural circulation can be adopted in the boiler or not.

Normally this kind of boilers can work with natural circulation but forced circulation is preferred because it is safer and more easily manageable.
To have natural circulation, the head due to the downcomer height should be bigger than the sum of the losses between the pump and the drum:

- *ΔP lower risers*: pressure losses in lower risers circuit.
- *ΔP boiler*: pressure losses in water wall tubes.
- *ΔP upper risers*: pressure losses in upper risers circuit.
- *ΔP drum*: pressure losses due to the drum.

$$\Delta P_{tot} = \Delta P_{low\_ris} + \Delta P_{boiler} + \Delta P_{up\_ris} + \Delta P_{drum} \tag{5.44}$$

While the head available is estimated as [43]:

$$Head = 9.81496E-05 \times \frac{L}{v} \tag{5.45}$$

where:

- L: is the downcomers length [m].
- v: is the specific volume of the fluid in the downcomers circuit [kg/m^3].

If:

$$Head > \Delta P_{tot} \tag{5.46}$$

Natural circulation is possible.

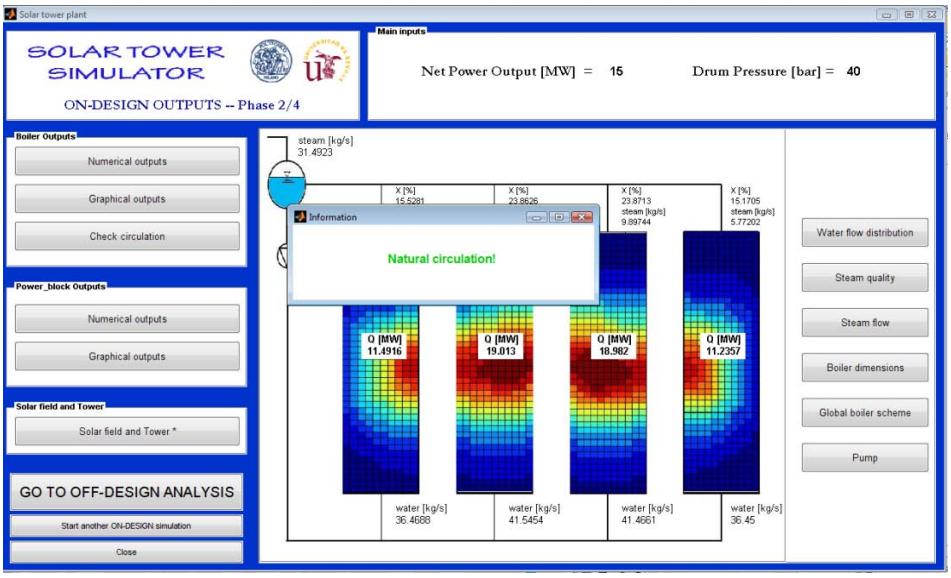

Figure 5.31:Natural circulation check

6. The Power Block

6.1 Introduction

Generally speaking, the steam cycle of a solar tower plant is not different from the one of a traditional fossil fuel plant. The steam performs a Rankine cycle, basically characterized by the pumping of water, its conversion into steam in a boiler, its expansion in a turbine and its final condensation, obtained thanks to the heat exchange with a coolant (Figure 6.1).

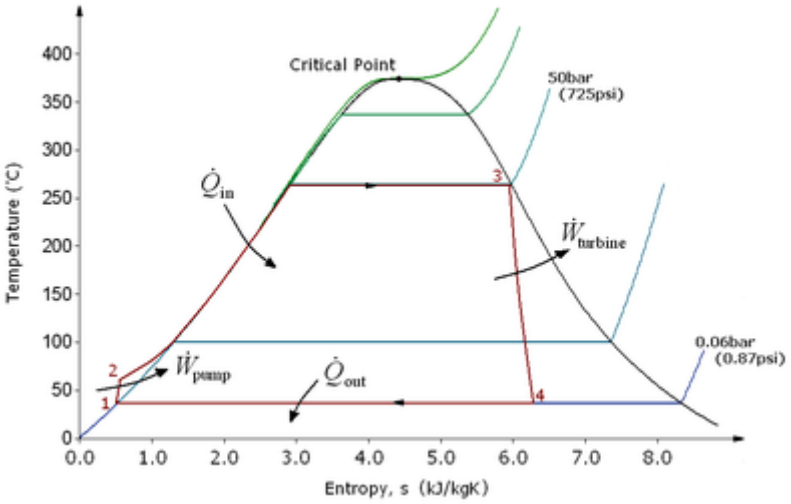

Figure 6.1: Example of Rankine cycle

On the other side, the characteristics of the cycle and so the design of the plant depend a lot on the characteristics of the steam produced.

In the case analyzed in this study, the particular technology of the boiler just described gives really specific directions on the characteristics of the whole cycle. The absence of both a super-heating and a re-heating section implies the turbine working with saturated live steam, while the low thermodynamic parameters of the live steam itself and the absence of the economizer determine the particular features of the pre-heating line.

In practice, the power block layout used as reference for the development of the model is the one of the PS10 plant. This is mainly composed by a single-case steam turbine, a vacuum condenser and four heat exchangers to pre-heat the feedwater. The pre-heating line is divided into a low-pressure section, composed

by one closed (surface) and one open (direct-contact) exchanger, and a high-pressure section, composed by two closed exchangers. The two low-pressure heaters and the first high-pressure one are fed with steam extracted from the turbine, while the last one before the boiler is fed with live steam directly coming from the turbine (Figure 6.2).

The particular features of the different components will be more deeply analyzed in the next sections.

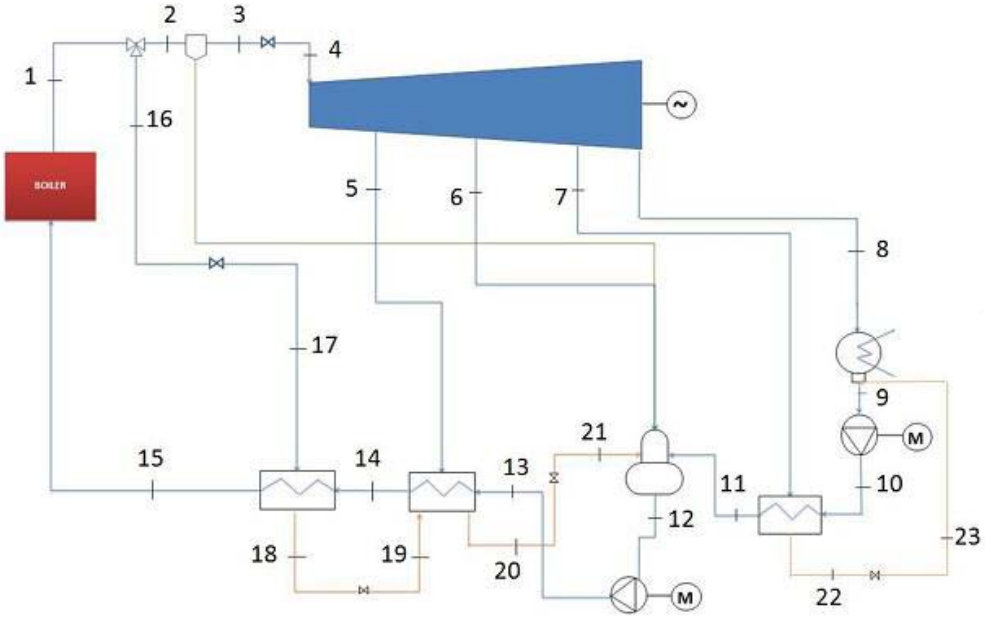

Figure 6.2: Simplified plant layout

The analysis of the cycle has been carried out with the simplifying hypotheses that all the components operate in stationary conditions, that the fluids do not experience phase changes while traveling from one component to the following and that all the steam flowing into the turbine contributes to the power production (leakages are so neglected).

Additionally, it has been assumed that water flowing out from both the condenser and the deaerator is in saturated liquid conditions ($x = 0$).

6.2 Steam Turbine

6.2.1 Design features

The design and choice of the turbine are strictly dependent on the power production and the characteristics of the steam that expands through it. In the case of conventional solar tower plants currently in operation (PS10 and PS20 typology), the rated net power output can be considered to lay within the 5 – 50 MW range and the boiler produces saturated steam in a pressure range between 10 and 100 bar, which corresponds to a temperature range of 180 – 310 °C. These are also the ranges for which the on-design model has been built.

In all these cases, the turbine works with saturated steam at the inlet and this requires a particular attention on its design.

During its expansion at the turbine, the steam flow crosses the saturation line, entering the wet region and partially condensing into tiny droplets of water [51]. Actually, due to the high steam expansion speed, this condensation does not take place just at the saturation line but at a lower pressure at a region referred to as "Wilson line". The steam between the saturation and the Wilson line is in the so-called super-cooled state [63].

The steam expansion process in wet turbine stages is extremely complex. Considering that in real inlet stage conditions humidity is characterized by different concentration and "dispersion rate" while water droplets move with both speed and direction different from the steam ones, a scheme to describe humid steam movement is, in fact, impossible to outline.

The general characteristics of humid steam flow in turbine stages can however be so summarized:

a) during the expansion, steam condensation is "delayed", with a different super-cooling both in longitudinal and cross sections and along the blade height.

b) at stage inlet, steam can contain water droplets with different sizes and directions; inside the channel new drops can rise and drops evaporation, destruction and transformation in water film take place.

c) droplets trajectories are generally deviated with respect to steam mean streamflow; unlike the steam which glides on to the moving blades, the water droplets impinge on the leading edge of them.

d) on blade surface and channel walls a water film is created, which can have different shape and thickness.

e) inside the channel, friction and heat and mass transfer between the two phases

take place.

As a result of this complex process, in comparison with a super-heated steam flux the parameters at the stage outlet change. In particular, flow speed and angles and pressure distribution change.

Research activities have demonstrated that energy losses in the steam flow across a turbine stage increase with wetness. This is mostly due to:

a) friction in water film and in steam and drops boundary layer

b) steam flow energy loss due to acceleration of liquid particles

c) friction between the two phases

d) increase of blade wake, film fragmentation at trailing edge and flux turbulence

e) secondary flux intensification on the channel walls.

A quantification of these losses is given by the Bauman Rule, which states that the loss of "dry stage" efficiency is roughly one per cent for every one per cent of wetness at the particular stage. [51]

Moreover, it has to be taken into account that the mechanical impact of the water droplets on the blades produces damages and erosion of the blades themselves.

These problems are crucial and, apart from the case of solar tower plants, are mostly typical of nuclear plants working with saturated steam [52].

To face them, the turbines are equipped with appropriate devices that allow for moisture control and removal such as grooves on the low-pressure turbine blades that channel moisture to extraction ports [50].

Another specific feature of these applications, as also of small nuclear reactors (used, for instance, in nuclear marine propulsion), is the high rotating speed of the turbine (between 5000 and 12000 rpm), which drives the electric generator through a gearbox/speed reducer.

6.2.2 Thermodynamic analysis

Live steam conditions at turbine inlet are immediately known when drum pressure is selected, default values of pressure and temperature being

respectively 40 bar and 250°C, which are representative of the PS10 design conditions. Enthalpy and entropy can be defined through the saturated steam tables.

On the other side, once studied the characteristics of the condenser (see paragraph 6.4), also the steam outlet pressure and temperature are identified.

It is well known that the performances of the turbine are defined thanks to the isentropic efficiency, defined as

$$\eta_{is,turbine} = \frac{(h_{steam,in} - h_{steam,out})}{(h_{steam,in} - h_{steam,out\ S})} \tag{6.1}$$

where $h_{steam,out\ S}$ represents the enthalpy of steam that has passed through an isentropic expansion from the inlet to the outlet pressure, which can be expressed as:

$$h_{steam,out\ S} = h\,(P_{steam,out}, s_{steam,in}) \tag{6.2}$$

It is worth noting that in a multistage turbine the exit kinetic energy from one stage is used in the next one; therefore, the most representative turbine and stage isentropic efficiency is the total-to-total efficiency, defined as

$$\eta_{tt} = \frac{(h_{total\ steam,in} - h_{total\ steam,out})}{(h_{total\ steam,in} - h_{total\ steam,out\ S})} \tag{6.3}$$

However, assuming that in an axial turbine the difference between inlet and outlet kinetic energies is small, definitions of $\eta_{is,turbine}$ and η_{tt} coincide [56].

The isentropic efficiency could be calculated thanks to the method presented by Spencer, Cotton and Cannon (1974). This involves consideration of the following parameters [50]:

- Total to static efficiency

- Exhaust loss

- Packing and valve steam leakage flows

- Mechanical losses

- Generator losses.

Due to the complexity of this method and in order to have a better control of the simulation by the user, it has been preferred to leave up to him the possibility to

introduce the isentropic efficiency of the turbine. The default value is 0.82, taken from the case-study PS10 plant. Nevertheless, it is worth noting that an interesting development of this project would be evaluating the performance of the turbine using the just mentioned methodology.

From the definition of isentropic efficiency, it is so possible to calculate outlet enthalpy and entropy, which complete the description of turbine exhaust. The expansion line of the turbine can therefore be drawn.

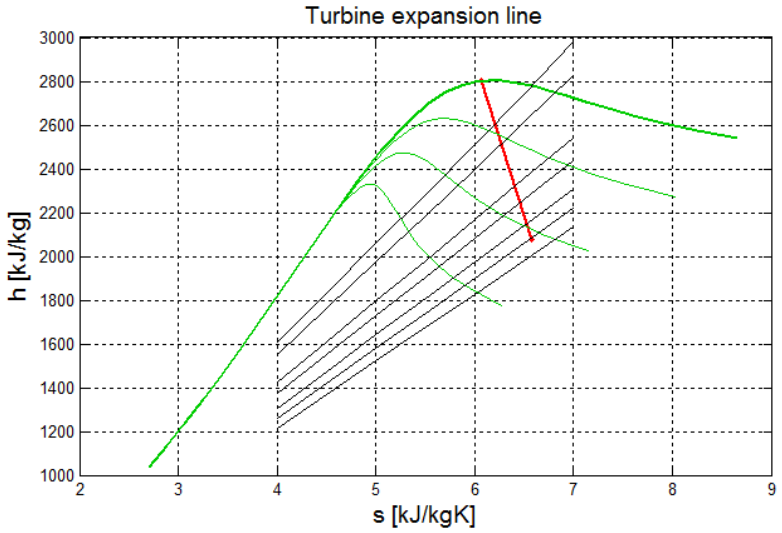

Figure 6.3: Turbine expansion line

Proceeding further, the expansion line lets us to identify the steam properties at the extractions.

As already mentioned, indeed, the pre-heating line of the plant is composed by three closed exchangers and one deareator, fed with steam extracted from the turbine (with the exception of the last HP feedwater heater). Extraction pressures are known from the study of the exchangers, so we can define all their other properties by matching them with the expansion line. The representation of three points characterizing the extractions for the example of a 15 MW / 40 bar plant is reported below (Figure 6.4).

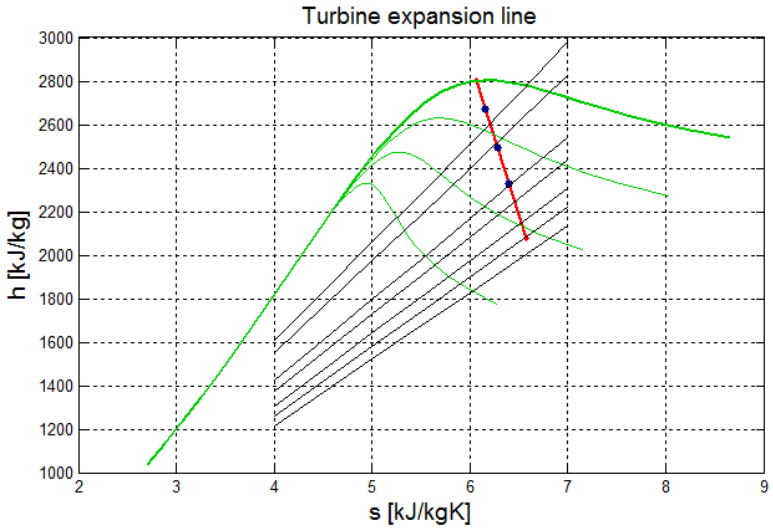

Figure 6.4: Steam extractions points

From the point of view of the code, the above calculations are performed by a small proper function named *expansion_line.* This function attempts values of enthalpy for the three extractions, calculates the correspondent values of entropy thanks to steam properties libraries and then imposes that these two values fit the expansion line already known.

Once the properties of the extractions are calculated, it is also possible to calculate the isentropic efficiency of each “stage” (each part of the turbine within one extraction and the following one). The results show that efficiency increases from first to last stage.

One last remark that can be made with regards to the turbine behavior is about the relevance of mechanical losses. These are above all function of the rotating speed. The main causes of mechanical losses are friction on bearings and, in some cases, in a gearbox for the coupling with electric generator and auxiliary systems drive like, for instance, oil pumps [52]. All these contributions decrease the power output and have so to be considered. In the model they have been summarized in a mechanical efficiency that presents a default value of 0.98.

6.3 Electrical generator

The most commonly used electrical generator is a synchronous type that produces a balanced three-phase power [50]. Not pretending to enter in a

detailed description of the device, its functioning has been included into the model through the definition of the two related losses components.

- Mechanical losses (bearing losses and losses related to windage and friction): these depend on weight and rotating speed. The first aspect is directly related with the rated power of the plant, as long as the machine is not excessively derated in which case mechanical losses would be greater than expected. The second aspect should be taken into account when shifting from 50 to 60 Hz in the model.
- Electrical losses: these depend on the apparent power produced by the generator and are calculated with polynomials that fit characteristic curves typical of electrical generators with similar rated output

It has to be noticed that, in some cases, the literature include both the turbine's and generator's mechanical losses in a single value of mechanical efficiency, while the generator's efficiency only refers to the electrical losses contribution [50]. In our case it has been preferred to keep the turbine and the generator efficiency separated, to permit a better comprehension of the two components.

In practice, once defined by the user the nominal power required, the model obtains the values of power losses directly from characteristic curves available both for mechanical and for electrical losses.

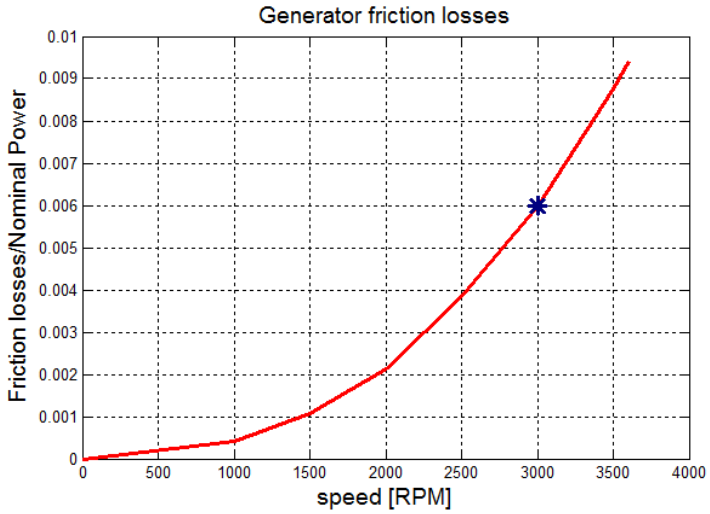

Figure 6.5: Generator mechanical losses

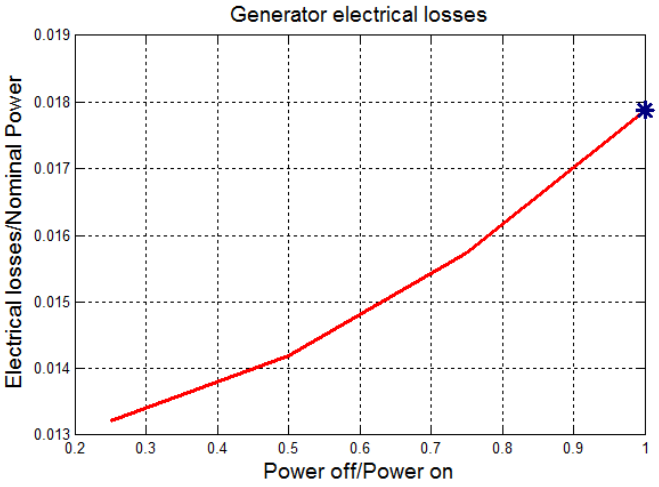

Figure 6.6: Generator electrical losses

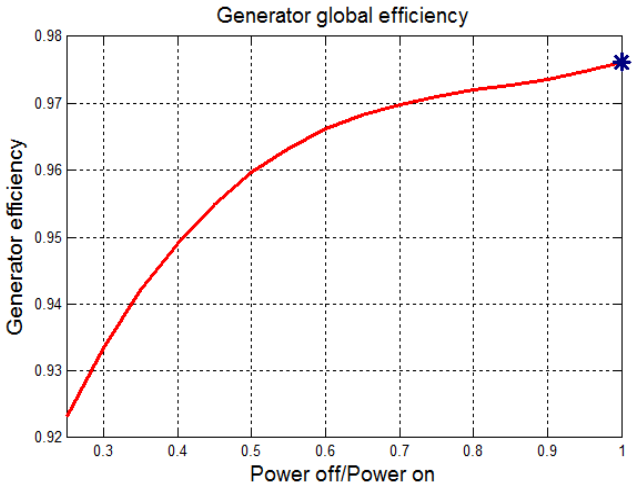

Figure 6.7: Generator global efficiency

The generator's performances in the case study plant are reported in the table below.

Table 6.1: Generator's performances

Gross Power produced by the turbine [kW]	16447
Mechanical losses [kW]	99.6
Electrical losses [kW]	286.9
Global generator efficiency [%]	97.54

6.4 Condenser

6.4.1 Design features

The selection of the condenser is very important, considering that its characteristics affect in several ways the behavior of the plant, condensing pressure and auxiliary power consumption for instance. A common choice for conventional power plants of similar power output is a water cooled condenser with forced draft cooling towers, even if air cooled condenser are becoming very popular.

This kind of device, indeed, is characterized by a quite high overall heat transfer coefficient and is so able to keep a low condensing pressure with small footprint and costs. Moreover, water temperature is not so remarkably affected by the external weather and climate conditions, going in this way to guarantee a condensing pressure always included in a small range.

In this case, however, a water cooled condenser could not be the optimal choice. Due to their nature, CSP plants require large sites with a high amount of direct solar radiation and this is often found in arid regions where water resources are scarce and their use, even if possible, is costly. Moreover, in certain wind conditions, the presence of the plume coming out from the cooling tower might represent a problem for the solar field; steam absorbs a relevant amount of solar radiation, therefore decreasing both the energy reaching the heliostats from the sun and the one reflected from the heliostats and directed to the receiver. Part of the plume condensation might also cause the formation of a water film on the mirrors surface, decreasing its reflecting capability.

To prevent these problems an air-cooled condenser (ACC) can be used; these are used in small power plants since the 1930s and in case of particularly arid regions, are adopted also for big plants, as happens in Matimba Power Plant, in South Africa, the world’s largest direct air-cooled power plant (6 x 665 MWe). This solution is at present the “default” one for solar plants.

The most common air cooled condensers are composed by arrays of bundles of finned tubes sloped at some angle up to 60° with the horizontal plane. This configuration, studied from Conradie and Kroger [55] and commonly known as "A-frame", allows to

- drain condensate effectively

- reduce the length of steam distribution piping

- minimize the condenser footprint (required ground surface area).

The forced flow of cooling air is draught by axial flow fans and a windwall is sometimes provided to reduce recirculation of the hot air plume (Figure 6.8).

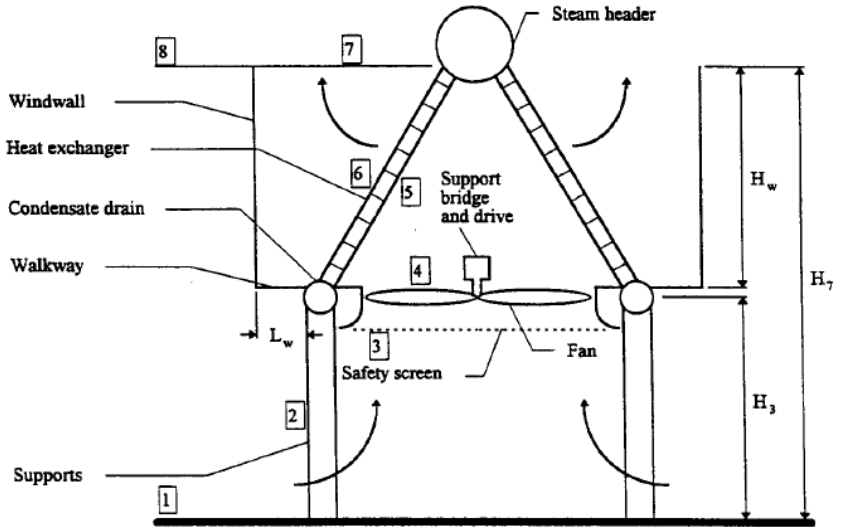

Figure 6.8: Typical A-frame ACC

The condenser can be considered to be composed by a certain number of cells, each of them composed by one fan and by the corresponding finned tubes. The reference/default cell used in the model is taken from [64] and its main characteristics are described in the following table.

Table 6.2: Condenser reference cell characteristics

Volumetric air flow rate [m3/s]	288.8
Fan Power [kW]	48.2

6.4.2 Thermodynamic analysis

The main issue in the analysis of the condenser is to determine the steam condensing pressure and the number of cells needed to evacuate the heat rejected by the changing-phase steam. The first parameter, indeed, remarkably affects the behavior of the steam turbine, while the second determines the auxiliary power consumption of the plant and, hence, its net power output.

To start modeling the condenser behavior, three first input data are necessary:

- Ambient temperature, $T_{air,amb}$ [°C]

- Air temperature increase at ACC, $\Delta T_{air,ACC}$ [°C]

- Terminal temperature difference at ACC, TTD_{ACC} [°C]

These data can be inserted by the user, but their default values are respectively 30 °C, 10 °C and 5 °C. It is worth noting that ISO standards would consider a 15°C (288 K) ambient temperature but, since the considered plants are installed in warm regions, is considered more realistic to choose 30 °C. Knowing these, the condenser temperature and pressure can be defined:

$$T_{cond} = T_{air,amb} + \Delta T_{air,ACC} + TTD_{ACC} \quad (6.4)$$

$$P_{cond} = P_{sat}(T_{cond}) \quad (6.5)$$

where:

T_{cond} = condenser temperature [K]

P_{cond} = condenser pressure [bar].

Working in this way, it becomes important to verify if the calculated condenser pressure is acceptable from the point of view of turbine exhaust humidity, considering that the lower the back pressure, the greater the wetness of steam at this point. As already said, the steam turbine is properly designed to work with saturated steam at the inlet, that's to say in wet conditions for the whole

expansion. By the other side, if the steam quality decreases, the isentropic efficiency of the turbine decreases too. It is generally a good approach to impose a lower limit to the steam quality at the outlet of the last stage of the turbine, to prevent an excessive decay of performances and damage to the blades; a common minimum value is 0.75.

The steam quality is completely defined by the condenser pressure and the enthalpy at the outlet of the turbine:

$$x_{outlet\ \ turbine} = x\left(h_{steam\ ,out}, P_{cond}\right) \tag{6.6}$$

and $h_{steam\ ,out}$ can be calculated from the definitions of $h_{steam\ ,out\ S}$ and of isentropic efficiency

$$h_{steam\ .out} = h_{steam\ ,in} - \eta_{is,turbine} * \left(h_{steam\ ,in} - h_{steam\ ,out\ S}\right) \tag{6.7}$$

where:

- $\eta_{is,turbine}$ = turbine isentropic efficiency

- $h_{steam\ ,in}$ = inlet turbine enthalpy [kJ/kg]

- $s_{steam\ ,in}$ = inlet turbine entropy [kJ/kgK]

Once defined the inlet turbine conditions and the isentropic efficiency of the turbine, in practice the exhaust steam quality depends only on condenser pressure. If the steam quality corresponding to this pressure calculated from the input data of the ACC is higher than a lower limit defined by the user, it is accepted. If not, condenser pressure is increased until humidity becomes acceptable.

This control and the possible corrections are carried on by a properly written routine called *turbine_outlet* that calculates the correct condenser pressure and outlet steam quality.

The calculation of the number of cells is based on the volumetric flow of air needed to reject the latent heat of condensing steam. This value can be easily calculated through an energy balance at the condenser:

$$Q_{cond} = \dot{m}_{steam} \cdot \left(h_{steam\ ,in} - h_{water\ ,out}\right) \tag{6.8}$$

$$\dot{m}_{air} = \frac{Q_{cond}}{c_{p,air} \cdot \Delta T_{air\ ,ACC}} \tag{6.9}$$

$$\dot{V}_{air} = \frac{\dot{m}_{air}}{\rho_{air,mean}} \tag{6.10}$$

where the mean air temperature and density are

$$T_{air,mean} = \frac{T_{air,amb} + T_{air,out}}{2} \tag{6.11}$$

$$\rho_{air,mean} = \frac{P_{amb}}{R_{air} T_{air,mean}} \tag{6.12}$$

Relating the required volume flow rate with that characteristic of a single condenser cell, it is immediate to define the number of cells needed.

Obviously, this flow ratio is rarely an integer value, and the number of fans is therefore defined considering the closest integer number (done with the function *round* of Matlab).

$$N_{ACC\ cells} = round\left(\frac{\dot{V}_{air}}{\dot{V}_{air,reference\ \ cell}}\right) \tag{6.14}$$

The obvious impossibility to have a non-integer number of fans implies a difference between the mass flow calculated previously and the new one, related to the real number of cells installed; this modifies the parameters of the condenser. Different approaches are possible; in this case it has been chosen to consider that the change of mass flow will affect only the temperature of air leaving the condenser. This way, we are practically neglecting the effect on condenser pressure for on-design calculations, avoiding other iterative processes and reducing the computational time significantly. At the same time, however, we are including in the calculation the effect of condenser efficiency, which will be re-used in off-design analysis.

The analysis of condenser performance relies on the ε-NTU approach, as in the case of feedwater heaters. For a detailed description of the method we refer to paragraph 6.5.2. Effectiveness and global heat transfer coefficient UA of the condenser are defined by the formulae:

$$\varepsilon_{cond} = \frac{T_{air,out} - T_{air,in}}{T_{cond} - T_{air,in}} \tag{6.15}$$

$$C_{min,cond} = \dot{m}_{air} * c_{p,air} \tag{6.16}$$

$$NTU_{cond} = -\ln(1 - \varepsilon_{cond}) \tag{6.17}$$

$$UA_{cond} = C_{min,cond} * NTU_{cond} \tag{6.18}$$

Considering the "default" conditions in a 15MW/40 bar plant, the condenser is characterized by the following data:

Table 6.3: On design condenser characteristics

$\dot{V}_{air}$ **[m3/s]**	3176.8
N_{cells}	11
$\dot{W}_{abs,cond}$ **[kW]**	530.2
$T_{air,out}$ **[°C]**	40.2
ε_{cond}	0.682
NTU_{cond}	1.144
UA_{cond}	4185.8

6.5 Feedwater heaters

6.5.1 General and design features

As well known, increasing the average temperature of heat addition increases the cycle efficiency. This can be accomplished with a reheat but also by increasing the temperature of feedwater entering the boiler.

Extracting a portion of the partially expanded steam from the turbine and directing it to a heat exchanger that heats the feedwater to the boiler, heat from within the cycle is exploited to elevate feedwater temperature. The average temperature of heat addition is hence increased, because the lowest temperature heat addition to the cycle is avoided.

The greater the number of feedwater heaters used, the higher cycle efficiency. However, each additional heater results in lower incremental heat rate improvement and considering increasing capital costs and limitations in turbine physical arrangement, the economic benefit of additional heaters is limited. The actual number used for a particular plant will be so decided on thermoeconomic principles; the typical configuration for a medium-size plant incorporates 5 -7 feedwater heaters [50].

In the case of a DSG solar tower plant with saturated steam, a pre-heating line is adopted, but the low pressure and temperature of live steam brings to adopt a low numbers of feedwater heaters. Hence, only three steam extractions are adopted, because the low enthalpy at turbine inlet makes it uneconomical to incorporate more extractions.

An additional preheater, that uses live steam, is introduced to increase feedwater temperature up to around five degrees below its corresponding saturation temperature (though the value of this "approach subcooling" can be changed by the user). This unconventional preheater is adopted because the boiler is designed to work as a pure closed loop evaporator, so the feedwater must be as close to saturation as possible. This solution is typical of solar tower plants and emerges from the difficult integration of an economizer into the solar receiver, especially at off-design operation when important water subcooling might be found at economizer exit.

In practice, the pre-heating line is so composed by two low-pressure (LP) feedwater heaters, one shell and tube and one direct-contact that works also as deareator (see paragraph 6.6), and two high-pressure (HP) feedwater heaters, both shell and tube.

The shell-and-tube is a very common configuration of heat exchangers. The simplest form involves single tube and shell passes with the feedwater in the tube side and the extraction steam and drains from higher pressure heaters in the shell side.

In Figure 6.9 the internal baffles can be seen, installed to induce turbulence and a cross flow velocity component in order to increase the convection coefficient of the shell-side fluid [45].

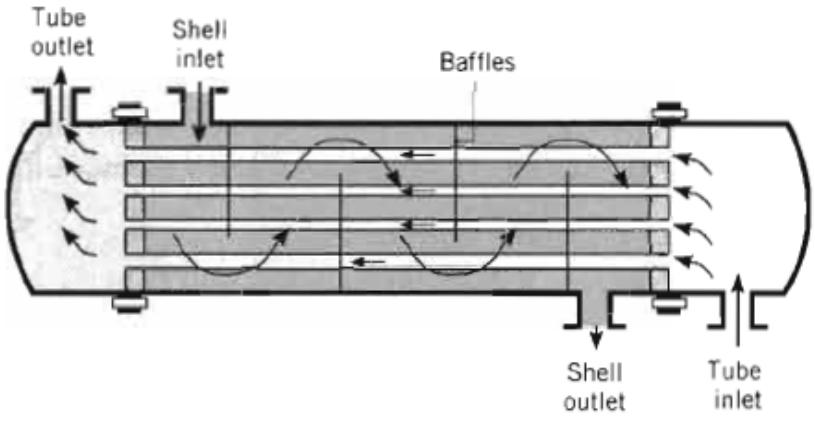

Figure 6.9: Example of shell-and-tube heat exchanger

Thermodynamically, it is often advantageous if the feedwater outlet temperature is raised above the steam saturation temperature or the drains cooled below the steam saturation temperature. In the case analyzed, the steam coming from the turbine is not super-heated and this advantage can be so obtained only with a drain sub-cooling.

Figure 6.10 illustrates a typical two-zone feedwater heater constructed with both condensing and sub-cooling zones. In this design, the tubes containing the inlet and coldest feedwater are enclosed in such a manner that the drains must pass over these tubes before exiting. This zone now becomes a water-to-water heat exchanger, and the outlet drain temperature can approach the inlet feedwater temperature [50].

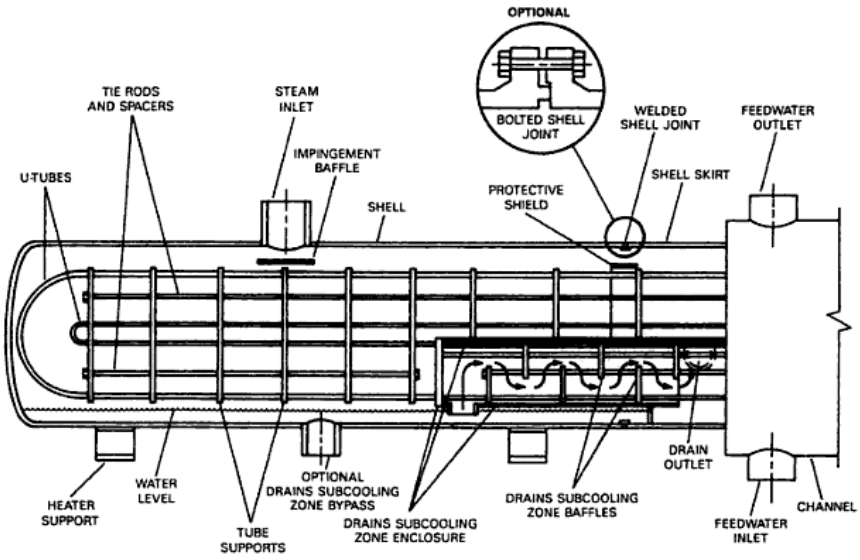

Figure 6.10: Example of condensing and subcooling shell-and-tube heat exchanger

6.5.2 Thermodynamic analysis

The model of the pre-heating line in nominal conditions is quite simple and it's based on the following assumptions, validated in literature and through the study of similar plants:

Table 6.4: Pre-heaters assumptions

TTD [°C]	5
DCA [°C]	10
$\Delta P_{fwh,steam}$ **[%]**	0%
$\Delta P_{fwh,water}$ **[%]**	5%

TTD stands for Terminal Temperature Difference -that is to say the difference between the temperature of water leaving the exchanger and steam entering it-

and DCA is the Drain Cooler Approach -that is to say the difference between the temperature of the drain and the temperature of the inlet water-.

$\Delta P_{fwh,steam}$ and $\Delta P_{fwh,water}$ are respectively the pressure losses of steam and water passing through the exchanger, expressed as a percentage of each inlet pressure.

Another relevant assumption is made on the steam pressure losses along the extraction line; i.e. from turbine extraction port and preheater.

$\Delta P_{extraction,steam}$ [%]	7.5 %

As for practically all the assumptions made, the values presented are only the "default" values and they can be easily changed by the user.

Having defined these parameters, the typical approach that equally divides the total temperature rise in the preheating section amongst all the feedwater heaters is adopted, as proposed by Haywood [54].

The total temperature rise is known, because condenser temperature and final feedwater temperature are known, the latter one thanks to TTD for the live steam extraction.

$$T_{in\ boiler\ ,water} = T_{live\ steam\ extraction} - TTD \tag{6.19}$$

$$\Delta T_{total\ ,fwh} = T_{in\ boiler\ ,water} - T_{cond} \tag{6.20}$$

$$\Delta T_{fwh} = \frac{\Delta T_{total\ ,fwh}}{N_{fwhs}} \tag{6.21}$$

where N_{fwhs} is the number of feedwater heaters.

To allow a simpler and faster modeling it has been chosen to neglect in this calculus the temperature rise in the pumps.

For the case study plant, the model describes the pre-heating line as shown in Figure 6.11.

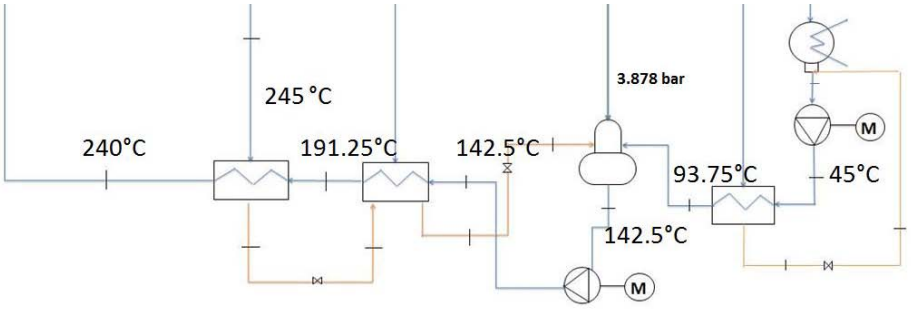

Figure 6.11: Pre-heating line scheme

It has to be noticed that working in this way, the pressure at the deareator is not a datum, but a result. The temperature of the feedwater going out from the deaerator, is indeed fixed by the just calculated ΔT_{fwh} and considering that water flows out as saturated liquid, the deareator pressure is fixed too. This approach is acceptable till this pressure value stays below an upper limit, commonly considered as 5 bar. Over this limit, the design of the deareator walls becomes critical and the cost rapidly increases.

To manage this problem, the model considers the Haywood approach till the deareator pressure is acceptable, and fixes instead 5 bar when the value would result too high. In this second case, the deareator temperature becomes fixed and the global ΔT is sub-divided differently in the LP and HP lines.

$$\Delta T_{fwh,LP} = \frac{T_{out\ \ deareator\ \ ,water\ } - T_{cond}}{N_{fwhs,LP}} \tag{6.22}$$

$$\Delta T_{fwh,HP} = \frac{T_{in\ boiler\ ,water\ } - T_{out\ \ deareator\ \ ,water\ }}{N_{fwhs,HP}} \tag{6.23}$$

Knowing the feedwater temperature rise in each pre-heater, all the temperatures are known. The above defined TTD and DCA allow then to calculate temperature and pressure of steam, first at the inlet to the exchanger and then at the extraction on the turbine itself.

$$T_{in\ fwh,steam} = T_{out\ fwh,water} + TTD \tag{6.24}$$

$$P_{in\ fwh,steam} = P_{sat}\left(T_{in\ fwh,steam}\right) \tag{6.25}$$

$$P_{extraction\ \ ,steam} = P_{in\ fwh,steam} * \left(1 + \Delta P_{extraction\ \ ,steam}\right) \tag{6.26}$$

$$T_{out\ fwh,drain} = T_{in\ fwh,water} + DCA \tag{6.27}$$

The second equation can be used without problems considering that the turbine works with saturated steam at the inlet section and therefore each extraction will certainly not be composed by super-heated steam.

Having defined all the temperatures, the behavior of the exchangers is completely described and the characteristic heat transfer diagrams can be drawn (Figure 6.12).

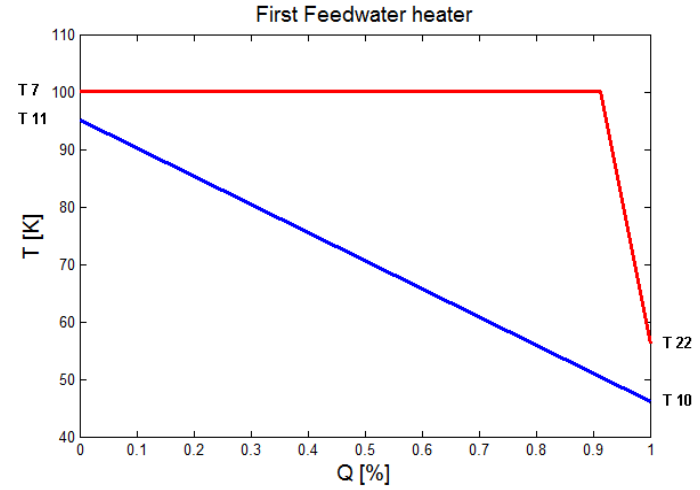

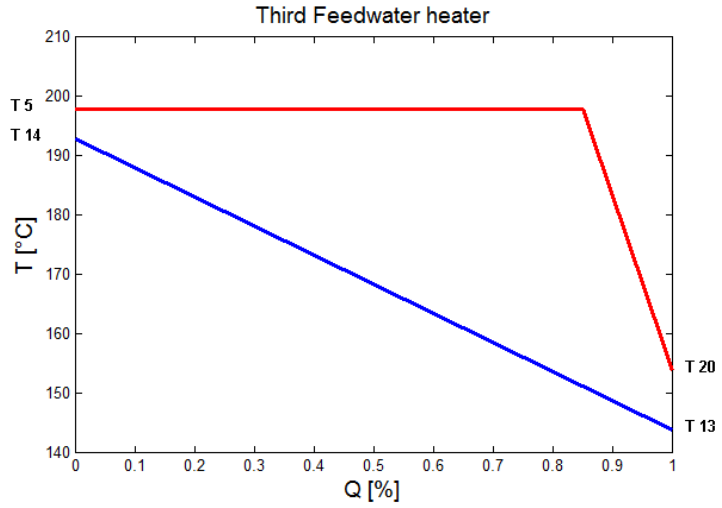

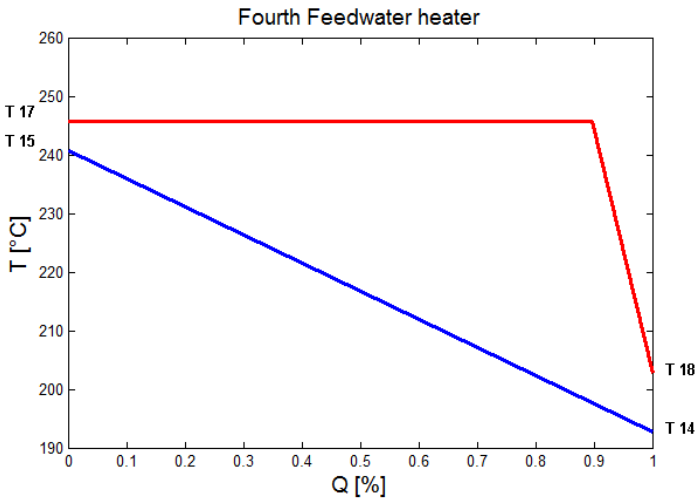

Figure 6.12: FWHs T-Q diagrams

It results interesting and moreover useful for the future off-design analysis to study more in detail the performances of these components.

To do that, the commonly used *Logarithmic Mean Temperature Difference* (LMTD) method could be used. But considering that in off-design conditions the thermodynamic properties of the fluids will not be totally known and that in this case the LMTD method requires a cumbersome iterative procedure, it has been preferred to use an alternative approach, that is to say the *effectiveness*-NTU method [45].

Let us consider a counter-flow heat exchanger; it can be described by the following diagram:

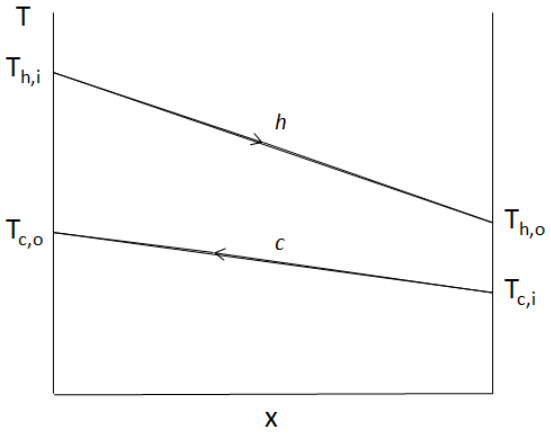

Figure 6.13: T-x diagram for a general counterflow exchanger

where *h* stands for *hot fluid*, *c* for *cold fluid*, *i* for *in* and *o* for *out*.

The hot and cold fluid heat capacity rates are defined as:

$$C_h = \dot{m}_h c_{p,h} \tag{6.28}$$

$$C_c = \dot{m}_c c_{p,c} \tag{6.29}$$

The first step to define the effectiveness of the heat exchanger is to determine the maximum possible heat transfer rate, q_{max} . This is the heat transfer rate that could, in principle, be achieved in a counterflow heat exchanger of infinite length. In such an exchanger, one of the fluid would experience the maximum possible temperature difference, $(T_{h,i} - T_{c,i})$. It's easy to demonstrate that q_{max} is determined by the fluid with the smallest heat capacity rate.

$$q_{max} = C_{min}\left(T_{h,i} - T_{c,i}\right) \tag{6.30}$$

The effectiveness, ε, can be now defined as the ratio of the actual heat transfer rate to the maximum possible heat transfer rate.

$$\varepsilon = \frac{q}{q_{max}} \tag{6.31}$$

or

$$\varepsilon = \frac{C_h(T_{h,i} - T_{h,o})}{C_{min}\,(T_{h,i} - T_{c,i})} = \frac{C_c(T_{c,o} - T_{c,i})}{C_{min}\,(T_{h,i} - T_{c,i})} \tag{6.32}$$

Given its geometry, it can be shown that for any heat exchanger:

$$\varepsilon = f\left(NTU, \frac{C_{min}}{C_{max}}, layout\right) \tag{6.33}$$

NTU is the number of transfer units, a dimensionless parameter widely used for heat exchanger analysis and defined as:

$$NTU = \frac{UA}{C_{min}} \tag{6.34}$$

where

U = overall heat transfer coefficient [W/m^{2}K]

A = heat transfer surface [m^2]

The overall heat transfer coefficient for a tubular heat exchanger is defined by the summation of the inverse thermal resistances.

$$\frac{1}{UA} = \frac{1}{h_{inner}\, A_{inner}} + \frac{R_{fou,inner}}{A_{inner}} + \frac{\ln(D_{outer}/D_{inner})}{2\pi kL} + \frac{R_{fou,outer}}{A_{outer}} + \frac{1}{h_{outer}\, A_{outer}} \tag{6.35}$$

where:

h = convective heat transfer coefficient [W/m^{2}K]

R_{fou} = fouling factor [m^{2}K/W]

D = pipe diameter [m]

k = thermal conductivity of the pipe material [W/mK]

L = exchanger length [m]

The relation between ε and NTU depends on the type and geometry of the heat exchanger and several expressions have been developed and are available in literature. The ratio C_{min}/C_{max} is often referred as *heat capacity ratio, C_r*.

It has to be noticed that the relations

$$\varepsilon = f\left(NTU, \frac{C_{min}}{C_{max}}\right) \tag{6.36}$$

can be clearly inverted, becoming

$$NTU = f\left(\varepsilon, \frac{C_{min}}{C_{max}}\right) \tag{6.37}$$

In the case of a solar plant, feedwater heaters are divided internally in two zones, namely condensing and subcooling. Each zone is characterized by a different heat capacity ratio and this involves the choice of different correlations.

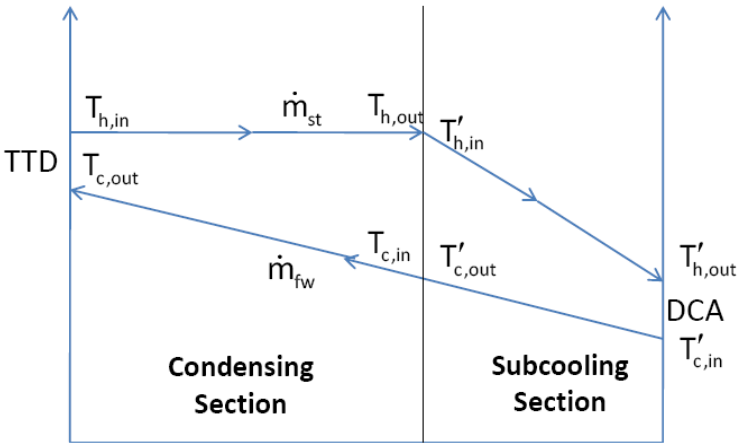

Figure 6.14: T-x diagram for a condensing-subcooling heat exchanger

More in particular, it is assumed that the heat capacity rate of steam in the condensing zone is infinite ($C_{max} = \infty$) what implies that $C_r = 0$. The proper relations are then:

$$\varepsilon = 1 - e^{(-NTU)} \tag{6.38}$$

$$NTU = -\ln(1-\varepsilon) \tag{6.39}$$

In the subcooling phase, instead, steam drains have the smallest heat capacity rate (due to the smaller mass flow) and the relations are

$$\varepsilon = 2\left\{1 + C_r + (1+C_r^2)^{1/2} * \frac{1 + exp\left[-NTU * (1+C_r^2)^{1/2}\right]}{1 - exp[-NTU * (1+C_r^2)^{1/2}]}\right\}^{-1} \tag{6.40}$$

$$NTU = \frac{1}{(1+C_r^2)^{1/2}}\, ln\frac{2 - \varepsilon\left[1 + C_r - (1+C_r^2)^{1/2}\right]}{2 - \varepsilon[1 + C_r + (1+C_r^2)^{1/2}]} \tag{6.41}$$

The objective of the analysis is in this case to determine the values of ε and of the parameter UA for each of the phases of the feedwater heaters. This, apart from giving further information on the exchanger, will be the starting point to study the off-design behavior of these components.

It has to be noticed that the inlet and outlet temperatures are all known thanks to the TTD and DCA but that the feedwater temperature at the exit of the drain

"subcooling" phase ($T_{M\ fwh,water}$) is not known a priori. It can however be calculated thanks to an energy balance and assuming a negligible pressure drop in that part of the exchanger.

$$h_{M\ fwh,water} = \frac{\dot{m}_{steam}\ (h_{sat\_liq@Tin\ fwh,steam} - h_{out\ fwh,drain})}{\dot{m}_{water}} + h_{in\ fwh,water} \tag{6.42}$$

$$T_{M\ fwh,water} = T\ (P_{in\ fwh,water}\ , h_{M\ fwh,water}) \tag{6.43}$$

As an example, we report the results for the first LP feedwater heater of a reference 15MW and 40 bar plant.

Table 6.5: First LP fwh on-design performances

$\boldsymbol{\varepsilon_{subcooling\ phase}}$	0.814
$\boldsymbol{UA_{subcooling\ phase}}$	17.1
$\boldsymbol{\varepsilon_{condensing\ phase}}$	0.899
$\boldsymbol{UA_{condensing\ phase}}$	211.5

One last thing to highlight is that the first HP feedwater heater receives the drains from the following one. To properly consider this flow, a particular approach has been used which represents the internal configuration of real heat exchangers.

Inasmuch as the drain coming from the last pre-heater is always subcooled liquid, this liquid is mixed with the condensed steam and contributes to the heat transfer "subcooling phase". In the condensing phase, instead, only the condensing steam exchanges heat and the drain does not intervene.

A practical scheme could be the following.

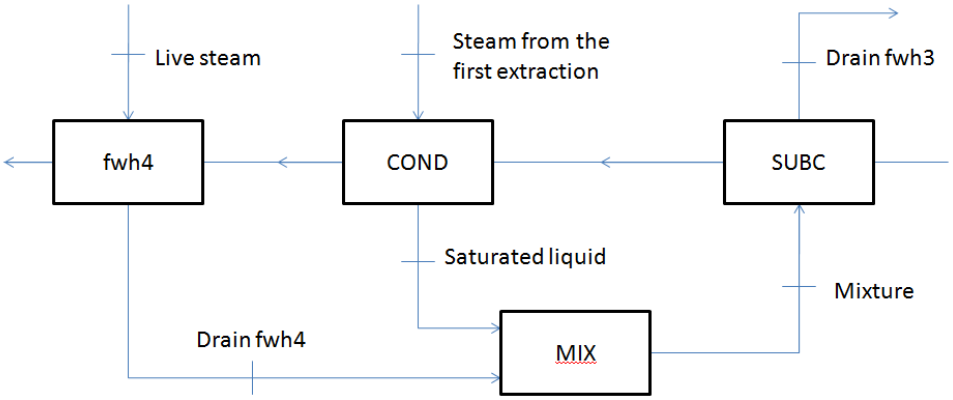

Figure 6.15: Conceptual scheme of the first HP fwh

From the point of view of the model, a relevant feature is that water temperature at the exit of the subcooling phase is obtained considering that the hot fluid is now composed by a mixture of drains coming from fwh4 and saturated liquid coming from steam condensation. The thermodynamic conditions of this mixture are properly calculated through the previous mass and energy balances.

$$\dot{m}_{mix} = \dot{m}_{drain\ \ fwh4} + \dot{m}_{saturated\ \ liquid} \tag{6.44}$$

$$h_{mix} = \frac{\dot{m}_{drain\ \ fwh4} h_{drain\ \ fwh4} + \dot{m}_{saturated\ \ liquid}\ h_{saturated\ \ liquid}}{\dot{m}_{mix}} \tag{6.45}$$

6.6 Deaerator

The deaerator, located after the first LP feedwater heater, is an open heater that directly mixes extraction steam and feedwater to be heated. The extraction steam is condensed and becomes part of the feedwater leaving the heater.

As clearly expressed by its name, the main function of this device is to deaerate the incoming condensate. This action eliminates dissolved, noncondensible gases consisting mainly of oxygen, nitrogen, ammonia and carbon dioxide, from the condensate. They are present as a result of leaks at those sections of the plant that operate under vacuum conditions and chemical reactions, and their removal is essential to the proper operation of the plant.

Deaeration of the condensate is based upon Dalton's and Henry's laws. These laws combine to state that the quantity of a gas that dissolves in a liquid decreases as the temperature of the liquid rises. In the limit, if the liquid is taken to the boiling point, dissolved gases will be completely eliminated.

An opening in the top of the heater section allows the released gases and some steam to be vented from the heater section.

In an open heat exchanger, the convective heat transfer is substituted by a mass transfer process, characterized by an efficiency that increases when the contact surface between the two phases water and steam increases. To improve the performances, therefore, the water is normally broken down into a fine spray or thin sheets.

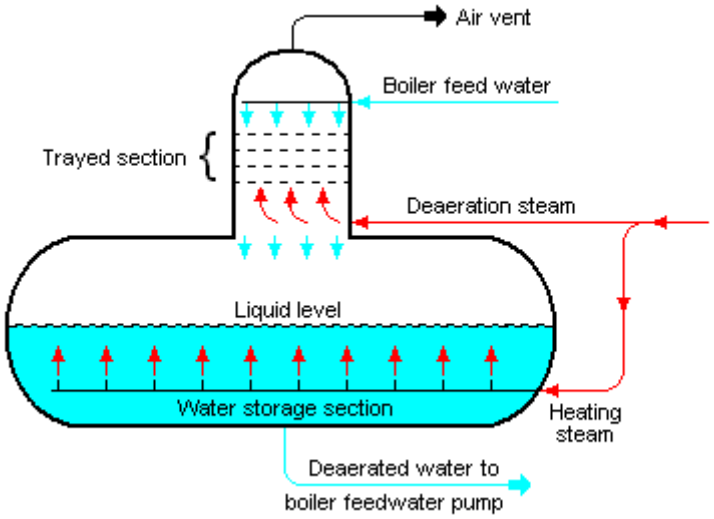

Figure 6.16: Simplified deaerator layout

In addition to deaeration, this heater provides proper suction conditions for the boiler feed pump and a natural discontinuity between high-pressure and low-pressure sections. Besides, drains from the high-pressure heaters are normally cascaded into the deareator.

The unit can be designed to operate at any pressure, although subatmospheric operation requires additional facilities to provide for removal of the released gases from the shell. Most units are designed for positive pressures only, and the shells are specified for a pressure exceeding the maximum pressure of the extraction steam [50].

Given the saturated conditions at the boiler, and knowing the design working temperature thanks to the Haywood approach, all the other thermodynamic parameters are completely defined.

6.7 Pumps

Pumps are present in both “boiler” and “power-block” sections of the plant. In the second one, two main “pumping stations” are present. The first and smaller one is located at the condenser outlet and has the objective to elevate the pressure till the deaerator one and to win the pressure losses in the first pre-heater. Its power consumption is generally small, in the order of 0.1% of the total power output and its behavior doesn’t really influence sensibly the plant performances.

The second station is located after the deaerator and the pressure increase supplied is an order of magnitude bigger than the first one. In heavy-duty power plants, the electrical consumption of this pump is often very high and in same cases it is preferable to drive it directly with a small steam turbine. This option allows for variable speed operation of the pump,

In the case of a solar tower plant, the size is remarkably smaller and the consumption will be a few hundred kW.

The “pumping stations” can be organized in different manners, in particular with reference to the number of pumps and their rotational speed characteristics.

For a deeper description, we refer to the dedicated chapter (5.1.6).

6.8 Global model description

The detailed description of the single components and the approach to their study carried on until now does not imply that each component can be analyzed and “solved” singularly. The peculiarity and the difficulty of the study of a power plant resides exactly in the fact that all the components are strongly interconnected and, moreover, that the equations that govern the phenomena are not always linear.

From this, the need to operate with iterative processes managed by the software.

In the case of the on-design model, the Matlab sub-routine *fsolve* is used to solve a system of non-linear equations. More in particular, the solving procedure starts from an initial guess of live steam and extraction mass flows (for each preheater in the latter case). In addition, also the enthalpy value of the drain leaving the first LP feedwater heater is guessed. With these initial values and exploiting the relations and the sub-functions described above for the plant components, all the characteristic points of the cycle can be determined. The energy balances at each

feedwater heater, the new definition of the first drain enthalpy thanks to the DCA and, most of all, the comparison between the calculated Net Power Output and the one specified by the user let the model to update and correct the initial guesses and "close" the system. From a mathematical point of view, the iterative process is solved by MATLAB® exploiting a matrix approach and the Trust Region dogleg method. Also Levenberg-Marquardt and Gauss-Newton algorithm have been tested but they have shown a less stable behavior.

To sum up, referring to the characteristic point of the plant reported in Figure 6.2, the model solves a system of six non-linear equations in six unknowns:

Unknown (guessed) variables:

1) $\dot{m}_1$
2) $\dot{m}_{16}$
3) $\dot{m}_5$
4) $\dot{m}_6$
5) $\dot{m}_7$
6) h_{23}

Equations:

1) $\dot{m}_{11} \cdot h_{11} + \dot{m}_{22} \cdot h_{22} = \dot{m}_{10} \cdot h_{10} + \dot{m}_7 \cdot h_7$ (6.46)

2) $\dot{m}_{11} \cdot h_{11} + \dot{m}_6 \cdot h_6 + \dot{m}_{21} \cdot h_{21} = \dot{m}_{12} \cdot h_{12}$ (6.47)

3) $\dot{m}_{13} \cdot h_{13} + \dot{m}_5 \cdot h_5 + \dot{m}_{19} \cdot h_{19} = \dot{m}_{14} \cdot h_{14} + \dot{m}_{20} \cdot h_{20}$ (6.48)

4) $\dot{m}_{14} \cdot h_{14} + \dot{m}_{17} \cdot h_{17} = \dot{m}_{15} \cdot h_{15} + \dot{m}_{18} \cdot h_{18}$ (6.49)

5) $h_{23} = h_{22}$ (6.50)

6) $Net\ Power\ Output_{calculated} = Net\ Power\ Output_{user\ defined}$ (6.51)

The software is able to manage the system quite easily, and with a medium-performance hardware (2.0 GHz processor, 2 GB DDR2 RAM memory), the computational time for this part of the model is lower than 30 seconds.

6.9 Plant performances

As output of the simulation, in addition to the thermodynamic properties of each significant section of the plant, the power output and the global conversion efficiency are displayed. The net power output is calculated considering the whole power produced by steam in the different "stages" of the turbine and then subtracting the different auxiliary consumptions and losses.

The first one is the mechanical loss in the turbine, expressed by the mechanical (organic) efficiency. Besides, the friction and electrical losses in the generator, the pumps electrical consumption and the condenser power requirement; all these components are expressed in terms of power and are so directly subtracted from the gross power produced.

$$NPO = \dot{W}_{turbine} \cdot \eta_{org,turbine} - \dot{W}_{generator\ \ friction\ \ losses} - \dot{W}_{generator\ \ electrical\ \ losses} - \dot{W}_{absorbed,pumps} - \dot{W}_{absorbed,ACC\ fans} \quad (6.52)$$

Finally, the net electric production efficiency is defined as:

$$\eta_{el,net} = \frac{NPO}{\dot{Q}_{in}} \quad (6.53)$$

where $\dot{Q}_{in}$ is the thermal power added to the cycle:

$$\dot{Q}_{in} = \dot{m}_{feedwater} \cdot \left(h_{feedwater,in\ boiler} - h_{steam,out\ boiler}\right) \quad (6.54)$$

This efficiency is clearly referred only to the power cycle conversion and does not take into account the losses from the initial sun radiation to the thermal power absorbed by the feedwater in the solar receiver nor the auxiliary power consumption at the steam generator.

6.10 Case study plant and model validation

As already said, the model can be used to describe plants with several sizes and characteristics. To provide an example and to let the reader identify the functioning parameters better, we report the on design description of a plant with a net electric production of 15 MW, a drum pressure of 40 bar and default values for all the other parameters.

Table 6.6: Relevant cycle parameters at on-design

POINT	PRESSURE [bar]	MASS FLOW [kg/s]	ENTHALPY [kJ/kg]	TEMP. [K]
1	40.00	30.49	2800.90	250.4
2	40.00	30.49	2800.90	250.4
3	40.00	30.49	2800.90	250.4
4	40.00	27.01	2800.90	250.4
5	15.90	2.84	2668.74	201.1
6	4.21	2.20	2491.44	145.5
7	1.09	2.15	2328.71	102.1
8	0.10	19.82	2075.56	45.0
9	0.10	21.97	193.01	45.0
10	4.12	21.97	193.54	46.1
11	3.92	21.97	398.64	95.1
12	3.92	30.49	601.61	142.9
13	45.20	30.49	607.58	143.7
14	43.05	30.49	820.62	192.6
15	41.00	30.49	1041.29	240.8
16	40.00	3.48	2800.90	250.4
17	37.00	3.48	2800.90	245.8
18	37.00	3.48	865.05	202.6
19	14.79	3.48	865.05	197.6
20	14.79	6.32	648.75	153.7
21	3.92	6.32	648.75	142.9
22	1.02	2.15	235.12	56.1
23	0.10	2.15	235.12	45.0

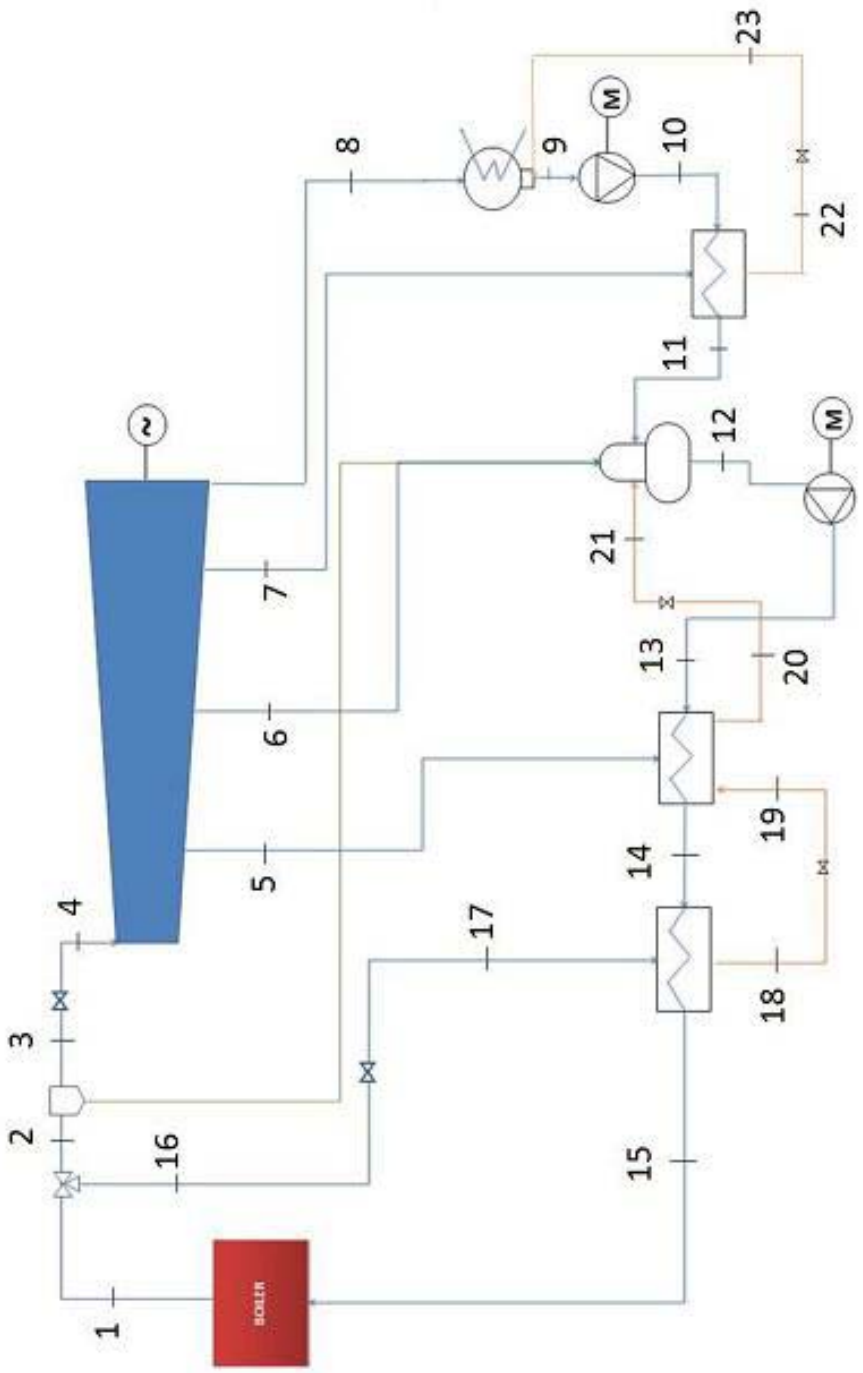

Figure 6.17: Simplified layout of the plant

Table 6.7: FWHs performances in on-design

	FWH 1	FWH 3	FWH 4
T_in [°C]	46.1	143.7	192.6
T_out_subc [°C]	50.5	153.6	197.8
T_out [°C]	95.1	192.6	240.8
Q_cond [kW]	4111.94	5203.17	6055.06
UA_cond [kW/K]	211.479	290.107	318.405
NTU_cond	2.295	2.175	2.262
Effectiveness_cond	0.899	0.886	0.896
Q_subc [kW]	396.58	1300.91	697.04
UA_subc [kW/K]	17.123	63.346	31.220
NTU_subc	1.895	2.279	1.928
Effectiveness_subc	0.815	0.815	0.812

Table 6.8: Power and performances for on-design operation

Turbine gross power [kW]	16446.97
Turbine mechanical losses [kW]	328.94
Generator fiction losses [kW]	99.62
Generator electric losses [kW]	286.90
Condensate pump power [kW]	12.10
Feed pump power [kW]	189.21
Condenser auxiliaries power [kW]	530.2
Incoming Thermal Power [kWt]	53649.0
NPO [kW]	15000
Cycle efficiency	0.280

To validate the model, the simulation of a 11MW Power Output, 42 bar drum pressure and 0.06 bar condenser pressure plant has been carried out, being these the actual main parameters of the PS10 power plant.

It has to be noticed that in public data the performance of the PS10 plant is usually reported in terms of power output at generator terminals, that is to say that pumps and auxiliaries power consumption is not considered in the calculus of cycle efficiency..

To validate the model and compare it with the real plant, the code has so been momentarily modified in this sense. The power and performances results are reported in Table 6.9.

Table 6.9: Power and performances in PS10 simulation

Turbine gross power [kW]	11500
Turbine mechanical losses [kW]	230.01
Generator fiction losses [kW]	69.66
Generator electric losses [kW]	200.61
Condensate pump power [kW]	7.38
Feed pump power [kW]	134.4
Condenser auxiliaries power [kW]	337.4
Incoming Thermal Power [kWt]	35714.2
Power output at generator terminals [kW]	11000
NPO [kW]	10520.8
Cycle efficiency	0.308

The comparison in Table 6.10 shows small differences between the calculated and the declared values and demonstrates a good accuracy of the model.

Table 6.10: Model results and PS10 project performances

	Model results	**Public PS10 data**
Output at generator terminals[MW]	11	11
Heat input [MW]	35.7	35.8
Steam cycle efficiency [%]	30.8	30.7

7. ON-DESIGN GLOBAL MODEL

As already described, the on design model works with a simple interaction between receiver and power-block sub-models.

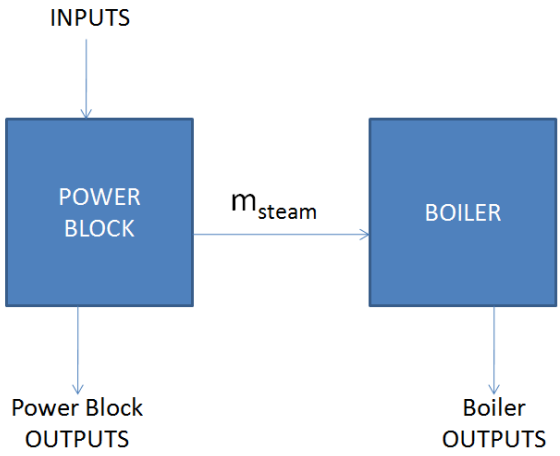

Figure 7.1: Schematic on-design model procedure

In Table 7.1 all the needed/changeable inputs are summarized, together with their default values.

Table 7.1: On-design model inputs

Input	Default value
Irradiance [W/m^2]	1000
Pump hydraulic efficiency	0.75
Pump mechanical efficiency	0.98
Pump electrical efficiency	0.98
Pipes internal diameter [mm]	50
Pipes thickness [mm]	4.4
Pipes absolute roughness [mm]	0.0547
Number of risers	15
Risers internal diameter [m]	0.1524
Number of downcomers	4
Downcomers internal diameter [m]	0.3

Additional length for water wall tube circuit [m]	3
Boiler thermal efficiency [%]	92
Boiler outlet steam quality [%]	20
Grid frequency [Hz]	50
Turbine isentropic efficiency [%]	82
Turbine organic efficiency [%]	98
FWH TTD [°C]	5
FWH DCA [°C]	10
FWH feedwater side pressure losses [%]	5
FWH steam side pressure losses [%]	0
Extraction line pressure losses [%]	7.5
Condenser inlet air temperature [°C]	30
Condenser air temperature increase [°C]	10
Condenser Pinch Point [°C]	5
Lower limit of turbine exhaust steam quality [%]	75

As obvious, changing these default values implies a modification in the plant design and behavior that can be remarkable or practically negligible according to the case studied.

Thanks to the model, it is therefore possible to identify the influence that certain parameters have on the plant performance; this information, merged with a mechanical and economical analysis, allows for the definition of the best plant design.

In this chapter, examples of parametric analyses carried on for the most representative inputs are reported.

7.1 Power Output variation

The model is designed to work with different plant sizes; according to the characteristics of conventional solar tower plants currently in operation, it has been considered that an interesting power output range is 5 – 50 MWe.

The parametric analysis has been carried on keeping all the other parameters constant, and a 40 bar drum pressure.

The immediate consequence of a higher power output is the increase of the steam mass flow required by the turbine and, therefore, of the central receiver dimensions (Figure 7.2).

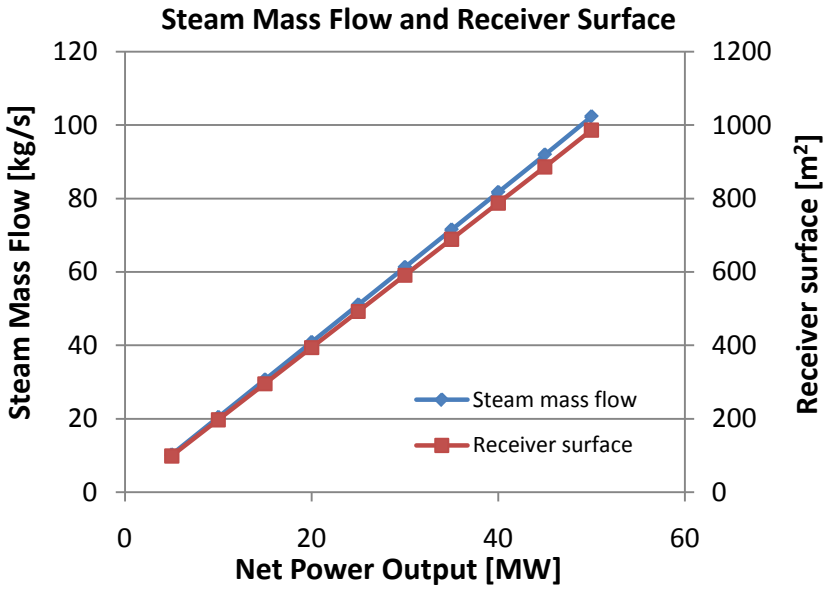

Figure 7.2: Steam mass flow and receiver surface variation with NPO

Using the absolute values the two curves obviously differ a bit but plotting the relative values, obtained through a ratio with the “default” values of a 15 MW plant, they overlap in a single curve.

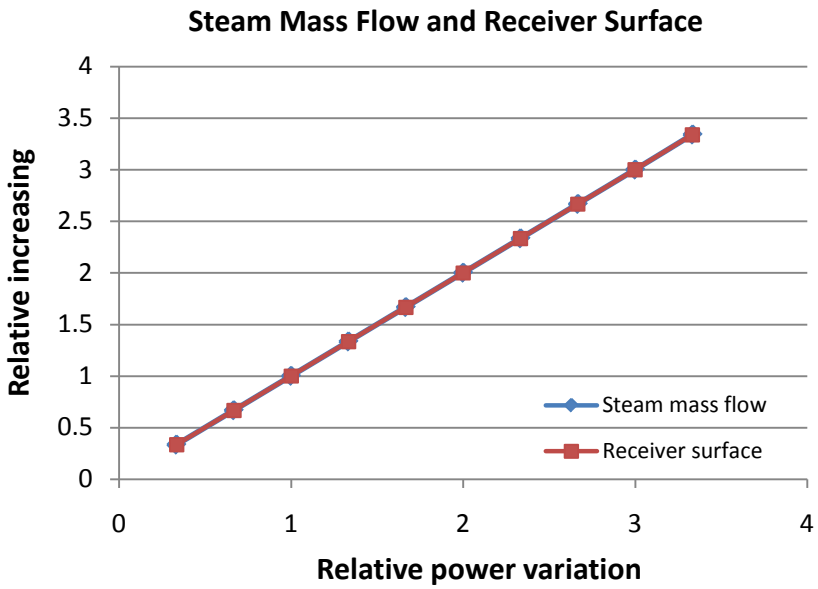

Figure 7.3: Relative steam mass flow and receiver surface variation with NPO

A twofold increase in power output requests a twofold increase in both steam mass flow and receiver surface. The model shows that the same proportionality can be found in practically all the other parameters as extraction mass flows, pumps power, and turbine losses.

This particular trend can be easily explained considering that we are maintaining all the parameters except power output and this means keeping the same working cycle (Figure 7.4) modifying the circulating mass flow.

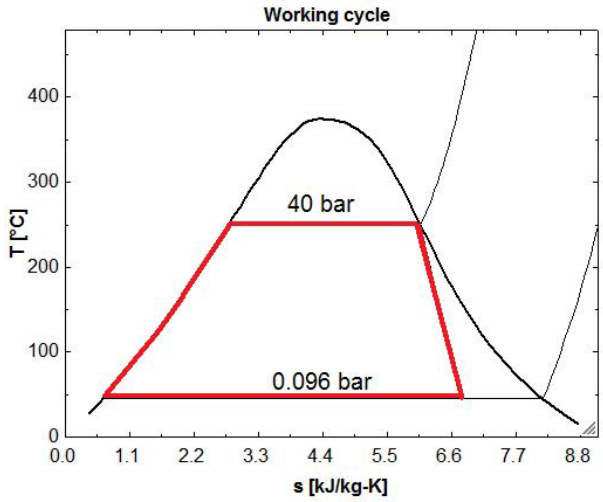

Figure 7.4: Default on-design working cycle

Due to the just described behavior of the plant, cycle efficiency remains constant.

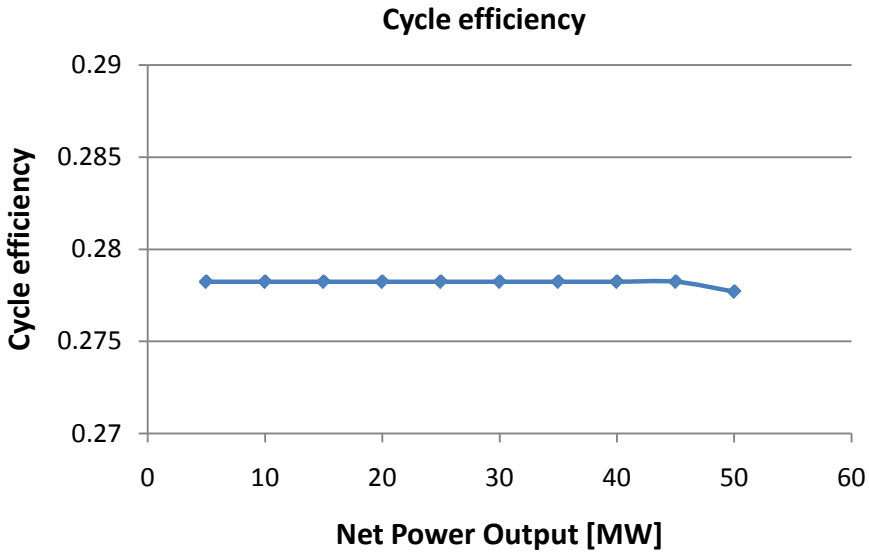

Figure 7.5: Cycle efficiency VS NPO variation

As showed by Figure 7.5, the last statement is true in the whole power range, with the exception of the 50 MW case. In this case, indeed, the proportional increase of steam mass flow in the condenser implies a “non-proportional” increase in the number of condenser cells used. To be more precise and as

already explained, the needed number of condenser cells is calculated considering the ratio between the needed air volumetric flow and the reference cell air volumetric flow and choosing the closest integer number. In the cases from 5 to 45 MWe, the volume flow ratio is always approximated by a smaller integer; for the 50 MWe case, instead, the volume ratio becomes 20.589 and the closest integer is so the bigger one. A non-proportional increase in the number of ACC cells causes a relative increase in the auxiliary consumption and, therefore, a small efficiency decreases due to higher auxiliary power consumption.

7.2 Drum pressure variation

A more relevant effect on plant performance is found due to drum pressure variations. According to the typical plant configurations, the value of drum pressure has been varied in the range 10 – 100 bar.

Figure 7.6 reports the trends of cycle efficiency and receiver surface.

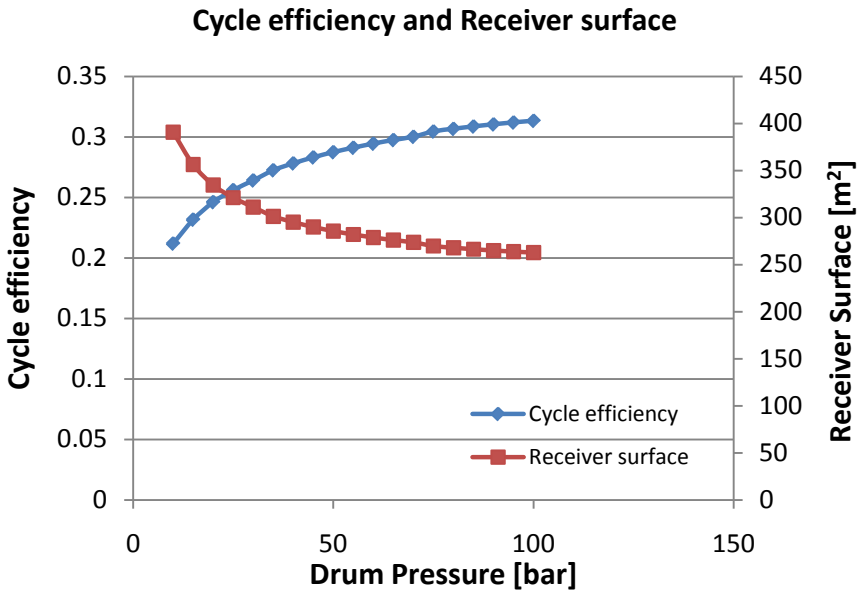

Figure 7.6: Cycle efficiency and receiver surface variation with Drum Pressure

The opposite trend of the two curves is easy to understand, considering that for constant power output, a cycle efficiency increase implies a decrease of incoming thermal power and therefore of boiler surface.

What is more interesting to study, instead, is the non-linear trend of the two curves. Let us consider the efficiency curve, it can be seen that the drum pressure increase brings about a progressively decreasing positive effect. This is due to a double effect of pressure on plant behavior.

Analyzing a Temperature-Entropy or a Enthalpy-Entropy water diagram (Figures 7.7 and 7.8), it can be observed that due to the particular shape of the saturation curve, a decrease of the enthalpy of vaporization always takes place when pressure increases. In the case of the solar tower model, this implies that to produce a certain amount of steam, less thermal power is needed.

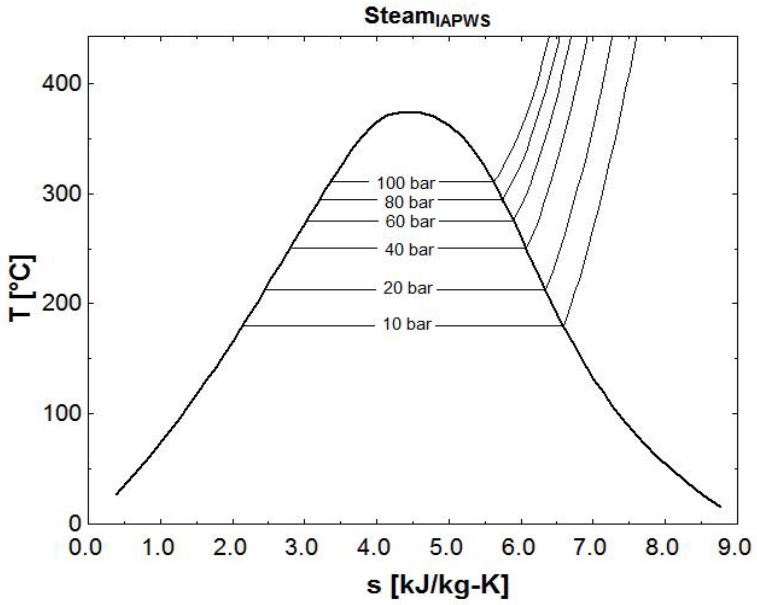

Figure 7.7: T-s water/steam diagram

In addition to this effect, a second one has to be taken into account. Analyzing a h-s water diagram, indeed, it can be seen how the drum pressure increase is related to an enthalpy increase from 10 to 30 bar, but to an enthalpy decrease going from 30 till 100 bar. This is due to the relative shape of constant pressure lines below the saturation curve and the constant temperature lines above, and implies an increase in the turbine specific work in the first phase and its decreasing in the second phase.

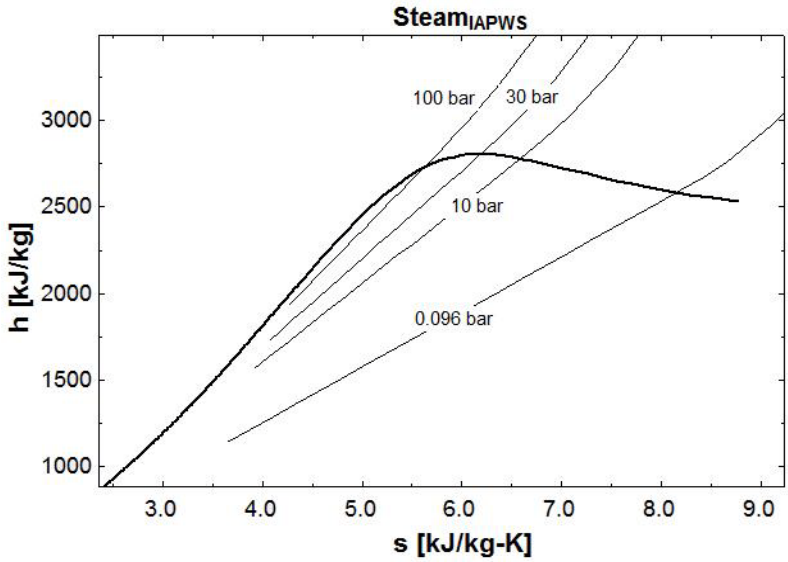

Figure 7.8: h-s water/steam diagram

To sum up, as shown in Figure 7.9 the increase of drum pressure from 10 to 30 bar implies the increasing of the enthalpy drop available for the turbine and therefore the decreasing of needed steam flow. Moreover, the production of this steam is obtained with a lower thermal input. The combination of the two effects brings to a significant efficiency rise. But increasing drum pressure more, the decrease of saturation enthalpy makes the steam mass flow required by the turbine start to increase too. The positive effect of the reduced enthalpy of vaporization is then attenuated.

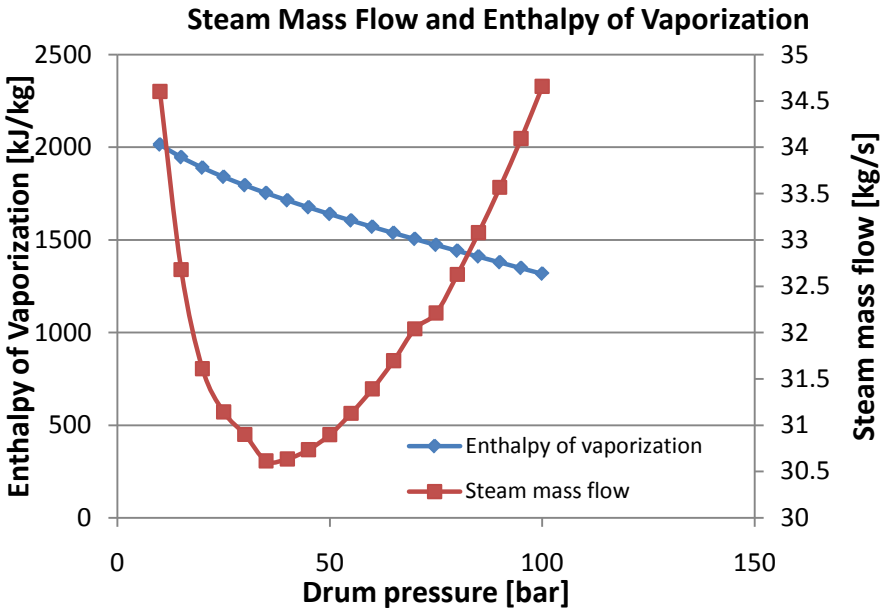

Figure 7.9: Steam mass flow and Enthalpy of vaporization variation with Drum Pressure

The irregularities in the steam mass flow curve are another time due to the ACC. discrete operation, consequence of adopting a fixed cell geometry.

In the end, the analysis shows that in the chosen range, the higher drum pressure, the higher efficiency. On the other hand, it has to be taken into account that, working with saturated steam, to a pressure increase is inevitably related a temperature increase. The benefits of the efficiency increase have therefore to be compared with the worsening of mechanical and thermal problems on the receiver pipes.

The drum pressure variation influences also the feedwater heaters behavior. When drum pressure increases, indeed, also receiver inlet temperature increases and being fixed both the condenser temperature and the number of feedwater heaters, the Haywood approach indicates a higher temperature increase in each exchanger.

On the other side, TTD and DCA remain constants and being related to a higher ΔT, their influence becomes progressively smaller. Due to this, the FWH effectiveness, which can be written as in (7.1 and 7.2) increase both in condensing and subcooling section.

$$\varepsilon_{cond} = \frac{\Delta T_{fw,cond}}{\Delta T_{fw,cond} + TTD} \tag{7.1}$$

$$\varepsilon_{subc} = \frac{\Delta T_{drains}}{\Delta T_{drains} + DCA} \tag{7.2}$$

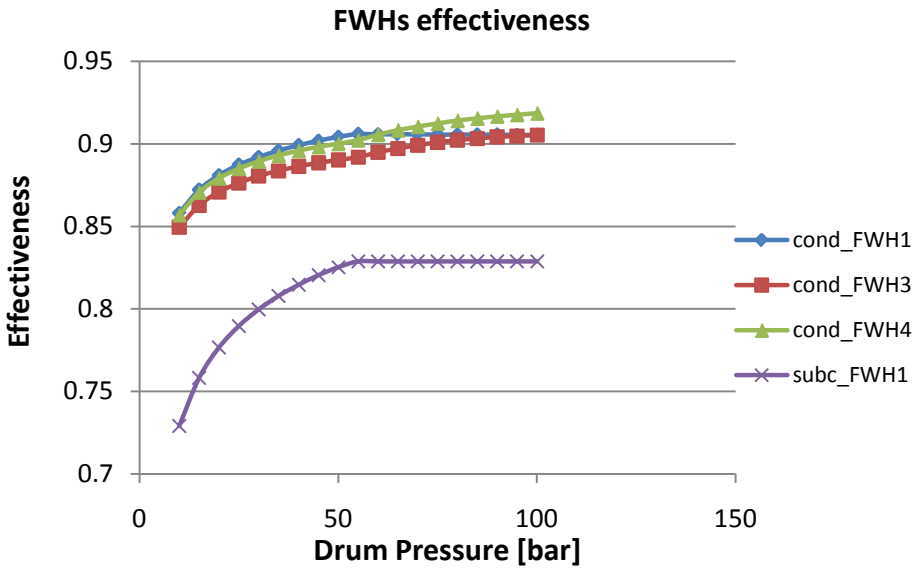

Figure 7.10: FWHs effectiveness variation with Drum Pressure

As can be seen in Figure 7.10, the effectiveness of the first FWH remains constant if pressure rises above 55 bar. This is due to the kind of deaerator design process adopted. As already reminded in Paragraph 6.5.2, indeed, the Haywood approach is used only until the deaerator pressure stays below the construction limit of 5 bar. When this limit is overcome, the model switches to a different design procedure, which fixes the deaerator pressure (and temperature); the ΔT of the first FWH is thus fixed too, and coherently its performance does not change.

The just described analysis highlights a problem in the chosen plant design. When the drum pressure is very high, indeed, the required effectiveness in the subcooling section of the 3rd FWH is too high for the chosen kind of heat exchanger and of heat transfer fluids. As an example, let us consider the case of a 100 bar drum pressure. The FWH3 subcooling phase will be characterized by the following parameters, determined exclusively by the fluid nature and temperatures:

Table 7.2: FWH3 parameters at 100 bar Drum Pressure

Effectiveness	0.873803
C*	0.3653

Confronting these data with the ε-NTU curve of the chosen heat exchanger, it can be seen that such a high effectiveness cannot be obtained having fixed water and drain mass flow on both sides. The curve corresponding to the particular value of C* does not reach the value of effectiveness required, that is to say that neither with an infinite Number of Thermal Units the feedwater heater could provide for the required performance.

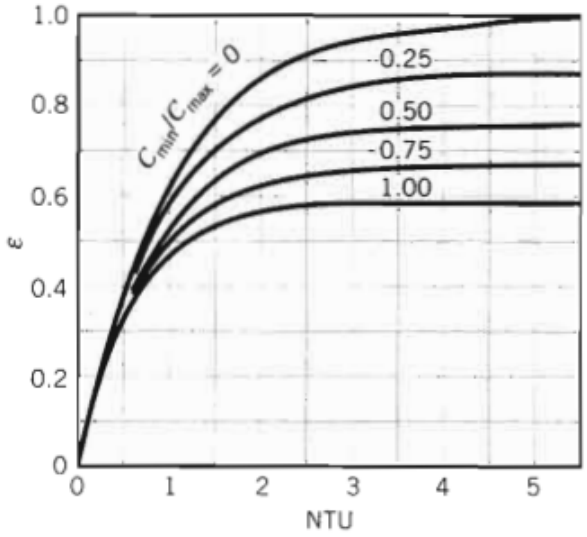

Figure 7.11: Effectiveness of a shell-and-tube heat exchanger with one shell and any multiple of two tube passes

In this case, the model would display an error message and stop. To solve this problem, it has been considered that when the desired drum pressure is higher than 70 bar, the third and fourth feedwater heaters have to be of a different type and therefore a two shell configuration is chosen. This way, the ε-NTU curves changes, and a solution can be found (Figure 7.12).

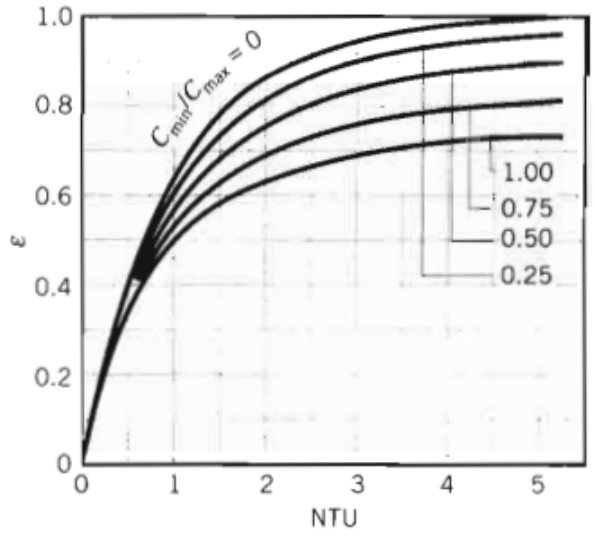

Figure 7.12: Effectiveness of a shell-and-tube heat exchanger with two shell passes and any multiple of four tube passes

7.3 Turbine isentropic efficiency variation

The isentropic efficiency is a characteristic parameter of the chosen turbomachine. It does not depend on the thermodynamic behavior of the rest of the plant and it can be thought that its value would vary due to future improvements in turbine design. The analysis has been developed considering a variation in the range 0.6 – 1.0.

In Figure 7.13 the effects on turbine specific work and cycle efficiency are shown.

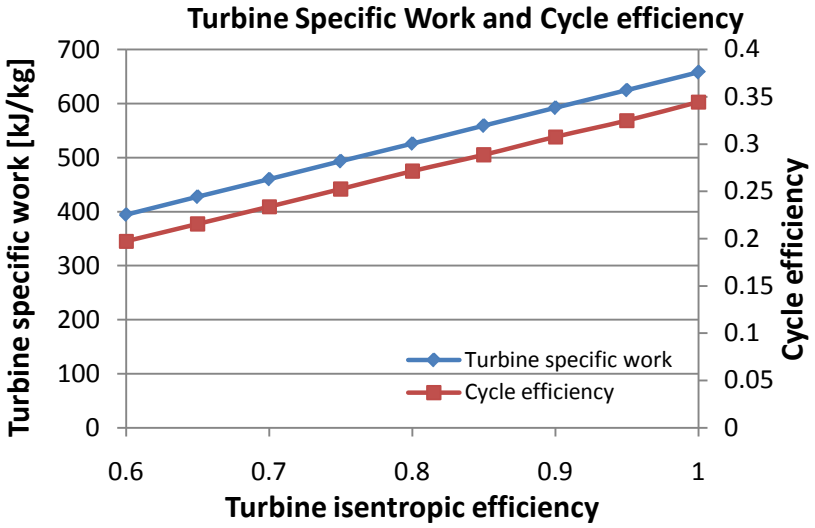

Figure 7.13: Turbine specific work and Cycle efficiency variation with Turbine isentropic efficiency

The first and most direct effect of increasing the turbine efficiency is the increase in the turbine specific work, as can be seen in an h-s diagram. Due to this effect, the steam mass flow required to generate the fixed power output decreases and, with it, the heat input to the cycle. Globally, cycle efficiency increases and the required receiver surface decreases.

The graph shows that the relation between turbine and cycle efficiency is strong and a 10% increasing of the former implies an almost 4% increasing of the latter.

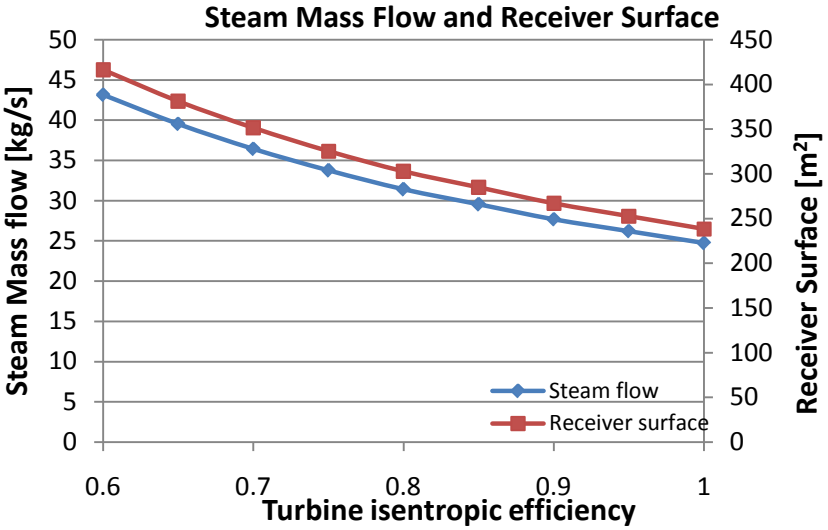

Figure 7.14: Steam Mass Flow and Receiver Surface variation with Turbine isentropic efficiency

The variation of turbine isentropic efficiency has a significant effect on turbine exhaust/condenser conditions as well (Figure 7.15). By increasing the efficiency, indeed, turbine exhaust steam quality decreases (or, on the other side, humidity increases). Apart from the negative effects on the steam turbine behavior, this aspect influences the condenser heat rejection. By an intuitive point of view, a humidity increase, indeed, is anything more than an increase of "already condensed" flow. This means that the condenser duty is lower. Thermodynamically, it can be simply said that enthalpy at turbine exhaust decreases and, therefore, the heat rejected in the condenser decreases too. It has to be noticed that this effect is combined with the most relevant one given by the steam mass flow decrease, as shown in Figure 7.16.

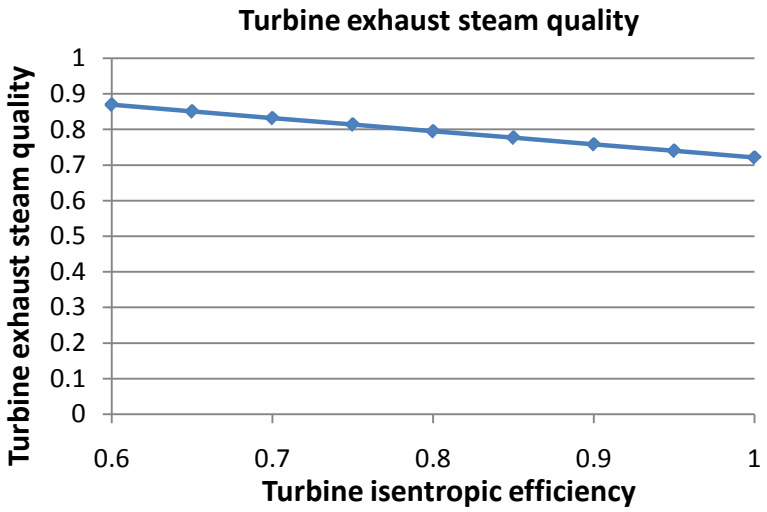

Figure 7.15: Turbine exhaust steam quality variation with Turbine isentropic efficiency

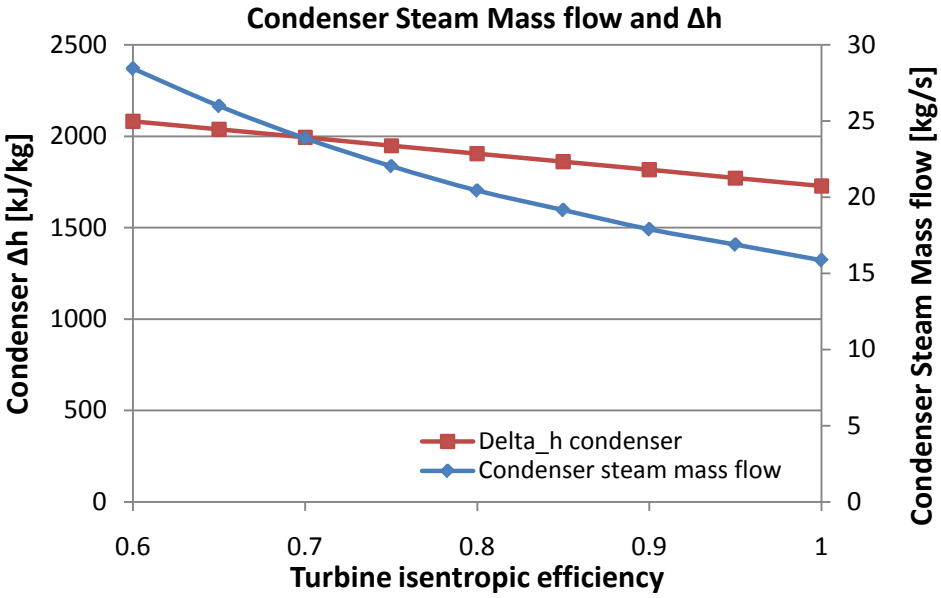

Figure 7.16: Condenser Steam Mass flow and Δh with Turbine isentropic efficiency

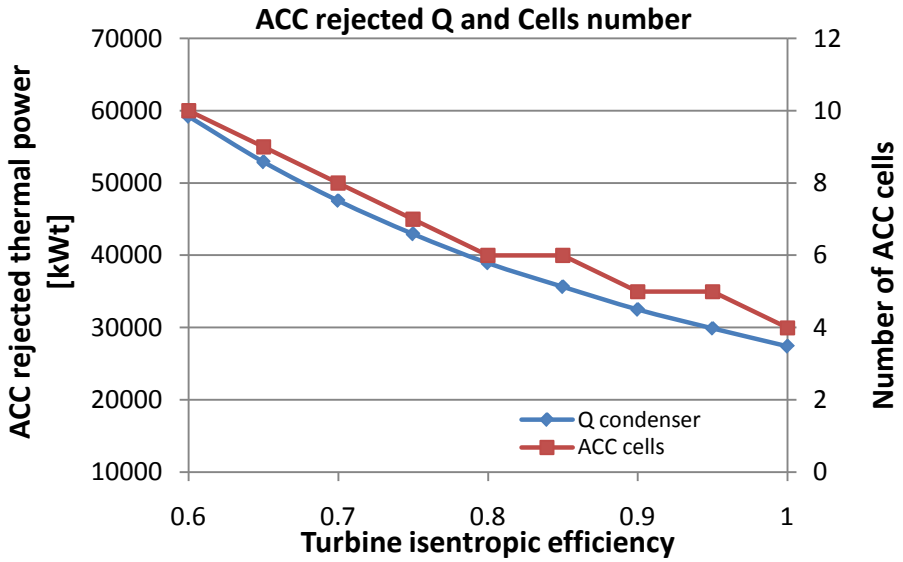

Figure 7.17: ACC thermal power rejected and Cells number variation with Turbine isentropic efficiency

Obviously, the less thermal power rejected by condenser, the less number of required cell, the less auxiliaries power consumption. The auxiliary power

consumption curve presents exactly the same trend than the ACC cells number one; from this, another contribution to the cycle efficiency increase.

Being fixed the condenser and drum pressure, at last, the pre-heating line performance does not change.

To sum up, an improvement in turbine efficiency is extremely desirable, considered its strong connection with the whole cycle efficiency. Considering that saturated steam turbines of this size have been used marginally in the past, only in nuclear war ships and other singular applications, improvements could be achieved, as the market grows.

7.4 Terminal Temperature Difference variation

As for the turbine isentropic efficiency, the Terminal Temperature Difference is a characteristic parameter of the heat exchanger. It mostly depends on the device dimensions and on its heat transfer capabilities. It could be said that the variation of the TTD is driven by an effectiveness variation; if the effectiveness increases, the feedwater outlet temperature is closer to the hot fluid inlet one, that means a TTD decrease. In spite of that, it is more useful and common to refer directly to the TTD, as done in the model.

The parametric analysis has been carried on considering a TTD variation in the range 0 – 30 °C. TTD variations involve modifications in several aspects:

1) FWHs effectiveness

As just said, the relationship between effectiveness and TTD is very strong. Recalling the definition

$$\varepsilon_{cond} = \frac{\Delta T_{fw,cond}}{\Delta T_{fw,cond} + TTD} \tag{7.3}$$

it is immediate to see that to a TTD increase corresponds an effectiveness decrease in the condensing section. Talking about the subcooling section, instead, a light effectiveness increase can be noticed. The Drain Cooler Approach is indeed kept constant, while the temperature drop experienced by the drains is increased. According to the definition

$$\varepsilon_{subc} = \frac{\Delta T_{drains}}{\Delta T_{drains} + DCA} \tag{7.4}$$

this corresponds to an effectiveness increasing.

The two effects can be clearly seen in Figure 7.18.

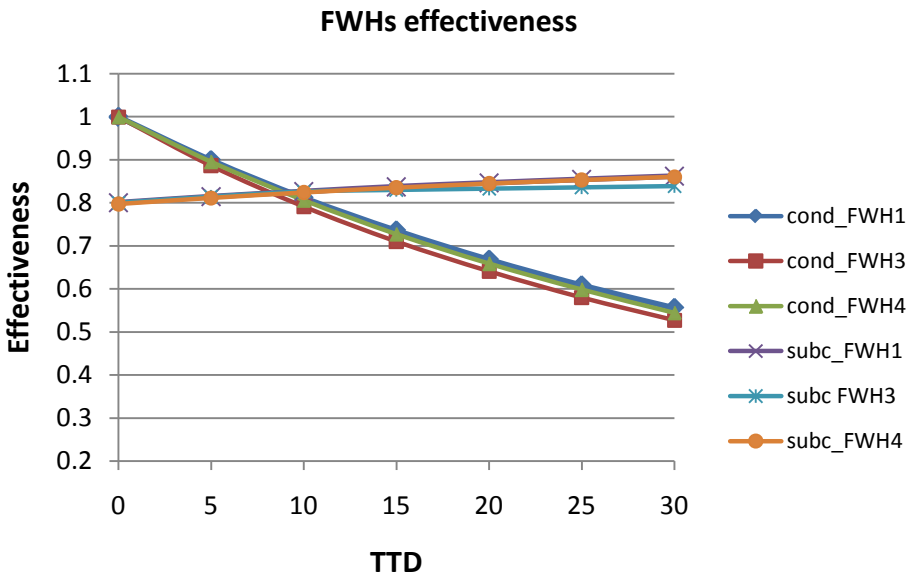

Figure 7.18: FWHs effectiveness variation with TTD

2) FWHs ΔT

As already discussed, ΔT in feedwater heaters is defined through the Haywood approach. In the case of the particular plant layout studied, if the TTD increases, feedwater flows out from the last feedwater heater before the boiler with a lower temperature. This is indeed calculated as $(T_{live\ steam\ extracion} - TTD)$ and the live steam temperature is kept constant.

Being constant also the condenser temperature, the overall ΔT, and therefore the ΔT of each feedwater heater, decrease.

The changes in the exchanger behavior are reported in Figure 7.19, which qualitatively represents the first FWH with two different TTDs (dotted lines correspond to higher TTD).

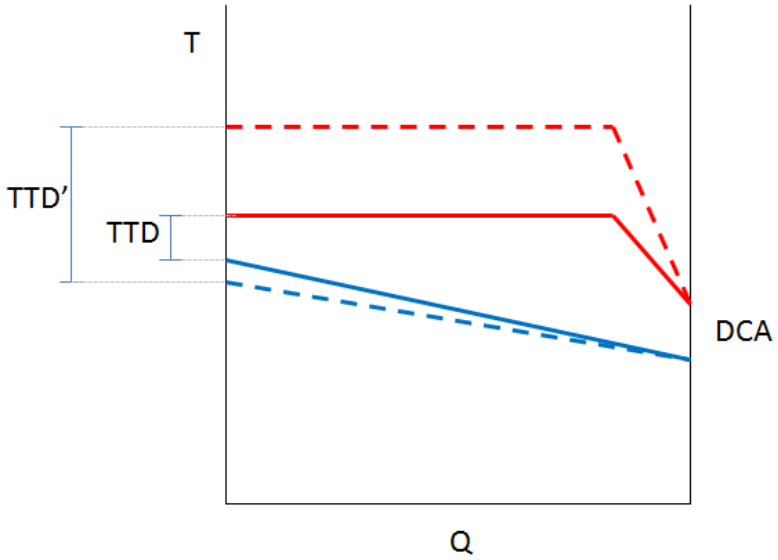

Figure 7.19: T-Q diagram for lower and higher TTD and fixed DCA

3) Steam extractions and Total Steam Mass Flow

As just said, when the Terminal Temperature Difference increases, feedwater outlet temperature slightly decreases; this effect does not "absorb" the whole TTD increase and therefore temperature and pressure of the steam extraction contemporarily increase too. In practice, steam with higher pressure has to be extracted from the turbine, and this implies that less power can be extracted by the same amount of steam. But at the same time, due to the smaller required feedwater heating and the higher ΔT between the two fluids, the mass flow of extracted steam is smaller. The two effects are opposite and, in the end, the result is a decrease in the required steam mass flow flowing into the turbine.

In the cases analyzed so far, the decrease of steam mass flow directly implied a cycle efficiency increase; in this case, instead, the steam mass flow decreases but the enthalpy increase in the boiler becomes higher and globally the heat input to the boiler increases. The final effect is, thus, a light cycle efficiency reduction.

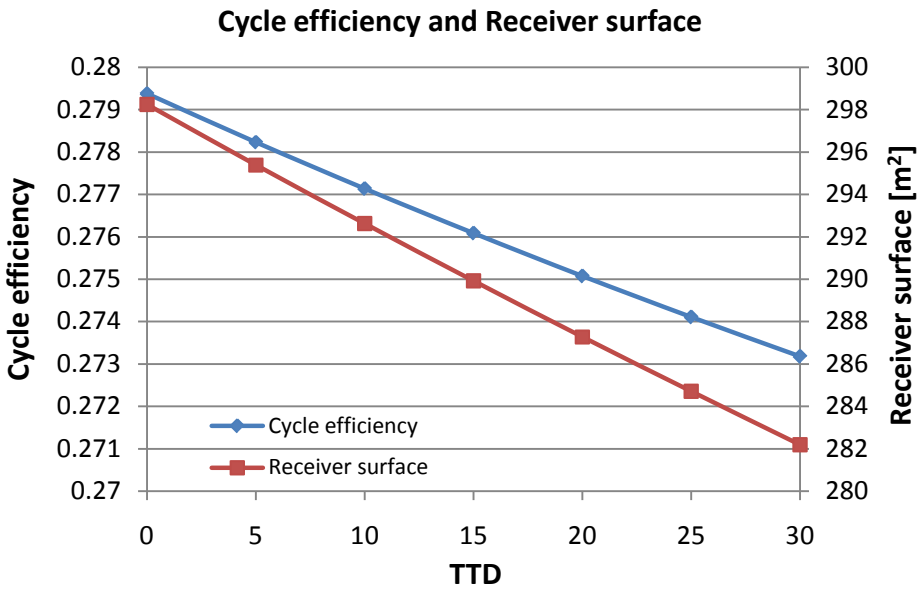

Figure 7.20: Cycle efficiency and Receiver Surface variation with TTD

7.5 Drain Cooler Approach variation

Drain Cooler Approach is the other feedwater heaters characteristic parameter and its value depends mostly on layout and size of the subcooling section. As for the TTD, the parametric analysis has been carried out varying its value in the range 0 – 30 °C.

The effects of changing DCA are less relevant than those of TTD, most of all because the overall temperature difference in the pre-heating line is not modified. An increase in the DCA, however, implies a lower Δh available for the heat transfer in the subcooling phase; to react to that, a small increase in the steam mass flow extracted by the turbine takes place. The thermodynamic conditions of the extracted steam do not change, therefore, the only effect is the decrease of the steam flowing into the turbine. The new reaction of the system to maintain the desired power output will thus be an increase in the steam demanded to the boiler.

As already seen in the previous analyses, the increase of steam demand causes a cycle efficiency decrease and a receiver surface increase, as shown in Figure 7.20.

With regards to the FWH performance, a DCA increase brings about a subcooling effectiveness decrease, while the condensing effectiveness does not vary (Figure 7.21).

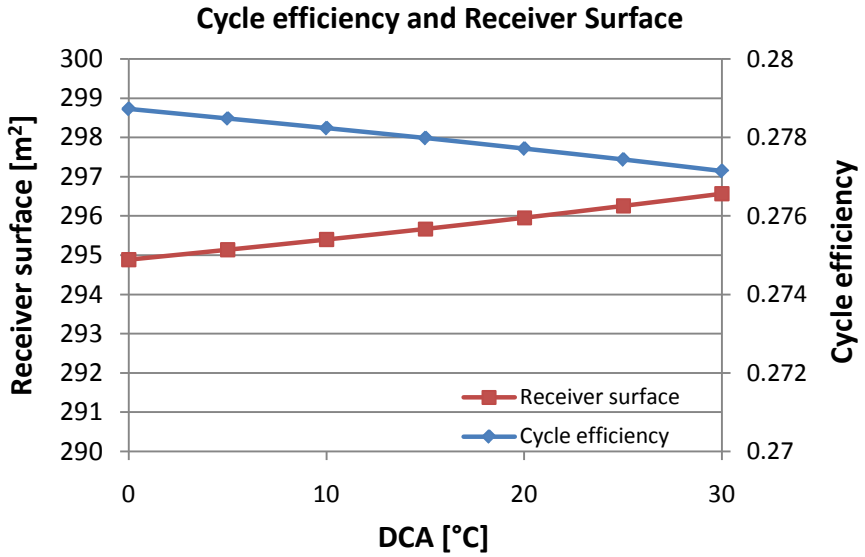

Figure 7.21: Cycle efficiency and Receiver Surface variation with DCA

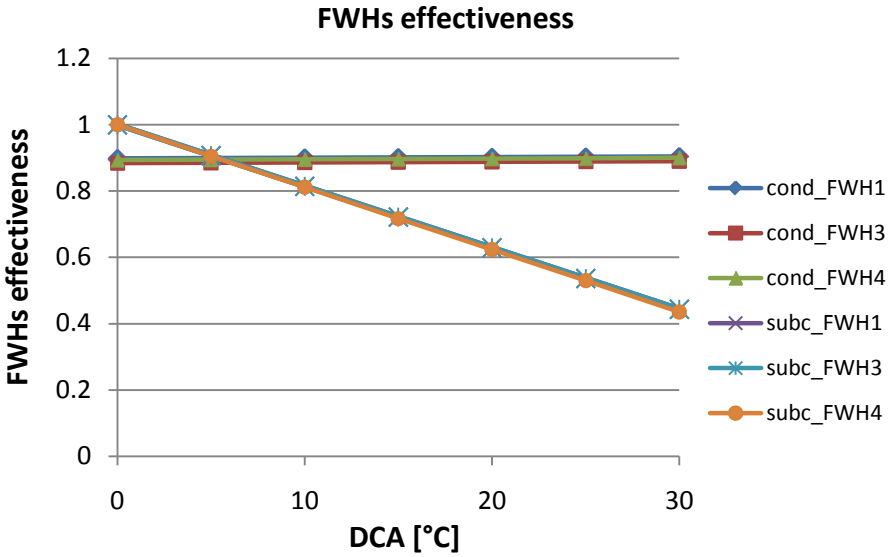

Figure 7.22: FWHs effectiveness variation with DCA

7.6 Condenser Pressure variation

Condenser pressure depends on the type of equipment and, mostly, on ambient temperature which can be changed in the model. The target of the analysis is anyway to define the effect of the condenser pressure variation on the plant changing the ambient temperature in the range 0 – 50 °C.

Considering a condenser pressure increase, the first consequence is the decrease of the useful turbine Δh. As known, to face this problem in order to keep the power output constant, increasing steam mass flow is needed. The corresponding cycle efficiency decrease and boiler surface increase are reported in Figure 7.22.

The other more direct effect is the increase in turbine exhaust/condenser inlet steam quality. This alleviates the turbine humidity problems but, at the same time, implies that the heat rejection at the condenser increases. Together with the increased steam mass flow, this produces an increase in the condenser heat load and, therefore in the number of required ACC cells (Figure 7.23).

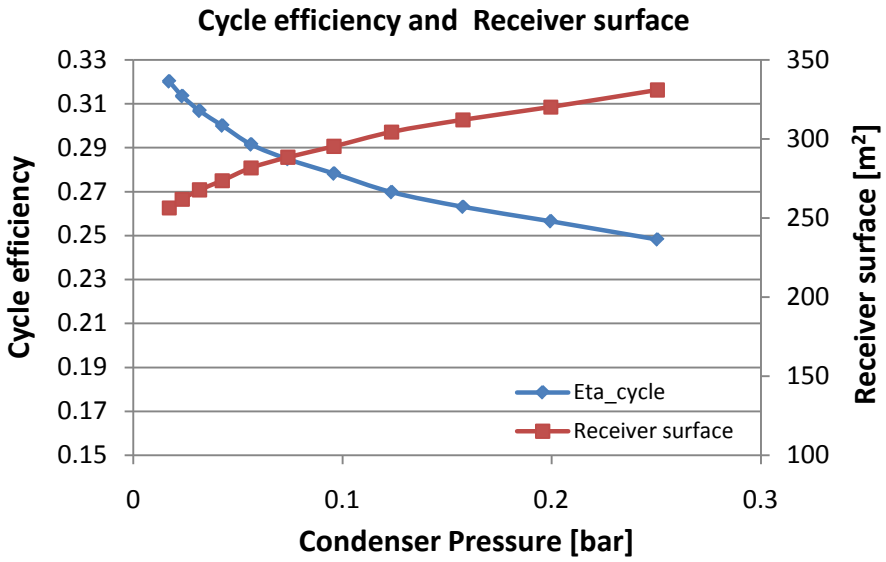

Figure 7.23: Cycle efficiency and Receiver surface variation with Condenser Pressure

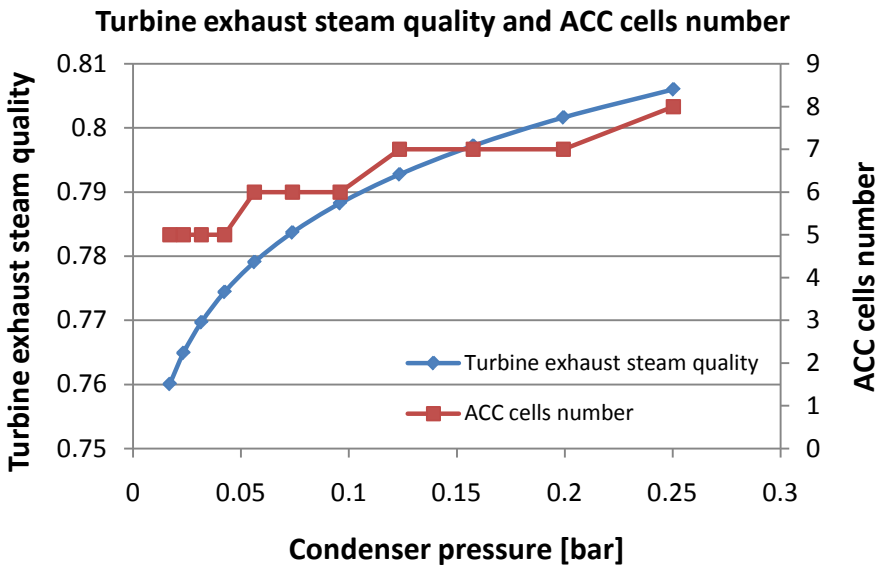

Figure 7.24: Turbine exhaust steam quality and ACC cells number variation with Condenser Pressure

Also the pre-heating line is strongly affected by the condenser pressure variation. When the pressure increases, the overall temperature difference between the condenser and the boiler inlet decreases and, with it, also the feedwater temperature increase in each exchanger. Being TTD and DCA constant, the FWHs effectiveness both in subcooling and condensing sections decrease, as shown in Figure 7.24.

Nevertheless, being all the feedwater line at a higher temperature and the TTD constant, the steam extractions take place at a higher temperature and pressure; the same steam contributes less to power production and this, even if slightly, contributes to the need to increase the total steam flowing in the turbine.

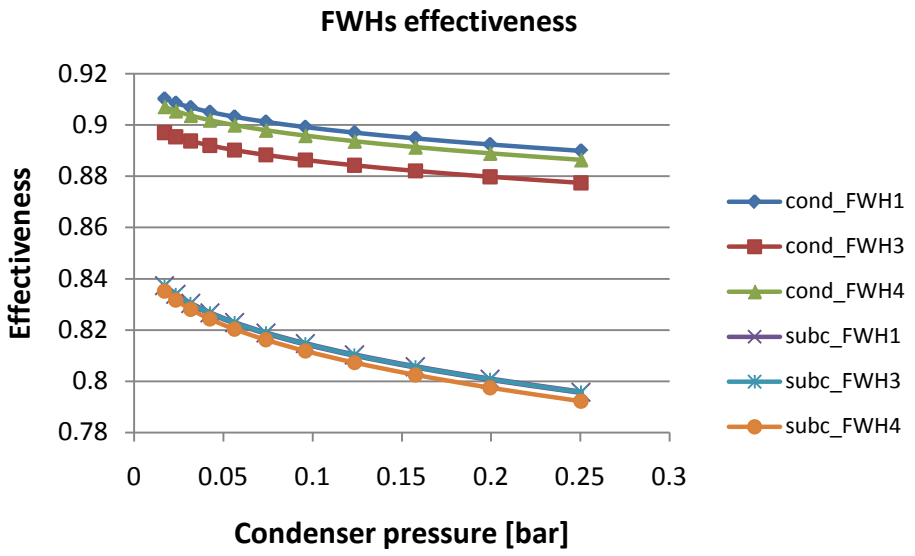

Figure 7.25: FWHs effectiveness variation with Condenser Pressure

7.7 Pressure drops in the FWHs variation

As default, pressure drop in the feedwater heaters has been assumed to be 5% for feedwater and negligible for condensing steam and drains. Actually, this value depends on particular features of the feedwater heaters, as pipes disposition, diameter and roughness or presence of bends and valves. The sensitivity analysis has been done varying the pressure drop value in the range 0 – 15%.

Figure 7.25 shows that increasing pressure drop, cycle efficiency decreases and consequently the receiver dimensions increase. The effect is not so remarkable, because it is given only by the increase of power absorbed by the pumping stations and this, although sensitive, is not so high, being given only by a pressure drop and not by a water flow variation (Figure 7.26).

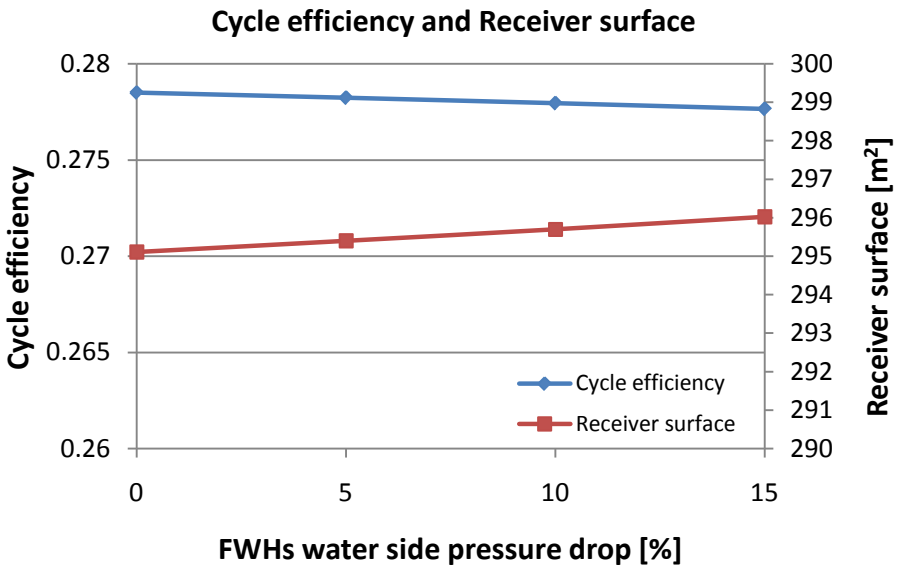

Figure 7.26: Cycle efficiency and Receiver Surface variation with FWHs Pressure Drop

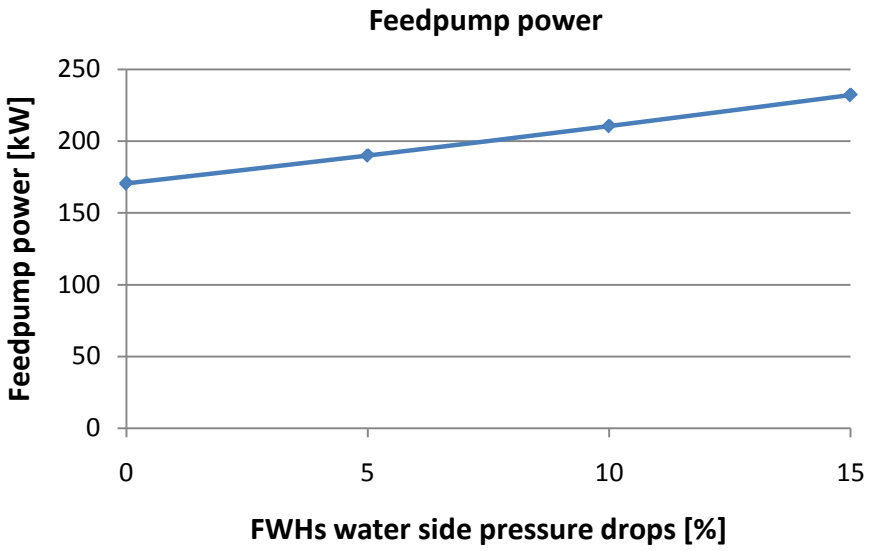

Figure 7.27: Feedpump power variation with FWHs water side pressure drops

Because of its definition (6.20), the overall temperature difference in the pre-heating line does not vary. The fourth feedwater heater, to the truth, experiences a small feedwater inlet temperature increase, due to the higher Δp provided by the feed pump. This, keeping fixed the DCA, brings to a small reduction in the

subcooling effectiveness. Also the condensing phase is partially affected by this phenomenon but the actual effectiveness variation is negligible (Figure 7.27).

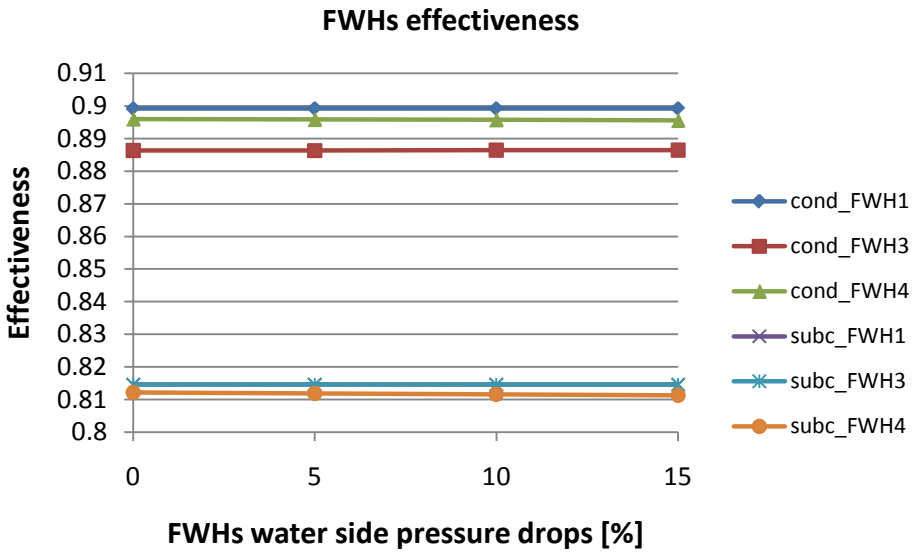

Figure 7.28: FWHs effectiveness variation with FWHs water side pressure drops

7.8 Type and design of pumping station

Among others, a choice left to the user is the adoption of a pumping station composed by a single pump with variable shaft speed or by 1 – 4 pumps with constant speed. All the cases have been tested with the model and, according to the design procedure described previously, no differences are appreciated among the results. The on design model, indeed, calculates the pressure drops that the pumping station has to overcome, the water mass flow and consequently the power absorbed. This power, is then divided into the user-defined number of pumps, not existing an influence of the pump rotational speed.

This result is actually trivial, but it has been considered useful to report it here to better highlight in the following chapters how a useless choice in on-design conditions will have an interesting relevance in part-load operation.

Table 7.3: Relative pumping station power consumption

	$W_{feedpump}/W_{gross,turbine}$
1 fixed speed pump	1.15%
2 fixed speed pumps	1.15%
3 fixed speed pumps	1.15%
4 fixed speed pumps	1.15%
1 variable speed pump	1.15%

7.9 Grid frequency variation

As well known, the grid frequency value is not really a design choice, as it depends on the national grid characteristics. The only choice in this case is between a 50Hz grid, typical of European, Asian and African countries, and a 60Hz grid, used in the U.S.A., Canada and in big part of the Southern America.

It has been considered interesting to analyze what effects could have the change of grid frequency, in order to understand if the geographical location of the plant could influence the performance in this sense.

Figures … show that the effect of shifting the grid frequency from 50 Hz to 60 Hz and therefore the generator rotational speed from 3000 to 3600 rpm is a generator friction losses increase and, therefore, a small increase of required steam mass flow. Due to that, also the pump power slightly increases and these two effects cause a cycle efficiency decrease, approximately equal to 0.1%.

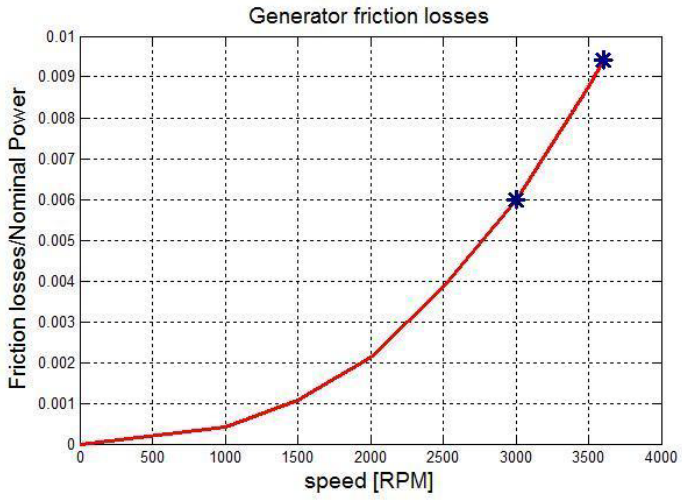

Figure 7.29: Generator friction losses for 3000 and 3600 RPM

In the case of multiple fixed speed pumping stations, the pumps rotating speed changes with the grid frequency, but this has been considered negligible for the pump performance.

Apart from the small mass flow increase, all the others components work thus without performance changes. It is worth noting that when switching to 60 Hz, turbine blade tip speed increases by 20% and the common limit of about 500 m/s might be surpassed. In this case, a different gearbox between turbine and generator would have to be installed.

7.10 ACC cell variation

The default solution in the model is a typical ACC cell taken from literature [64] and at the moment the user do not have the possibility to change it. It has been considered interesting, however, to study how a change in the size of the ACC cell could affect the plant performance considering a second cell with a higher air volumetric flow:

Table 7.4: Default and Bigger ACC cell air voulmetric flow

Air volumetric flow reference cell [m^3/s]	288.8
Air volumetric flow bigger cell [m^3/s]	529.4

The results of the simulations show that the effect of using a difference cell size is positive or negative depending on the plant size, especially on the difference between the needed air mass flow and the real one provided by the cells. With a 20 MW plant, for example, the air mass flow required to reject the condenser thermal power is 4985 kg/s. Considering the bigger cell, the ratio between required and single-cell mass flow is so

$$Mass\ flow\ ratio = 8.22$$

To keep the conditions the most possibly similar to that desired, the number of cells will be defined as the nearest integer number (see also Paragraph 6.4.2).

$$Cells\ number = 8$$

and the real air mass flow will so be

$$Elaborated\ air\ mass\ flow = 4852\ kg/s$$

With the smaller, default cell, the same rule is employed, but the smaller size let a more precise approximation of the desired mass flow. In this case, therefore, the mass flow ratio and the number of cells would be

$$Mass\ flow\ ratio = 15.006$$

$$Cells\ number = 15$$

and, finally, the air mass flow draught by the condenser will be:

$$Elaborated\ air\ mass\ flow = 4963\ kg/s$$

In the case of a 20 MW plant, so, to use a smaller cell implies a bigger amount of air treated and, therefore, a higher fan power consumption.

With a 50 MW plant, instead, the situation is overturn. Using the just described relations, the following results appear:

Table 7.5: Default and bigger ACC cell parameters for a 50 MW plant

	Reference cell	**Bigger cell**
Required air mass flow [kg/s]	12407	12488
$\dot{m}_{required\ air}/\dot{m}_{cell\ air}$	37.497	20.589
Cells number	37	21
Actual air mass flow [kg/s]	12243	12737

Notice that the small difference in the condenser required air mass flow is due to the fact that the model is already considering a slightly difference steam mass flow. This is due to the difference in cycle efficiency related with the two cases (ACC power increases → cycle efficiency decreases → steam mass flow increases → condenser heat rejection increases → required air mass flow increases).

Basically, in this case, to the capability of the smaller cell to better approximate the desired air mass flow corresponds a decrease in the air draught by the fan, and therefore a lower power consumption. This non-linear behavior is given by the discrete variation in air mass flow.

As said, the model does not currently include the possibility for the user to change the ACC cell, but in the future the possibility to design the desired or to choose among a set of pre-designed cells could be implemented.

7.11 Reference irradiance with different intensity fluxes

The multiplying factor of the radiation map is an important parameter for the boiler sizing and is related to the peak flux used in the design process. A variation of this parameter can be directly linked to the solar radiation of the site where a solar plant will be built. In the case of the PS10 in Seville this value is 981 W/m^2 but everyone knows that in other part of the world (middle East, norh-american deserts) the radiation can reach higher values.

The simulation has been conducted changing the multiplying factor of the radiation map from 0.5 to 2, considering the distribution map of 21st March at 12.00.

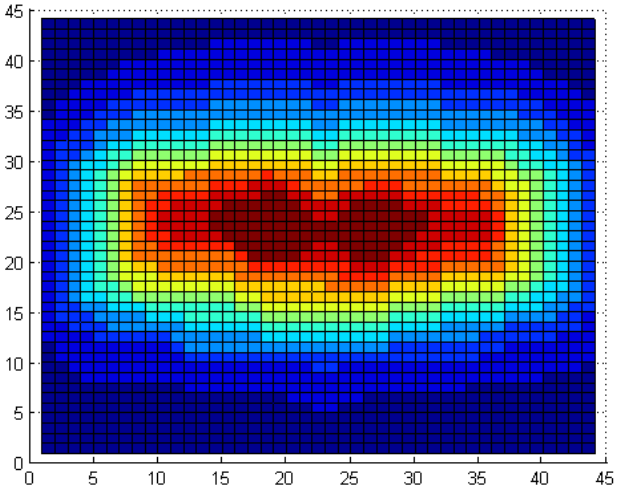

Figure 7.30: Radiation map on 21st March at 12.00

First of all what can be noticed is that the power block is not influenced because the steam production remain the same as requested at the fixed conditions (15MW,40 bar), while the main change is the boiler size because the on-design boiler model works to find the right size to provide the necessary steam flow to the power cycle.

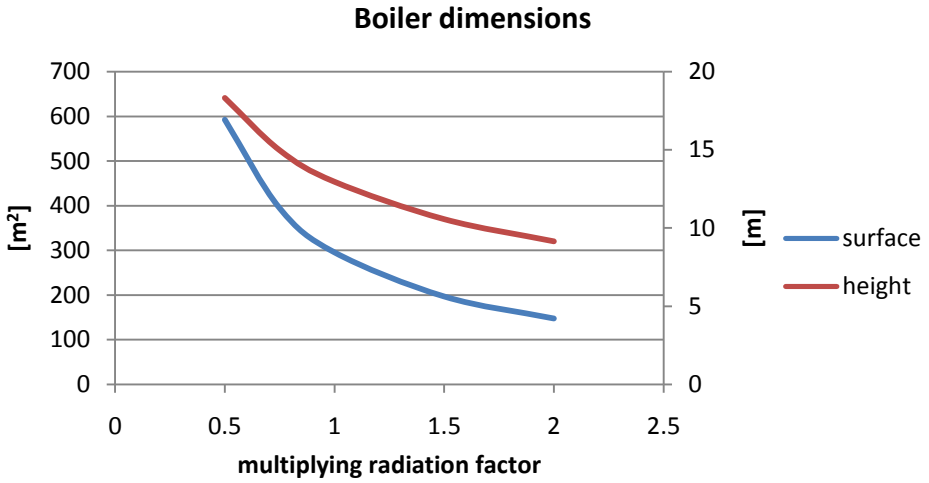

Figure 7.31: Boiler dimensions variation with multiplying radiation factor

Once the steam quality requested at the outlet, and therefore its enthalpy, is fixed, so is the amount of thermal energy Q to the fluid to produce a certain steam flow. Increasing the multiplying radiation factor the amount of energy per square meter increases and, therefore, the boiler surface necessary to provide the same Q decreases as shown in Fig. 7.31.

A decrease of boiler height has a double effect on pressure drops:

- The length of the lower raiser, considering fixed the pump position according to the power of the plant chosen, increases and therefore the pressure drops of the lower riser circuit increase too.
- The pressure drops linked to the boiler decrease because the most important component is due to gravity , which depends on boiler height.

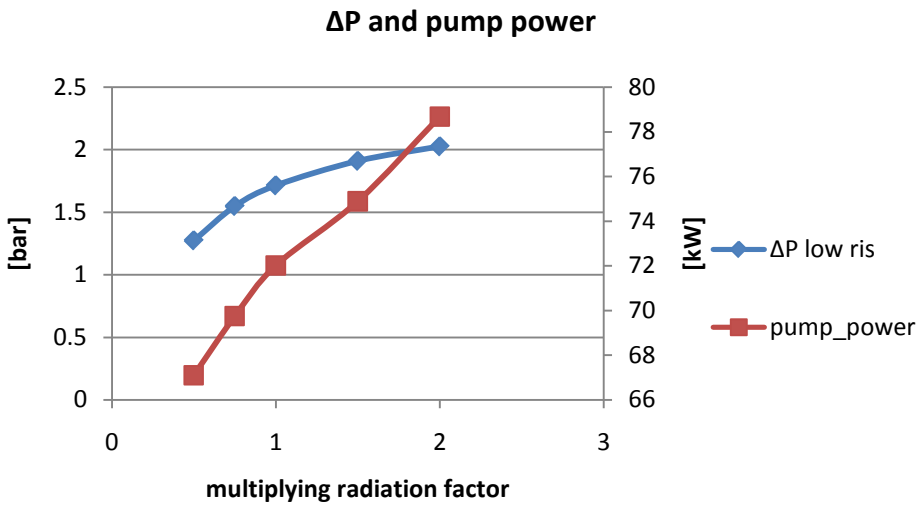

Figure 7.32: Pump power and ΔP variation with multiplying radiation factor

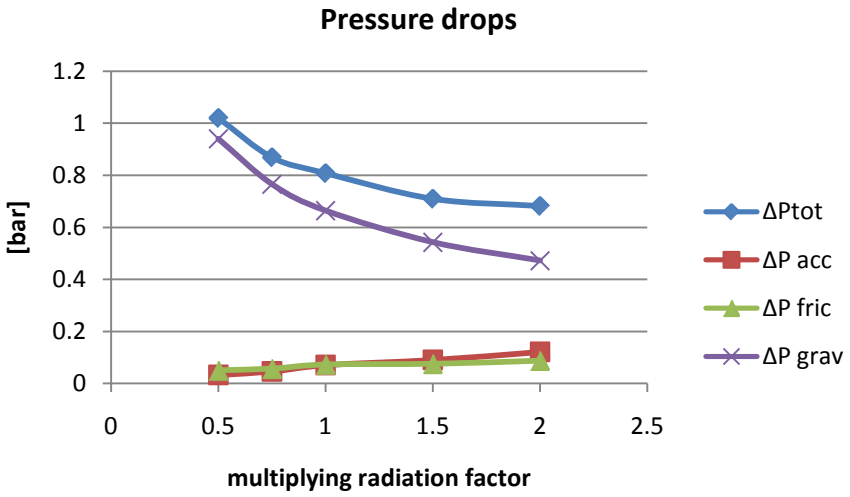

Figure 7.33: Pressure drops variation with multiplying radiation factor

The water flow distribution changes in the shape because, if the solar radiation increases and the steam quality is controlled, the water flow in each pipe must increase. At the same time the water flow for each pipe increases because the pipe diameter is fixed and if the boiler width decreases a smaller number of tubes will be used for the same total mass flow.

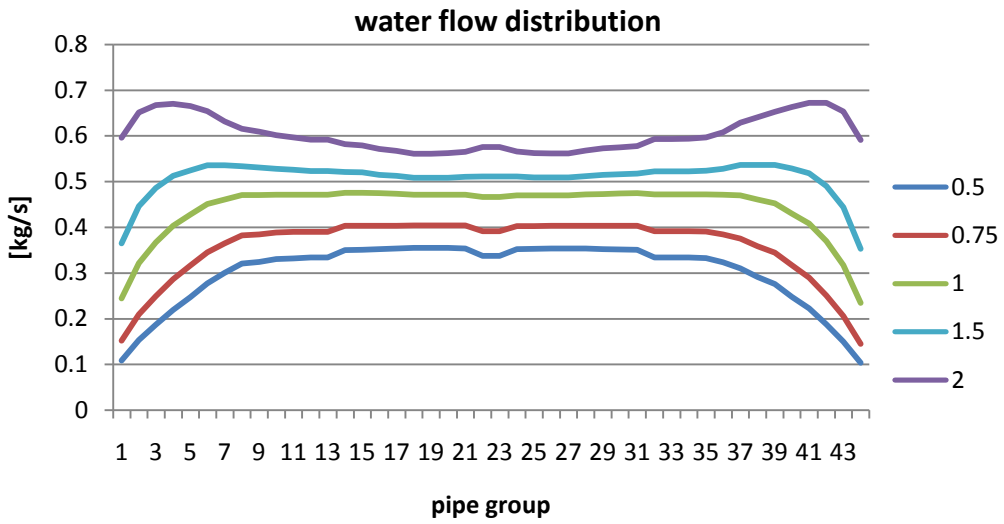

Figure 7.34: Water flow variation with multiplying radiation factor

From values of the multiplying factor from 0.5 to 1 the water flow distribution shows a bigger flow for the central group of pipes that are more radiated and smaller for side pipes. Instead, considering, the multiplying factor above 1 the water flow distribution shows a mass flow peak near the sides and lowest flow in the centre where there is a higher radiation.

This happens because the water flow distribution is found looking for the same pressure drop in each pipe. When the solar flux and the steam production increase the water flow needed by each pipe to not reach high steam quality values increases and therefore the acceleration and friction pressure drop components begin to be relevant with respect to the gravity component, especially when more steam is produced, imposing the new different configuration.

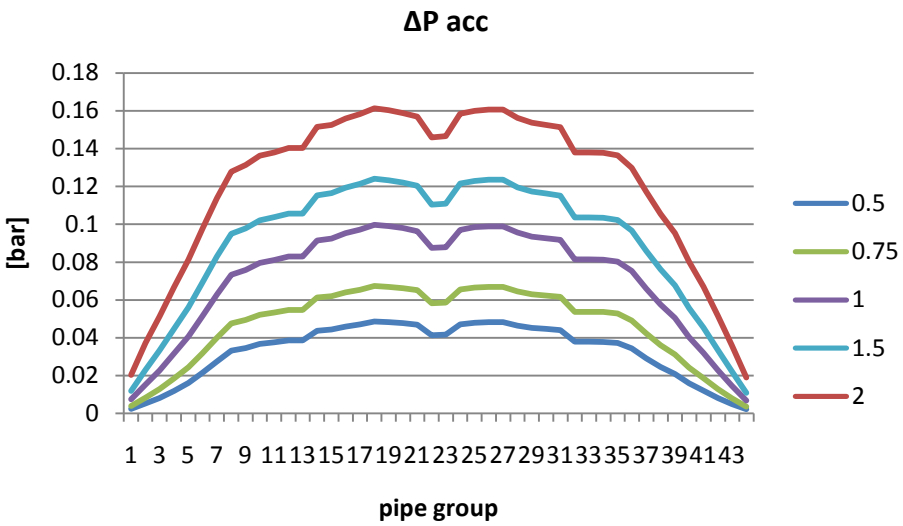

Figure 7.35: Accelerative ΔP variation with multiplying radiation factor

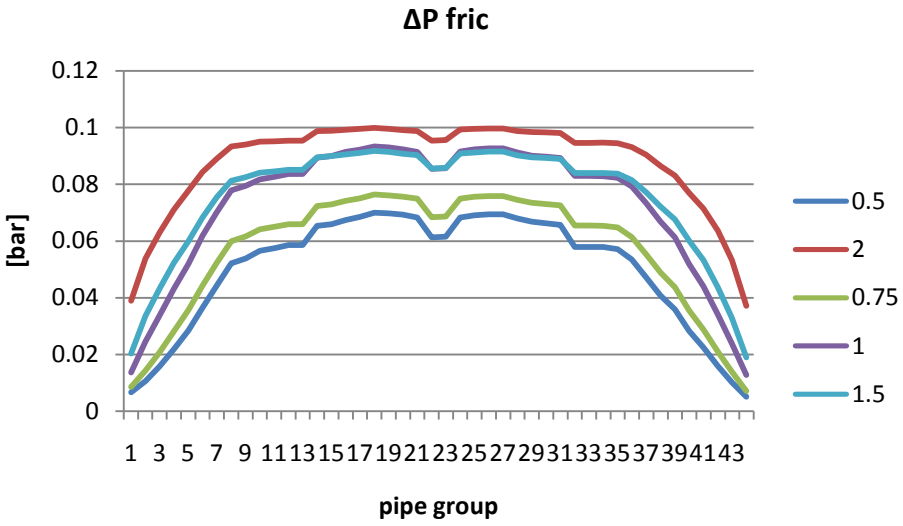

Figure 7.36: Frictional ΔP variation with multiplying radiation factor

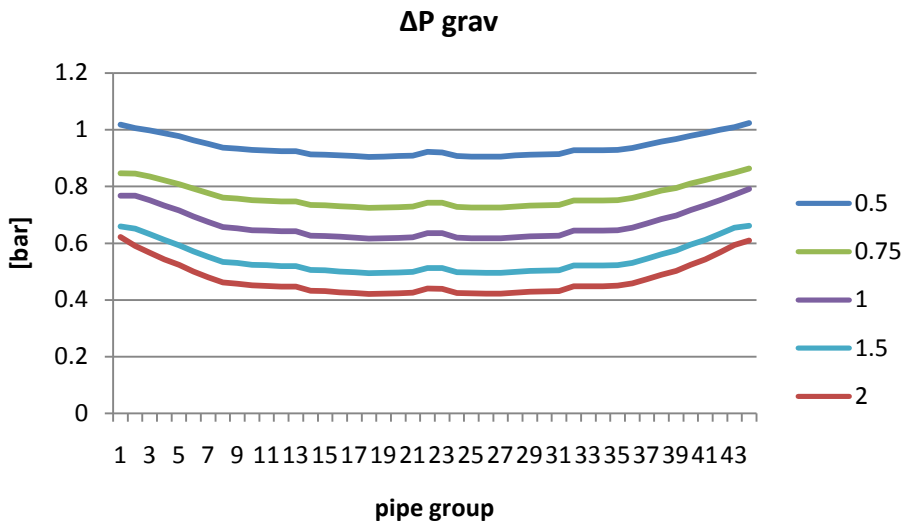

Figure 7.37: Gravitational ΔP variation with multiplying radiation factor

The steam quality at the outlet of each pipe reaches higher values for a bigger multiplying factor but at the same time to obtain the 0.2 average value the side tubes present a lower quality with respect to side pipes with a lower multiplying factor.

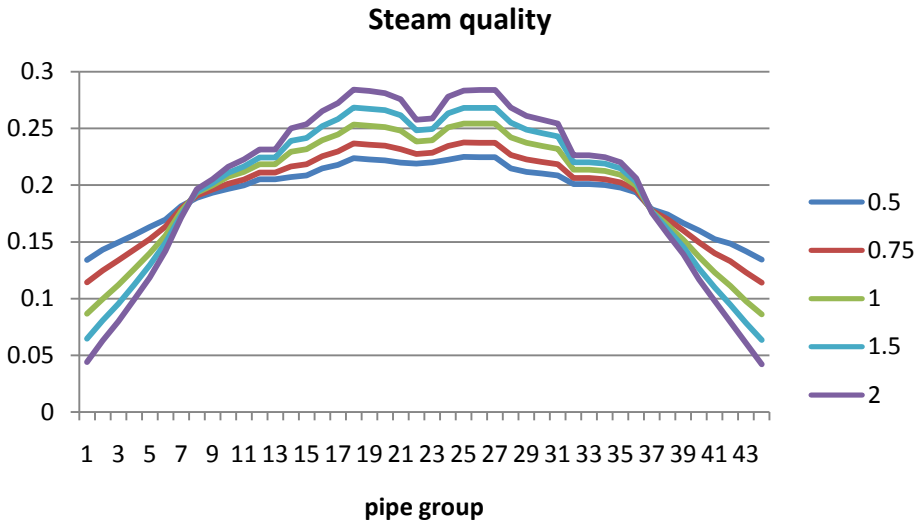

Figure 7.38: Steam quality variation with multiplying radiation factor

7.12 Average steam quality

The average steam quality at the outlet of the boiler pipes is a very important parameter to control the heat transfer and then the wall temperature of the tubes. To avoid very high temperatures, that would induce to use costly material, a very high internal heat transfer coefficient must be assured in the boiler pipes. As shown by Fig. 5.12 the highest value of this coefficient is reached in the *saturated flow boiling region* with a steam quality from 0 to 0.8. Above this value problems of *dry-out* (lack of boiling water in contact with internal walls) or *departure from nucleate boiling* (steam film making in contact with internal walls) can occur largely increasing the wall temperature and creating cracks or deformations . For this reason a control on steam quality is needed, for example the PS10 operates with an average value of 0.2 that is the default value in the model.

Changing the average steam quality at the outlet of the boiler does not affect the power block because the steam production is fixed, while it influences the boiler size, the water flow distribution, the steam quality distribution and the pump power for boiler circulation.

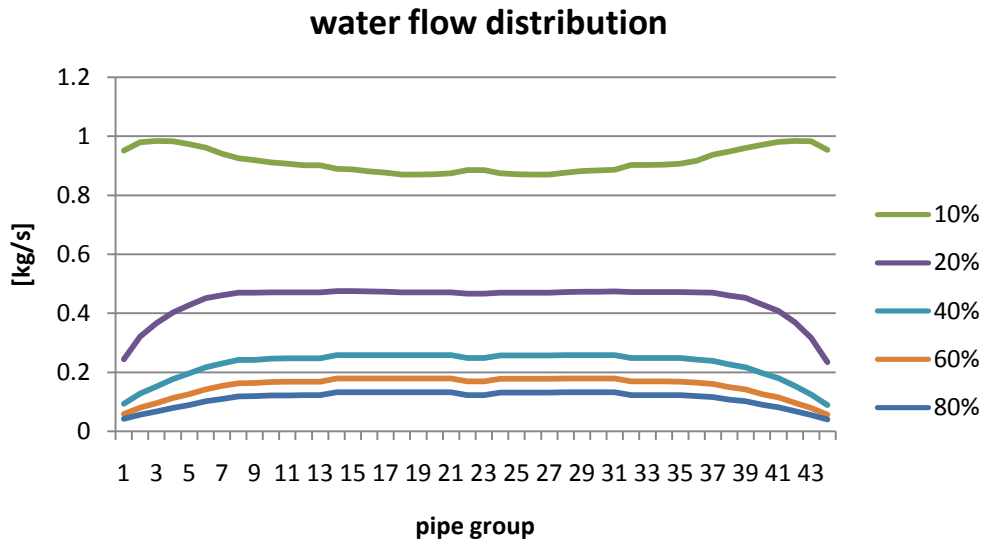

Figure 7.39: Water flow variation with steam quality

Once fixed the input radiation, the lower the admissible average steam quality the higher the water mass flow in each pipe. The different distribution for the 10% average quality is linked to the fact that increasing the mass flow the

accelerative and friction pressure drops components begin more relevant as already explained in par. 7.11.

Increasing the average steam quality implies a slight reduction in boiler surface because on one side the enthalpy difference between inlet and outlet flow increases but at the same time the total water flow circulating inside the boiler decreases, reducing the heat necessary to promote the phase change.

$$Surface \propto \frac{mass\ flow}{\Delta h} \tag{7.5}$$

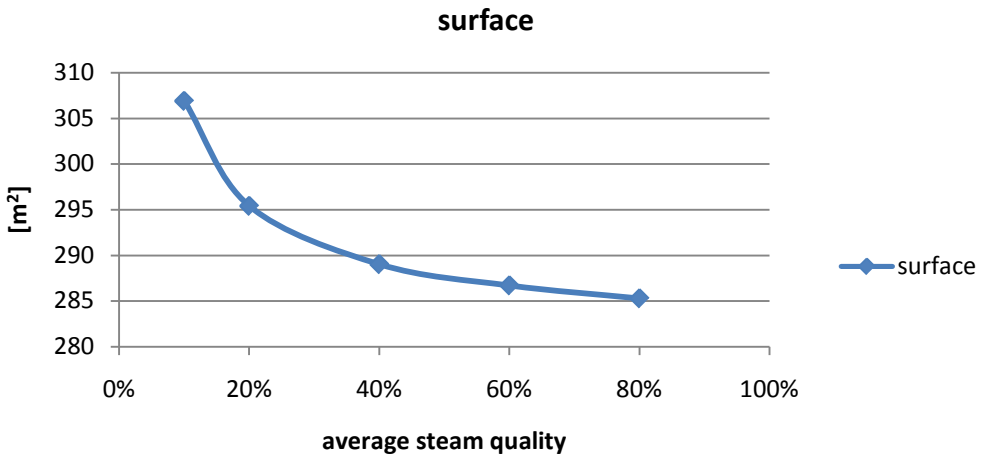

Figure 7.40: Surface variation with steam quality

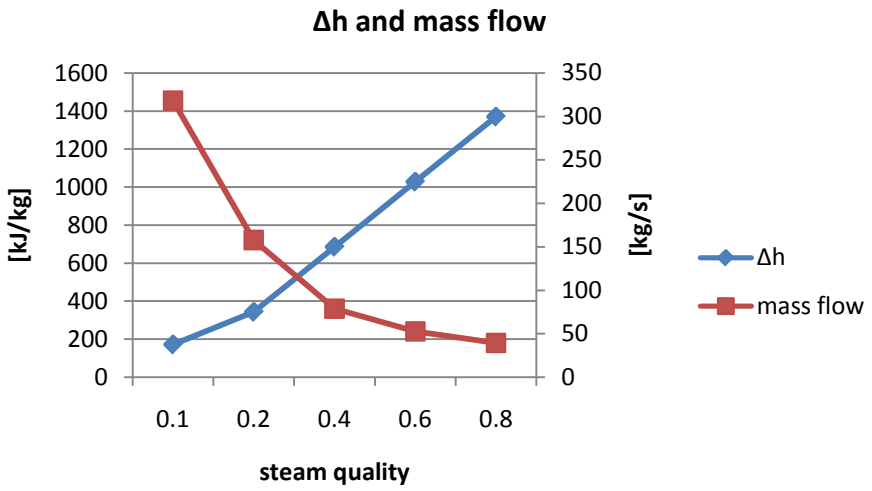

Figure 7.41: Δh and mass flow variation with steam quality

The decrease of boiler height causes a reduction in the gravity component of the pressure drops that is the most relevant and, for this reason, this affects very much the total loss.

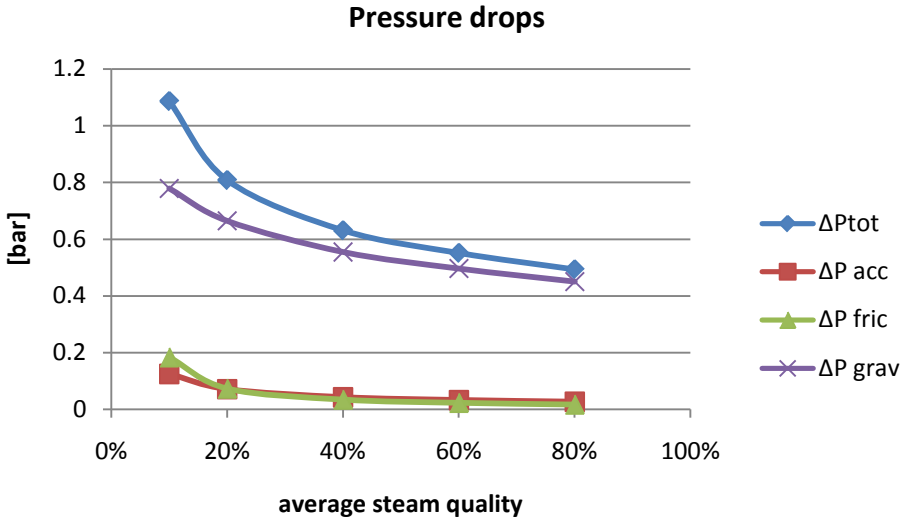

Figure 7.42: Pressure drops variation with steam quality

Obviously the steam quality distribution also changes, maintaining an average value around the chosen one. Fig. 7.42 shows an important information for the problems of thermal crisis of the pipe. Imposing an average value, in fact, means that steam quality is below the average at some pipes and above it at others

(where there is more radiation). In the case of 0.8 mean steam quality, central pipes reach 0.9 what is likely to bring about mechanical integrity problems due to thermal stresses.

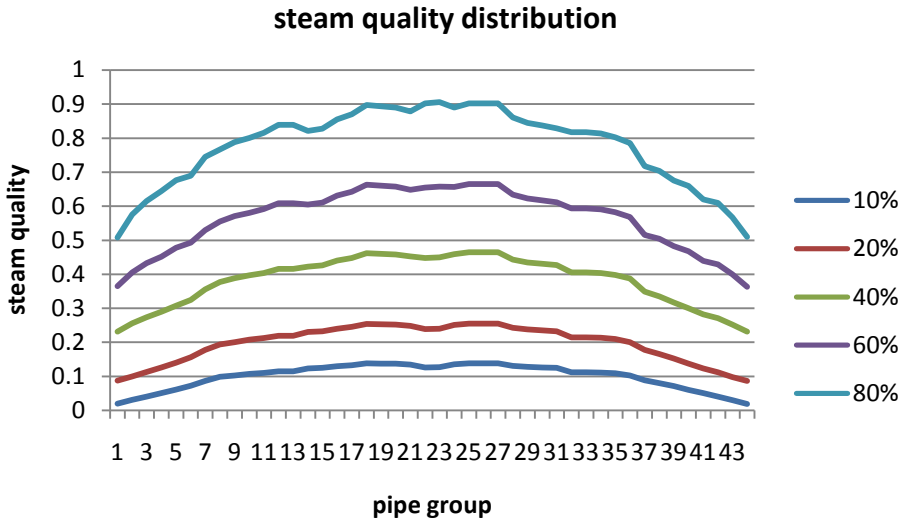

Figure 7.43: Steam quality distribution variation with average steam quality

7.13 Boiler efficiency

The boiler efficiency contains all the information about the thermal performance of the boiler. It changes according to the type of receiver (external, internal), air temperature, wind velocity, etc.. as shown in paragraph 5.2.2. Changing this value can be help the user to understand what happens if the boiler technology changes.

Changing the boiler efficiency will affect principally the boiler size and therefore pressure drops. Decreasing the boiler efficiency increases the radiation that must insolate the boiler surface for the same heat input to the steam cycle. Hence, boiler size increases for a given radiation map or another option would be to use a bigger heliostat field with the same receiver, therefore having more radiation at each cell of the map, even if this is not included in the model because of the lack of an heliostat field model.

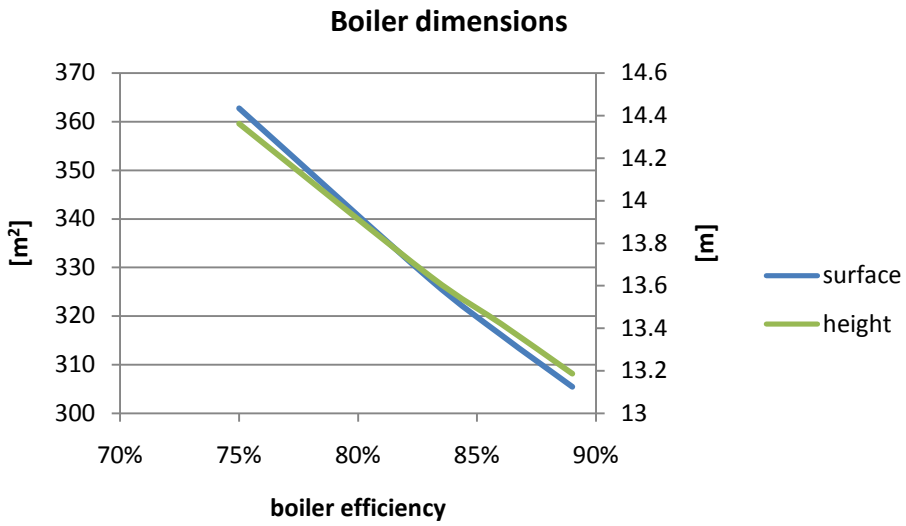

Figure 7.44: Boiler dimensions variation with boiler efficiency

The pressure drops decrease when boiler efficiency is increased because the gravity component, which is strictly linked to the boiler height, is the most relevant.

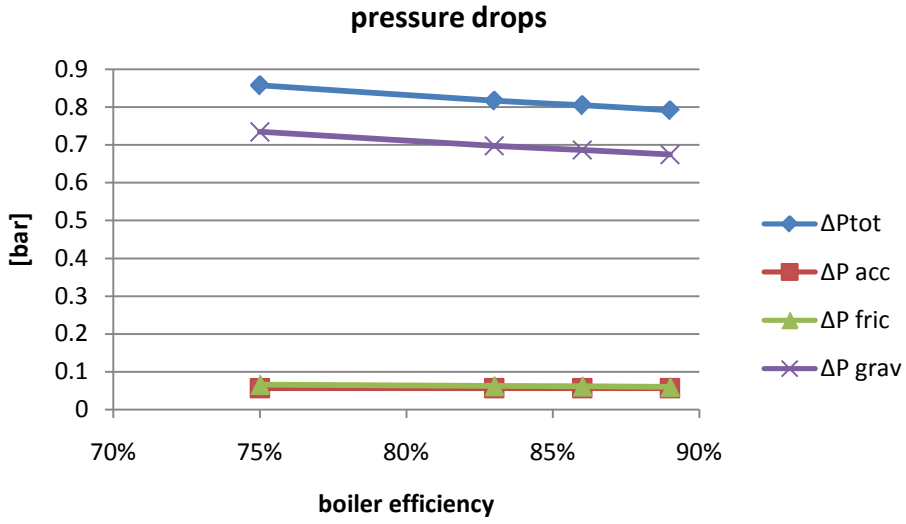

Figure 7.45: Pressure drops variation with boiler efficiency

7.14 Pipe diameter

The boiling pipe diameter chosen in the plant design is a tradeoff between pump/s consumption and boiler surface and for this reason it is an important parameter to study.

Changing the internal diameter of boiling pipes (from 25 to 100 mm) the first great impact is on the boiler pressure drops. In particular reducing the diameter under 50 mm, considering a constant absolute roughness (0.0547 mm), the friction and the accelerative component increase enormously achieving the same order of magnitude as the gravity one.

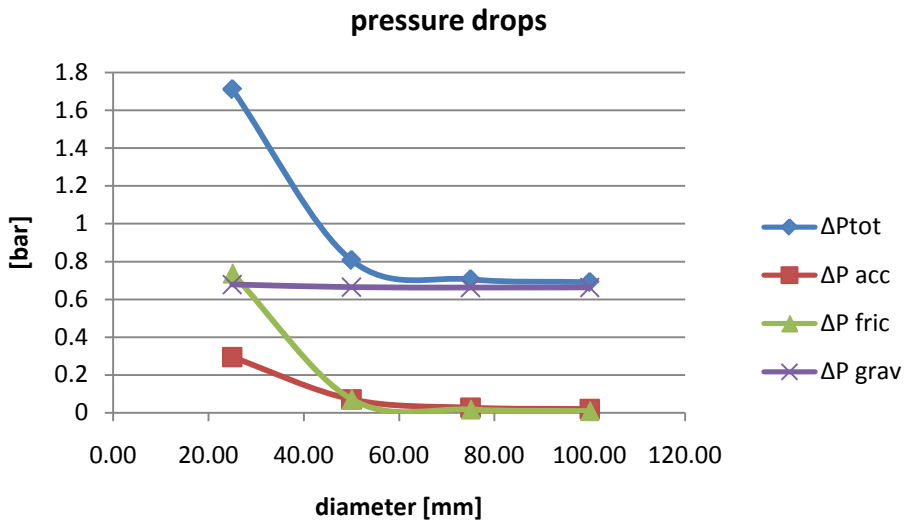

Figure 7.46: Pressure drops variation with pipe diameter

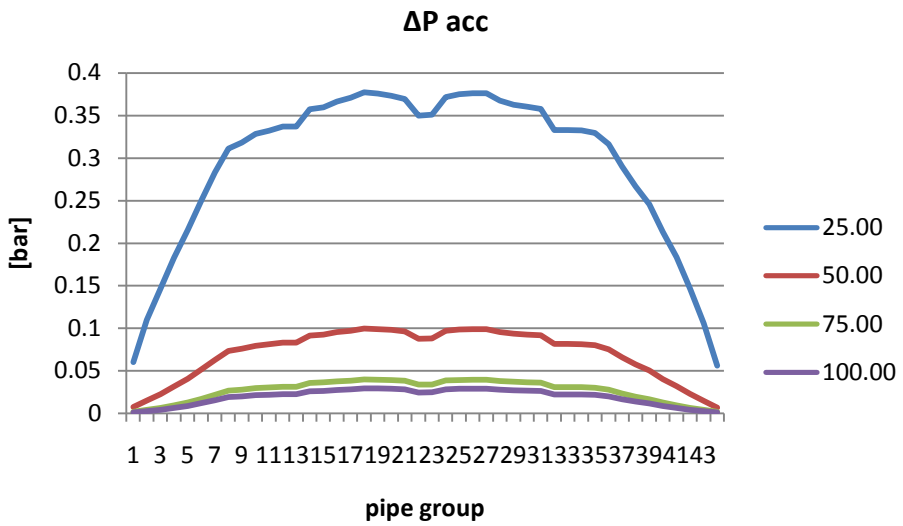

Figure 7.47: Accelerative ΔP variation with pipe diameter

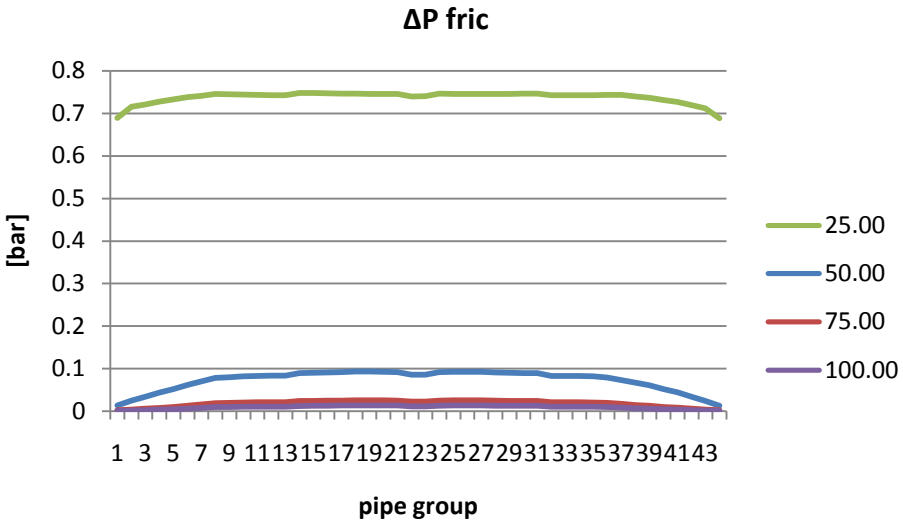

Figure 7.48: Frictional ΔP variation with pipe diameter

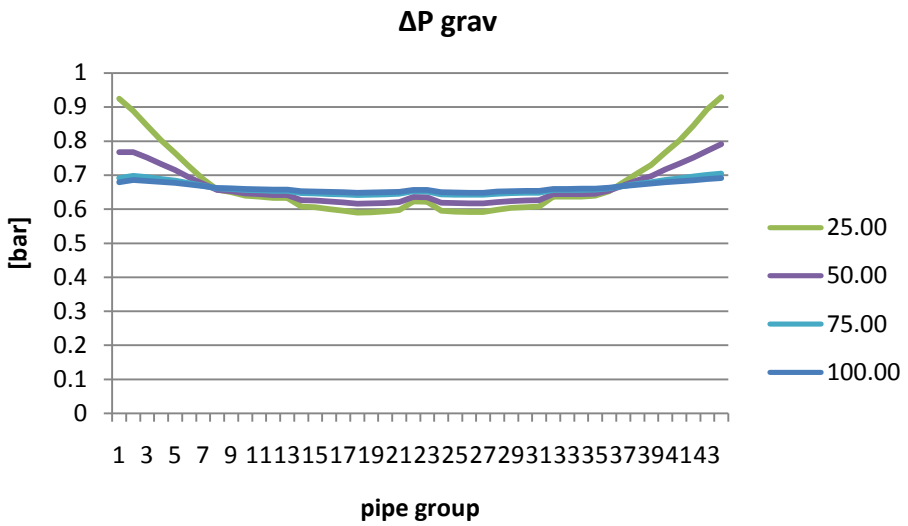

Figure 7.49: Gravitational ΔP variation with pipe diameter

The total heat input practically does not change and therefore the total mass flow; for these reasons, an increase of pressure drops turns into an increase of pump consumption.

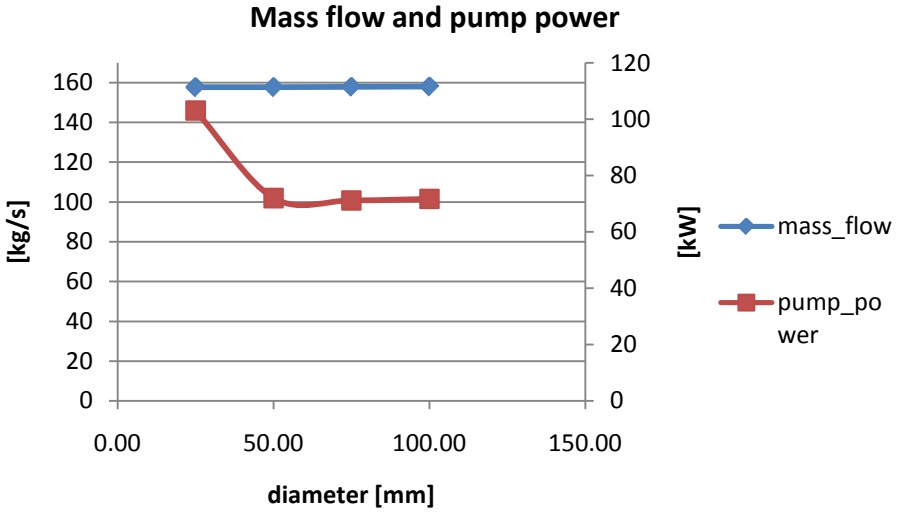

Figure 7.50: Mass flow and pump power variation with pipe diameter

Even the surface necessary practically doesn't change, meaning that the pipes diameter influences the number of pipes in the boiler. Changing the number of pipes the mass flow distribution for each pipe changes showing an increase of the absolute values for a bigger diameter.

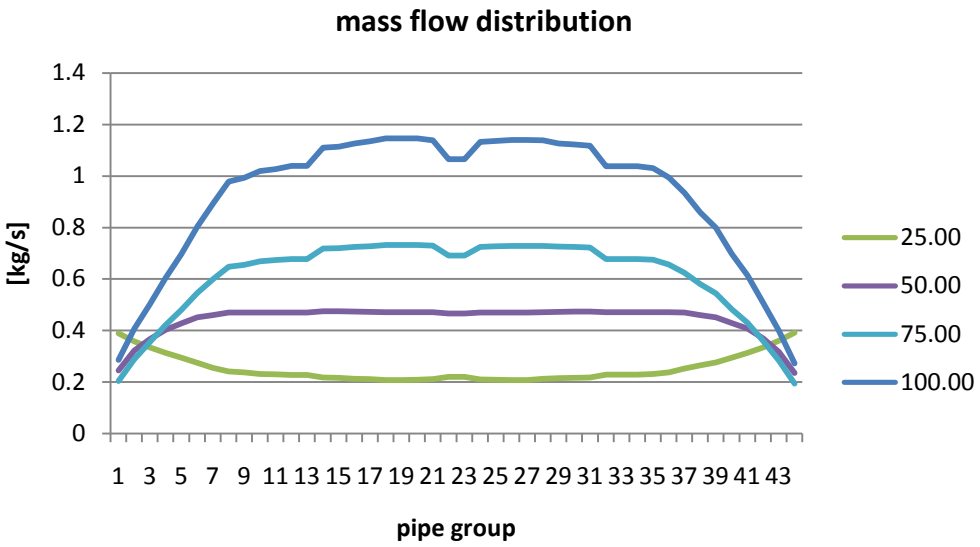

Figure 7.51: Mass flow distribution variation with pipe diameter

The different distribution for a 25 mm diameter piping is caused by the higher impact of accelerative but most of all of the friction component of pressure drops.

8. OFF DESIGN MODEL

Solar tower power plants operation is inevitably related with the particular features of solar insulation. As well known, solar energy availability on the heliostats varies depending on the day of the year, the hour in the day and weather conditions, which have relevant influence also on energy losses from the collector field to the central receiver and from this latter component itself. Due to that, the plant seldom operates in rated conditions and a tool to describe the so called off-design or part-load operation becomes fundamental.

Starting from the variation of thermal power reaching the receiver, both in terms of intensity and distribution, the new behavior of the plant has so been described thanks to appropriate assumptions and correlations. As in the on design case, the global model is composed by a boiler and a power-block sub-model, which interact each other to identify the new operating point.

8.1 Off-design boiler model

Off-design performance of the boiler is analyzed with a very simple approach. Actually, off and on-design models differ basically on a macroscopic scale. Steam production and thermodynamic properties are indeed calculated starting from a different radiation map, assuming that the boiler geometry calculated in on-design conditions remain constant and considering a matching pressure between drum and turbine. Besides these differences, the off-design boiler model follows the methodology exposed in par. 5.2.1 and 5.2.2 with regard to pressure losses and thermal performance calculations. Water flow distribution, pressure drops and energy balance at each segment of the pipes are calculated similarly and, therefore, will not be discussed further in this chapter.

Considering the pumping station as a fundamental component of the boiler, its off-design behavior has been studied and properly described too. In particular, this is strongly dependent on the kind of pumping station adopted and on the corresponding part-load regulation strategy.

To sum up, boiler off-design behavior is basically influenced by:

- Off-design radiation map.
- Boiler-turbine matching (described in Par. 8.3)

– Off-design pump behavior.

8.1.1 Off-design radiation map

The main parameter that can be given as input in the off-design simulation is the new radiation map, according to the particular condition that the user wants to analyze. The availability of a high number of radiation maps on the receiver would allow the calculation of the plant part-load operation in the most representative conditions, allowing also for an annual approximate simulation. Regrettably, the public availability of radiation maps is extremely scarce and, hence, only three maps, representatives of three different times of the day and of the year, are currently available in the model.

– March 21st, 12.00. Seville latitude and PS10 heliostat field [31]

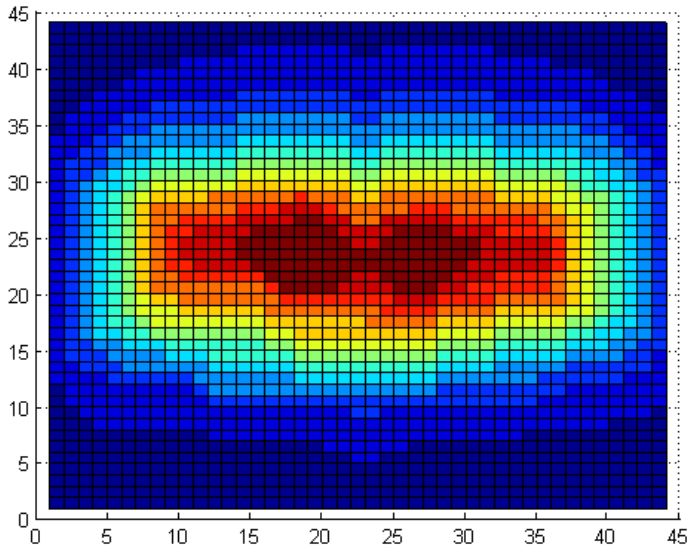

Figure 8.1: March 21st at 12.00

This map is even the on-design map. It can be chosen because the intensity value of the radiation can be changed, as explained in the following paragraph.

– June 21st , 4 PM. Seville latitude and PS10 heliostat field [31]

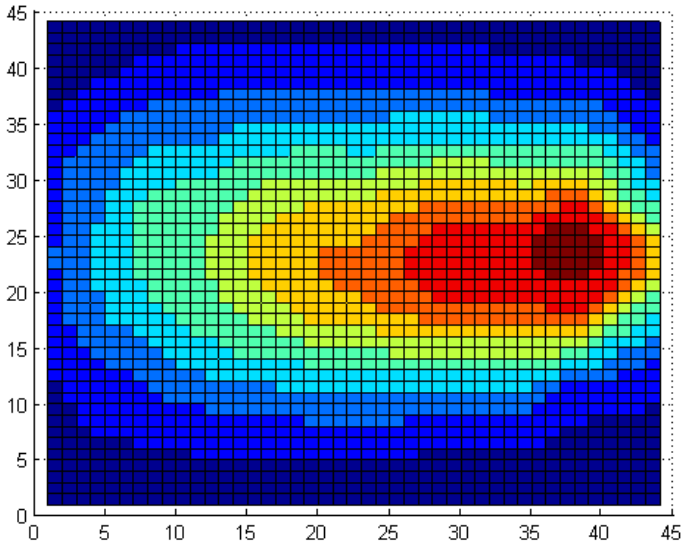

Figure 8.2:June 21st at 16.00

– June 21st , 10 AM. Seville latitude and PS10 heliostat field.
This map has actually been created as a mirror of the previous one, but it can be considered to represent the real map with a good approximation.

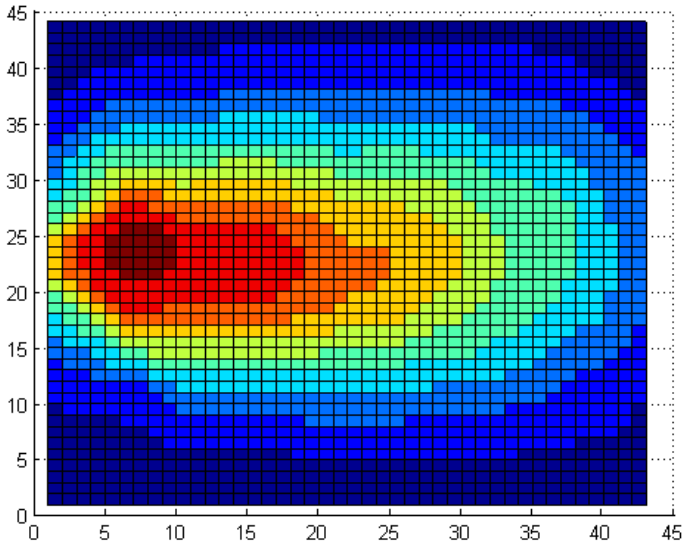

Figure 8.3: June 21st morning

To let the user study the off-design behavior on a higher number of different incoming radiation conditions, it has been considered that the previous radiation maps represent three possible radiation *distributions*, but that also the *intensity*

of radiation can be chosen. This would be the case of a different irradiance at ground level.

More precisely, for each off-design radiation map it is possible to change the radiation intensity by a "decreasing radiation coefficient" *I_red* that will be multiplied for each cell flux.

$$radiation_{real} = radiation * I_{red} \tag{8.1}$$

where:

- $I_{red} < 1$
- *Radiation*: is the radiation map (a 44 x 44 matrix with the solar flux values).

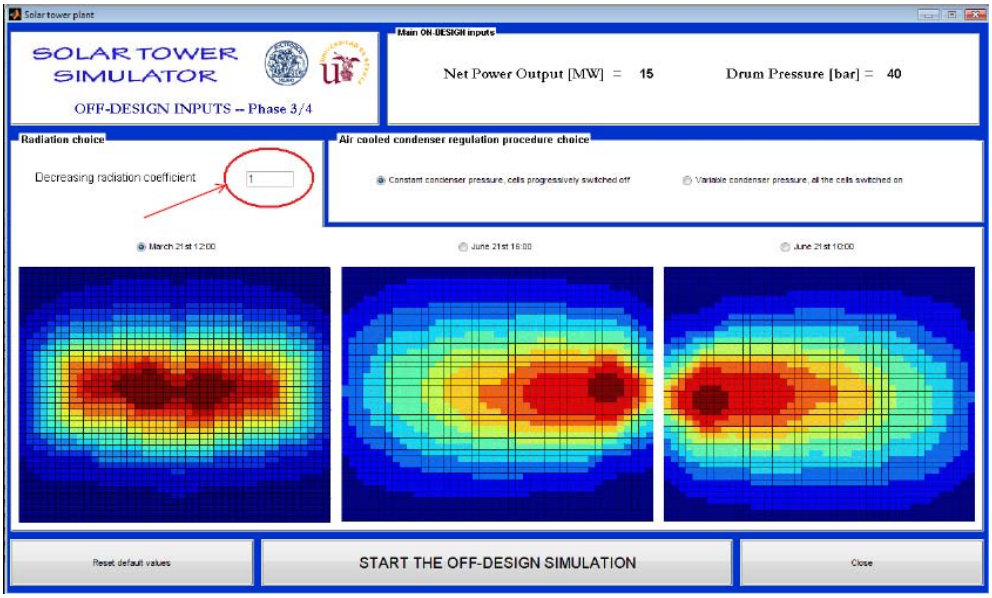

Figure 8.4: Decreasing radiation coefficient

The decreasing radiation coefficient homogenously decreases the thermal receiver input, keeping the distribution characteristic of the chosen map. This phenomenon can be thought to represent a case of hazy sky.

8.1.2 Off-design pump/s behavior

A pump normally operates within a pumping system to provide flow and head in accordance with the requirements of the pumping system itself. It is common to size the pumps in order to provide a “design” flow and head; during part-load operations, therefore, they will require some type of flow or head control to adequately satisfy the instantaneous demands of the pumping system.

As alredy described, the model includes two different pumping systems (several constant speed pumps or a single variable speed pump) and the choice will affect the boiler off-design performance because of the different control strategies.

Control strategy for constant speed pump/s

In the case of constant speed pump selection, is possible to choose the number of pumps to adopt in parallel disposition: from 1 to 4 pumps. Alligning more pumping equipments, in fact, provides flexibility to the operator of the system since he can start and stop pumping equipment based on system load or demand, thus reducing auxiliary power consumption.

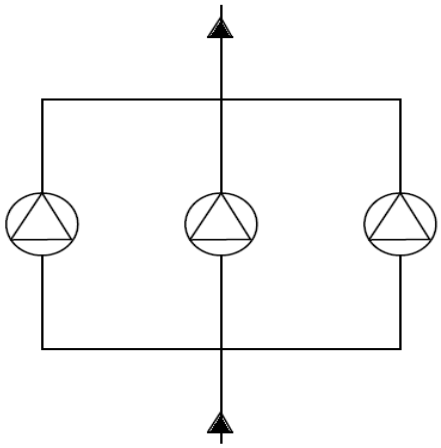

Figure 8.5:Example of three parallel pumps

For this pumping system, the pump capacity control in off-design conditions is done by *discharge throttling* which is the most common and economical (with respect to the capital costs of the capacity control devices required) means of capacity control. With this type of pump capacity control, the partial closure of a discharge piping throttle valve will increase the pumping system friction losses, causing the system head curve to move up and intersect the pump characteristc curve at a lower capacity.

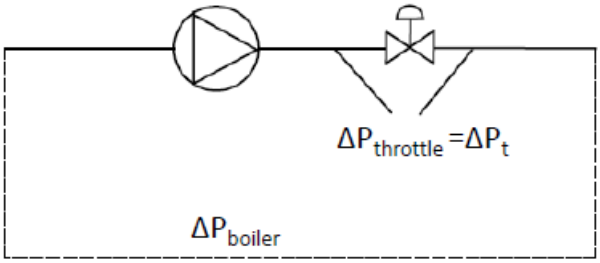

Figure 8.6: Single speed pump regulation scheme

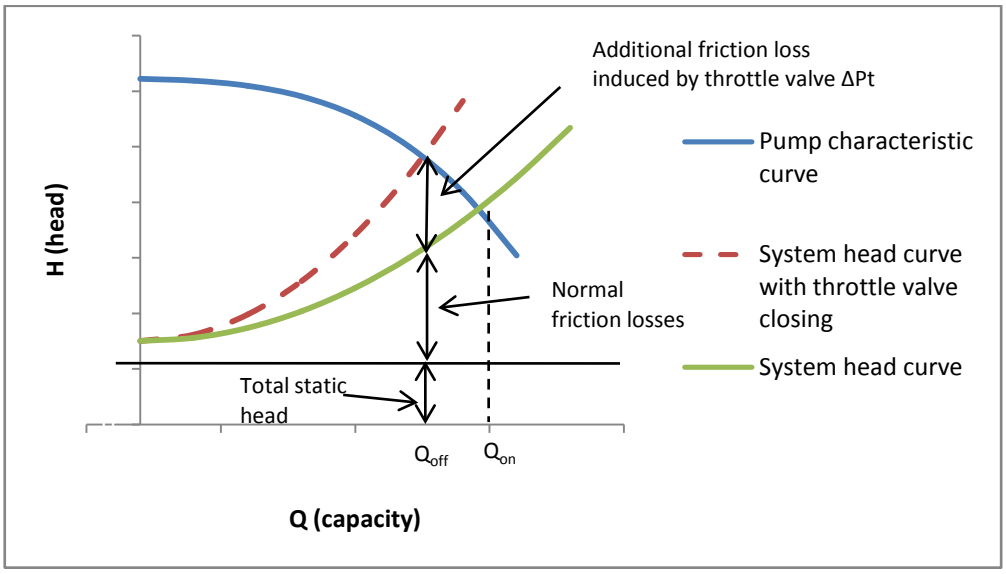

Figure 8.7: Pumping system with throttle flow

Fig. 8.7 shows that, using a throttle valve, it is possible to move from the nominal volumetric flow Q to a smaller value Q* according to the plant needs. In this condition the pump power will be:

$$W_{pump} = \frac{Q \cdot (\Delta P_t + \Delta P_{boiler\ \_off})}{\eta_{is} \cdot \eta_m \cdot \eta_{el}} \tag{8.2}$$

The main disadvantage of this kind of regulation is that, inducing more friction losses in the system, the pump operating point moves to one at lower efficiency and increased horsepower loss. On the other side, the advantages are that single speed pumps cost less and, moreover, adopting more pumps in parallel it is possible to maintain in service only the minimum number of pumps needed by the plant.

From the point of view of the model, the new working point is obtained substituing the new volumetric flow in the characteristic curves (Pag. 5.1.6) and extrapolating the new isoentropic efficiency and the new head pressure of the pump. Regarding the electrical efficiency, which depends on the power absorbed by the pump, an iterative cycle is necessary, the power itself depending also on the electrical losses and therefore on the electrical efficiency.

Control strategy for variable speed pump

Using variable speed pumps, capacity control is simply obtained by raising or lowering the pump speed; this way, the intersection of the pump characteristic curve with the system head curve changes. This configuration implies higher pump costs, but is economically justified for use in major power plant pumping systems. Additionally, with this type of control both a bigger and smaller flow can be obtained, differently from the case of a throttle valve, which can only reduce the flow.

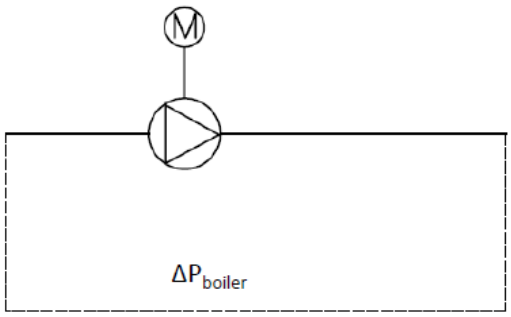

Figure 8.8: Variable speed pump regulation scheme

To study this configuration, the model generates a new set of curves for $n < n_{ref}$ using similarity/affinity laws:

$$\frac{H_1}{H_2} = \left(\frac{n_1}{n_2}\right)^2 \tag{8.3}$$

$$\frac{Q_1}{Q_2} = \frac{n_1}{n_2} \tag{8.4}$$

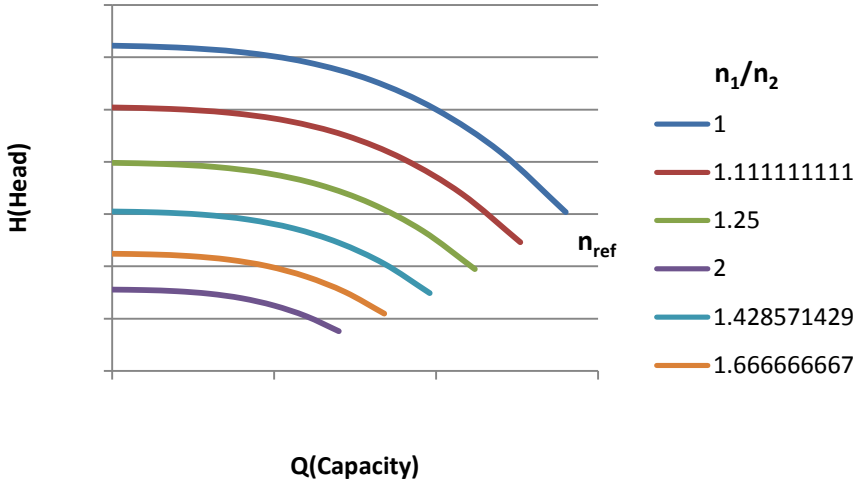

Figure 8.9: Set of new characteristic curves changing pump speed

This way, a new value of speed (n_2) that provides the new flow (Q_{off}) and pressure drop (H_{off}) values requested by the plant in the off-design condition is easily obtained.

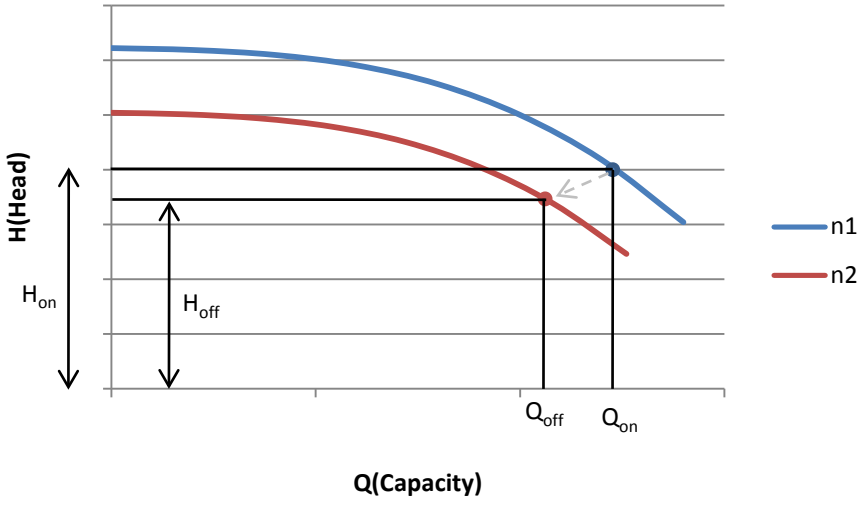

Figure 8.10:Variable speed pump regulation

By this control strategy, the pump will keep maximum efficiency and the power will be:

$$W_{pump} = \frac{Q_{off} \cdot \Delta P_{boiler\_off}}{\eta_{is} \cdot \eta_m \cdot \eta_{el}} \quad (8.5)$$

8.2 Off-design power-block model

Different insulation conditions generate the just described variations on the behavior of the boiler. The first immediate consequence for the power block system is a contemporary decrease in the steam mass flow and in the live steam pressure. In these conditions, the devices that compose the plant cannot be more reliably described with the simple assumptions made in the on-design conditions. This makes it necessary to identify proper laws that describe with an acceptable accuracy the behavior of the different components in these so called off-design conditions.

8.2.1 Turbine

During the off-design operation of the plant, it has been considered that the turbine is regulated with the so-called sliding pressure technique. This technique allows the steam cycle to automatically regulate itself within certain limits of load decreasing, varying the evaporation pressure and the steam mass flow without the need to intervene on regulating devices as the steam chest valves. For any generic load variation, a proper variation of the steam mass flow and temperature can be indeed always determined. The new conditions will satisfy the system's characteristic equations.

This strategy is extremely simple, but in real plants is often replaced by a "partial admission" strategy, from 50% to 15% of the nominal load approximately. This technique is based on the variation of the effective flow area of the first turbine nozzles, through the manipulation of the admission valves. In this way, the pressure admission can be controlled and kept constant at the desired value.

Looking for simplicity, the model at present considers only the first kind of regulation, also for loads lower than the 50%. A proper modeling of the second regulation strategy is currently being studied and it can be foreseen that it will be shortly introduced in the code.

The performance of the turbine at off-design with a sliding pressure regulation, is so considered to be reliably described by Stodola's *Law of the Ellipse*, whose mathematical implementation is exposed by Cooke in [58]. This law states that a multistage turbine expansion segment with several uncontrolled extraction groups and constant final back pressure can be treated as a series of "equivalent nozzles", each one of which is analogous to an extraction group. The governing law for each nozzle is described by the following formula, known as of Stodola's Ellipse:

$$\Phi = \frac{\dot{m}\sqrt{T_i}}{P_i} = \frac{\dot{m}_i}{\sqrt{P_i/v_i}} \propto \sqrt{1 - \left(\frac{B_i}{P_i}\right)^2} \tag{8.6}$$

where:

- Φ: mass flow coefficient.
- P_i: total pressure at inlet to any segment.
- T_i: total temperature at inlet to any segment.
- v_i: total specific volume at inlet to any segment.
- B_i: total pressure at exit from any segment.

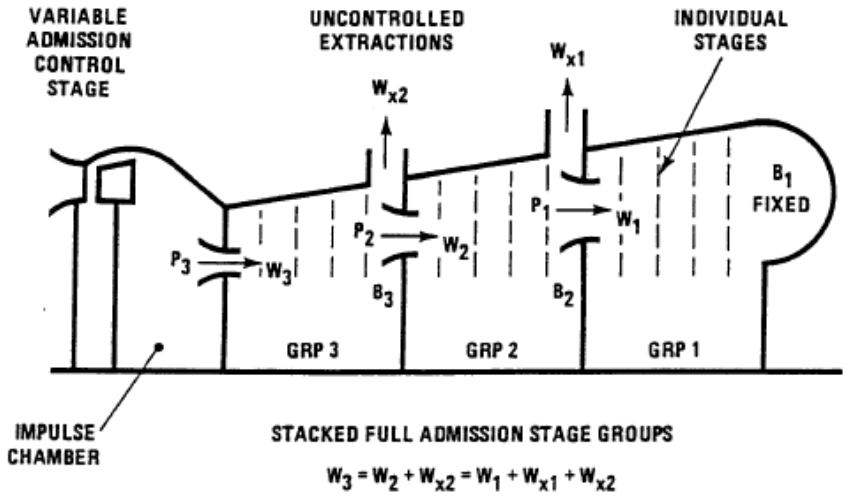

Figure 8.11: Schematic turbine expansion according to Stodola/Cooke approach

This proportionality, based on chocked turbine inlet section under any operating conditions, can be restated referring to a known "design point" which is regarded here as on-design operation:

$$\frac{\Phi_{i,OFF}}{\Phi_{i,ON}} = \frac{\sqrt{1-\left(\frac{B_{i,OFF}}{P_{i,OFF}}\right)^2}}{\sqrt{1-\left(\frac{B_{i,ON}}{P_{i,ON}}\right)^2}} \tag{8.7}$$

Through algebraic rearrangements and reductions, a codable formula can be obtained:

$$P_{i,OFF} = \sqrt{\dot{m}_{i,OFF}{}^2 T_{i,OFF} Y_{i,ON} + B_{i,OFF}{}^2} \tag{8.8}$$

where:

$$Y_{i,ON} = \left(\frac{{P_i}^2 - {B_i}^2}{{P_i}^2 {\Phi_i}^2}\right)_{ON} \tag{8.9}$$

Knowing the turbine behavior in on-design conditions, equations (8.8) and (8.9) permit solving the system "backwards", starting with the known fixed back-pressure imposed by the condenser (whose off-design working condition will be described later), and calculating the extraction pressures of each expansion segment.

A significant influence on the off design performances is given by the variations of the isentropic efficiency of each section in which we have sub-divided the turbine. To consider them, according to Macchi and Perdichizzi [60], we can refer to the corrective coefficient Ψ_η, given as a function of the off-design on on-design ratio of the so called *isentropic charge factor* k_{is} .

$$\Psi_\eta = f\left(\frac{k_{is,OFF}}{k_{is,RATED}}\right) \tag{8.10}$$

$$k_{is} = \frac{\Delta h_{is}}{\frac{u^2}{2}} \tag{8.11}$$

where:

$u =$ peripheral speed [m/s]

Hypothesizing that in an axial steam turbine the peripheral speed doesn't change much, it can be said that

$$\frac{k_{is,OFF}}{k_{is,RATED}} = \frac{\Delta h_{is,OFF}}{\Delta h_{is,RATED}} \tag{8.12}$$

The law that relates Ψ_η and $k_{is,OFF}/k_{is,RATED}$ can be expressed through the following graph properly proposed for the study of the off-design behavior of axial steam turbines. To be more easily managed by the code, the relation has also been approximated through a 4th degree polynomial curve.

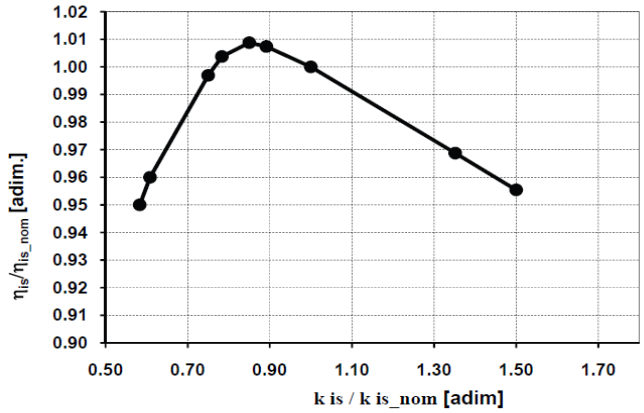

Figure 8.12: Turbine isentropic efficiency variation

It is worth noting that the particular shape of the curve is mostly due to the variation in the turbine exhaust losses. Future developments of the code will introduce a more complete analysis of this aspect.

From a practical point of view, two approaches could have been followed in this case:

1- Apply the correction factor to the overall isentropic efficiency and then work as in the nominal conditions, therefore calculating the expansion line thanks to a proper routine.

2- Apply the correction factor "separately" to the isentropic efficiencies characteristics of each segment of turbine.

During the development phase both approaches have been tested and the first one, although theoretically preferable and more coherent with the on design analysis, has demonstrated to be quite "heavy" for the model, giving way to very critical instabilities.

The second one has so been preferred.

Having defined the pressures thanks to the Stodola's Ellipse, this approach lets us to completely determine the conditions of each extraction with simple relations, reported below for the case of the first turbine extraction.

$$h_{steam,first\ extraction\ \ S} = h\left(P_{steam,first\ extraction}\ , s_{steam,in}\right)$$

$$\Delta h_{is,first\ extraction} = h_{steam,in} - h_{steam,first\ extraction\ \ S}$$

$$\Psi_{\eta,first\ extraction} = f\left(\frac{\Delta h_{is,first\ extraction}}{\Delta h_{is,first\ extraction\ \ RATED}}\right)$$

$$\eta_{is,first\ extraction} = \Psi_{\eta,first\ extraction} \cdot \eta_{is,first\ extraction\ ,RATED}$$

$$h_{steam\ ,first\ extraction} = h_{steam\ ,in} - \eta_{is,first\ extraction} \cdot \Delta h_{is,first\ extraction}$$

$$s_{steam\ ,first\ extraction} = s\left(P_{steam\ ,first\ extraction}\ , h_{steam\ ,first\ extraction}\right)$$

$$T_{steam\ ,first\ extraction} = T\left(P_{steam\ ,first\ extraction}\ , h_{steam\ ,first\ extraction}\right)$$

Figure 8.13 shows how the expansion line and its corresponding extraction points change when passing from the nominal conditions to the case-study part-load conditions, what will be more deeply analyzed in the next chapter.

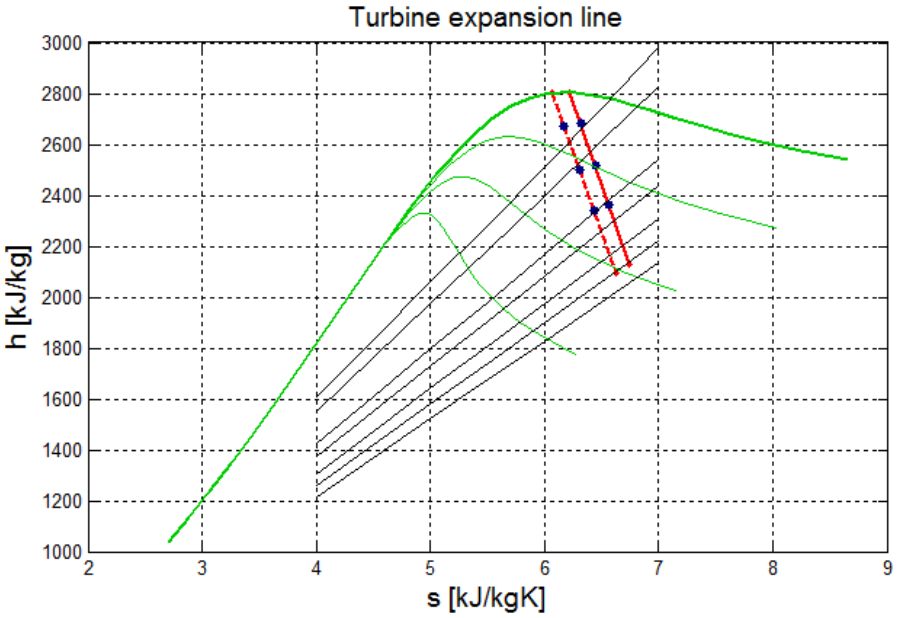

Figure 8.13: On and off-design turbine expansion lines

8.2.2 Electric generator

The weight and rotating speed of the machine are constant so that the mechanical losses are the same for on and off-design operation.

On the contrary, the contribution of the "electrical" losses depends on the power output and can be calculated as a function of the percentage load, i.e. the ratio of

generated to rated power output, as described by the following polynomial, extrapolated from available curves corresponding to state of the art electrical generators:

$$\frac{\dot{W}_{loss,elec}}{\dot{W}_{output\ ,ON}} = 0.0001 \cdot \theta^3 + 0.0044 \cdot \theta^2 + 0.0005 \cdot \theta + 0.00128 \tag{8.13}$$

where:

$$\theta = \frac{\dot{W}_{output\ ,OFF}}{\dot{W}_{output\ ,ON}} \tag{8.14}$$

In practice, the electrical losses decrease if related to the nominal power, as visible in Figure 8.14 (grey star = nominal conditions, blue star = part-load conditions), but considering the decrease in the real power production they are increasing in percentage. The generator efficiency will then decrease, as represented in Figure 8.15.

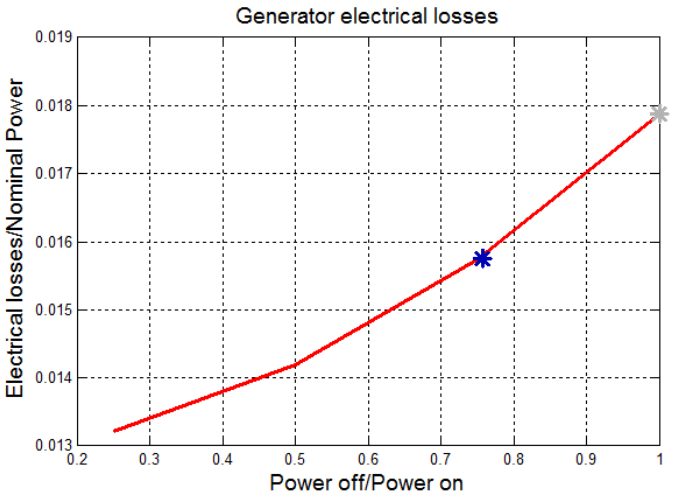

Figure 8.14: On and off-design generator electrical losses

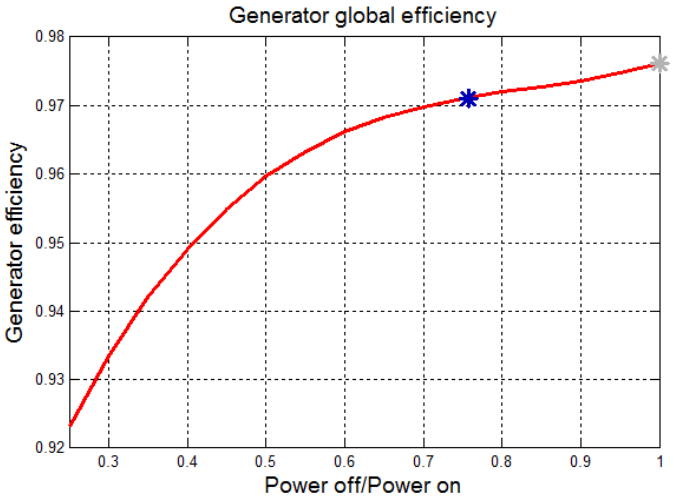

Figure 8.15: On and off-design generator global efficiency

8.2.3 Feedwater heaters

In nominal conditions the behavior of the heat exchangers that compose the pre-heating section has been easily described knowing the temperature increase for each exchanger (thanks to the Haywood approach), the Terminal Temperature Difference (TTD) and the Drain Cooler Approach (DCA). In part load conditions these values cannot be considered valid anymore, and the inlet and outlet temperatures of the two fluids have to be determined through different procedures.

In practice, modelling feedwater heaters at off-design requires describing the variation of pressure drops and of heat transfer coefficients, in order to exploit the energy balances and the ε-NTU approach to completely describe the component.

The law that describes the variation of pressure drops is based on the assumption that they are proportional to the square of the mass flow (velocity) through a pressure drop coefficient k_i that is calculated at on-design conditions, according to the Darcy equation for turbulent flows, assuming a negligible variation of the friction factor:

$$k_i = \frac{\Delta P_{ON,i}}{\dot{m}_{ON,i}^{\ 2}} \tag{8.15}$$

$$\Delta P_{OFF,i} = k_i \cdot \dot{m}_{OFF,i}^{\ 2} \tag{8.16}$$

or, more simply

$$\Delta P_{OFF,i} = \Delta P_{ON,i} \cdot \left(\frac{\dot{m}_{OFF,i}}{\dot{m}_{ON,i}}\right)^2 \tag{8.17}$$

where the pedix i indicates a general stretch of the plant.

For what concerns the overall heat transfer coefficient and the law to describe its variation in different off-design situations, it is convenient to start from the general definition already mentioned in paragraph 6.5.2.

$$\frac{1}{UA} = \frac{1}{h_{inner}\, A_{inner}} + \frac{R_{fou,inner}}{A_{inner}} + \frac{\ln(D_{outer}/D_{inner})}{2\pi kL} + \frac{R_{fou,outer}}{A_{outer}} + \frac{1}{h_{outer}\, A_{outer}} \tag{8.18}$$

The effects of internal and external fouling and of the conduction heat transfer can be neglected in both sections and therefore it can be said that the heat flow is controlled by convection.

$$\frac{1}{UA} = \frac{1}{h_{inner}\ A_{inner}} + \frac{1}{h_{outer}\ A_{outer}} \tag{8.19}$$

The convective heat transfer coefficient h is a function of the Nusselt number

$$h = \frac{Nu \cdot k_{fluid}}{D} \tag{8.20}$$

Nu = Nusselt number

k_{fluid} = fluid thermal conductivity [W/mK]

D = hydraulic diameter [m]

and this one can, in turn, be expressed through the Reynolds and Prandtl numbers.

For a completely developed (both hydro-dynamically and thermally) and turbulent flow for both fluids, two correlations properly describe the phenomenon:

1- Dittus-Boelter correlation, for forced convection inside circular smooth pipes

$$Nu_D = 0.023 \cdot Re_D^{0.8} \cdot Pr^n \tag{8.21}$$

where:

$$n = \begin{cases} 0.4 \rightarrow fluid\ heating \\ 0.3 \rightarrow fluid\ cooling \end{cases}$$

2- Zukauskas correlation, for forced convection with transverse flow on pipes

$$Nu_D = C \cdot Re_D^{0.6} \cdot Pr^{0.36} \cdot \left(\frac{Pr_f}{Pr_w}\right)^n \tag{8.22}$$

where:

Pr_f = Prandtl number calculated at the mean fluid temperature

Pr_w = Prandtl number at the wall temperature

$$n = \begin{cases} 0 \rightarrow gas/steam \\ 0.25 \rightarrow viscous\ flows \end{cases}$$

The definitions of Reynolds and Prandtl let us finally to find a relation between the convective transfer coefficient h and the fluid mass flow:

$$Re_D = \frac{4 \cdot \dot{m}_{fluid}}{\pi \cdot D \cdot \mu} \tag{8.23}$$

$$Pr = \frac{\mu \cdot c_p}{k_{fluid}} \tag{8.24}$$

where:

μ = fluid dynamic viscosity [Ns/m^2]

c_p = fluid specific heat [kJ/kgK]

It can indeed be said, at this point, that

$$h \propto Nu \rightarrow h \propto Re^n \rightarrow h \propto \dot{m}_{fluid}^n \tag{8.25}$$

This is real both for the inner and for the outer h, but keeping in mind that for the first one the exponent n will be 0.8 (from the Dittus-Boelter correlation) while for the second one it will be 0.6 (from the Zukauskas correlation).

How already reminded in the on-design study, to describe the behavior of the heat exchanger it's essential to divide it into two parts, the first related to the steam condensing phase and the second one related to the subsequent drain subcooling one.

In this case of part-load study, this subdivision lets us to adopt different assupmtions according to the zone.

The condensing phase

During the condensing phase, the steam presents a really high value of heat transfer coefficient. Similarly to what we said for the condenser, we can so assume with a good approximation that

$$\left.\frac{1}{UA}\right|_{cond} = \left.\frac{1}{h_{in}\,A_{in}}\right|_{cond} \propto \left.\frac{1}{\dot{m}_{fw}^{0.8}}\right|_{cond} \tag{8.26}$$

Relating the nominal value of UA with the part-load one will so bring to the expression

$$\left.\frac{UA_{OFF}}{UA_{ON}}\right|_{cond} = \left(\frac{\dot{m}_{fw,OFF}}{\dot{m}_{fw,ON}}\right)^{0.8} \tag{8.27}$$

that let us to completely describe the variation of the overall heat transfer coefficient in off design conditions.

The subcooling phase

In the subcooling zone, the heat exchange happens between water on the outer side of the pipes and water also on the inner side of the pipes. The convective heat transfer coefficients cannot so be considered a priori too different and it becomes important to analyze better what side of the preheater controls the heat flow.

The overall heat transfer coefficient can be written as:

$$\left.\frac{1}{UA}\right|_{subc} = \left.\frac{1}{h_{in}\,A_{in}}\right|_{subc} + \left.\frac{1}{h_{out}\,A_{out}}\right|_{subc} \propto \left.\frac{K_1}{\dot{m}_{fw}^{0.8}}\right|_{subc} + \left.\frac{K_2}{\dot{m}_{st}^{0.6}}\right|_{subc} \tag{8.28}$$

where K_1 and K_2 are the proportionality constants.

This expression is not easily reduced since K_1 and K_2 depend on the particular geometry of the heat exchanger, which is not calculated. Nevertheless, it is worth noting that, first, there is a ten to one approximate ratio between shell and tube mass flows and, second, that the Dittus-Boelter exponent is higher than Zhukauskas'. Both these informations drive us to say that the heat flow is controlled by the outer side of the tubes and, therefore, Eq. (8.28) can be simplified as reported in Eq. (8.29).

$$\left.\frac{UA_{OFF}}{UA_{ON}}\right|_{subc} = \left(\frac{\dot{m}_{drain\ ,OFF}}{\dot{m}_{drain\ ,ON}}\right)^{0.6} \tag{8.29}$$

This law completely describes the part load variations of the UA in the subcooling phase of the preheaters.

Code modifications

If in the on-design analysis the temperatures were known and were used to calculate the efficiency of the preheaters, in this case the procedure is exaclty the opposite one. Knowing all the parameters that outline the on design behavior of the components, the just described laws let us to define the same parametrs also in part load conditions, having the specific objective to identify the new exchanger efficiencies (both for subcooling and condensing phases).

These allow, indeed, to calculate the feedwater temperature at the outlet of the subcooling phase and the feedwater and drain temperatures at the outlet of the preheater. Only the temperatures of the extraction and of the inlet water are needed as input.

The procedure could be so described:

$$\begin{matrix} UA_{subc\ ,ON} \\ UA_{cond\ ,ON} \end{matrix} \rightarrow \begin{matrix} UA_{subc\ ,OFF} \\ UA_{cond\ ,OFF} \end{matrix} \rightarrow \begin{matrix} NTU_{subc\ ,OFF} \\ NTU_{cond\ ,OFF} \end{matrix} \rightarrow \begin{matrix} \varepsilon_{subc\ ,OFF} \\ \varepsilon_{cond\ ,OFF} \end{matrix} \rightarrow \begin{cases} T_{exit\ \ subc\ ,water\ ,OFF} \\ T_{exit\ ,drain\ ,OFF} \\ T_{exit\ ,water\ ,OFF} \end{cases} \tag{8.30}$$

The last step, from the efficiencies to the temperatures, is made simply considering the already mentioned efficiency definition.

$$\varepsilon = \frac{C_h\left(T_{h,i} - T_{h,o}\right)}{C_{min}\left(T_{h,i} - T_{c,i}\right)} = \frac{C_c\left(T_{c,o} - T_{c,i}\right)}{C_{min}\left(T_{h,i} - T_{c,i}\right)} \tag{8.31}$$

A complication in this procedure comes from the fact that for the two high pressure feedwater heaters only three temperatures are known, more precisely the feedwater temperature at the inlet of the first feedwater heater and the temperatures of the steam extractions. To solve this "block", it has so been necessary to attempt the value of the feedwater temperature between the two exchangers (exit of the first one and inlet of the second one) and to implement an iterative cycle. In practice, with the attempted value of temperature the characteristics of the second HP exchanger can be completely calculated. Having defined those, included the drain temperature and enthalpy, the first HP heater can be studied and the attempted value of temperature can be refreshed. In a small time the program finds the correct solution, according to a tolerance of 0.01 °C.

In Figure 8.16 a comparison between on-design and reference off-design behavior of the first feedwater heater is reported (dot lines = on-design, full lines = off-design).

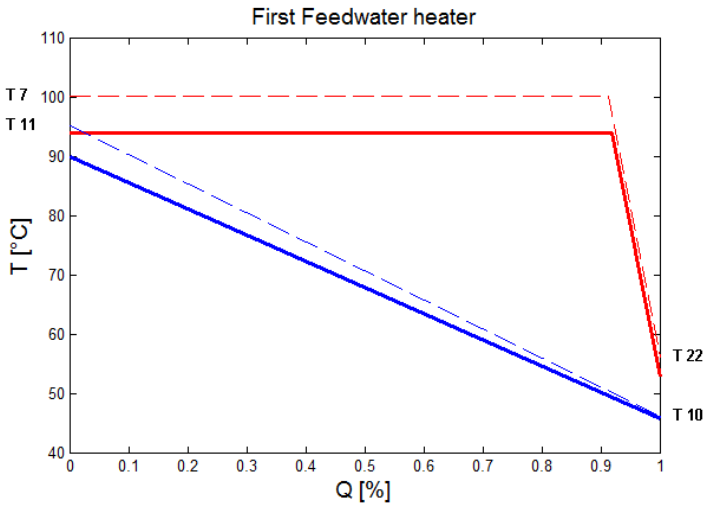

Figure 8.16: On and off-design T-Q diagram of FWH1

8.2.4 Condenser

During part load operation, the thermal duty of the ACC is reduced since the mass flow of exhaust steam from the turbine decreases. Under these circumstances, two possible strategies can be adopted for managing the new operating point of the condenser:

• Decrease the condenser pressure keeping all the cells of the condenser in

operation.

• Maintain the operating pressure at its rated value and put a number of cells out of service.

With the first option we consider that the performances of the condenser do not change. In this case all the cells are indeed switched on and, being fixed the fan speed, this implies that UA, NTU and ε present the same values than in nominal conditions. Starting from this assumption, the definition of the new condenser pressure is possible through an iterative cycle based on energy balances on the device.

Attempting a first value of P_{cond} (or T_{cond}) is indeed possible to calculate, through the turbine analysis described above, the enthalpy at the turbine discharge/condenser inlet section. This value lets us determine the temperature of air leaving the condenser, through the energy balance:

$$\dot{m}_{steam\ ,cond\ \ IN}\left(h_{steam\ ,cond\ \ IN}-h_{water\ ,cond\ \ OUT}\right)=\dot{m}_{air}\,c_{p,air}\left(T_{air\ ,OUT}-T_{air\ ,IN}\right) \tag{8.32}$$

With this value of $T_{air\ ,OUT}$ and with the known effectiveness is then possible to define a new value of T_{cond} (with the related P_{cond}) and so to refresh the first attempt.

$$T_{cond}=\frac{T_{air\ ,OUT}-T_{air\ ,IN}}{\varepsilon_{cond}}+T_{air\ ,IN} \tag{8.33}$$

After a few iterations, the solution converges to a lower value of T_{cond} and P_{cond}, because of the lower steam mass flow.

From a more practical point of view, in this case the turbine expansion work increases but at the same time the reduction of the discharge turbine pressure implies an exhaust humidity increase.

Since exhaust quality is a primary concern in steam turbines, this first strategy is not usually adopted, but it has been included for the completeness of the model.

The second regulation strategy is the most common one in this kind of power plants. According to the decrease of thermal duty, the air mass flow is proportionally reduced and a certain number of cells are switched off. Working in this way, the condensing temperature can be considered to remain constant, while it becomes important to define the new number of active cells.

Also in this case, due to the constant fan speed, the active cells work exactly as in nominal condition and therefore with the same UA, NTU and ε.

The only small difference in cells functioning takes place when the heat rejection decreases, but yet not enough to switch off a cell. In this case, the air mass flow and heat rejection are higher than necessary; this could provoke either a condenser pressure decrease, or a outlet air temperature increase. Normally, the common procedure is to keep the condenser pressure constant through a small dedicated pump. The only sensitive variation is therefore a small air temperature increase, but this effect has been considered negligible.

From the point of view of the code, this kind of regulation is analyzed first of all calculating the number of active cells related to the new decreased steam mass flow. This is simply done another time through the energy balance in the condenser:

$$\dot{m}_{steam\ ,cond\ \ IN}\left(h_{steam\ ,cond\ \ IN}-h_{water\ ,cond\ \ OUT}\right)=\dot{m}_{air}\,c_{p,air}\left(T_{air\ ,OUT}-T_{air\ ,IN}\right) \tag{8.34}$$

The number of active cells is then identified by the closest higher integer number to the ratio $\dot{m}_{air\ ,OFF}/\dot{m}_{air\ ,cell}$.

Once known the number of active cells the new power consumption is immediately calculated.

At the end, in this case we have that fan power consumption is reduced, while the turbine expansion work and the steam quality at the exhaust do not change significantly.

8.2.5 Pumps

The off-design behavior of the pump has been considered separately for the condensate extraction pump and for the feed pump. In the first case, indeed, the power absorbed by the pump is almost negligible (approximately 10 kW for the case study plant) and it's not so important to consider very accurately the off design behavior. It has so been modeled considering only a correction in the hydraulic efficiency, analogously to what has been done with the turbine.

According to Lippke [61] the hydraulic efficiency of the pumps in off-design conditions can be considered a function of the mass flow variation:

$$\eta_{idr\ ,OFF}=\ \Psi_{pump}\ \ \eta_{idr\ ,NOM} \tag{8.35}$$

where:

$$\Psi_{pump} = 2 \cdot \frac{\dot{m}_{fluid\ ,OFF}}{\dot{m}_{fluid\ ,NOM}} - \left(\frac{\dot{m}_{fluid\ ,OFF}}{\dot{m}_{fluid\ ,NOM}}\right)^2 \quad (8.36)$$

For the feed water pump, instead, it has been chosen to model it more precisely and considering different possibilities of regulation. The used procedure is exactly the same as for the boiler pumping station, already described in Paragraph 8.1.2.

The results for the off design case study are well-represented by the characteristic curves. The first one (Figure 8.17, grey star = on-design, blue star = off-design) reports the variation in the functioning of a fixed-speed pump; it can be seen that to a water flow decrease corresponds a pressure drop increase, according with the characteristic curve. Figure 8.18 (grey star = on-design, blue star = off-design), instead, reports the new functioning point for the case of a single pump with variable rotating speed. In this case, the pumps responds to the new requirements through the definition of a new rotating speed (and the subsequent new displacement of the characteristic curve).

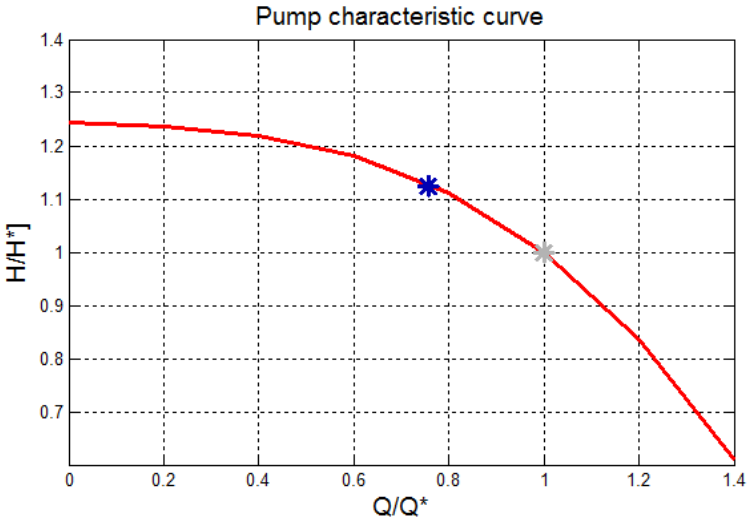

Figure 8.17: On and off-design feed pump operating point – three fixed speed pumps case

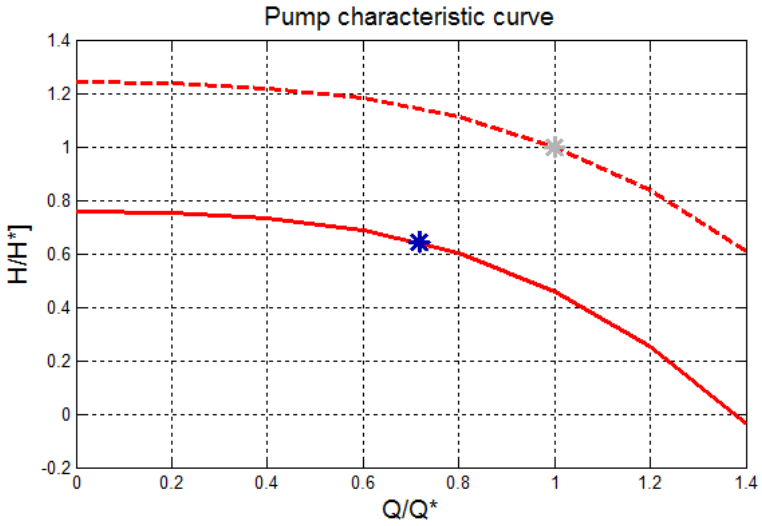

Figure 8.18: On and off-design feed pump operating point - single variable speed pump case

8.2.6 Off-design non-linear equations system

As for the on-design case, the global resolution of the power-block model needs the adoption of the Matlab sub-routine *fsolve*, to solve a system of non-linear equations. Being some assumptions no more valid, the number of unknown variables is increased in comparison with the on-design case. The system is therefore composed by 10 variables an 10 equations. More precisely, the variables are:

1) $\dot{m}_{16}$
2) $\dot{m}_{5}$
3) $\dot{m}_{6}$
4) $\dot{m}_{7}$
5) p_{16}
6) p_{5}
7) p_{6}
8) p_{7}
9) T_{8}
10) h_{23}

and the equations used to close the system are:

1) $\dot{m}_{11} \cdot h_{11} + \dot{m}_{22} \cdot h_{22} = \dot{m}_{10} \cdot h_{10} + \dot{m}_{7} \cdot h_{7}$ (8.37)

2) $\dot{m}_{11} \cdot h_{11} + \dot{m}_{6} \cdot h_{6} + \dot{m}_{21} \cdot h_{21} = \dot{m}_{12} \cdot h_{12}$ (8.38)

3) $\dot{m}_{13} \cdot h_{13} + \dot{m}_{5} \cdot h_{5} + \dot{m}_{19} \cdot h_{19} = \dot{m}_{14} \cdot h_{14} + \dot{m}_{20} \cdot h_{20}$ (8.39)

4) $\dot{m}_{14} \cdot h_{14} + \dot{m}_{17} \cdot h_{17} = \dot{m}_{15} \cdot h_{15} + \dot{m}_{18} \cdot h_{18}$ (8.40)

5) $p_7 = \sqrt{\left(\dot{m}_{7x}{}^2 \cdot T_7 \cdot Y_{7xd} + p_8^2\right)}$ (8.41)

6) $p_6 = \sqrt{\left(\dot{m}_{6x}{}^2 \cdot T_6 \cdot Y_{6xd} + p_7^2\right)}$ (8.42)

7) $p_5 = \sqrt{\left(\dot{m}_{5x}{}^2 \cdot T_5 \cdot Y_{5xd} + p_6^2\right)}$ (8.43)

8) $p_4 = \sqrt{\left(\dot{m}_{4x}{}^2 \cdot T_4 \cdot Y_{4d} + p_5^2\right)}$ (8.44)

9) $h_{23} = h_{22}$ (8.45)

10) $\begin{cases} T_8 = T_{8,on\ design} & if\ ACC\ regulation = 1 \\ T_8 = \frac{\left(T_{air,out} - T_{air,in}\right)}{\varepsilon_{cond}} - T_{air,in} & if\ ACC\ regulation = 2 \end{cases}$ (8.46)

where *ACC regulation* defines the regulation strategy of the Air Cooled Condenser: 1 for the progressive cells shut down, 2 for the change in condenser pressure.

8.3 Global model functioning: boiler-turbine matching

The procedure to define the new equilibrium point in terms of drum pressure and steam production represents the main difference between on and off-design boiler models.

The reduced heat input at off-design cuts down steam production and this, in turn, makes live steam pressure, and therefore drum pressure at the boiler to decrease, due to the sliding pressure part load operation of the steam turbine.

Being steam production related to drum pressure and at the same time drum pressure related to steam production through the part-load turbine operation, an iterative cycle to find the matching point between the two components is necessary.

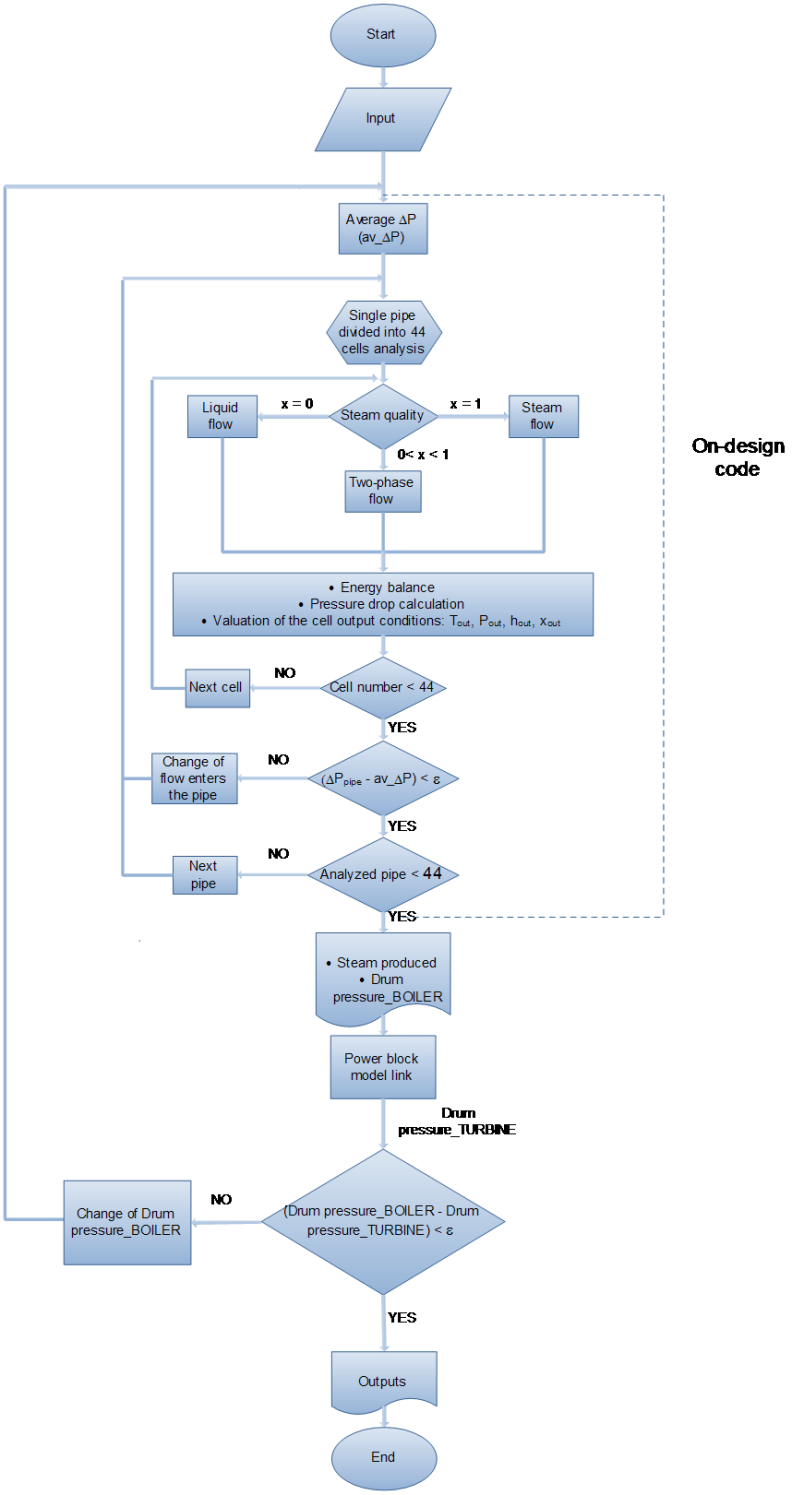

Figure 8.19: Off-design model detailed flow chart

A first drum pressure (*Drum pressure_BOILER*), equal to the on-design one, is so initially considered. The steam flow production of the boiler is calculated and sent to the power block model that imposes a new value of inlet pressure *Drum pressure_TURBINE* that will be lower because of the lower steam flow. This pressure value is, therefore, imposed as drum pressure in the next cycle. The "while" cycle will terminate when the difference between the current drum pressure and that one from the turbine will be smaller than an arbitrary little value ε.

$$Drum\ pressure_{BOILER} - Drum\ pressure_{TURBINE} < \varepsilon \qquad (8.47)$$

The interaction is evidently more complicated that in the on-design case and therefore also the computational time increases. With a medium-performance hardware (2.0 GHz processor, 2 GB DDR2 RAM memory), the computational time for this part of the model is approximately 10 minutes.

9. OFF-DESIGN SIMULATIONS

With the aim of understanding the off-design model and acquiring more sensitivity about the influence of some important parameters on the plant behaviour, four off-design simulations have been conducted:

1. Considering fixed the ACC behaviour (cells progressively switched off) and the pumping system for the boiler and the power block (3 fixed speed pumps):
   1.1. Analysis of the effect of changing the irradiance values of the radiation map corresponding to March 21st at 12.00 on the principal parameters of boiler and power block. This is the typical condition of hazy sky.
   1.2. Analysis of the principal parameters of boiler and power block in a real off-design condition with clear sky and the July 21st at 16.00 radiation map.
2. First regulation choice: analysis of the impact of varying the absolute value of heat input in the radiation map corresponding to March 21st at 12.00 radiation map (hazy sky) on power-block and boiler performance when either multiple fixed speed pumps or a single variable speed pump are adopted and analysis of pumping system behaviour.
3. Second regulation choice: analysis of the impact of varying the absolute value of heat input in the radiation map corresponding to March 21st at 12.00 radiation map (hazy sky) on plant and boiler performances when ACC cells are progressively switched off or ACC cells are all in operation.

The reference plant, as in on-design analysis, is a 15MWe, 40 bar plant.

9.1 Hazy sky with March 21st at 12.00 radiation map with ACC progressively switched off and three pumps.

This simulation has been performed considering the March 21st at 12.00 radiation map and scaling the heat fluxes by a decreasing coefficient.

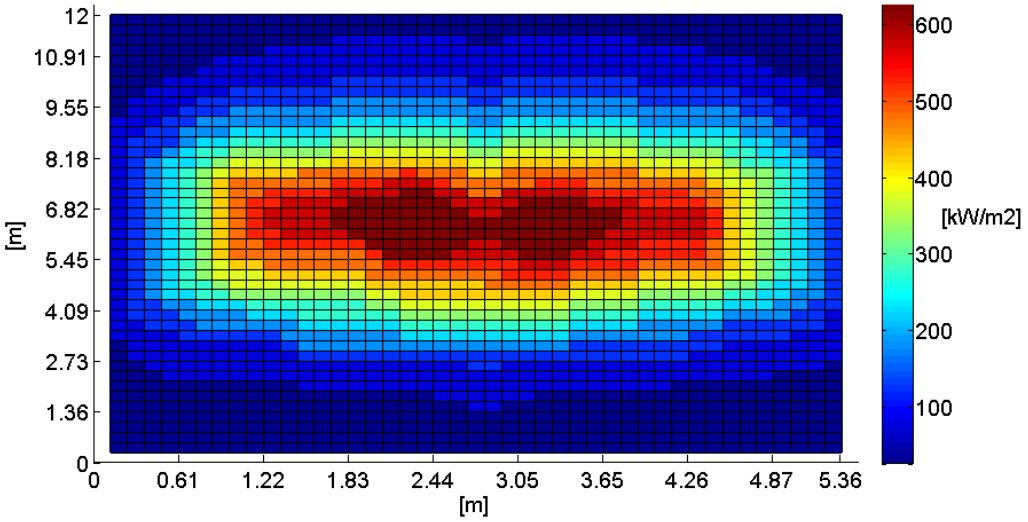

Figure 9.1: March 21st, 12:00 radiation map

9.1.1 Power production and cycle efficiency

When radiation reaching the fixed-dimensions receiver decreases, the first consequence is a decrease in steam production. Working in sliding-pressure regulation, the turbine behavior described by the Stodola's Law of Ellipse imposes that also the drum pressure decreases. In Figure 9.2, it can be seen that on a percentage basis (referred to the on-design conditions) the decreasing trends of steam mass flow and drum pressure are extremely similar.

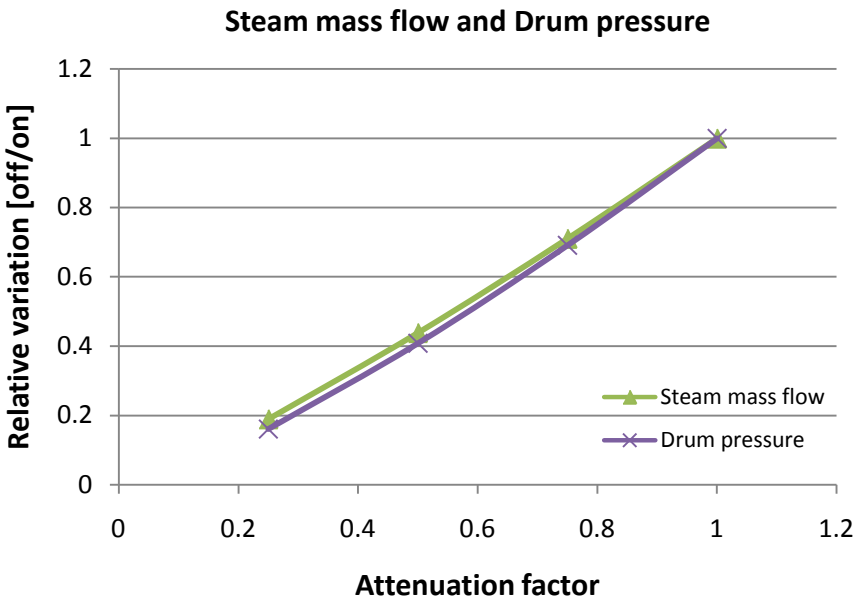

Figure 9.2: Steam mass flow and Drum pressure variation with the Attenuation factor

A second interesting effect is the decrease in cycle efficiency. Both the Net Electrical Power Output and the thermal power added to the cycle decrease, but the first one presents a lower slope (see Figure 9.3). Also the gross turbine power production curve has been reported, and its divergence with the Net Power Output one points out that losses components and auxiliary power consumption increase in percentage during part load operation, according to the discussion in the last chapter. Curves referring to the single power components subtracted to power produced are reported in Figure 9.4.

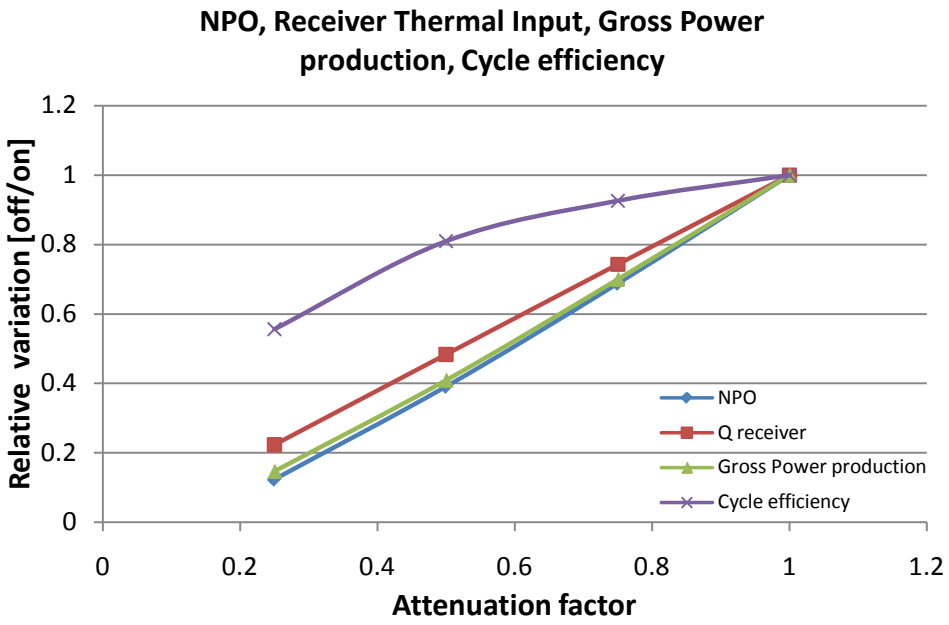

Figure 9.3: NPO,$Q_{receiver}$,Gross Power Production and cycle efficiency variation with the Attenuation factor

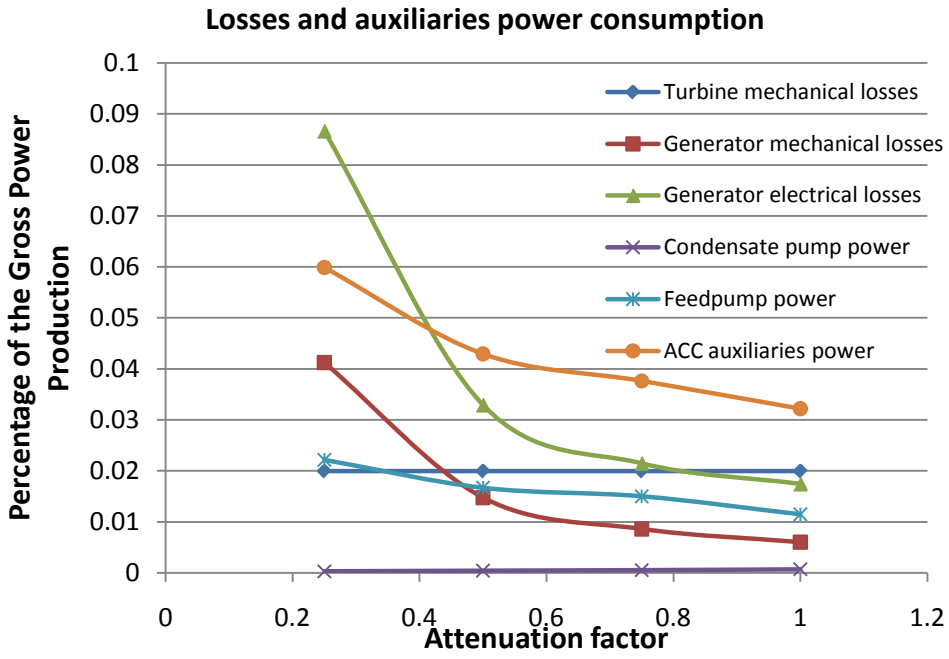

Figure 9.4: Losses and auxiliary power consumption variation with the Attenuation factor

It can be noticed how generator friction and electrical losses present a particularly leaning curve; in part load conditions, indeed, the first remains constant in absolute value, while the second decreases with a progressively flatter curve.

9.1.2 Turbine behavior

As said in Chapter 8.2.1, in off-design turbine isentropic efficiency varies according to the curve reported in Figure 8.12. Two effects are particularly visible when working in part load conditions: the expansion line displacement due to the change in the inlet conditions and its slope variation due to the decreasing efficiency. In Figure 9.5 the expansion line in four cases of reduced radiation on the receiver are reported.

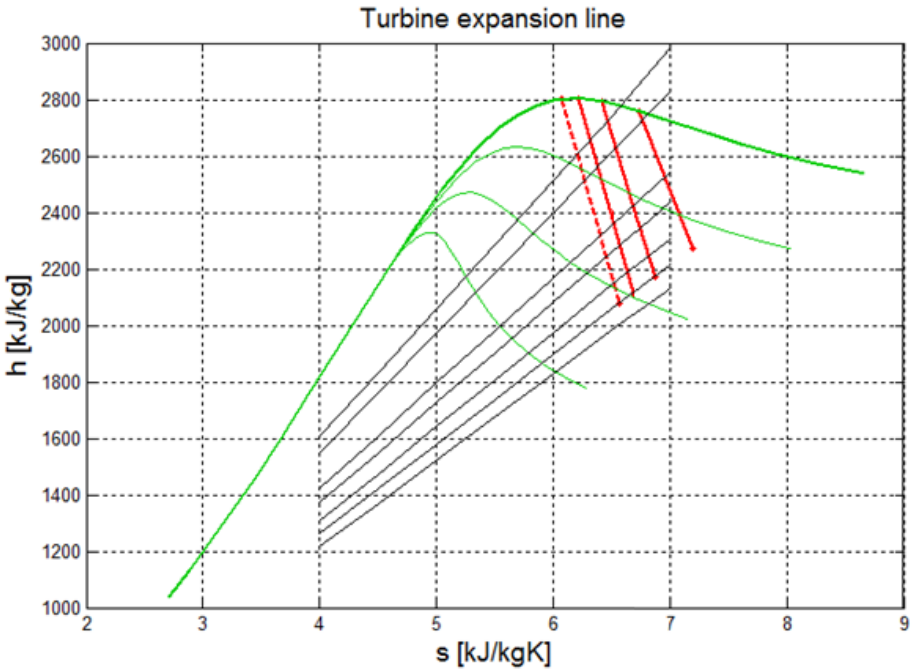

Figure 9.5: Turbine expansion line with attenuation factor 1, 0.75, 0.5, 0.25 (from left to right)

Both these effects contribute to a decrease in available enthalpy drop and, therefore, a decrease in gross power production that is more appreciable than the steam mass flow reduction in each stage (Figure 9.6).

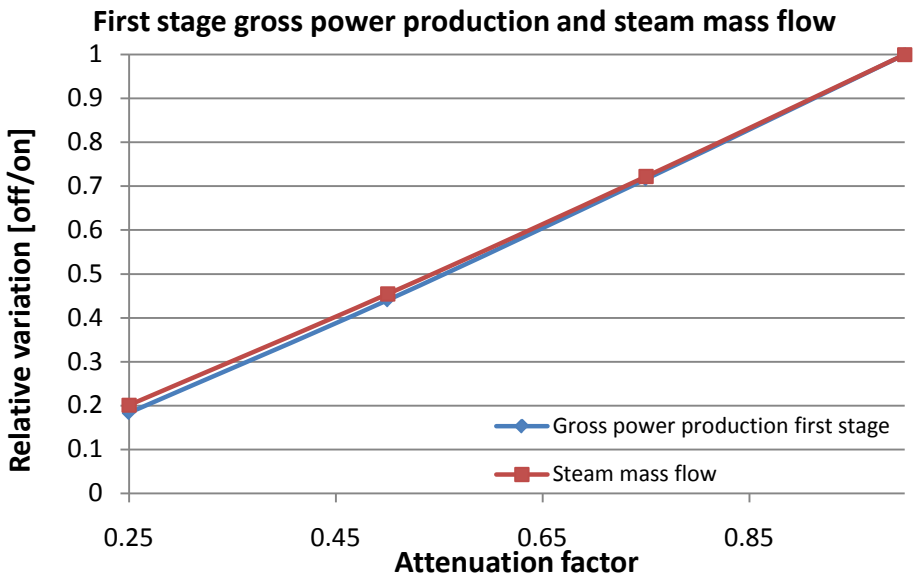

Figure 9.6: First stage gross power production and steam mass flow variation with the Attenuation factor

The evolution of extraction pressures at part load depend on the particular turbine design at on design through Stodola's ellipse approach. Thus, it is possible to calculate how these pressures are affected by a change in heat input (Figure 9.7).

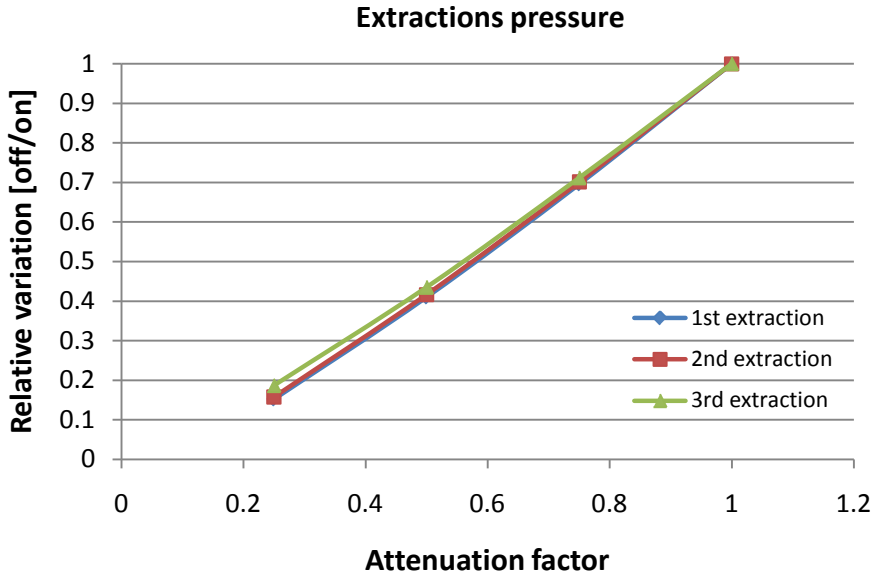

Figure 9.7: Extractions pressure variation with the Attenuation factor

9.1.3 Pre-heating line

When heat input decreases, the preheating train is influenced substantially in two senses: ΔT and mass flow of feedwater decrease. Due to the reduced drum pressure, indeed, steam extractions are characterized by lower thermodynamic parameters and overall ΔT decreases in comparison with the on design case.

The decrease of feedwater mass flow has a strong influence on the heat exchangers performance. Dimensions being fixed, indeed, the device is actually over-sized when mass flow decreases, since the specific heat transfer surface is incremented. From the point of view of the model, this corresponds to an NTU increase and, consequently, an effectiveness increase. Accordingly, smaller values of terminal temperature difference and drain cooler approach follow a better heat exchanger performance . It has to be reminded, indeed, that in off-design conditions neither the Terminal Temperature Difference nor the Drain Cooler Approach are fixed, being instead calculated by the new feedwater and extractions conditions. Variation trends of effectiveness, TTD and DCA are reported in Figure 9.8 and Figure 9.9.

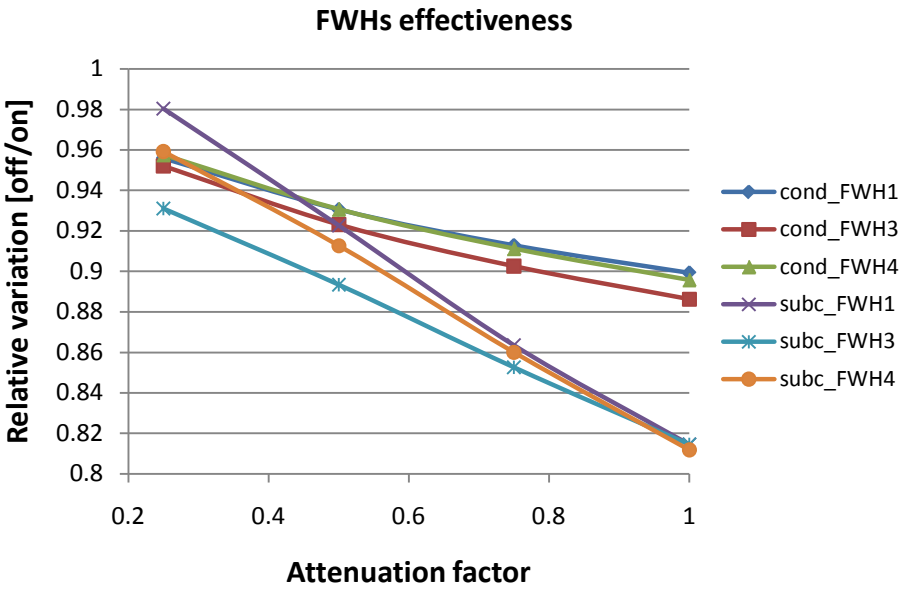

Figure 9.8: FWHs effectiveness variation with the Attenuation factor

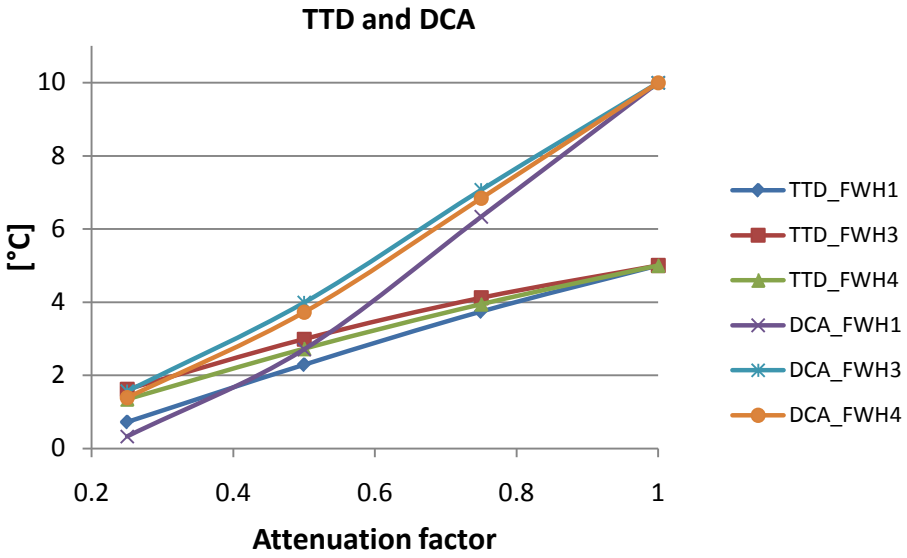

Figure 9.9: FWHs TTD and DCA variation with the Attenuation factor

It can be noticed that effectiveness increases more in the subcooling section than in the condensing one (and, consequently, DCA decreases more rapidly than TTD).This is due to the fact that heat transfer in the subcooling section is governed by forced convection with transverse flow on pipes, while in condensing by forced convection inside the pipes; in practice, different correlations link nominal and part-load UA in condensing and subccoling sections (Eq 8.27 and Eq 8.29).

An immediate view of how parameters change in FWHs is given in Figure 9.10 and 9.11 , representing nominal and part-load operation of the first FWH with 0.75 and 0.25 of incoming radiation respectively.

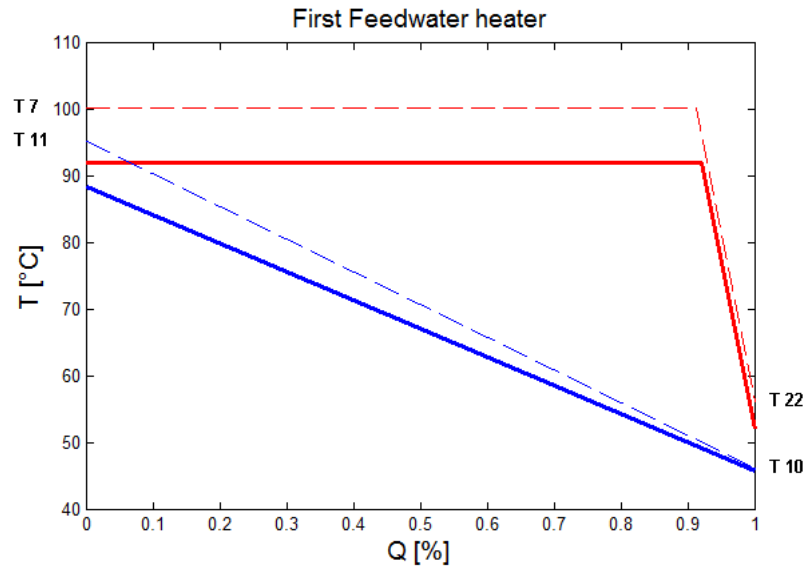

Figure 9.10: FWH1 T-Q diagram for 0.75 Attenuation factor

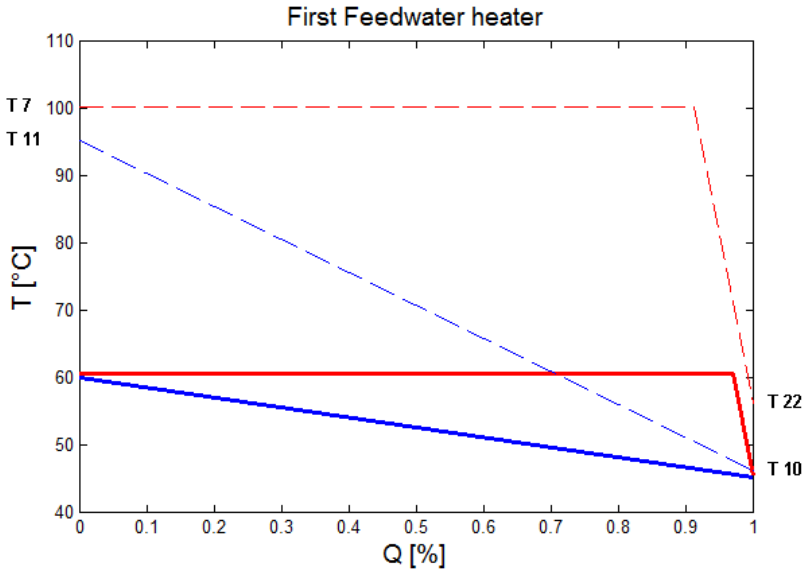

Figure 9.11: FWH1 T-Q diagram for 0.25 Attenuation factor

9.1.4 Boiler behavior

Because of the lower heat input brought about by the reducing radiation factor, a reduction of the total circulating mass flow in the boiler and the steam flow produced occur.

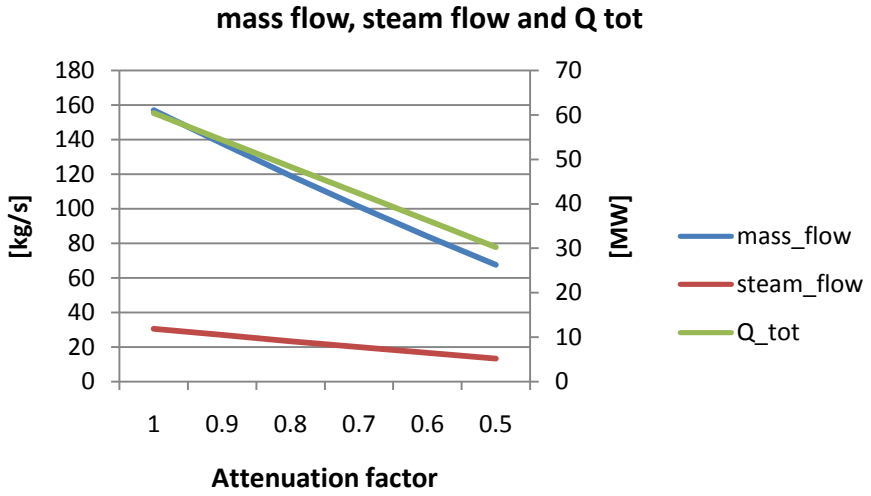

Figure 9.12: Mass flow, steam flow and Q tot variation with the Attenuation factor

At the same time a global reduction of mass flow distribution can be seen (*steam flow and mass flow*) due to the effect of heat reduction that causes a decrease of the total circulating mass flow necessary at the boiler and therefore also the steam production.

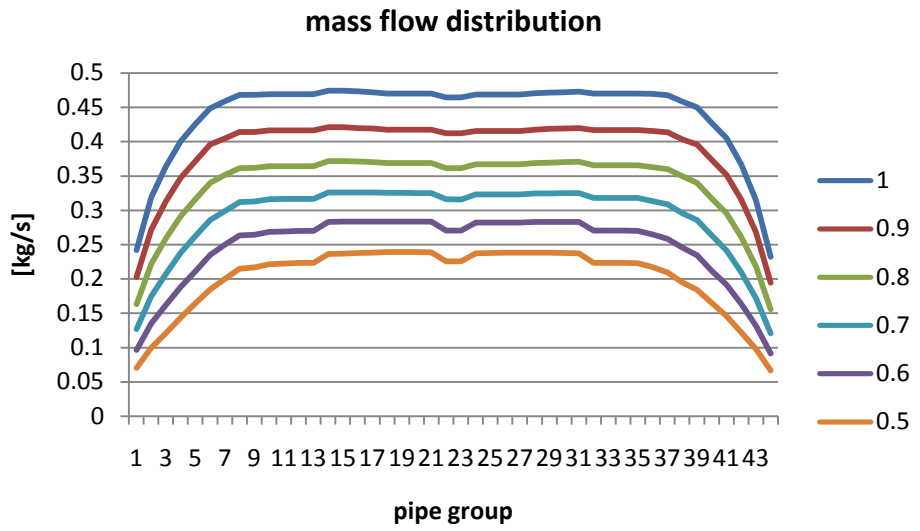

Figure 9.13: Mass flow distribution variation with the Attenuation factor

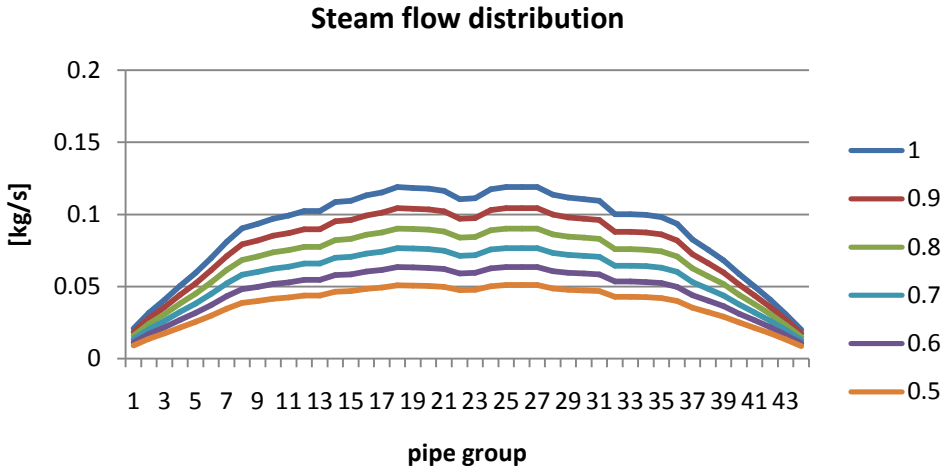

Figure 9.14: Steam flow distribution variation with the Attenuation factor

By decreasing heat input, the steam quality distribution becomes flatter around the average value requested (in this case 0.2) since the reduction of inlet heat causes a flatter mass flow distribution due to the higher relevance of gravity pressure drops and therefore of steam quality.

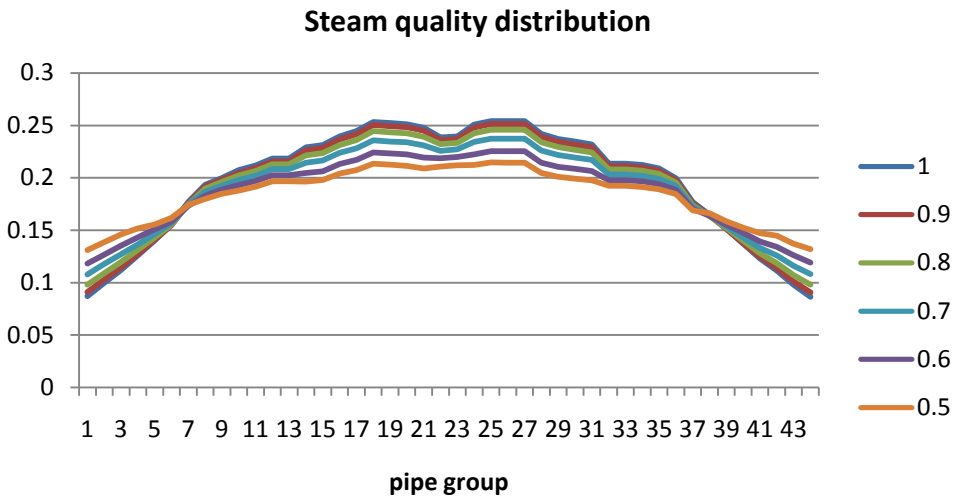

Figure 9.15: Steam quality distribution variation with the Attenuation factor

At the same time pressure drops show a global reduction of all their values, more important for the accelerative and friction component because of the lower mass flow and therefore lower velocity. The gravity component decreases less because it depends on the liquid fraction inside the pipe which does not change so much.

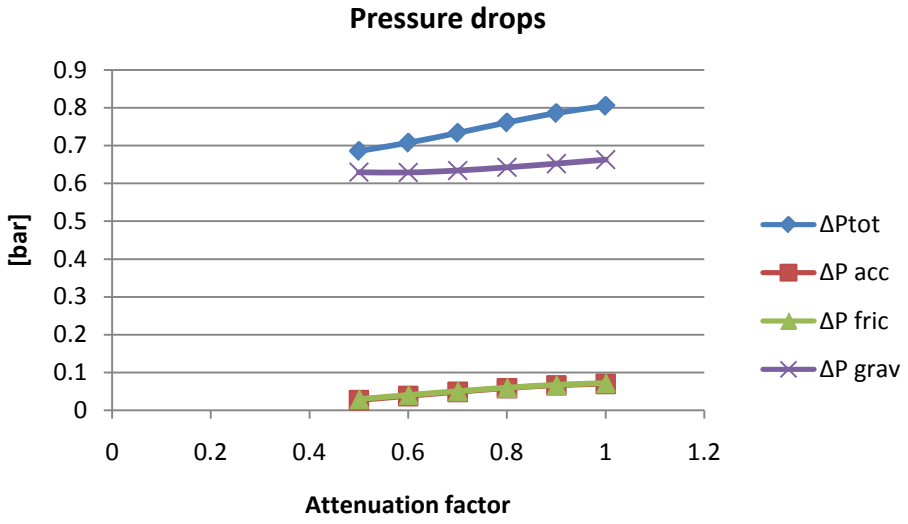

Figure 9.16: Pressure drops variation with the Attenuation factor

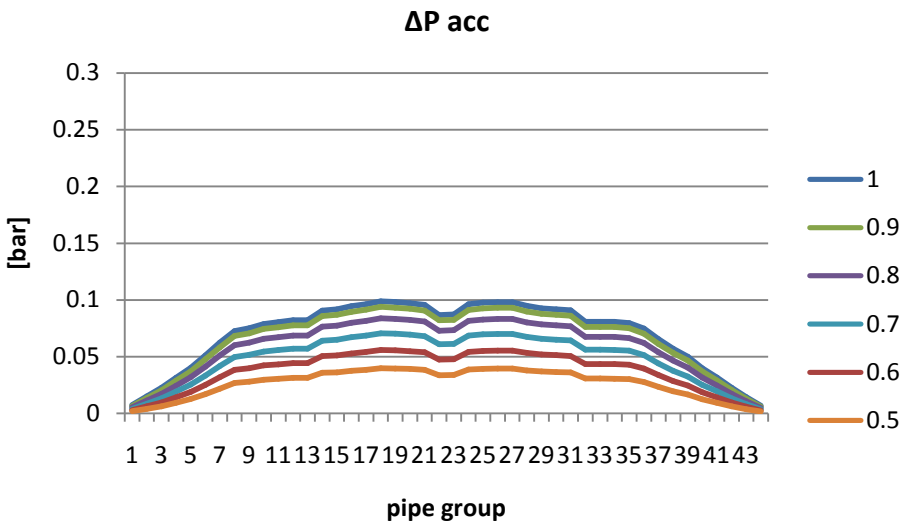

Figure 9.17: Accelerative ΔP variation with the Attenuation factor

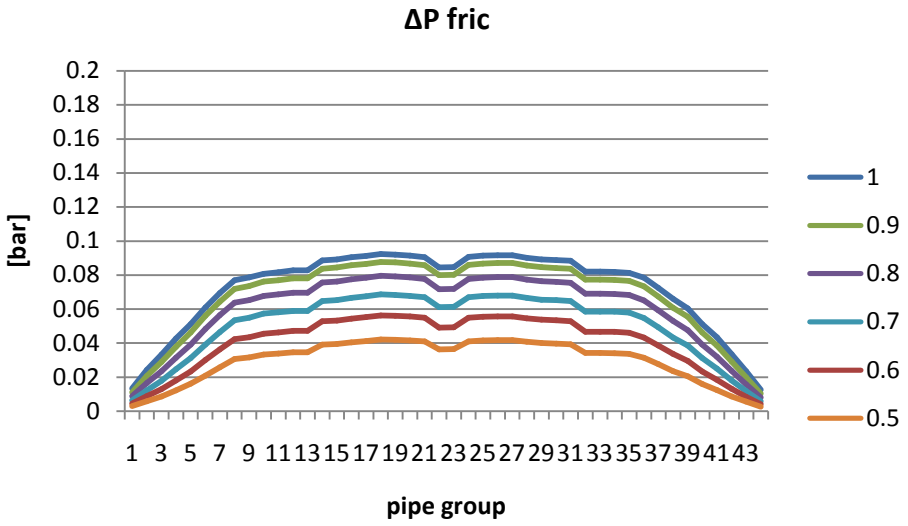

Figure 9.18: Frictional ΔP variation with the Attenuation factor

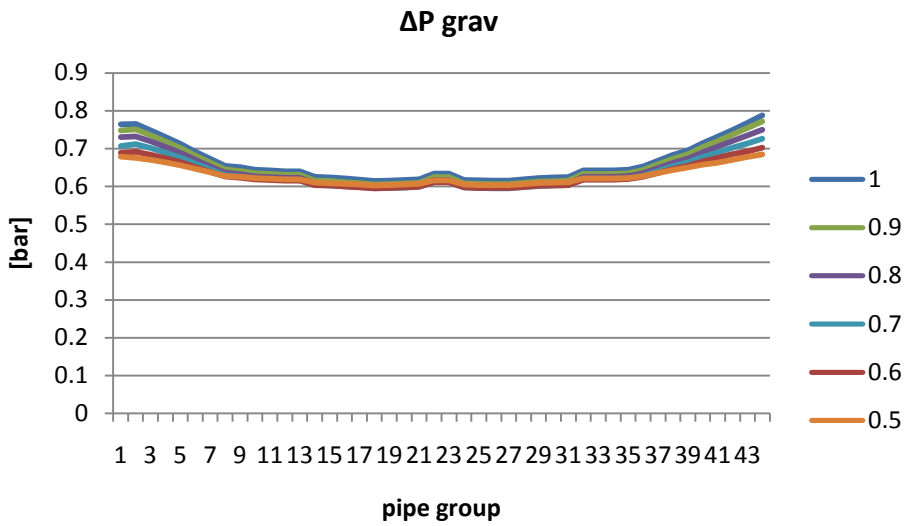

Figure 9.19: Gravitational ΔP variation with the Attenuation factor

9.2 July 21st at 16.00 radiation map with clear sky, ACC progressively switched off and three pumps.

On June 21st at 4 PM, the radiation on the central receiver presents the distribution already shown in Figure 9.20 With respect to the on-design situation, two main effects are experienced: the total thermal power decreasing and its different distribution among modules and pipes.

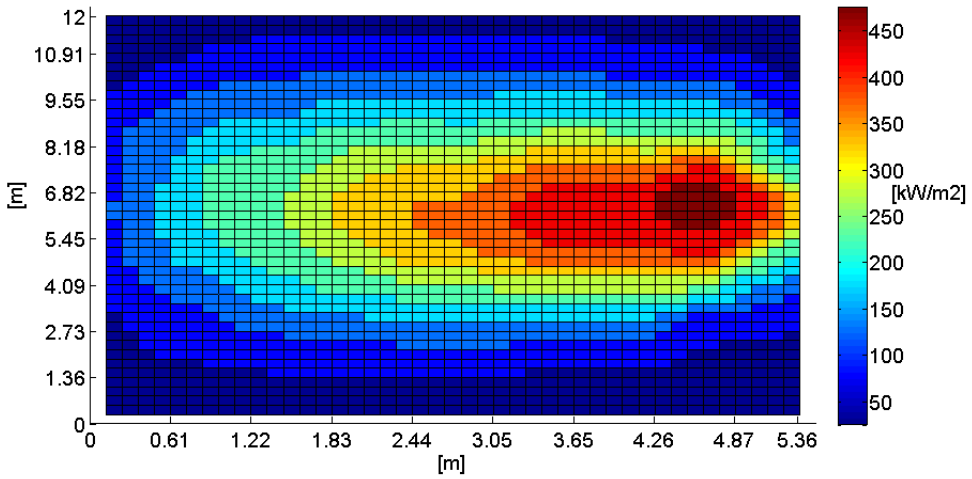

Figure 9.20: June 21st, 16:00 radiation map

9.2.1 Boiler behavior

First of all, from a macroscopic point of view, the new radiation map accounts for 80% the total heat input with respect to on design conditions. In this sense, this case corresponds to a heat reduction with an attenuation factor of 0.8, whose total and steam mass flow decreases were shown in par. 7.11.

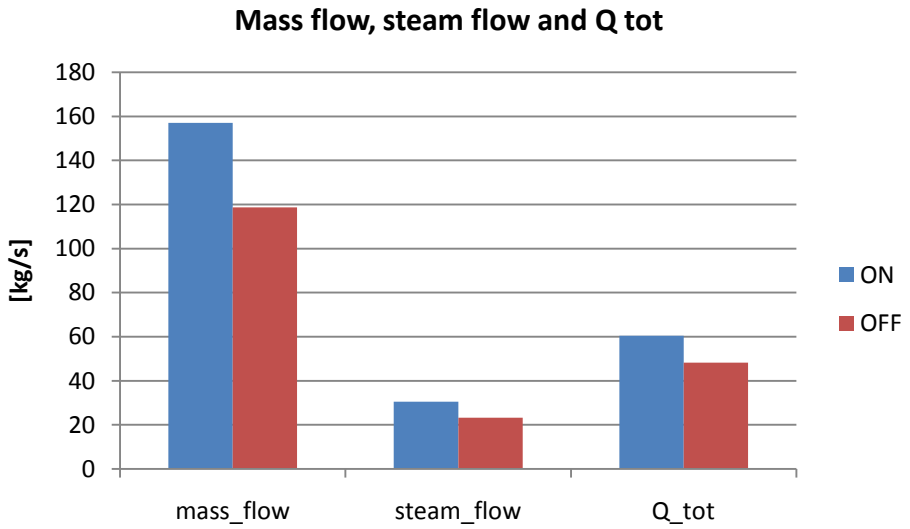

Figure 9.21: Mass flow, steam flow and Q tot variation with the off-design radiation map

Since the peak heat flux is shifted to the right the higher steam production occurs in this part of the boiler. More steam means lower gravity pressure drops, therefore to guarantee the same pressure drops of the other pipe the water mass flow in these pipes increases shifting the water flow distribution to the right. Obviously, confronting this distribution with the on-design one, the absolute values are lower because of the lower total circulating mass flow.

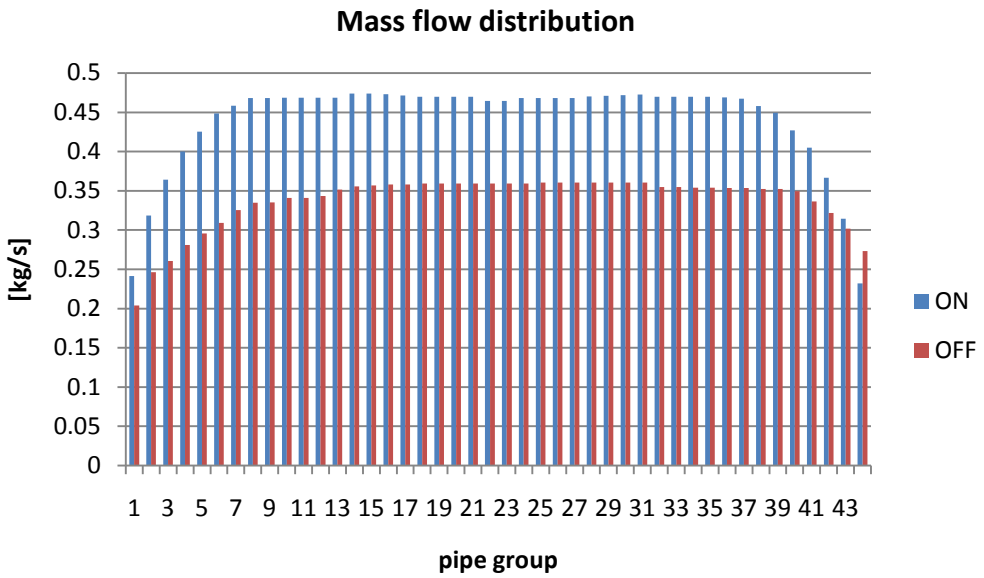

Figure 9.22: Mass flow distribution variation with the off-design radiation map

The same trend is shown for steam quality and steam flow distributions.

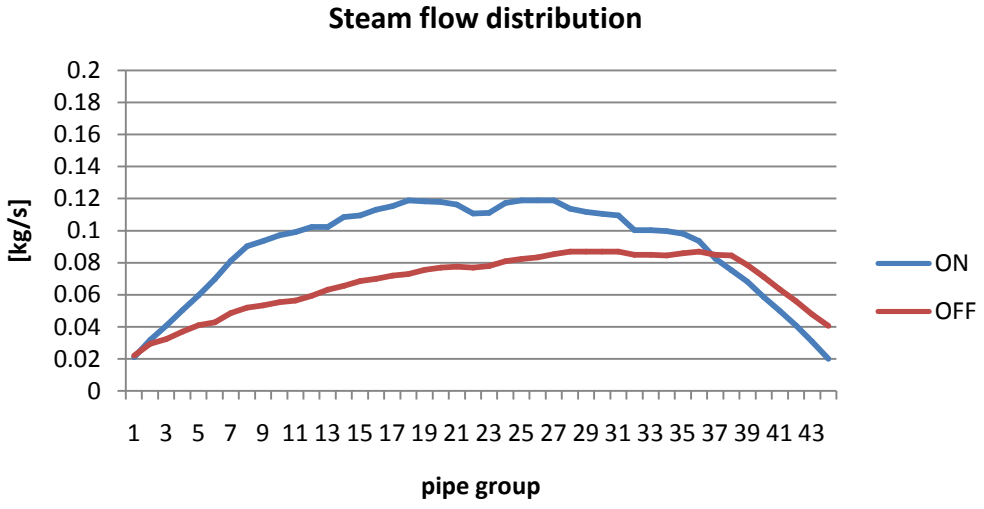

Figure 9.23: Steam flow distribution variation with the off-design radiation map

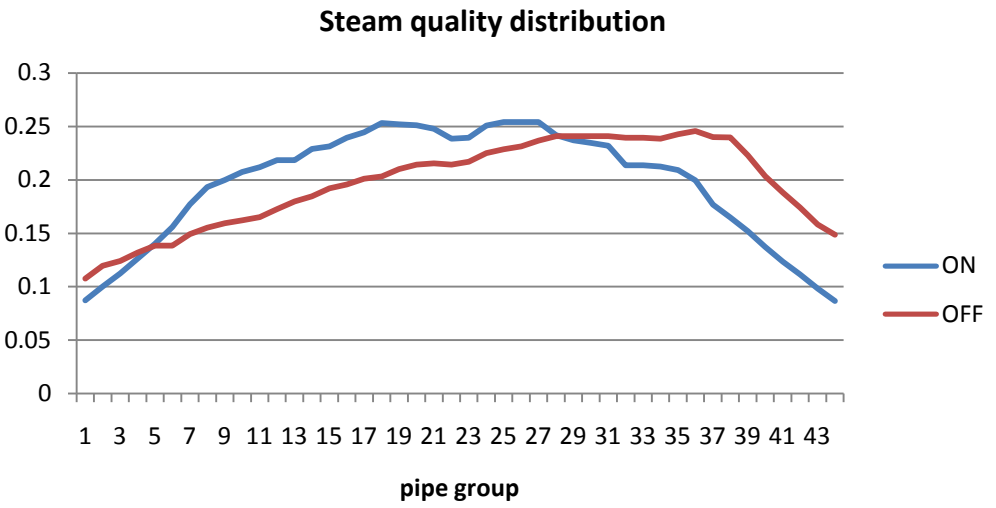

Figure 9.24: Steam quality distribution variation with the off-design radiation map

The pressure drops distribution shows the same pattern shifted to the right but with lower values with respect to the on-design case because of the lower mass flow in the pipes.

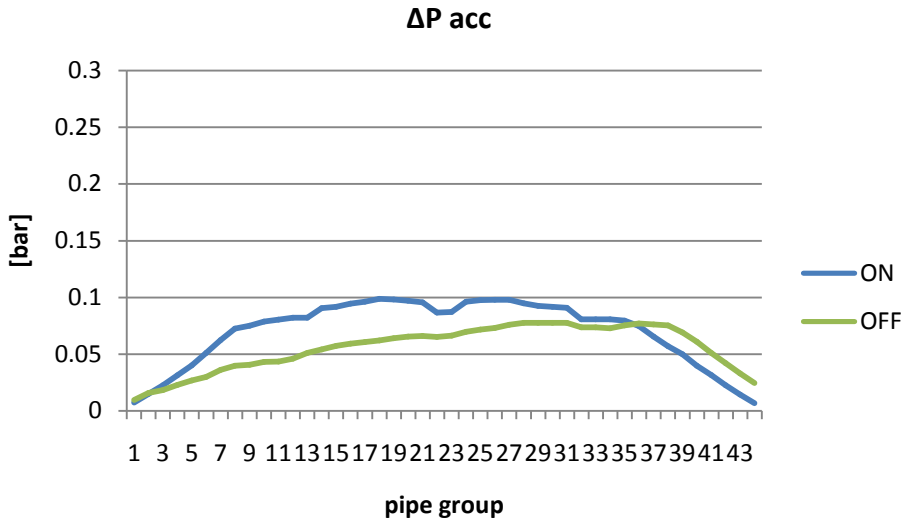

Figure 9.25: Accelerative ΔP variation with the off-design radiation map

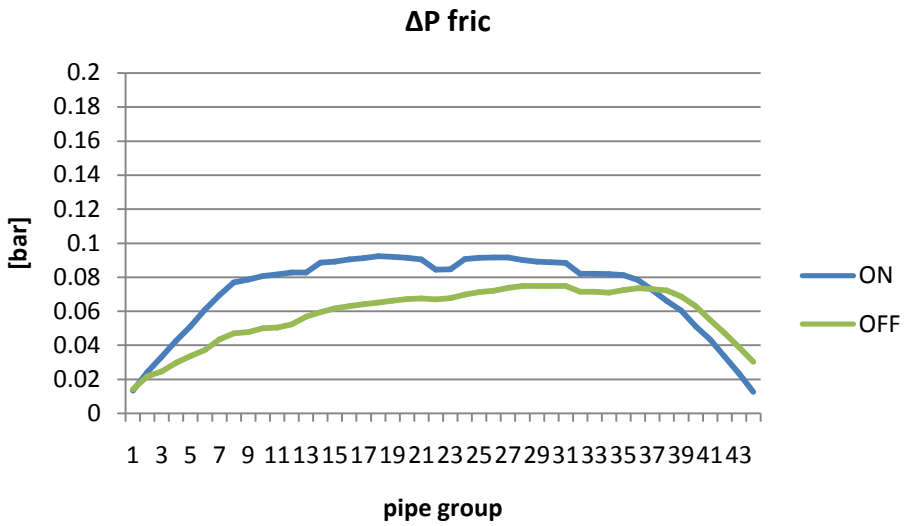

Figure 9.26: Frictional ΔP variation with the off-design radiation map

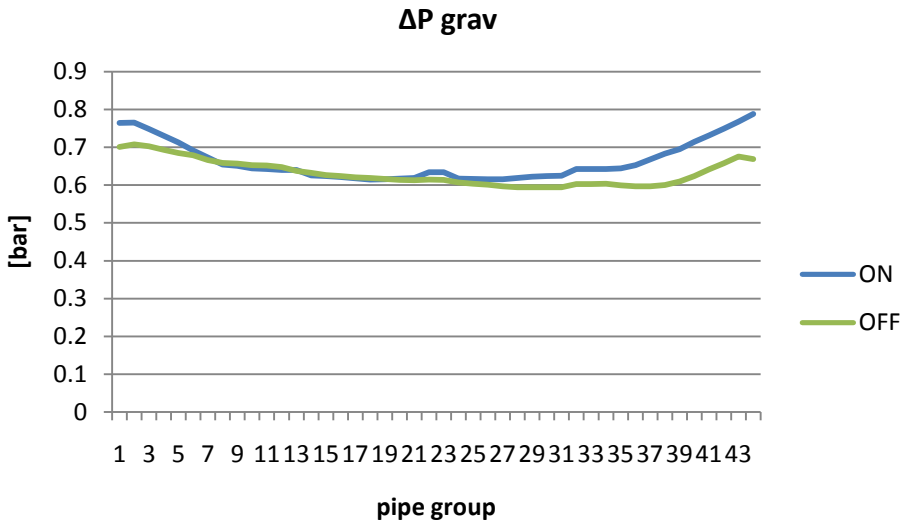

Figure 9.27: Gravitational ΔP variation with the off-design radiation map

9.2.2 Power-block behavior

Power block and boiler are in fact linked only by the amount of steam produced and by the consequent drum pressure. These two aspects depend only on the

total amount of thermal power on the receiver and are independent from the radiation distribution on the receiver.

If it was only macroscopically true for the boiler, it can be surely stated that the reaction of all the different power-block components in the case of June 21st map is exactly the same as for the cases just described for March 21st with hazy sky (the respective attenuation factor being approximately 0.8).

Figures from 9.28 to 9.36 and Tables from 9.1 to 9.9 report the most significant operating parameters of all the power-block components; to permit a better confrontation, also the on-design values have been reported.

Turbine

off design

Table 9.1: Turbine off-design points

Point	p [bar]	m [kg/s]	h [kJ/kg]	T [°C]	s [kJ/kgK]	x [%]
4	29.947	20.9	2803.26	233.8	6.19	1
5	11.993	2.1	2671.57	187.9	6.28	0.9435
6	3.198	1.6	2495.17	135.7	6.40	0.8921
7	0.839	1.5	2334.14	94.8	6.51	0.8533
8	0.096	15.7	2105.22	45.0	6.66	0.8007

on design

Table 9.2: Turbine on-design points

Point	p [bar]	m [kg/s]	h [kJ/kg]	T [°C]	s [kJ/kgK]	x
4	40.00	27.01	2800.90	250.4	6.07	1
5	15.90	2.84	2668.74	201.1	6.16	0.936
6	4.21	2.20	2491.44	145.5	6.28	0.883
7	1.09	2.15	2328.71	102.1	6.39	0.844
8	0.10	19.82	2075.56	45.0	6.57	0.788

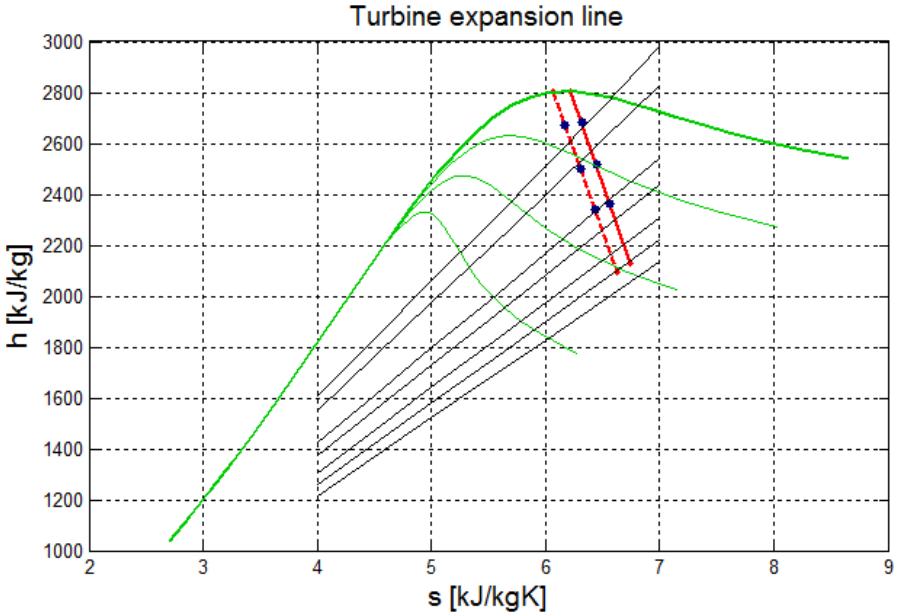

Figure 9.28: March 21st 12:00 and June 21st 16:00 turbine expansion lines

Electrical generator

Table 9.3: On and off-design main generator parameters

	Off-design	On-design
Generator mechanical losses [kW]	99.62	99.62
Generator electrical losses [kW]	253.8	286.9
Generator efficiency [%]	97.1	97.6

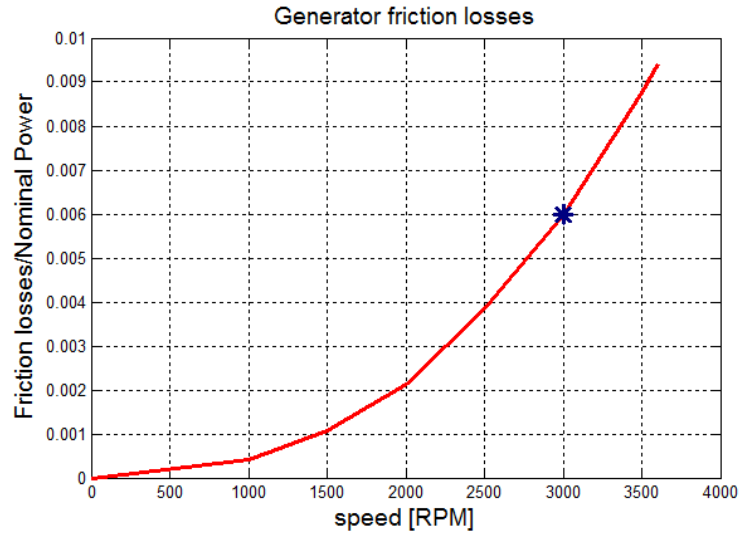

Figure 9.29: On and off-design generator friction losses (overlapped points)

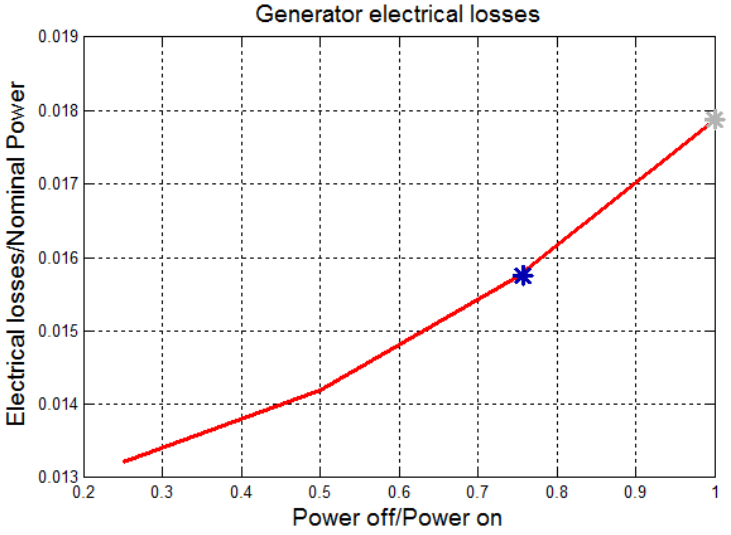

Figure 9.30: On and off-design generator electrical losses

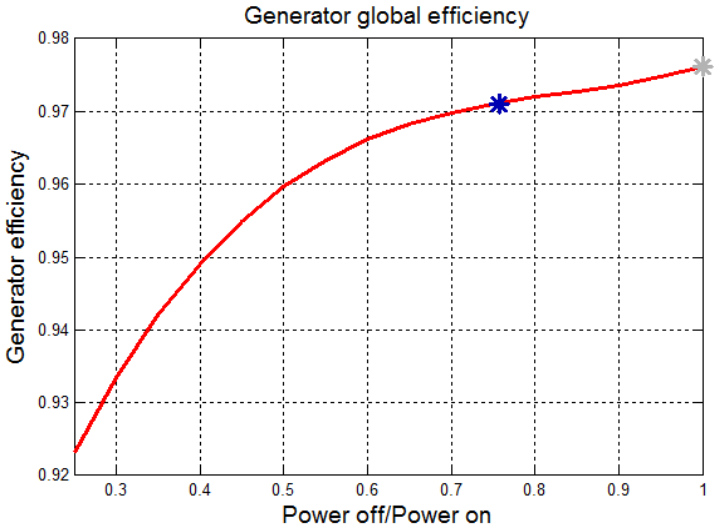

Figure 9.31: On and off-design generator global efficiency

Air Cooled Condenser

Table 9.4: On and off design ACC main parameters

	Off-design	On-design
Number of active fans	10	11
Absorbed power [kW]	482	530.2

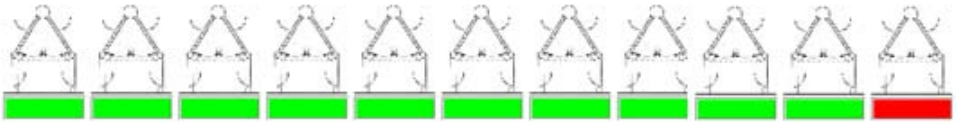

Figure 9.32: Off-design active and switched off ACC cells

Pumps

Table 9.5: On and off-design feed pumping station main parameters

	Off-design	On-design
Feedwater pumping station power [kW]	176.8	189.2
Condensate pump power [kW]	7.4	12.1

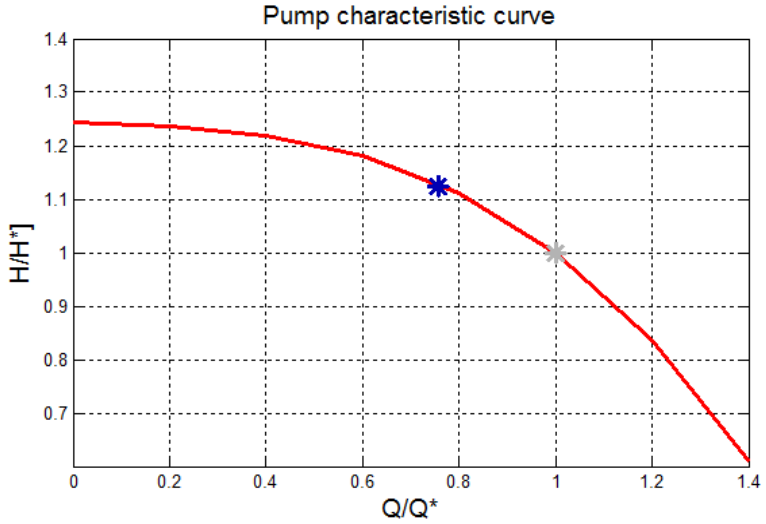

Figure 9.33: On and off-design feed pump operating points

Feedwater heaters

Table 9.6: Off-design FWHs main parameters

	FWH 1	FWH 3	FWH 4
T_in	45.7	134.9	181.9
T_out_subc	49.3	143.4	186.5
T_out	89.8	181.9	227.6
Q_cond	2927.84	3923.52	4424.14
UA_cond	174.255	234.024	256.852
NTU_cond	2.409	2.295	2.387
Effectiveness_cond	0.910	0.899	0.908
Q_subc	259.58	850.05	475.64
UA_subc	13.826	51.388	25.053
NTU_subc	2.185	2.620	2.233

Effectiveness_subc	0.853	0.845	0.850
TTD	4.0	4.3	4.2
DCA	7.0	7.7	7.5

Table 9.7: On-design FWHs main parameters

	FWH 1	**FWH 3**	**FWH 4**
T_in	46.1	143.7	192.6
T_out_subc	50.5	153.6	197.8
T_out	95.1	192.6	240.8
Q_cond	4111.94	5203.17	6055.06
UA_cond	211.48	290.11	318.41
NTU_cond	2.30	2.17	2.26
Effectiveness_cond	0.899	0.886	0.896
Q_subc	396.58	1300.91	697.04
UA_subc	17.123	63.346	31.220
NTU_subc	1.895	2.279	1.928
Effectiveness_subc	0.815	0.815	0.812
TTD	5	5	5
DCA	10	10	10

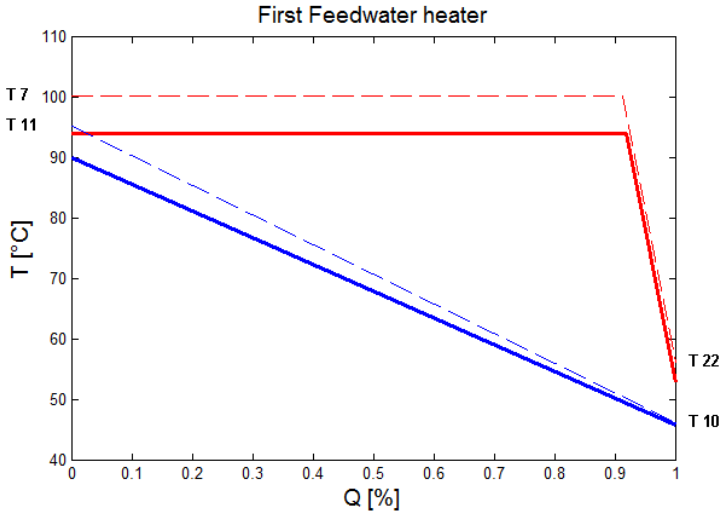

Figure 9.34: On (dot line) and off design (full line) FWH1 T-Q diagram

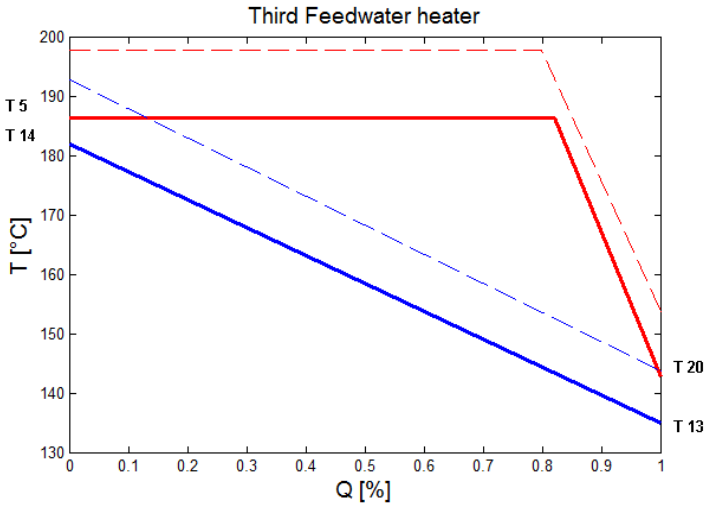

Figure 9.35: On (dot line) and off design (full line) FWH3 T-Q diagram

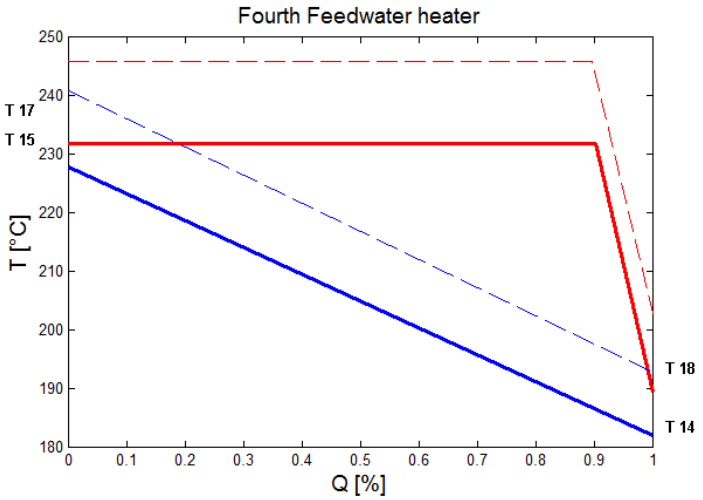

Figure 9.36: On (dot line) and off design (full line) FWH4 T-Q diagram

To better understand the global behavior of the plant in this part-load condition, the thermodinamic conditions of the most representative plant sections and the final global performances of the plant are reported in Tables 9.8 and 9.9.

Table 9.8: Off-design cycle points thermodynamic parameters

	p [bar]	m [kg/s]	h [kJ/kg]	T [°C]
1	29.95	23.31	2803.26	233.8
2	29.95	23.31	2803.26	233.8
3	29.95	23.31	2803.26	233.8
4	29.95	20.90	2803.26	233.8
5	11.99	2.05	2671.57	187.9
6	3.20	1.60	2495.17	135.7
7	0.84	1.51	2334.14	94.8
8	0.10	15.74	2105.22	45.0
9	0.10	17.25	191.28	45.0
10	3.17	17.25	191.70	45.7
11	3.08	17.25	376.33	89.8
12	3.08	23.31	565.09	134.4
13	31.72	23.31	569.33	134.9
14	30.82	23.31	772.62	181.9
15	29.95	23.31	979.03	227.6
16	29.95	2.41	2803.26	233.8
17	28.87	2.41	2803.26	231.8
18	28.87	2.41	805.49	189.4
19	11.54	2.41	805.49	186.2
20	11.54	4.46	600.90	142.6
21	3.08	4.46	600.90	134.4
22	0.81	1.51	221.00	52.8
23	0.10	1.51	221.00	45.0

where the section number is clarified in Figure 9.37.

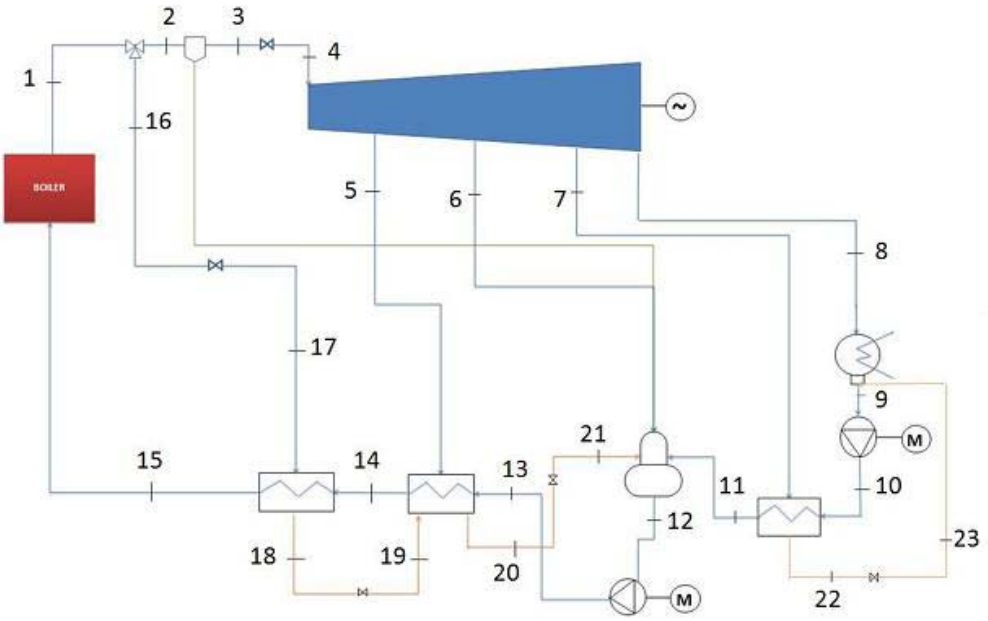

Figure 9.37: Simplified plant layout

Table 9.9: On and off-design main performance parameters

	June 21st 4PM	March 21st 12:00
Heat input [kWt]	42521	53649
Steam generation [kg/s]	23.32	30.49
Net Power Output [kWe]	11189	15000
Cycle efficiency	0.2631	0.2796

9.3 Hazy sky with March 21st radiation map with multiple fixed speed pumps or a single variable speed pump

9.3.1 Different pumping system behavior

In the case of hazy sky, as for all the off-design cases where radiation on the boiler surface decreases, the pump/s behavior is very interesting to study. By reducing the amount of heat that reaches the boiler, the total water mass flow

decreases and the pressure drops change influencing the pumping power absorbed.

For this reason, an interesting analysis involves the different pumping system behavior in the case of a single variable speed pump or more pumps in parallel. In the case of adopting a variable speed pump, pump power decreases in a linearly, while using a system of three parallel pumps produces discontinuities in pump power when one pump is switched off.

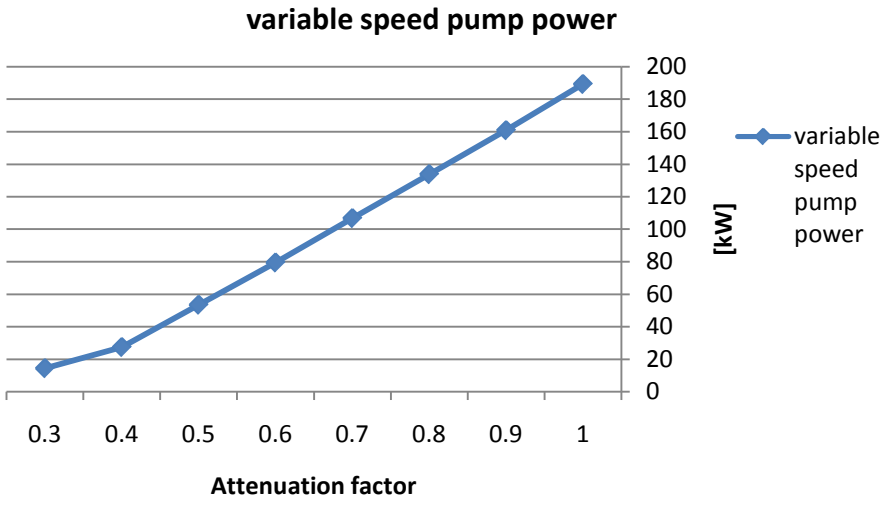

Figure 9.38: Power block variable speed pump power variation with attenuation factor

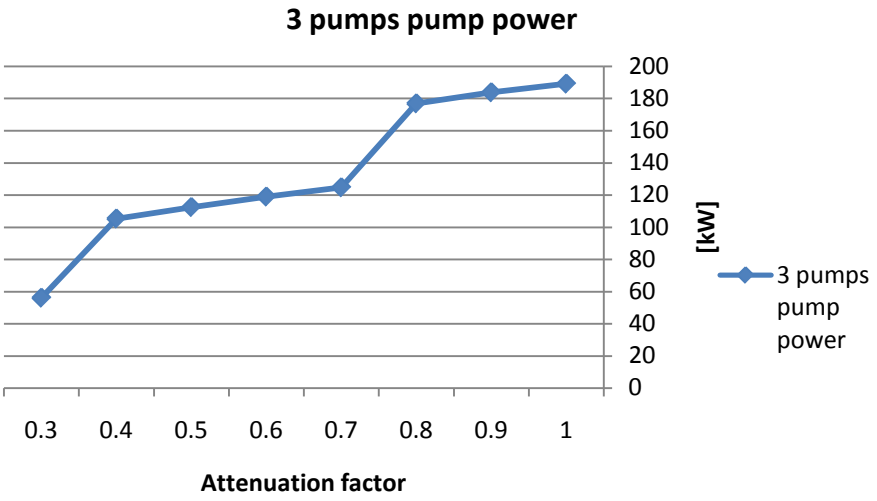

Figure 9.39: Power block 3 pumps system power variation with attenuation factor

Obviously the three tilt changes are linked to the use of three pumps.

Regarding all the other performance parameters like *isentropic and electrical efficiencies* and *volumetric flow* in the case of three pumps, an increase of both efficiencies and of the volumetric flow is observed each time a pump is switched off since the remaining pumps work closer to their rated conditions.

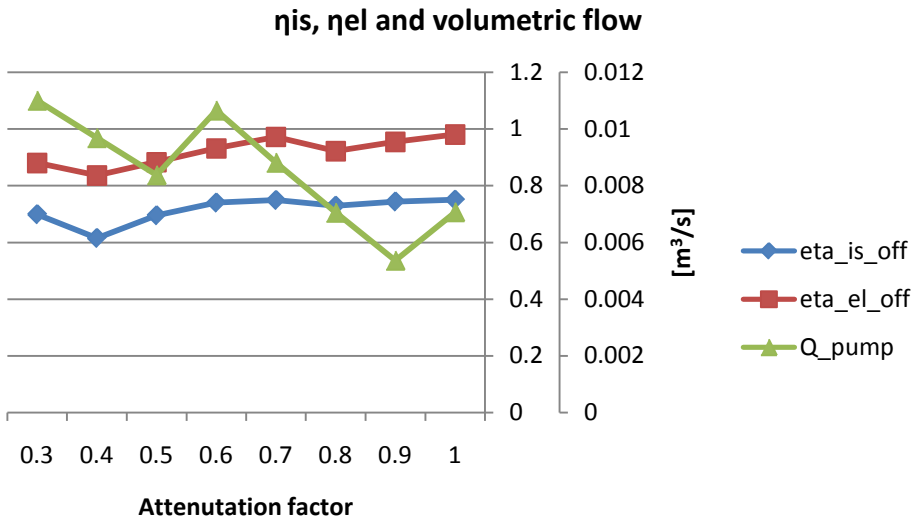

Figure 9.40:3 pumps system isentropic efficiency, electrical efficiency and volumetric flow variation with attenuation factor

On the contrary, if a single variable speed pump is used, off-design conditions are referred to a single pump and, therefore, the part load characteristic values of isoentropic efficiency and electrical efficiency follow those showed in Table 5.6 and 5.8. The off design working condition of the pump is characterized by the new speed regime *n_off*.

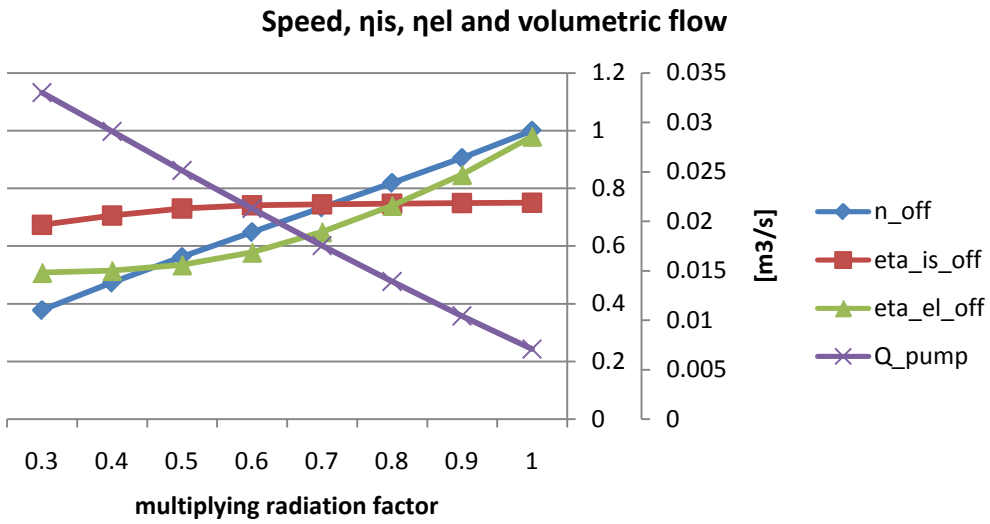

Figure 9.41: Single variable speed pump speed, isentropic efficiency, electrical efficiency and volumetric flow variation with attenuation factor

The speed regime with the attenuation factor equal to 1 corresponds to 3000 RPM for the European grid frequency (50 Hz).

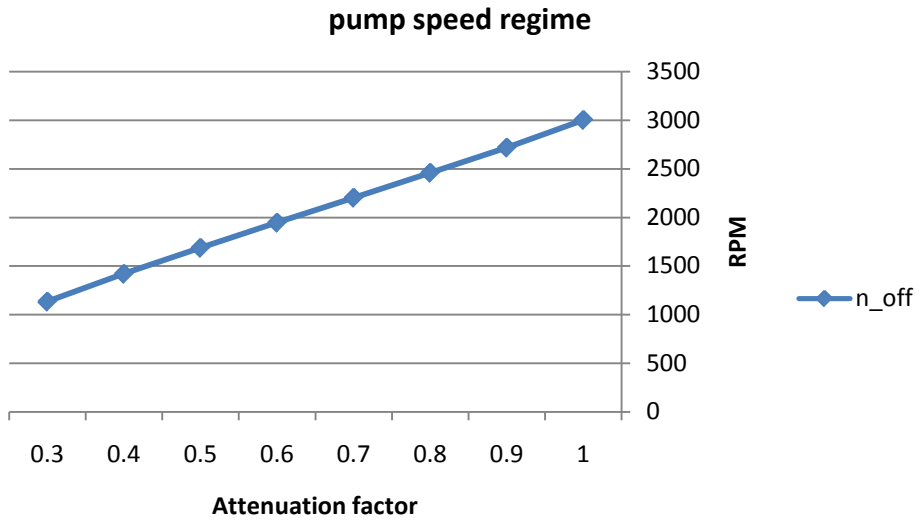

Figure 9.42: Pump speed regime variation with attenuation factor

Figure 9.41 shows that for a linear reduction of the volumetric flow, the electrical efficiency decreases at the beginning with the same tilt angle and then reaches an asymptotic value of 0.5. While the isentropic efficiency remains quite

constant until the volumetric flow reach 0.4 times the nominal flow, which corresponds to an attenuation factor of 0.5.

Confronting the pump power trends in case of three pumps or a single variable speed pump it is possible to note a substantial difference between the boiler pump and the power block pump as shown by Fig. 9.43 and 9.44.

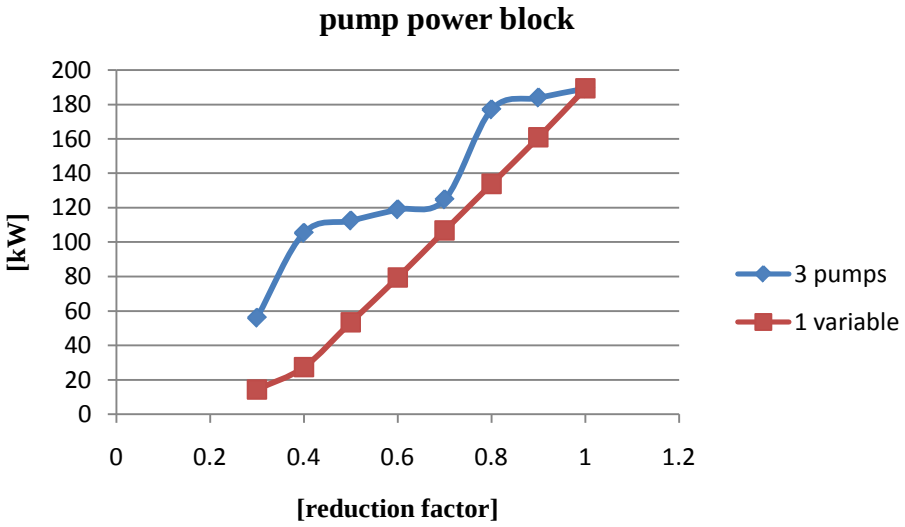

Figure 9.43: Power block pump power trend

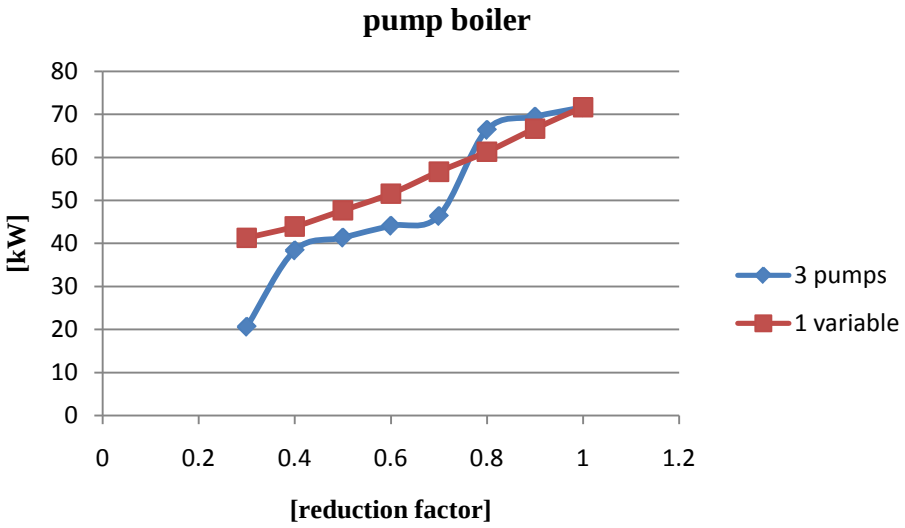

Figure 9.44: Boiler pump trend

What is interesting is that in the case of the boiler pump when there is the switch from 3 to 2 pumps the 3 pumps system absorbs less power than the variable speed pump because this one suffers a high reduction of the isentropic efficiency and most of all of the electrical efficiency, while the 2 pumps work near the nominal values. For this reason in the case of the boiler pump for lower load is more convenient a system with three pumps in parallel.

In the case of the power block pump the main concept is that the influence of the pressure drop value on the pump power is very high (40 bars instead of 1 bar of the boiler pump). The variable speed pump works with the real pressure while the 3 pumps system works with pressure drops near the nominal value; reducing the inlet radiation there is a great decrease of the pressure drop that reduces in a severe way the variable speed pump power. For this reason in the case of the power block pump the variable speed pump is always more convenient than a system of three pumps in parallel.

9.3.2 Boiler behavior

Considering a condensing system that maintains the condenser pressure constant and changing the pumping system from three single speed pumps to a single variable speed pump hardly affects the boiler performance.

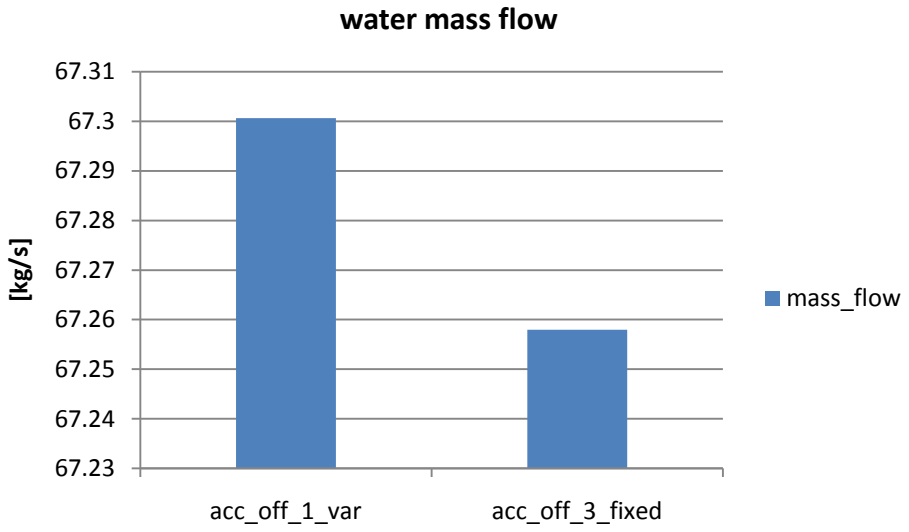

Figure 9.45: Water mass flow variation with ACC

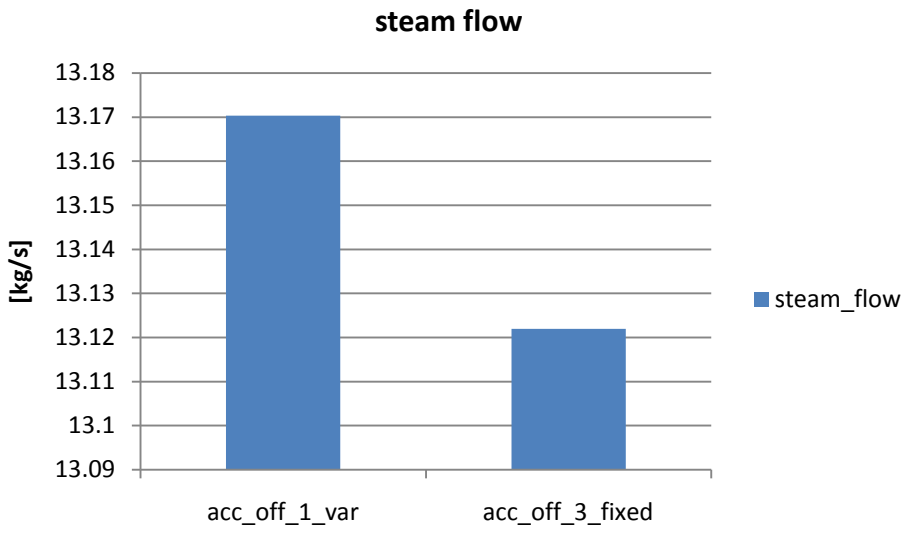

Figure 9.46: Steam flow variation with ACC

The slight differences do not represent a real different behavior because the tolerance in the pressure matching between power block and boiler model is 1.00E-01 that affects a little bit the solution found.

9.3.3 Power-block behavior

The adoption of different pumping stations and of the correspondent regulation strategy does not sensibly affect the thermodynamic parameters of the cycle, the required pressure drop being properly provided in both cases. The basic difference is found in power consumption and, therefore, cycle efficiency and Net Power Output, as shown in Figure 9.47. Considering that feed pump consumption is approximately 1% of gross power production, the effect on global plant performance is not so remarkable. The single variable speed pump presents a lower power request in all part-load conditions, thanks to the possibility to immediately adapt to water mass flow variations. As obvious, the difference between the two systems becomes less relevant if the number of fixed speed pumps increase and their size decreases accordingly.

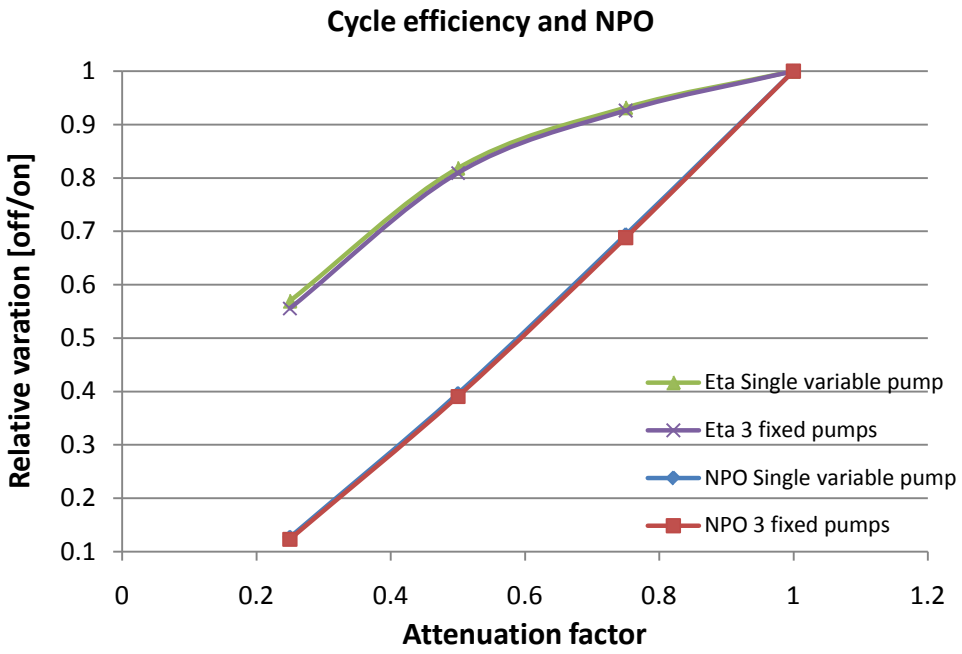

Figure 9.47: Cycle efficiency and NPO variations in case of single variable speed pump or multiple fixed speed pumps

9.4 Hazy sky with March 21st radiation map with ACC cells progressively switched off or ACC cells all on.

As described in paragraph 8.2.4, the Air Cooled Condenser can be regulated in two different manners during part-load operation. The first and most common one consists in progressively switch off ACC cells, according to the heat rejection decrease. This way, the condenser pressure is kept constant and a control on exhaust turbine steam quality is possible. Adopting the second strategy, instead, all the ACC cells are kept in operation; this way, the condenser pressure will decrease because of the higher amount of heat rejected.

To analyze the convenience and the characteristic features of both strategies, a comparison between them has been carried out with different values of incoming radiation (obtained, another time, multiplying the nominal radiation map for a decreasing factor).

9.4.1 Condenser and power-block behavior

The change in ACC regulation strategy basically influences the condenser performance in two aspects:

- auxiliary (fan) power consumption

- steam turbine Δh

Using the first regulation strategy, that is to say switch off ACC cells progressively, the auxiliary power absorption clearly decreases due to the lower number of fans operating. With the second regulation strategy, that is to say keeping all the cells switched on, the power consumption will instead inevitably remain constant.

In Figure 9.48 the different trend of this parameter is shown.

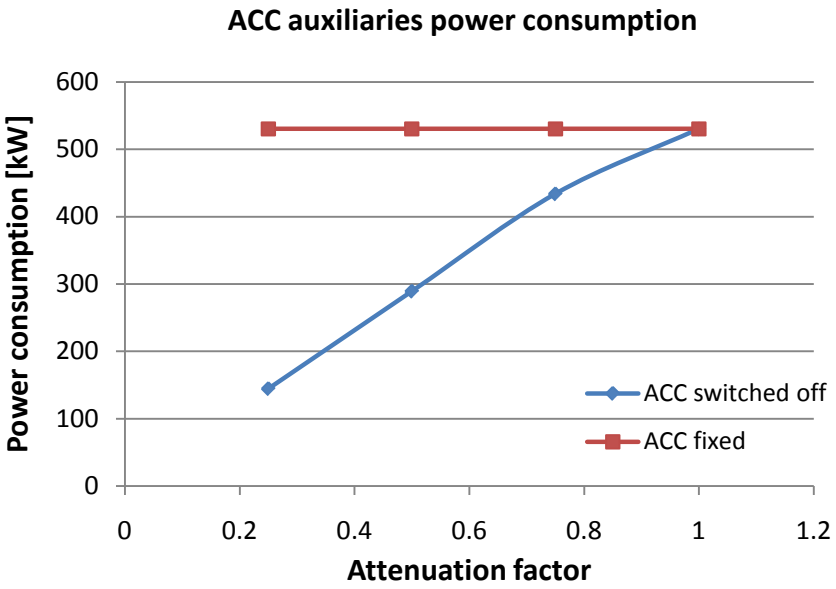

Figure 9.48: ACC auxiliaries power consumption in case according to the adopted regulation strategy

A quite similar graph can be obtained drawing the evolution of condenser pressure. When cells are progressively switched off, indeed, heat rejection capacity decreases along with steam mass flow and the condenser pressure remains approximately constant; on the other hand, if all the cells are kept switched on, to a steam mass flow decrease does not correspond a decrease in rejected heat and the immediate consequence is a lower condenser pressure (Figure 9.49).

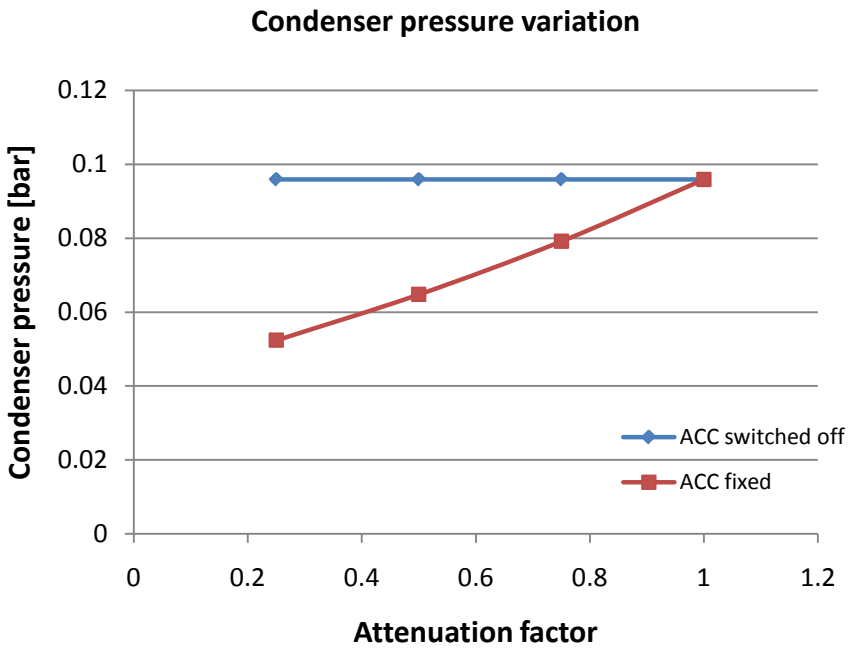

Figure 9.49: Condenser pressure variation according to the adopted regulation strategy

During part-load operation, the turbine expansion line moves right on an h-s diagram and the exhaust enthalpy increases. Using the second regulation strategy this effect is mitigated by the condenser pressure decrease; with the first one, instead, the effect is more visible. Being the inlet turbine enthalpy common to both cases, this phenomenon is directly reflected on the overall turbine Δh, as shown in Figure 9.50.

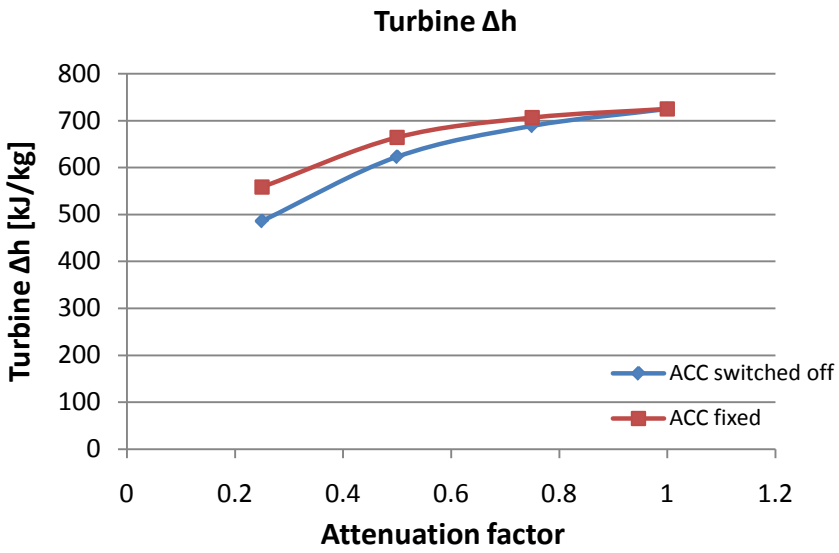

Figure 9.50: Turbine Δh according to the adopted regulation strategy

To understand the real advantages and disadvantages of both strategies, the information about the two aspects just described have to be merged. The first strategy brings about an improvement in terms of power consumption but also a lower Δh and therefore less power production; vice versa with regards to the second strategy.

The results of the simulations show that the advantage in terms of Δh are predominant for a small reduction of thermal input, making the second type of regulation more convenient. But when the thermal input decreases more, the decrease in auxiliary power consumption becomes more important and the first regulation strategy becomes preferable. This phenomenon can be seen drawing the evolution of cycle efficiency for both cases (Figure 9.51).

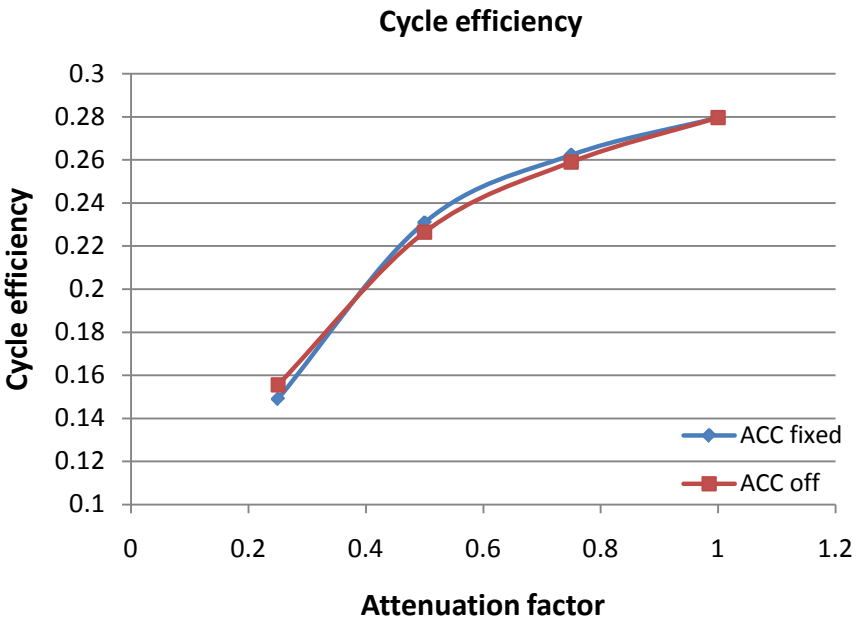

Figure 9.51: Cycle efficiency according to the adopted regulation strategy

Actually, due to the need of an effective control on turbine exhaust conditions, the first regulation strategy is more often adopted.

Apart from these small efficiency variations, the power-block components do not present particular modifications in one or the other case. The pre-heating line presents basically the same thermodynamic parameters and performance; the only remarkable effect is a lower Terminal Temperature Difference in the first feedwater heater due to the lower inlet temperature.

9.4.2 Boiler behavior

To highlight if and how the change in ACC regulation strategy influences the boiler behavior, a single off-design simulation has been performed with a radiation map characterized by the nominal distribution and a 0.5 *attenuation factor*. Considering a pump system composed by three single speed pumps, it can be seen that the different condensing regulation does not affect the boiler performances in terms of steam production, water flow distribution and steam quality distribution.

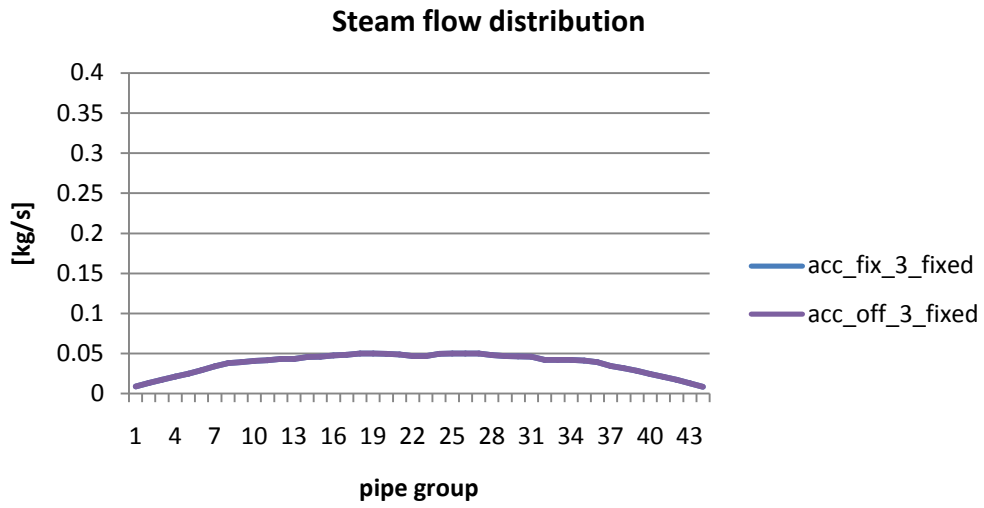

Figure 9.52: Steam flow distribution variation with ACC

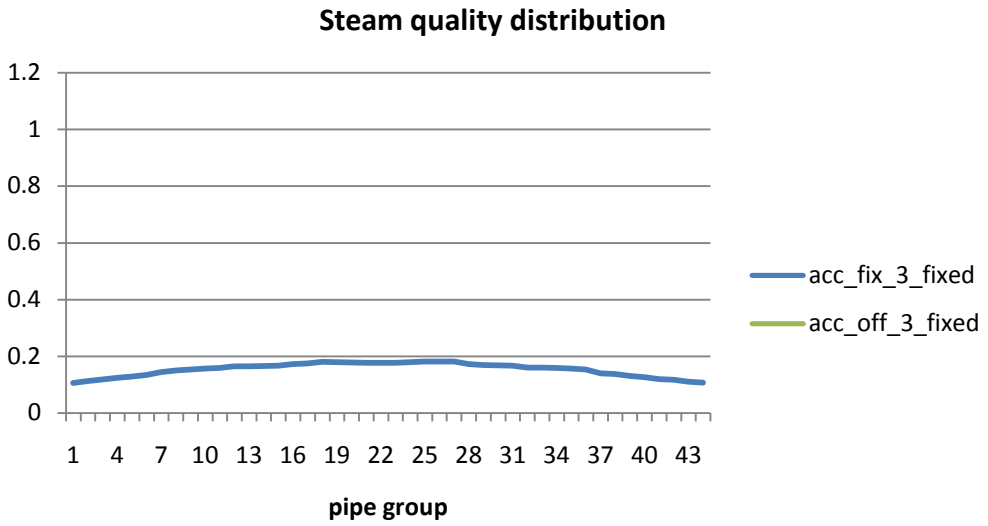

Figure 9.53: Steam quality distribution variation with ACC

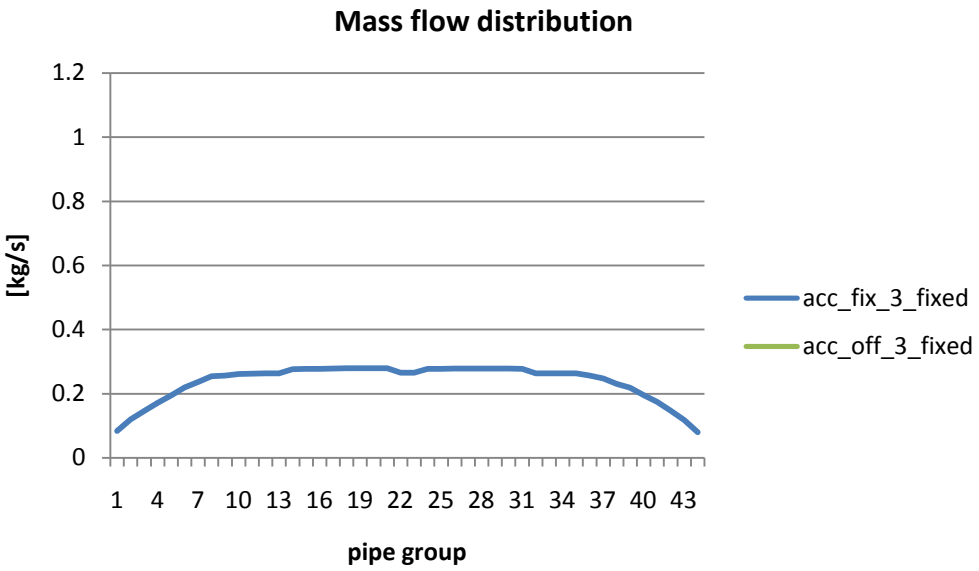

Figure 9.54: Mass flow distribution variation with ACC

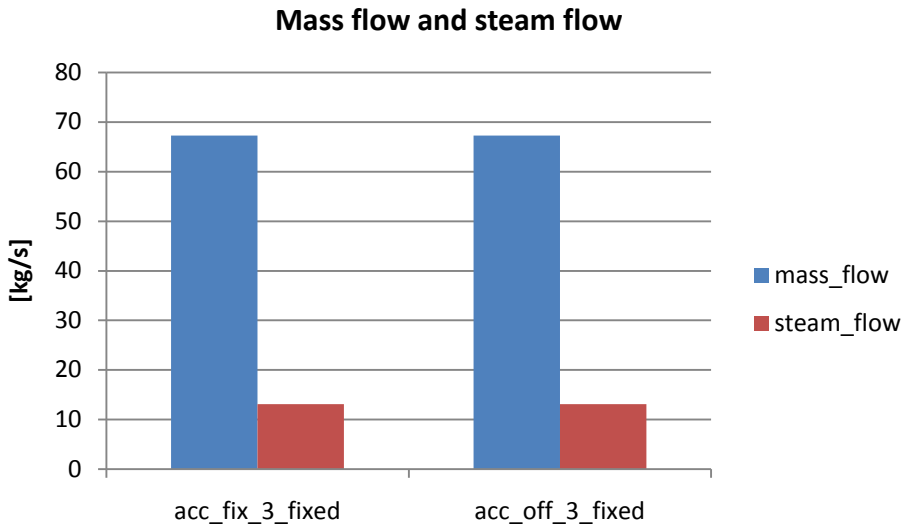

Figure 9.55: Mass flow and steam flow variation with ACC

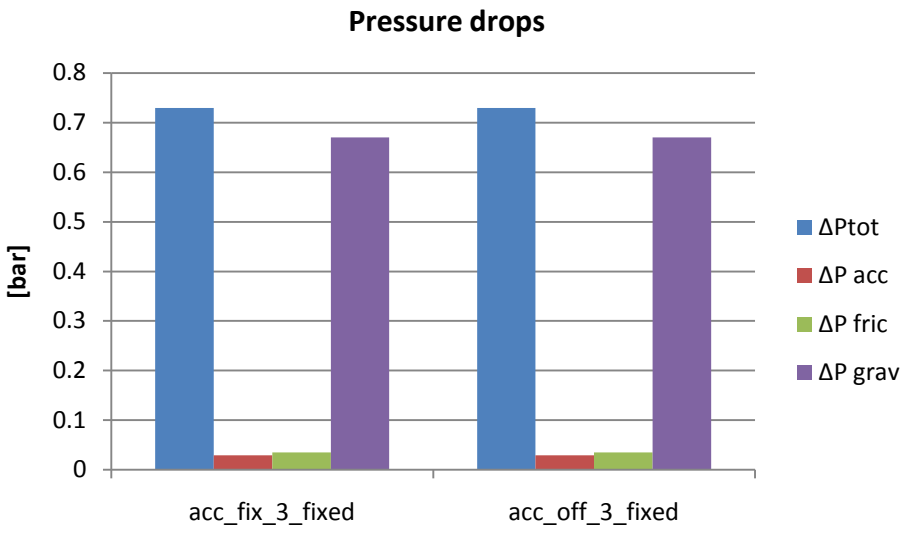

Figure 9.56: Pressure drops variation with ACC

This happens because the condensing regulation does not influence the pressure imposed by the turbine to the drum.

CONCLUSIONS

Considering the increasing importance of solar tower technology and the absence of easy and reliable specific models to simulate the behavior of this kind of plant, a Matlab based code has been developed in order to clarify the particular characteristics of the plant at either on or off-design operations

In particular, the developed model allows for the description of both on and off design behavior of plants with saturated steam receiver and air cooled condenser, being this technology the most representative of current commercial tower plant.

Intrinsic flexibility and a user friendly interface make the model suitable for modeling of several different plants; net power output and drum pressure can be chosen respectively in the range 5 – 50 MWe and 10 – 100 bar, while the majority of the initial assumptions can be easily changed to adapt to several different cases.

The reliability of the model has been tested through the comparison with the public data of PS10, with satisfactory results. Model outputs and PS 10 project values are reported in Table 10.1.

Table 10.1: Model - PS10 comparison

	Model results	**Public PS10 data**
Output at generator terminals[MW]	11	11
Heat input [MW]	35.7	35.8
Steam cycle efficiency [%]	30.8	30.7
Receiver surface [m^2]	195.69	192.96*

*The real PS10 surface is 257.28 m^2 (12 m x 5.36 m x 4 panels) but the 25% of the steam is used in the storage, for this reason this value is 257.28*0.75.

On-design model results

The model can be used to carry on a wide range of studies and analyses. Simulating the nominal conditions, it can be seen how the power-block part of the plant does not differ too much from a traditional steam power plant, except for the low steam thermodynamic parameters and the subsequent wet turbine expansion. More particular is instead the behavior of the central receiver, where

thermodynamic parameters in pipes are function of their position, due to the particular shape of the radiation map.

With regards to the boiler, it has so been understood that the most critical aspect is the pipes temperature. This has been analyzed by a separate thermal model that has shown the importance to fix a low value of steam quality at boiler outlet. In order not to reach high temperature of the pipe walls, the internal heat transfer coefficient must be indeed kept at elevated values, which can be obtained in the saturate flow boiling region. If the steam quality increases, the heat transfer coefficient decreases and the pipes temperature becomes inevitably higher. Considering that each pipe behaves differently due to the radiation map shape, the average steam quality must be kept very low (e.g. 20%) in order to avoid the central pipes, that are the most irradiated, reaching high local steam quality values and consequently very high wall temperatures. Few simulations have been conducted in this sense and have shown that in a pipe characterized by 25% steam quality a peak temperature of 285°C is achieved on the pipe wall while considering an only steam flow, with the same radiation map, the temperature can reach almost 500°C, with severe consequences for the pipe resistance.

It is worth noting that to obtain lower average steam quality values, higher amounts of water have to circulate in the boiler, which involves a higher consumption of the pump and a bigger drum, with remarkable influences on the dynamic behaviour of the plant.

The study of pressure drops and steam quality have underlined that the radiation map influences greatly the water flow distribution. To avoid reaching high temperature and to avoid backflow problems, a constant control of water distribution must be assured. This distribution is most of all affected by the influence of each pressure drop component: for a high water mass flow or for high steam production the accelerative and friction components become more significant changing completely the water flow distribution.

Being pressure drops and steam quality affected mainly by the radiation map, the model has shown that to avoid risks in the boiler operations, it is of fundamental importance a contemporary control on:

- Radiation incident on the boiler surface.
- Water flow distribution in each pipe.
- Steam quality at the outlet of each pipe.

As said, the particular configuration of the model permits the easy variation of a high number of power-block and boiler parameters. To provide examples of the

model reaction to these changes and at the same time obtain useful information on the plant behavior, the following parametric analyses have been conducted:

a) Fixed Net Power Output and Drum Pressure; changes in

- $\eta_{is,turbine}$ (0.6 – 1)

- Terminal Temperature Difference (0 – 30 °C)

- Drain Cooler Approach (0 – 30 °C)

- Pressure Drops in the FWHs (0 – 15%)

- Ambient temperature/condenser pressure (0 – 50 °C)

- Type and design of pumping stations

- Type and design of Air Cooled Condenser

- Grid frequency (50/60 Hz)

- Nominal Radiation/Thermal power input on the boiler (default value: 60.43 MW);

- Boiler outlet steam quality (default value: 0.2);

- Boiler efficiency (default value: 0.92);

b) Fixed Drum Pressure, changes in Net Power Output (5 – 50 MWe)

c) Fixed Net Power Output, changes in Drum Pressure (10 – 100 bar).

The results of the parametric analyses can be used to identify the influence of different parameters on the global plant performance. In particular, the effect that “power-block side” parameters modification has on cycle efficiency and that “boiler side” parameters modification has on boiler dimensions have been analyzed. Summary plots of these aspects are reported in Figure 10.1.

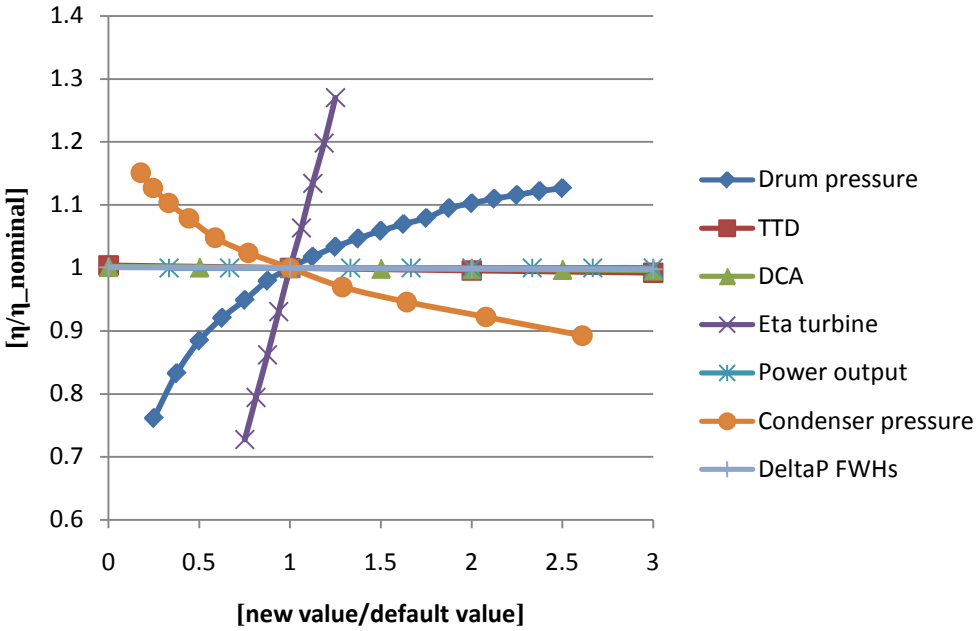

Figure 10.1: Influence of "power block side" parameters on cycle efficiency

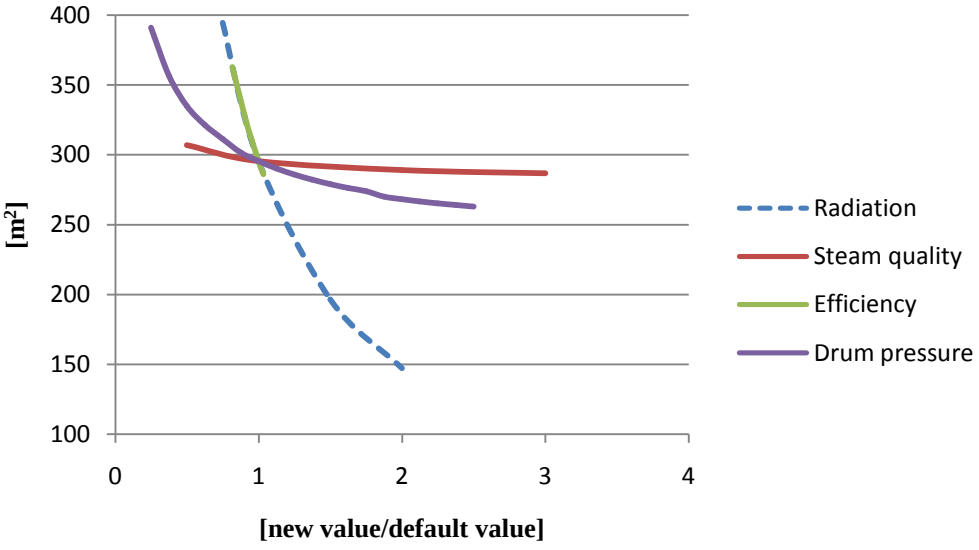

Figure 10.2: Influence of "boiler side" parameters on boiler surface

In Figure 10.1 horizontal lines show a practically negligible influence of TTD, DCA and ΔP_{FWHs} on plant performance. To intervene on their modification appears therefore a quite useless effort. Also the plant size does not influence the global performance, considering that the model keeps constant values of efficiency for each component.

A more relevant effect is obtained by changing drum or condenser pressure, which are respectively inlet and exhaust turbine pressures. The model clearly shows that, according to the changes in turbine Δh, the effect of these variations is opposite: cycle efficiency increases with a condenser pressure decrease and a drum pressure increase, and vice versa. The aim of obtaining a higher efficiency operating on these aspects is in contrast with technical issues and should be object of appropriate optimizations. Without entering into details, it can be said that a condenser pressure decrease can be obtained to the detriment of the fan power consumption or, alternatively, by using a Water Cooled Condenser, with the correspondent already mentioned difficulties. On the other hand, a drum pressure increase in case of saturated steam boiler implies also a temperature increase and the combining of these two components results in a relevant worsening of pipes thermo-mechanical stresses.

The most remarkable effect on plant performance is given by the variation of isentropic turbine efficiency. The high slope of the line shows that also small improvements in the turbomachinery fluid dynamic permit a relevant cycle efficiency increase.

It has to be noticed that this last aspect is strongly correlated with turbine wet conditions. The absence of a steam super-heating section in the boiler involves the turbine working in humid conditions in the whole expansion; according to the Bauman rule, the loss of efficiency is roughly one per cent for every one per cent of wetness at the particular stage and the effect on cycle efficiency is therefore sensitive.

This aspect, in addition to the thermodynamic benefits that could be obtained, stimulates to focus on the possibility to introduce a super-heating section in the receiver. A relevant cycle efficiency increase could take place in this case, against an increase of capital cost investments due to the higher receiver and solar field dimensions.

To increase the cycle performance, also a steam re-heating can be planned, obtained another time by the “solar part” dimensions increase.

The power-block part of the model is currently designed to work with a saturated steam turbine and it is not able to simulate the case of a super or a re-

heating. Among the future developments of the work, the introduction of these two possibilities represents anyway one of the most relevant aspects.

In Figure 10.2 it can be instead first of all noticed that the curves representing the variation of boiler dimensions in case of boiler efficiency and nominal radiation changes are overlapped; actually, an efficiency or a radiation decrease produce macroscopically the same effect on the boiler. As done for the cycle efficiency, the graph permits to evaluate which parameters affect more the boiler dimensions, extremely important because of their immediate correlation with plant costs. In particular, having higher fluxes in the radiation map causes a drastic reduction of the absorbing surface but implies higher pipe wall temperatures and a bigger heliostat field; both these effects are linked to an increase of the plant cost (high performance pipes material and higher number of heliostats).

Interesting is also the influence of drum pressure, due in particular to the changes in vaporization enthalpy. Increasing the drum pressure the global heat demand decreases and therefore, considering the same heliostat field, there is a reduction of boiler dimensions. The problem is that an increase of the internal pressure in the pipes means thicker wall and so an elevated receiver cost. Another parameter that influences the boiler surface, even if slightly, is the average steam quality at the outlet of boiling pipes. An increase in the steam quality means a severe decrease of the total mass flow but a contemporary increase of the Δh and therefore a reduction of the boiler surface. It can be clearly noticed in the graph 10.2 that this reduction is asymptotic and therefore, considering that an increase of the steam quality involves an increase of pipes wall temperature, increasing this value does not appear particularly convenient.

Off-design model results

While the just mentioned analyses were basically referred to the plant design in nominal conditions, the off design model provides a set of useful information on the plant behavior during part-load operation. The model is designed to get as input a radiation map and to calculate the thermodynamic characteristics of the plant, particularly the new power output and cycle efficiency. This way, having a sufficient number of radiation maps, a daily or also yearly energy production analysis can be conducted with a good level of approximation. Through these results, an economical analysis could be performed, in order to obtain the Levelized Cost Of Electricity related to this kind of plant and to identify the most relevant economic parameters. Unluckily, only a few radiation maps are nowadays publicly available, and the economic analysis had to be leaved aside in this work. Nevertheless, once obtained more radiation maps or developed an appropriate sub-model to describe the heliostat field and the reflected radiation,

the current off-design model will represent a reliable tool for performing these studies.

At the moment, the off-design model has demonstrated its usefulness allowing the study of different components reactions whit a thermal power input variation. New turbine expansion lines can be drawn, obtaining useful information on the wetness decrease too. Moreover, the analysis of the Thermal Temperature Difference variation has let to identify a progressive decreasing of this parameter in part-load operation. The small variation and, besides, the small influence that this parameter has on the global cycle efficiency (see Figure 10.1), can lead us to accept the simplifying hypothesis of a constant TTD in part-load operations.

The analysis of different pumping stations and regulation strategies has let the identification of the best solution in terms of pump power consumption during part-load operations. An interesting result has arisen from the parallel study of the boiler and the feed pumping stations. As visible in Figures 10.3 and 10.4, the first one has shown a lower power consumption from 1 to 0.6 load with a single variable speed pump and with three fixed speed pumps below 0.6 of nominal load. Differently, the feed pump consumption results always lower in the case of a single variable speed pump.

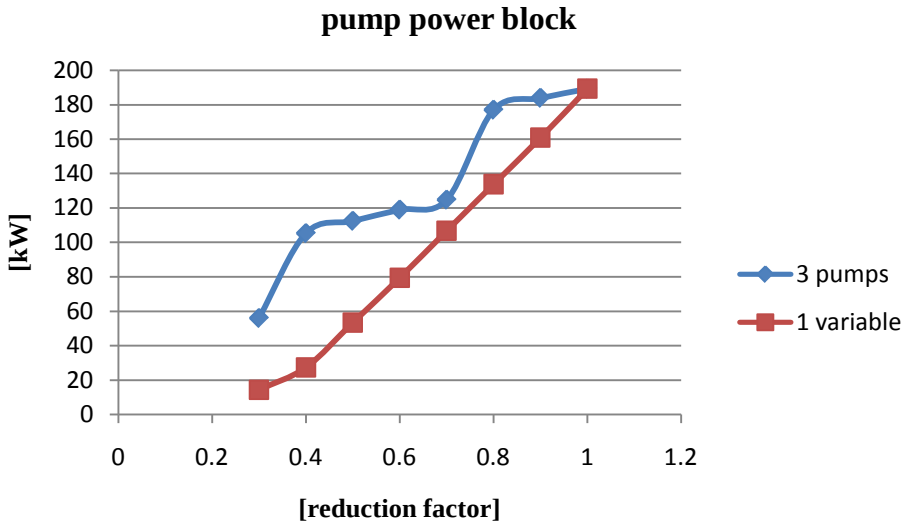

Figure 10.3: Power block pump power trend

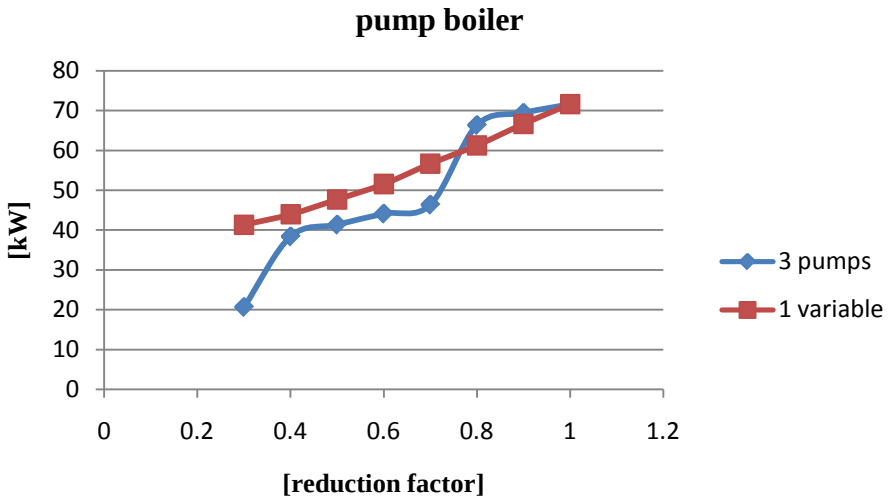

Figure 10.4: Boiler pump power trend

As for the pumps, also the Air Cooled Condenser regulation strategy has been analyzed through the model. Results shown in Figure 10.5 indicate that keeping all the condenser cells switched on therefore lowering the condenser pressure presents advantages for part load operations till approximately a 50% load. For lower loads, the positive effect on cycle efficiency given by the reduced fans power consumption becomes predominant and the other kind of regulation strategy becomes preferable.

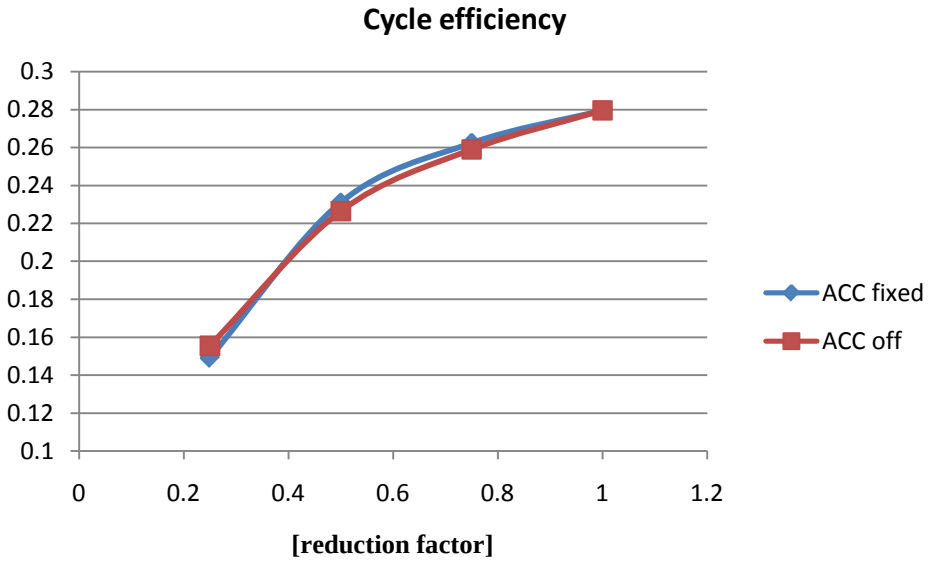

Figure 10.5: ACC influence

These analyses have been performed with a “reference” power plant, but they could be repeated with different parameters in terms for instance of plant size, pumps or ACC cells size and characteristics curves and off-design maps. According to the simulated situation, the best regulation strategy could be so defined.

Project future developments

According to the current trend in solar tower technology, the model will be developed in order to introduce several other aspects. At first, a heliostat-field sub-model wants to be introduced, in order to avoid the need for given radiation maps and to correlate the Net Power Output directly to the irradiation conditions. Besides, the thermal storage and the possibility of steam super-heating and re-heating will be analyzed and possibly included in the model, such as the use of a different fluid (molten salts). On a smaller scale, a more precise description of the steam turbine behavior is already being developed, including the efficiency definition through Spencer, Cotton and Cannon method [50] and the analysis of exhaust and wetness losses.
Two other important aspects that could improve the accuracy and the value of the model are the implementation of a different piping configuration and the thermal model insertion inside the global code. With the first addition it should be possible to study the best piping layout to exploit the chosen radiation map and with the second one a direct control on the pipe temperature could be obtained.

More challenging but planned is also the introduction of a set of transient situations in the model. This way, critical behaviors of the plant could be deeply analyzed, in order to define the best possible solutions.

References

[1] ENEA, *Calore ad alta temperature dall'energia solare*

[2] International Energy Agency (IEA), *Key world energy statistics. 2009*

[3] Conference of the parties, *Copenhagen accord*, 18 December 2009, Copenhagen

[4] IPCC, *Fourth Assessment Report, Climate Change 2007*

[5] International Energy Agency (IEA), *World Energy Outlook 2009*

[6] Emerging energy research, *Global concentrated solar power markets and strategies, 2007-2020*

[7] European Solar Thermal Electricity Association (ESTELA), *Solar power from the sun belt, June 2009*

[8] J. Duffie, W. Beckman, *Solar Engineering of thermal processes,* John Wiley & Sons, inc., New York

[9] European Photovoltaic Industry Association (EPIA), *Solar photovoltaic electricity: A mainstream power source in Europe by 2020.*

[10] Schlaich J., Bergermann R., Schiel W., Weinrebe G., *Design of commercial solar updraft tower systems – Utilization of solar induced convective flows for power generation, 2005*

[11] Manuel Romero, CIEMAT, PP presentation, *Produccion de hidrogeno con energia solar*

[12] *Enciclopedia degli idrocarburi, Vol.III, Cap.6 – Generazione elettrica da fonti rinnovabili,* available on-line at www.treccani.it

[13] Available on-line
http://www.torresolarenergy.com/en/proyecto_gemasolar.html

[14] Wei, X. et al. A new code for the design and analysis of the heliostatfield layout for power tower system. Sol. Energy (2010), doi:10.1016/j.solener.2010.01.020

[15] R. Kistner, H.W. Price, *Financing Solar Thermal Power Plants*, Proceedings of the ASME Renewable and Advanced Energy Systems for the 21st Century Conference, 1999, Maui

[16] Holmgren M., *XSteam for MATLAB*, 2006, available on www.x-eng.com

[17]MATLAB R2007b Product Help, Optimization Toolbox, fsolve

[18] Dennis, J. E. Jr., *Nonlinear Least-Squares*, State of the Art in Numerical Analysis, ed. D. Jacobs, Academic Press, pp. 269-312.

[19] Levenberg, K., *A Method for the Solution of Certain Problems in Least-Squares*, Quarterly Applied Mathematics 2, pp. 164-168, 1944.

[20] Powell, M. J. D., *A Fortran Subroutine for Solving Systems of Nonlinear Algebraic Equations,* Numerical Methods for Nonlinear Algebraic Equations, P. Rabinowitz, ed.,Ch.7, 1970.

[21] Falcone, P.K., 1986, *A Handbook for Solar Central Receiver Design*, Sandia National Laboratories, Livermore, CA

[22] *Handbook of Energy Efficiency and Renewable Energy*, Frank Kreith (Editor), D. Yogi Goswami (Editor)

[23] Ruiz Hernandez, V. *La electricidad solar termica, tan lejos, tan cerca*, gasNatural Fundaciòn, 2009

[24] Kistler B. L., 1986. *A user's manual for DELSOL 3, A computer Code for Calculating the Optical Performance and Optimal Design for Solar Thermal Central Receiver Plants*, Sandia National Laboratories, Livermore, CA, SAND86-8018.

[25] Collado F. J., *Quick evaluation of the annual heliostat field efficiency* SolarEnergy 82 (2008) 379–384

[26] Schell, S. *Design and evaluation of esolar's heliostat fields.* Sol. Energy (2010), doi:10.1016/j.solener.2010.01.008

[27] Yao et al., *Modeling and simulation of the pioneer 1MW solar thermal central receiver system in China*, Renewable Energy 34 (2009) 2437–2446

[28]Sanchez, M., Romero, M., *Methodology for generation of heliostat field layout in central receiver systems based on yearly normalized energy surfaces*. Solar Energy 80, 861–874, 2006.

[29] Alpert D.J., Kolb G.J. *Performance of the Solar One Power Plant as simulated by the SOLERGY Computer Code*, Sandia National Laboratories, Livermore, CA, 1988, SAND88-0321

[30] Pacheco, J.E., *Summary of the Solar Two test and evaluation program*, Sandia National Laboratories, Livermore, CA, 2000, SAND2000-0372C

[31]*PS10: a 11.0 MW Solar Tower Power Plant with Saturated Steam Receiver*, 2005. Available from http://www.upcomillas.es/catedras/crm/report05/Comunicaciones/Mesa%20IV/D%20Valerio%20Fern%C3%A1ndez%20-%20Solucar%202.pdf

[32] *10MW Solar Thermal Power Plant for Southern Spain*, 2006. Available from: http://ec.europa.eu/energy/res/sectors/doc/csp/ps10_final_report.pdf

[33]Power digest: *Abengoa begins commercial operation of PS20 solar tower in Spain*, Power volume 153-6, 2009

[34] H.Hasuike, Y. Yoshizawa, A. Suzuki, Y.Tamaura, *Study on design molten salt solar receivers for beam-down solar concentrator*, May 2006

[35] M.Yang, X.Yang, X.Yang, J.Ding, *Heat transfer enhancement and performance of the molten salt receiver of a solar power tower*, April 2009

[36] J. Pacheco, R.Gilbert *Overview of recent results of the Solar Two test and evaluations program*, Sandia National Labs

[37] C.Tyner, G.Kolb, M.Prairie *Solar Power Tower Development: Recent Experiences*

[38] J.M.Lata, M. Rodriguez, M. Alvarez de Lara, *High flux central receivers of molten salts for the new generation of commercial stand-alone solar power plants*, SolarPACES 2006

[39] R. Pitz-Paal, *High temperature solar concentrators*,

[40] G.Koll, P. Schwarzbozl, K.Hennecke, T.Hartz, M.Schmitz and B. Hoffshmidt, *The solar tower Jülich – A research and demonstration plant for central receiver systems*,

[41] Ing. Mazzi, *Corso su generatori di vapore ad ingegneria solare*, Lesson 15 June 2009, Politecnico di Milano

[42] M.Epstein, D.Liebermann, M.Rosh, A.J.Shor, *Solar testing of 2 MW_{th} water/steam receiver at the Weizmann Institute solar tower,* Solar Energy Materials 1991

[43] V. Ganapathy, *Industrial boilers and heat recovery steam generators,* Ed. Marcel Dekker, 2003

[44] J.R.S. Thom, *Prediction of pressure drop during forced circulation boiling of water,*1964

[45] Incropera, DeWitt, Bergman, Lavine, *Fundamentals of Heat and Mass transfer*, 6th edition, Wiley,

[46] Xin Li, W.Kong, Z.Wang, C.Chang, F.Bai, *Thermal model and thermodynamic performance of molten salt cavity receiver,* 2009

[47] *The steam and condensate loop*, Spirax Sarco, 2005

[48]Friedel. *Improved friction pressure drop correlations for horizontal and vertical two-phase pipe flow.*1979

[49] Awad and Muzychka. *A simple two-phase multiplier calculation method.* 2004

[50] Black & Veatch, *Power Plant Engineering,* Chapman & Hall, New York, 1996

[51] Gill A.B. *Power Plant Performance*, Butterworths, 1984

[52] Mataix C., *Turbomaquinas termicas*, Editorial dossat,s.a. Madrid, 1988

[53] Spencer, R.C., Cotton K.C. and Cannon, C.N. *"A method for Predicting the Performance of Steam Turbine-Generator, 16,500 kW and larger"*, ASME Power Division, Paper No. 62-WA-209, USA, 1974.

[54] R.W. Haywood, *Analysis of Engineering Cycles (2nd Ed.),* Pergamon Press, 1975, Oxford

[55] Conradie, A. E., Kroger D.G., "Performance Evaluation of Dry-Cooling Systems for Power Plant Applications", Applied Thermal Engineering. 16-3:219-232, 1996

[56] Dixon S. L., *Fluid mechanics and thermodynamics of turbomachinery*, 4th edition Paperback, 1998

[57] Stodola, *"Steam and Gas Turbines"*, ed. Mc Graw Hill.

[58] D.H. Cooke, *Modeling of off design multistage turbine pressures by Stodola's ellipse*, presented at Energy incorporated Pepse users' group meeting, 1983, Richmond

[59] Vitalis, Riley Power Inc., *Constant and sliding-pressure options for new supercritical plants*, www.powermag.com. February 15,2006.

[60] E. Macchi, A. Perdichizzi, *A theoretical prediction of the off-design performance of axial-flow turbines.* s.l. : Martinus Nijhoff Publishers, 1977, pp.1867-1896.

[61] Lippke, Frank (1995). *Simulation of the Part Load Behavior of a 30MWe SEGS Plant.* Albuquerque : Sandia National Laboratories,.

[62] Kolb, G.J., Jones, S.A., Donnelly, M.W., Gorman, D., Thomas, R.,Davenport, R., Lumia, R., *Heliostat Cost Reduction Study*, (2007) SAND2007-3293.

[63] Schegliàiev, A.V., *Turbinas de Vapor, la teoria del proceso termico y las construcciones de turbinas*, Editorial Mir Moscù, 1978

[64] A.M. Patnode, *Simulation and performance evaluation of parabolic trough power plants*, Master thesis, 2006, University of Wisconsin – Madison

[65] Thermoflow Suite 19 User's Manual, Thermoflow Inc. 2010.

[66] J.Agüera, *Mecánica de fluidos incompresibles y turbomáquinas hidráulicas*, Editorial Ciencia 3, Madrid, 1996.

[67] G.M. Jones (ed.), *Pumping Station Design*, Butterworth-Heinemann, Oxford, 2006.

[68] C. Mataix, *Turbomáquinas hidráulicas*, Ed. ICAI, Madrid, 1975.